Bourban, Sébastien; Durand, Noémie; Hervouet, Jean-Michel (Hg.)

Proceedings of the XIXth TELEMAC-MASCARET User Conference 2012, 18 to 19 October 2012, St Hugh's College, Oxford

HR Wallingford
Working with water

Proceedings of the

XIXth TELEMAC-MASCARET User Conference

18 to 19 October 2012, St Hugh's College, Oxford

Edited by Sébastien Bourban, Noémie Durand and Jean-Michel Hervouet

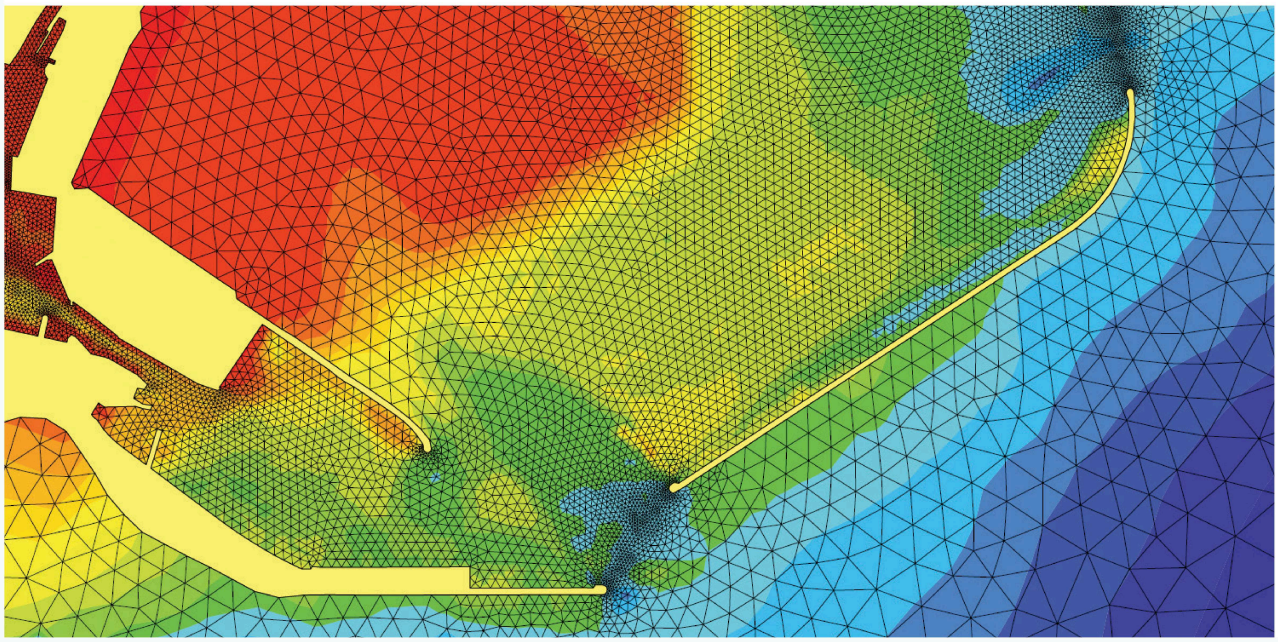

HR Wallingford *Working with water*
ARTELIA
Ministère de l'Écologie, du Développement durable, des Transports et du Logement
cetmef
eDF
BAW Bundesanstalt für Wasserbau
Federal Waterways Engineering and Research Institute
Science & Technology Facilities Council
Daresbury Laboratory

HR Wallingford

Proceedings of the

XIXth TELEMAC-MASCARET User Conference

18 to 19 October 2012, St Hugh's College, Oxford

Editors
Sébastien Bourban
Noémie Durand
Jean-Michel Hervouet

Proceedings of the

XIXth TELEMAC-MASCARET User Conference

18 to 19 October 2012, St Hugh's College, Oxford

Organised by

HR Wallingford
Howbery Park, Wallingford, Oxfordshire OX10 8BA
www.hrwallingford.com

Edited by

Sébastien Bourban

Noémie Durand

Jean-Michel Hervouet

Credits

Cover pictures by
HR Wallingford

Published by HR Wallingford Ltd, Howbery Park, Wallingford, Oxfordshire OX10 8BA
Telephone +44 (0)1491 835381, Fax +44 (0)1491 832233
www.hrwallingford.com

ISBN-10: 1-898485-15-1
ISBN-13: 978-1-898485-15-5

HR Wallingford

Sébastien Bourban, editor

October 2012

Foreword to the XIXth TELEMAC-MASCARET User Conference

Dear participants,

HR Wallingford is delighted to organise the XIXth TELEMAC-MASCARET User Conference in Oxford, a beautiful town renowned worldwide for Alice in Wonderland and the Mini Cooper car factory, but most relevant here, for its academic excellence. Oxford is just a short drive from HR Wallingford where those of you who participated in the pre-conference workshops will remember the tour around its impressive physical modelling halls and the immersion in its virtual world ship simulator.

The TELEMAC-MASCARET user community is now strong of c.3000 users and organisations, i.e. c.1000 more users than last year. HR Wallingford is proud to host, develop and maintain for the community a series of access sites, including the website (www.opentelemac.org, www.openmascaret.org), the source code repository (svn), the source code documentation (docs), the general documentation (wiki) and several other sites critical for the organisation and activities of the TELEMAC-MASCARET Consortium.

Following on last year lead by EDF-LNHE, the user club meeting is again organised as an international conference with published proceedings. The scientific committee has received 34 abstracts, of which 25 were turned into 6 to 8 page articles, here enclosed. The conference features oral presentations from all 34 authors. Participants to the conference are mainly coming from Europe (UK, France, Germany, Austria, The Netherlands, Ireland, Italy), but also from the Middle East (The Emirates), from Asia (South Korea) and from Oceania (Australia).

On behalf of HR Wallingford and of the TELEMAC-MASCARET Consortium, I am happy to welcome you to Oxford for this XIXth TELEMAC-MASCARET User Conference.

Thank you for your participation

Sébastien Bourban

HR Wallingford
Howbery Park
Wallingford
Oxfordshire
OX10 8BA

Contents

Day 1

Session 1

Session 2

Session 3

Session 4

** (Paper not available at time of publication)*

Day 2

Session 5

Session 6

Session 7

Session 8

Session 9

Application of TELEMAC-3D to sediment-laden flow on flat bed configuration

Nicolas Huybrechts
Roberval Laboratory, LHN (joint research unit UTC-CETMEF), UMR CNRS 7337
Compiègne, France
nicolas.huybrechts@developpement-durable.gouv.fr

Pablo Tassi and Catherine Villaret
EDF R&D – LNHE – LHSV
Chatou, France
pablo.tassi@edf.fr
catherine.villaret}@edf.fr

***Abstract*—The development of three-dimensional (3D) sediment transport model remains a challenging task, due to our limited knowledge of the complex sediment turbulent flow interactions, as well as the inherent difficulty to represent numerically the large gradients of flow and sediment distribution. In this work, we compare 3D numerical simulations of coupled flow and suspended sediment transport with some well documented flume data. In order to isolate the effect of particles in suspension on the turbulent flow field, we mimic starved bed experiments, where sediment is progressively added to the clear flow below saturation (no deposit). Numerical simulations are based on the TELEMAC-3D module of the open-source TELEMAC Modelling System release 6.2.**

I. INTRODUCTION

Despite some recent progress, the development of full three-dimensional (3D) sediment transport models remains a challenging task [1,2,3]. In addition to our limited knowledge of complex processes which govern sediment/turbulent flow interactions, the inherent difficulty to capture both flow and sediment concentration vertical structures has not been emphasised enough. Other issues such as the influence of suspended sediment on the damping of turbulence level are still subject to continual development and discussion.

The effect of sediment particles and turbulent flow interactions is an intriguing and difficult problem: the inhomogeneous and anisotropic characteristics of a turbulent flow, added to the broad range of involved length and time scales [4], make the problem challenging from both theoretical and computational point of view. In the high concentrated bed-load layer, the effect of particle/particle interaction plays a dominant role and a complete two-phase flow approach is required to capture entirely the near-bed processes [4,5]. In the upper part of the flow, in the dilute suspension regime, particles in suspension can be treated as a passive scalar which interacts with the turbulent flow through density gradients [6].

Turbulence models play a crucial role for predicting both velocity and sediment distribution in the water column, and therefore to estimate accurately the suspended sediment transport rate. The simplest turbulence models assume the turbulent eddy viscosity to be either constant over the flow region, or proportional to the velocity or length scales. The value of the eddy-viscosity is therefore determined entirely by the local flow conditions. The widely used k-ε turbulence model solves two additional transport equations to determine both turbulent kinetic energy k and the rate of dissipation rate ε. The k-equation can be derived in its exact form from the Navier-Stokes equations, while in the ε-equation, all terms are modeled and introduced as a set of semi-empirical 'invariant' model coefficients [7]. In k-ε turbulence models, the sediment induced stratification effect is accounted for, in a straight-forward manner, by the buoyancy term. In eddy viscosity models, the effect of sediment concentration on the turbulence can be represented by using damping functions. These semi-empirical functions are in general expressed as a function of the flux Richardson number, which is defined as the ratio between the gravity term versus the production term in the k-equation.

The objective of this paper is to propose a database for validation of the hydrodynamic module TELEMAC-3D and its sediment transport library Sedi-3D based on the numerical reproduction of the experimental tests by Lyn [4, 8]. In order to isolate the effect of particles in suspension on the turbulent flow field, we mimic the starved bed experiments, where sediment is progressively added to the clear flow below saturation (no deposit). We discuss the sensitivity of the model results to the choice of turbulence closure, friction equation and damping functions, in order to provide practical recommendations for modelling three-dimensional flows and suspended transport. For this work, the numerical simulations are based on the open-source TELEMAC Modelling System release 6.2.

This paper is organised as follows. In Part II, we present the hydrodynamics and sediment transport equations, as well as the different turbulence closure relationships which are implemented in TELEMAC-3D. In Part III, we give a short

literature review on the problem of turbulent flow interactions with suspended sediments. In Part IV, we present the experimental setup used by Lyn [4, 8]. In Part V, we present the discretization of the domain as well as a brief description of the boundary conditions implemented in the flow and sediment transport models. In Part VI, the comparison between data and numerical results is presented and discussed for the clear water and starved bed conditions. Finally, the conclusions and practical recommendations for the TELEMAC-3D end-user are given in Part VII.

II. 3D MATHEMATICAL MODEL OF SUSPENDED SEDIMENT TRANSPORT

A. 3D flow model

The 3D flow field is determined by solving the continuity and Reynolds-averaged Navier-Stokes equations (RANS) in the Cartesian coordinate system:

$$\begin{cases} \dfrac{\partial u_i}{\partial x_i} = 0 \\ \dfrac{\partial u_i}{\partial t} + \dfrac{\partial u_i u_j}{\partial x_j} = F_i - \dfrac{1}{\rho}\dfrac{\partial p}{\partial x_i} + \dfrac{1}{\rho}\dfrac{\partial \tau_{ij}}{\partial x_j}, \end{cases} \quad (1)$$

where the summation convention for repeated indices is used. Above, let $x_i=(x_1,x_2,x_3)=(x,y,z)$ denote the spatial coordinates; $t \geq 0$ the time; $u_i=(u_1,u_2,u_3)=(u,v,w)$ the mean flow velocity, F_i the components of external forces, such as gravity, Coriolis force, etc.; p the mean pressure; ρ the fluid density; and τ_{ij} the components of the stress tensor calculated with the Boussinesq hypothesis and related to the gradients of the velocity and the turbulence eddy viscosity ν_t :

$$-\frac{1}{\rho}\frac{\partial \tau_{ij}}{\partial x_j} = \frac{\partial}{\partial x_j}\left[(\nu + \nu_t)\left(\frac{\partial u_i}{\partial x_j} + \frac{\partial u_j}{\partial x_i} \right) - \frac{2}{3} k \delta_{ij} \right] \quad (2)$$

Above, ν is the kinematic viscosity, k is the turbulent kinetic energy and δ_{ij} is the Kroneker delta.

B. Turbulence closure

In TELEMAC-3D, the eddy viscosity ν_t is determined by the choice of the turbulence closure models. In this paper, we will compare two models: the mixing-length model [9] and the standard k-ε model [7].

In mixing length models, the eddy viscosity model is calculated as a function of mean flow velocity gradients and mixing length l_m:

$$\nu_t = l_m^{\,2} \sqrt{\left(\frac{\partial U}{\partial z}\right)^2 + \left(\frac{\partial V}{\partial z}\right)^2} \quad (3)$$

Following [9], the mixing length is assumed to vary with distance from the bed z,

$$l_m = \kappa z \sqrt{(1 - z/h)} \quad (4)$$

where z =0 is the bed level, h the local water-depth and κ = 0.4 the Karman constant.

In k-ε turbulence models, the eddy viscosity ν_t is related to the turbulent kinetic energy k and the rate of dissipation ε :

$$\nu_t = c_\mu \frac{k^2}{\varepsilon} \quad (5)$$

with c_μ a constant. The governing equations for k and ε are given by:

$$\frac{\partial k}{\partial t} + u_j \frac{\partial k}{\partial x_j} = \frac{\partial}{\partial x_j}\left(\frac{\nu_t}{\sigma_k} \frac{\partial k}{\partial x_j} \right) + P + G - \varepsilon \quad (6)$$

$$\frac{\partial \varepsilon}{\partial t} + u_j \frac{\partial \varepsilon}{\partial x_j} = \frac{\partial}{\partial x_j}\left(\frac{\nu_t}{\sigma_\varepsilon} \frac{\partial \varepsilon}{\partial x_j} \right) + c_1 \frac{\varepsilon}{k} P + c_3 \frac{\varepsilon}{k} G - c_2 \frac{\varepsilon^2}{k} \quad (7)$$

Above c_1, c_2, c_3, σ_k and σ_e are constants. P is the shear production and G the buoyancy term due to density effects (as discussed in Part III), defined as :

$$P = -\overline{u_i' u_j'} \frac{\partial u_i}{\partial x_j} \quad (8)$$

$$G = -g \frac{\overline{\rho' w'}}{\rho} \quad (9)$$

with g the gravity acceleration ($g=9.81 m^2/s$), and $-\overline{u_i' u_i'}$ the turbulent Reynolds stress components. The mean (time or spatially) averaged and fluctuating components of instantaneous quantity x are designated by $\bar{x}$ and x', respectively.

The standard coefficients of the turbulence k-ε model [7] are implemented and can be modified (see for example subroutine CSTKEP):

$c_\mu = 0.09$, $c_1 = 1.44$, $c_2 = 1.92$
$\sigma_k = 1.0$, $\sigma_\varepsilon = 1.3$

C. Sediment transport model

Assuming sediment particles follow the mean and turbulent flow component, except for an additional settling term, the following 3D transport/diffusion equation can be derived:

$$\frac{\partial c}{\partial t} + \frac{\partial u_j c}{\partial x_j} - w_s \frac{\partial c}{\partial x_3} = \frac{\partial}{\partial x_j}\left(\varepsilon_s \frac{\partial c}{\partial x_j} \right) \quad (10)$$

with $c = c(x_i, t)$ the suspended sediment mean (volume) concentration, $w_s > 0$ the vertical-settling sediment velocity and ε_s the turbulent eddy diffusivity coefficient.

The turbulent eddy diffusivity coefficient is assumed to be proportional to the turbulent eddy viscosity: $\varepsilon_s = \nu_t / \sigma_s$,where σ_s is the turbulent Schmidt number.

The advection-diffusion equation (10) is completed with initial and boundary conditions. In this work (starved bed experiments), we assume zero flux at the free surface (z=h), and at the bed: $-\varepsilon_s \, \partial c/\partial z - w_s = 0$. Further details on the implementation of the boundary conditions are given in Part V.

III. SEDIMENT-TURBULENT FLOW INTERACTIONS

A. Sediment induced density gradients

Assuming dilute suspension, such that particle interactions can be neglected, the effect of sediment particles is to increase the density of the flow-sediment mixture:

$$\rho = \rho_s c + \rho_0 (1 - c) \tag{11}$$

where ρ_s is the solid density (assumed ρ_s=2650 kg/m^3), c the volume concentration and ρ_0, the fluid density. The density variation is calculated (subroutine DSRUR) :

$$\frac{\Delta\rho}{\rho_0} = \frac{(\rho_s - \rho_0)}{\rho_0} \frac{C_s}{\rho_s} \tag{12}$$

where $\Delta\rho = \rho - \rho_0$, and $C_s = \rho_s c$ is the mass concentration.

Since most particles are carried near the bed ($\partial\rho/\partial z$ <0), the effect of stable density gradients is to extract turbulent kinetic energy. Indeed the gravity term G in the turbulent kinetic energy equation (7) is a dissipative term:

$$G = \frac{g}{\rho_0} \frac{\nu_t}{\sigma_s} \frac{\partial\rho}{\partial z} < 0 \tag{13}$$

The damping of turbulence can be expressed in terms of the flux Richardson number R_i which is defined as the ratio of the gravity term and the production term in Eqs (8, 9).

$$Ri = -\frac{G}{P} = -\frac{g}{\rho_0} \frac{1}{\sigma_s} \frac{\dfrac{\partial\rho}{\partial z}}{\left(\dfrac{\partial u}{\partial z}\right)^2 + \left(\dfrac{\partial v}{\partial z}\right)^2} \tag{14}$$

B. Damping functions

The effect of particles is analogous to the effect of thermal stratification, and can be represented in eddy viscosity models by use of damping functions [10].

Damping functions are semi-empirical functions that characterise the degree of stratification for both eddy viscosity and eddy diffusivity. They can be expressed as a function of the flux Richardson number R_i, as follows:

$$F_t = (1 + AR_i)^{-a} = \frac{\nu_t}{\nu_0}, \quad F_s = (1 + BR_i)^{-b} = \frac{\varepsilon_s}{\varepsilon_0} \tag{15}$$

with ν_0 and ε_0 the eddy viscosity and sediment diffusion coefficient in neutral conditions respectively, and A, B, a and b a set of empirical coefficients. Different values have been proposed in the literature, as synthesised in Table I.

TABLE I. EXAMPLES OF DAMPING FUNCTION

Damping function	Coefficients			
	A	***a***	***B***	***b***
Munk and Anderson 1948 [10	10	0.5	10/3	1.5
Kranenburg 1998 [11]	2.4	2	2.4	4

According to Villaret and Trowbridge [6], the effect of particles induced stratification effect can be represented by the Munk and Anderson damping function.

C. Effect of particles on the Schmidt number

The value of the Schmidt number for sediment may differ from the classical value used for thermocline (in TELEMAC-3D, this value can be implemented in the subroutine CSTKEP, the default value is σ_s=1.0). For the turbulent Schmidt number (the neutral value), predictive equations were introduced by Graf and Cellino [12] and van Rijn [13]. These equations involve the ratio $ws/u*$, with u_* the friction velocity. For instance, the van Rijn equation [13] is:

$$\frac{1}{\sigma_S} = 1 + 2\left(\frac{W_S}{u_*}\right) \tag{16}$$

Other equations rather link the turbulent Schmidt number to the Richardson number [14].

D. Effect of sediment particles on the apparent bed roughness

The effect of particles in the high concentrated near bed region is to increase the apparent bed roughness [4, 5]. Various semi-empirical formulae have been proposed in the literature in order to account for this process, refer [15, 16] for example.

IV. EXPERIMENTAL DATA

Detailed velocity and concentration profiles have been measured by Lyn [4, 8] using LDV and sediment sampling techniques (or turbidity meter). He conducted flume experiments combining 4 runs with clear water, 7 runs under capacity condition (starved bed) and 4 runs at capacity conditions. This high quality data set will be used here as a new test case for the TELEMAC-3D sediment transport model.

As a first step, we mimic the starved bed experiments, where the concentration is increased progressively in order to isolate the effect of sediment in suspension on the turbulent flow field. The equilibrium data set will be used next to validate the sediment transport model boundary condition.

The flume dimensions are 13 m long and 0.2667 m wide. Velocity and concentration profiles were measured at 9 m from the channel inlet. The main characteristics of each experiment are summarised in Table II. The sediment is a fairly uniform sand of mean diameter d_{50}=0.19 mm and measured settling velocity is approximately w_s=0.023m/s.

TABLE II. SUMMARY OF FLOW AND SEDIMENT PARAMETERS

Runs	Q (l/s)	h (cm)	S (*0.001)	C at 0.1*h (*0.001)	u* (cm/s)
C1	10.84	6.54	2.06	-	3.11
C2	12.66	6.53	2.70	-	3.73
C3	10.77	5.75	2.96	-	3.61
C4	12.66	5.69	4.01	-	4.33
ST1A	10.30	5.69	2.99	0.55	3.74
ST1B	10.30	5.68	2.98	0.24	3.69
ST2A	12.10	5.84	4.00	2.08	4.25
ST2B	12.40	5.77	3.95	0.80	4.31
ST2C	12.60	5.75	4.00	0.47	4.28
ST2D	12.60	4.74	4.00	0.31	4.34

where Q is the flow rate, h the water depth, S the bottom slope and C the concentration level at 10% of the water depth. The friction velocity u* has been computed from the Reynolds stresses measurements [4, 8].

For this work, we have selected the runs C4, ST2B, ST2A as they present relatively similar hydraulic conditions (flow rate, water depth, bed slope) and the highest concentration levels (for the starved bed runs).

V. NUMERICAL SIMULATION

A. Mesh description

The 3D finite element mesh is obtained by first dividing the two-dimensional domain in non-overlapping linear triangles and then by extruding each triangle along the vertical direction into linear prismatic columns that fix the bottom and the free surface and partitioned into a number of non-overlapping layers. In this work, the computational domain is discretised with an unstructured triangular mesh consisting of 2611 nodes, 4682 elements and 12 horizontal layers with vertical grid size increasing with the distance from the bed, in order to represent the large variations of both velocity and concentration profiles. The triangular elements are about 0.85 m size and the first grid plane is located at z/h=0.0178 from the bed level.

B. Hydrodynamic boundary conditions

At the inflow boundary, all flow components are prescribed by imposing a constant flow rate, corresponding to the measurements. The upstream boundary is *indeed* located sufficiently far upstream that is beyond the influence of the channel inflow. Numerical tests with a fully-developed velocity profile calculated from the experimental data showed little variation on the results.

At outlet boundaries, the normal gradients of the flow velocity and sediment concentrations are set equal to zero, whereas the water depth is imposed, according to the experimental measurements. At the sidewalls, the velocities tangential and normal to the boundary are set to zero (no-slip condition).

C. Boundary condition for sediment transport

Boundary conditions for Equation (10) are prescribed as follows. At the inflow boundary, the sediment is assumed to enter the three-dimensional domain with constant concentration. Numerical tests with a local equilibrium concentration profile, calculated from the experimental data, have shown little variation on the results. At outlet boundaries, the normal gradient of sediment concentration is set equal to zero. At the bottom boundary, the vertical fluxes of sediment (both erosion and deposition rates) are set equal to zero. This condition is implemented to mimic the starved-bed flow condition, that assumes that the sand-bed is not present and simplifies the analysis of results [4]. Numerical simulations for the equilibrium bed condition are subject of future work.

D. Friction equation

The Nikuradse friction law is applied, where the velocity at the first elevation plane is related to the friction velocity assuming a classical logarithmic velocity profile:

$$u(z_1) = \frac{u_*}{\kappa} \log\left(\frac{z_1}{z_0}\right) \tag{17}$$

where z_1 is the vertical distance to the first e levation plane from the bed level, u_* is the shear velocity, related to the bed shear stress by $u_* = \sqrt{\tau_b / \rho}$, κ is the von Karman constant (≈ 0.40), $z_0=k_s/30$ is a length scale related to the bottom roughness and k_s the Nikuradse equivalent bed roughness.

E. Turbulence model

For the two-equation turbulence model *k-ε*, the boundary conditions are specified according to Burchard [17]. At the bed level (*z*=0), the boundary condition for the turbulent kinetic energy is given by:

$$k = \frac{u_*^2}{\sqrt{C\mu}} \tag{18}$$

The dissipation decays rapidly with distance from the bed, so it is assumed that $\varepsilon = u_*^3 / \kappa\delta$, where $\delta = z_0$.

At the free surface (*z*=h) and in the absence of wind stress, *k* decreases to zero, we assume $\partial k / \partial z = 0$ whereas ε is reduced to $\varepsilon = k^{3/2} / 0.43h$.

At the channel inlet, the *k-ε* profiles are imposed. Assuming production to balance dissipation, the following analytical expression can be derived [17]:

$$k(z) = \frac{u_*^2 (1 - z/h)}{\sqrt{C_\mu}} \tag{19}$$

$$\varepsilon(z) = \frac{u_*^3 (1 - z/h)}{\kappa z} \tag{20}$$

VI. NUMERICAL RESULTS

A. Results for clear water run C4

For the clear water run, computations have been performed with the mixing length model ('NML', [9]) and the *k-ε* model. For both computations, the roughness height is assumed to be equal to 0.05 mm. The selected value is obtained from a trial and error procedure. The comparison between measured and computed profiles is illustrated in Fig.. 1, where the velocities are normalised by the shear velocity. For this case, the main measured and computed hydrodynamic variables are summarised in Table III.

TABLE III. MAIN HYDRODYNAMIC FEATURES OF RUN C4

C4	data	NML simulation	k- ε simulation
U (m/s)	0.87	0.9	0.9
H (m)	0.0569	0.0557	0.0554
u* (m/s)	0.043	0.038	0.036

Water depth, depth averaged velocity, and shear velocity have mostly the same values for both turbulence models. The computed shear velocity is under-estimated compared to the measured data.

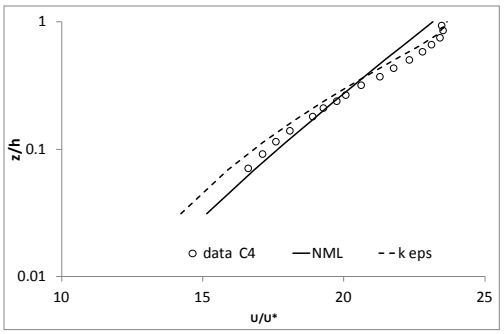

Figure 1. Comparison avec NLM and k- ε models for clear water run C4.

As expected, the computed profile with the NLM model is logarithmic up to the free surface. Below *z/h* = 0.25, the velocity profile is well captured by the NLM model. For *z/h* > 0.25, the measurements do not follow the logarithmic velocity profile. This is probably due to the presence of secondary currents and free surface effects which are not captured in the simple eddy viscosity model: in the upper part of the flow, computed results do not reproduce the observed deviation from the log profile. The velocity profile is overall well captured by the *k-ε* model even if the depth-averaged velocity seems slightly under-predicted.

B. Velocity profiles for sediment-laden flows

The comparison between the NML and the *k-ε* models is performed on the starved bed data sets ST2B and ST2A. These runs are characterised by the highest concentration levels up to 0.64 g/l and 1.46 g/l near the bed (*z/h* = 0.1), respectively. NML simulations are run with and without damping function. To analyse the effect of sediment on the velocity profile for the *k-ε* model, simulations are conducted with and without sediment. The equivalent bed roughness is set equal to 0.7 mm and 1.25 mm for ST2B and ST2A respectively. The velocity profiles for runs ST2B and ST2A are plotted in Fig. 2. The main measured and computed hydrodynamic features are provided in Tables IV and V. The computed water depth, depth averaged velocity and shear velocity are relatively close to the measurements (Tables IV and V).

TABLE IV. MAIN HYDRODYNAMIC FEATURES OF RUN ST2B

ST2B	data	NML simulation	k- ε simulation
U (m/s)	0.862	0.865	0.87
H (m)	0.0577	0.0582	0.0576
u* (m/s)	0.043	0.053	0.047

For run ST2B, even if the concentration level is relatively high, both turbulence models produce almost the same velocity profiles with or without the sediment influence (Fig.

2a). For Run ST2A, *k-ε* model still predicts unchanged velocity profile with or without sediment (Fig. 2c) whereas the velocity profile is influenced by the damping functions with NLM model. For both runs, the detail of the velocity profile is better reproduced by the *k-ε* model. The profiles of the Richardson number (equation (14)) for run ST2B and ST2A are plotted in Fig. 3. The Richardson number reaches high value up to 0.1 near the bed for run ST2A and up to 0.05 for Run ST2B. However, R_i decreases rapidly with distance from the bed, down to less than 1% at about 10% of the water depth which could explain why the *k-ε* model seems not affected by the presence of sediment.

TABLE V. MAIN HYDRODYNAMIC FEATURES OF RUN ST2A

ST2A	data	NML simulation	k- ε simulation
U (m/s)	0.81	0.83	0.83
H (m)	0.0584	0.0583	0.0583
u* (m/s)	0.043	0.046	0.048

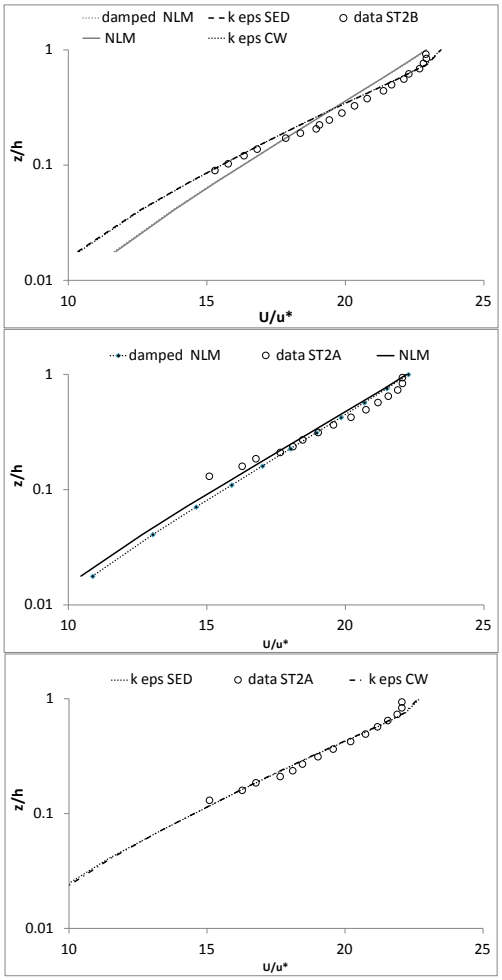

Figure 2. Figure 2. Comparison of NML and k-□ models for runs ST2B and ST2A: (a) velocity profiles for ST2B run; (b) velocity profiles with NML for ST2A run; (c) velocity profiles with k-□ for ST2A run

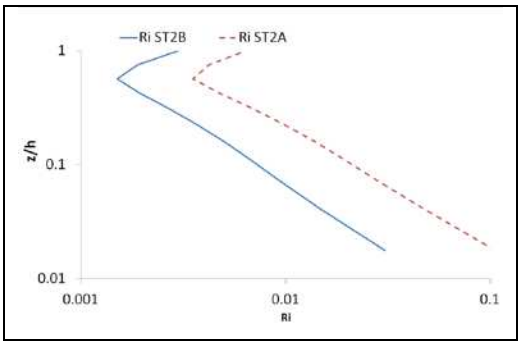

Figure 3. Richardson profiles for run ST2B and ST2A obtained with k-ε model.

C. *Concentration profiles for runs ST2B and ST2A*

For the sediment concentrations, profiles are plotted in Figs. 4a and 4b for runs ST2B and ST2A respectively. The concentration levels are normalised by near bed concentration C_a measured at 10% of the water depth. Results for the concentrations are only shown for the *k-ε* model because the velocity profile is better captured with this turbulence closure. Computations were performed with different values of the turbulent Schmidt number. Best agreements are obtained with σ_s =1.3 or 1.4 for runs ST2B and ST2A respectively. For both runs, the computed concentration profiles match well the experimental data.

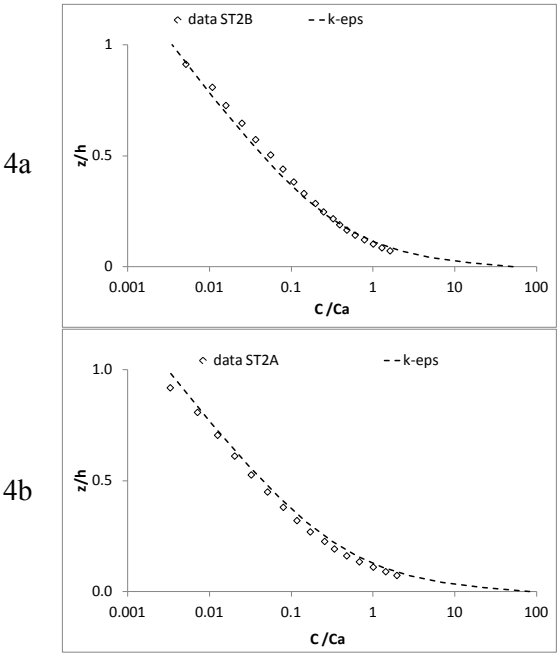

Figure 4. Comparison of NML and k-□ models for runs ST2B and ST2A: (a) concentration profile for ST2B run and (b) concentration profile for ST2A run.

VII. CONCLUSIONS

From the analysis of the experiences of Lyn [4, 8], the recommended modelling strategy is to use the k-ε model because it allows to obtain simultaneously the correct velocity and concentration profiles for the whole range of concentration levels. The NML model is efficient for the clear water runs but it appears to be less effective to reproduce the velocity profile in presence of sediment in suspension, even when the turbulence model is implemented in combination with damping functions. The comparison between TELEMAC-3D results and measured profiles of suspended sediment needs to be extended to other flume series, for example the experimental setup of Graf and Cellino [18], and validated with in-situ measurements.

ACKNOWLEDGEMENT

The authors would like to thank Professor Lyn for access to his dataset.

REFERENCES

[1] Amoudry L.O. and Souza A., 2011. Impact of sediment-induced stratification and turbulence closures on sediment transport and morphological modelling. Continental Shelf Research, 31, 912-928.

[2] Lesser G.R., Roelvink J.A., van Kester J.A.T.M and Stelling G.S. (2004) Development and validation of a three-dimensional morphological model. Coastal Engineering, 51 883-915.

[3] Tassi P., Villaret C., Huybrechts N., Hervouet J.M. : Numerical modelling of 2D and 3D suspended sediment transport in Tubulent Flows, RCEM 2011.

[4] Lyn D.A. (1991) Resistance in flat-bed sediment-laden flows. Journal of Hydraulic Engineering, vol. 117 (1).

[5] Villaret, C. and Davies, A.G. (1995) Modeling sediment turbulent flow interactions, Applied Mechanics Review, Vol.48, N°9, ASME, pp.601-609.

[6] Villaret C. and Trowbridge J.H. (1991) Effects of stratification by suspended sediments on turbulent shear flows, Journal of Geophysical Research, 96, C6, 10659-10680, 1991

[7] Rodi, W. (1993) Turbulence Models and Their Applications in Hydraulics, 3rd ed., IAHR Monograph, Rotterdam, The Netherlands.

[8] Lyn D. A. (1986) Turbulence and turbulent transport in sediment-laden open channel flows. Ph. D thesis, California Institute of Technology, Pasadena, California

[9] Nezu, I. and Nakagawa, H. (1993) Turbulence in Open-Channel Flows, IAHR Monograph, Rotterdam, The Netherlands.

[10] Munk, W.H. & E.A. Anderson (1948). "Notes on a theory of the thermocline", J. Marine Research, 3(1):276-295.

[11] Kranenburg C. (1998). Saturation concentrations of suspended fine sediment. Computations with the Prandtl mixing-length model. Report No.5-98, Faculty of Civil Engineering and Geosciences, Delft University of Technology.

[12] Graf W.H. and Cellino M. (2002) Suspension flows in open channels; experimental study. Journal of Hydraulic Research, vol. 40 (4).

[13] van Rijn, L.V (2003) "Principes of sediment transport in Rivers, Estuaries, Coastal Seas and Ocean", Lecture Notes Vol 1, University of Utrech, 327 p.

[14] Violeau, D., S. Bourban, C. Cheviet, M. Markofsky, O. Petersen, W. Roberts, J. Spearman, E. Toorman, H. Vested & H. Weilbeer (2000). Numerical simulation of cohesive sediment transport: intercomparison of several numerical models. Overview paper on COSINUS task E, 6th Int. Conf. On Nearshore and Estuarine Cohesive Sediment Transport (INTERCOH 2000), Delft, September 2000.

[15] Wilson, K.C (1989) Mobile-bed friction at high shear stress. Journal of Hydraulic Engineering, Vol. 115, (6), 825-830

[16] Sumer, B.M, Kozakiewicz, A, Fredsoe, J and Deigaard, R (1996) Velocity and concentration profiles in sheet-flow layer of movable bed. Journal of Hydraulic Engineering, Vol 122 (10), pp 549-558.

[17] Burchard H. (2002) Applied Turbulence Modelling in Marine Waters, 100, Lecture Notes in Earth Sciences. Springer Verlag, ISBN: 3-54043795-9.

[18] Cellino M. and Graf W. H. (1999) Sediment-laden flow in open-channels under noncapacity and capacity conditions. Journal of Hydraulic Engineering, Vol. 125 (5).

Continuous Vertical Grain Sorting for TELEMAC & SISYPHE v6p2

Uwe H. Merkel
Consulting Engineer
Karlsruhe, Germany
uwe.merkel@uwe-merkel.com

Rebekka Kopmann
Department of Hydraulic Engineering
Bundesanstalt für Wasserbau
Karlsruhe, Germany
rebekka.kopmann@baw.de

***Abstract*— Vertical grain sorting is one of the leading processes for many hydrodynamic and morphodynamic simulations. Like most hydraulic & morphological software packages TELEMAC & SISYPHE calculate sediment transport, sediment sorting and development of bed forms depending on the active layer of the bed. The empiric active layer thickness concept has been developed in 1971 by Hirano and expanded by Ribberink among others to fit the numerical models and demands of their time. With new high performance computers and the here presented continuous vertical grain sorting models with dynamically estimated active layer thickness it is now possible to overcome several limitations of this meanwhile 40 year old concept. Results of this model are compared to the classic Hirano-Ribberink implementations using measured data off 3 flume experiments performed at the Universities of Delft, Zürich and Illinois to validate and proof this concept.**

I. The Hirano-Ribberink Vertical Grain Sorting Model (HR-VSM)

A. *Motivation*

Many medium and long term hydrodynamic numerical simulations of rivers cannot be operated successfully without considering the flow-sediment interaction. Sediment layer thickness and grain size distributions influence the bed roughness and the flow field. Vice versa the flow field sorts sediments and develops bed forms. TELEMAC-2D/3D and SISYPHE enables interactive coupling of morphodynamic and hydrodynamic simulations and includes the state of the art grain sorting algorithm for numerical morphodynamic models: The Hirano (1971) concept with extensions of Ribberink (1987) and other research groups.

The basic idea of Hirano is the interaction of flow with a fully mixed top-most layer of the sediment, while the deeper sediment stratigraphy remains untouched. The thickness of this active layer describes the common depth of morphological processes in the riverbed per time step, which equals the maximum impact of the hydraulic shear forces. The empirical variable active layer thickness (ALT) is usually chosen as a multiple of the characteristic grain diameter and the mean height of bed forms. For numerical reasons it is the maximum depth that can be eroded in one time step. Below the active layer follows another empirical layer, the active stratum, which has no measurable equivalent in nature. It is used to refill or reduce the active layer to the predefined thickness after evolution calculations changed the active layer thickness.

The implementation in TELEMAC / SISYPHE v6p1 adds up to 7 more storage layers below these 2 layers. They keep different sediment mixtures until they are activated by erosive processes. Within 1 time step evolution only affects the active layer and the active stratum.

B. *Limitations*

This meanwhile 40 year old concept was developed as an averaging empirical approach at a time where the available computational performance was 1010 times less than in 2012. Saving computational resources by spatial averaging was necessary but comprehends several limitations:

- The number of discrete layers is limited to 9.
- The a priori chosen layer thickness depends on dune heights, grain roughness, depth of the rigid bed, mesh density and other parameters.
- The active layer + active stratum concept in fact mixes the second layer as well, Fig. 2.
- Contrary requests of the active layer concept cannot be fulfilled in every case. e.g. the theoretical active layer filling is homogenous and cannot be subdivided. If the topmost layer is used to reproduce the stratigraphy, it cannot be used for the natural impact depth of the driving shear forces at the same time.

While the first two limitations could be easily removed, the last two require a new concept with less averaging effects on the bookkeeping.

II. The New Continuous Vertical Grain Sorting Model (C-VSM)

A. *Divided in bookkeeping model and transport model*

One of the main disadvantages of the Hirano method is

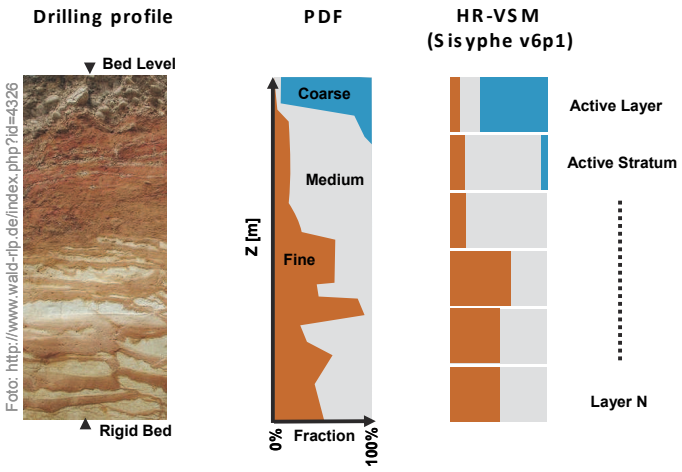

Figure 1. Legend for all following diagrams: Imagine the new continuous vertical grain size sorting model C-VSM as the drilling profiles probability density functions in polyline form, where grains are sorted from fine to coarse, left to right, resulting in 100% at any depth. The widespread Hirano / Ribberink layer sorting model HR-VSM is a simplified version.

the continuous mixing of the active layer and the active stratum after every time step, even with minor or without evolution.

This is done to numerically refill or reduce the active layer content with active stratum content

- for example to restore the full theoretical thickness of the active layer after evolution,
- or even when just a dynamic active layer thickness formula resizes the thickness based on turbulence shuffled flow conditions.

But it is not necessarily a process that happens in nature. Fig. 2 shows the dynamic formula effect to the ALT, due to turbulence influenced shear stress variability in between 2 time steps (ALT i = +/- 0.000001 * ALTi-1), but with a long term equilibrium state ($E\infty \sim 0$). After 1 000 000 refill and reduction cycles for an alignment of the active layer and active stratum each time, the content of both layers is almost fully mixed, without any change in bed level. Even though this is mathematically correct it leads to wrong vertical grain sorting. Hirano demanded morphological activity ends below the active layer, but here the mixing reaches one layer deeper.

The solution is to separate the grain storage model from the evolution calculation model. This means that 2 datasets are used for the grain sorting. Dataset 1 is a storage model that keeps the information about the vertical grain sorting, without regard to any layer boundary, like the drilling profile, with as much resolution as possible. Dataset 2 is again the Hirano active layer, newly filled with the actual average grain mixture of the equivalent top sections of the Dataset 1. It is newly averaged at each time step and used for evolution calculations. This works not different than the original Hirano concept. But now any evolution is not shifted to the active stratum, but to the fine resolution storage model,

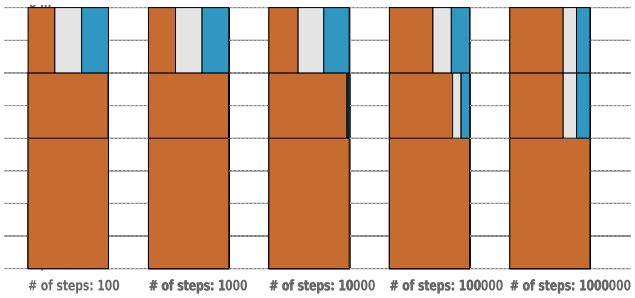

Figure 2. Development of an academic sorting profile in HR-VSM (SISYPHE v6p0). For a channel with equilibrium transport, but short term evolution of 0,0001% of the active layer thickness.

which gets an addition or subtraction of volumes. Exchange goes from top to bottom as deep as necessary to get the needed volumes. It is not anymore a shifting of fractions over the full strength of a theoretical layer.

B. The new bookkeeping model

We decided to add a depth dependent bookkeeping model for each grain size fraction with unlimited numerical resolution for each node of the 2D morphological model. As the transport model remains unchanged and does not directly interact with the bookkeeping model, both are kept in separate software modules without knowing the existence of each other.

As shown in Fig. 1 a drilling core is the physical equivalent to the storage model. The numerical implementation is a set of depth dependent probability density functions (PDF) for each grain size fraction. The sum of all grain fraction PDFs is always 100% at any depth. These PDFs are stored as polylines. The number of line sections is theoretically unlimited. For visualisation, the grain size fractions of each profile are always drawn additive from

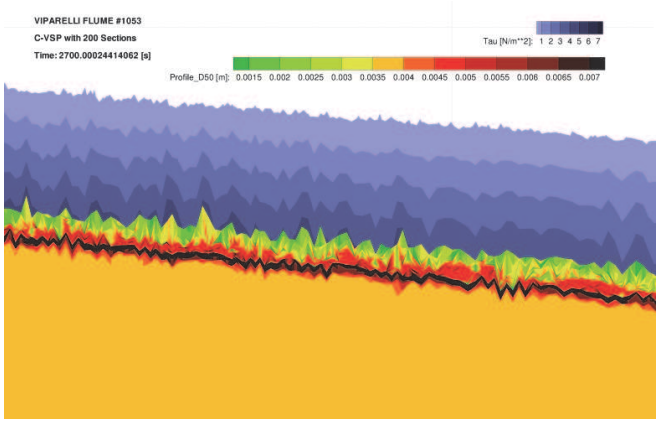

Figure 3. In case of immobile coarse fractions within the active layer, the active layer itself can develop a sub ordinary stratigraphy which is relevant for the development of bed forms and armoring effects. This figure shows the mean grain diameter d_{50} (green to red) in the middle of a laboratory flume and the corresponding hydraulic impact, shown as shear stress (blue). Fine grains separate from the mixture and move on top of the coarse ones, which stay behind as an immobile under layer.

fine (left) to coarse (right) (Fig. 1 is the legend to all other figures). In contrast to the classic Hirano-Ribberink layer model there are no theoretical limitations to the discretisation of thicknesses except the capabilities of the hardware.

Additionally a fraction gradient over depth is modelled as a single trapezoid instead of an approximation with many rectangular layers. This saves resources. The main benefit can be found in simulations where the real layering is finer than the ALT (Fig. 4).

This is especially helpful for fine grain lentils or armouring layers within the sediment body which might significantly influence the calculation in a subsequent time step. Fig. 4 shows the main advantage of the polyline C-VSM version against the fine layer C-VSM versions. To describe declining fractions of a single material only few points (= double precision variables) are necessary while the fine layer sorting profile needs many datasets more.

1) Depositing sediments: Sedimentation can occur in 2 modes. The first mode is a plain sedimentation of one or all fractions. The already lying sediments are not moved, incoming sediments can only be placed on top. Numerically this is a new polyline section on top of the C-VSM. The bed level is lifted while storing the new material. See Fig. 5c, which is Fig. 5b plus sedimentation on top.

The second mode is sedimentation of some coarse grain fractions while finer fractions are eroded from the active part of the bed. Here the sediments within the active layer are also in motion. Therefore depositions are placed as an addition to the active part of the bed, inside the existing top section. See Fig. 5b which adds material in the top section of Fig. 5a.

2) Eroding sediments: Erosion always starts from bed level and ends where the transport capacity is satisfied. This leads to complete or partial erosion of grains within C-VSM polyline sections. If a grain class within a section (which equals a volume!) is eroded completely, like grain class 2 in Figs. 6b and 6c, only the bed level elevation has to be updated and the fraction variables of the remaining sediment

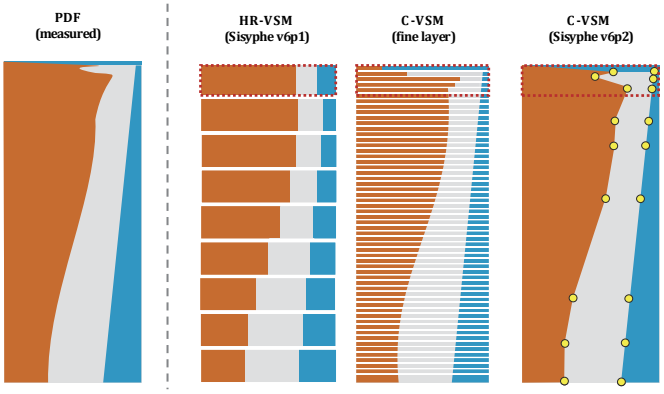

Figure 4. Comparison of stratigraphy abstraction models with active layer (red dotted): Measured Profil (far left); Hirano/Ribberink (left), Continuous model based on very fine layers (middle) , Continuous model based on polylines (right).

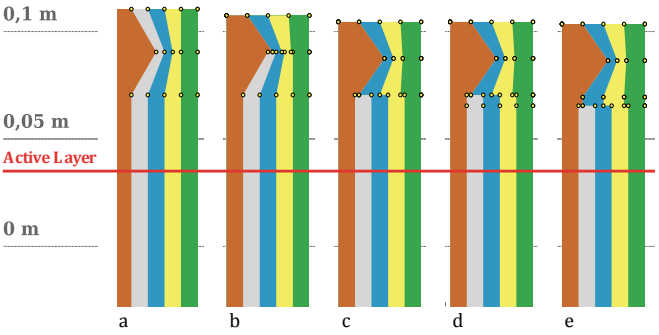

Figure 5. Eroding a certain volume of grain fraction No2 (grey) from the storage model. Example in 4 Steps: a) Initial state; b) & c). Erosion of sorting profile section 1 and 2 leads to a lowering of the surface, while the sum of all fractions is normalised to 100%. d) & e) Section 3 is not eroded completely, but split into two sections where only the upper part is eroded.

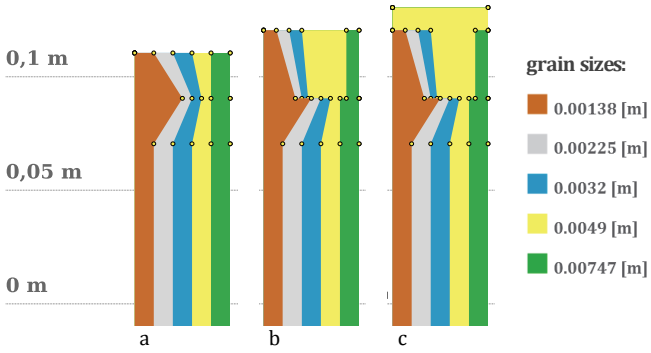

Figure 6. There are 2 modes of adding fractions: a) a random profile in its initial state; b) Sedimentation of fraction #4 mixed in the topmost section of (a); c) Only sedimentation of fraction #4 on top of the profile (b), without mixing in the top section.

have to be normalised to 100%. If the section contains more material than can be eroded, only the necessary volume is extracted. This forces a splitting into two parts (Fig. 6d). It remains one section without grain class 2 and below another section with grain class 2 (Fig. 6e).

3) Avoiding excessive fragmentation: After a longer series of sedimentation and erosion cycles the C-VSM is fragmented in many very small sections, which is sometimes only 10-15 m strong. To avoid too excessive memory consumption a compression algorithm reduces the number of sections based on user defined quality threshold values. This algorithm is a modified version of the Douglas Peuker line generalisation algorithm. It works iterative until a maximum fraction error or a minimum point number is reached. See Fig. 7.

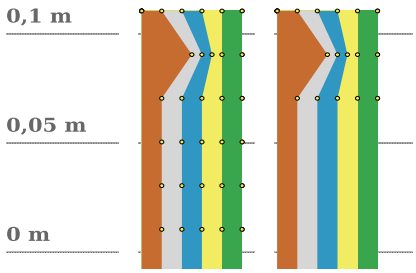

Figure 7. The yellow points mark the polyline PDF sections of the C-VSM. The intial profile (left) is simplified with the line generalisation algorithm without significant change in volume.

4) Updating the transport model: When the bed load formula is calculated, the supplied active layer hasn't got the content of the active layer of the last time step. It is an updated content from the C-VSM by integration of the grain class volumes over the newly estimated active layer thickness.

C. Reduced smearing effects

Fig. 8 shows clearly how the high resolution vertical sorting is preserved even though the transport model itself works with the averaged and therefore coarse Hirano active layer. It shows 3 sub steps of one time step for both deposition and erosion.

- The active layer is averaged from the bookkeeping.
- Evolution is calculated with any well known transport formula and the Exner equation based on the active layer and without impact on the bookkeeping.
- Evolution is added or subtracted from the top of the PDF.

The resulting C-VSM surface is free from eroded and buried materials, while the HR-VSM mixes in other materials from the active stratum as well.

D. Dynamic active layer thickness

The original Hirano idea assumes the active layer bottom as the limit of the moving part of the bed. It is clear that a fix active layer thickness can not account for changing hydraulics, morphology and grain sorting.

This empirical mean value is hard to measure and

- has growing uncertainties the coarser the spatial steps get (mesh width),
- is sensitive to the length of the observed morphological activity (time step),
- and is dependent on the shear stress magnitude.

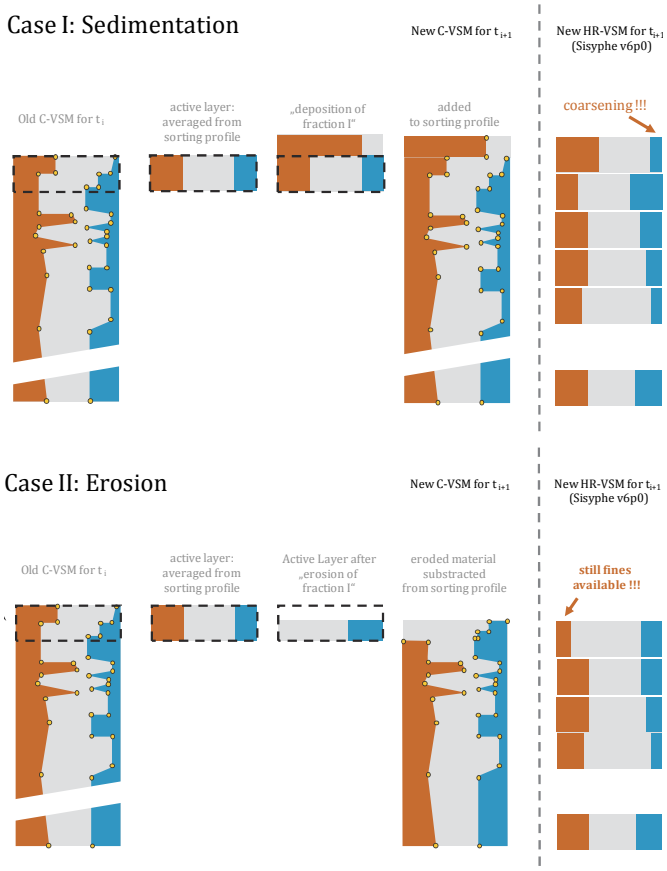

Figure 8. The changed and finer bookkeeping of Continuous Vertical Sorting Profiles (C-VSM) avoids smearing problems due to averaging in the classic Hirano/Ribberink layer method (HR-VSM). This sketch shows the behavior for sedimentation and erosion of both algorithms within one time step.

Replacing these influence factors with mean values increases the morphological uncertainties. A collection of formulas for dynamic ALT approximations during a simulation are available in Malcherek (2007), using the bottom shear stress τ_B, the critical shear stress τ_C, the characteristic diameters d_{50}, d_{90}, d_{MAX} and transport stage parameter D^*.

- Hunziker & Günther

$$ALT = 5 * d_{MAX} \tag{1}$$

- Fredsoe & Deigaard, 1992

$$ALT = \frac{2 \cdot \tau_B}{(1-n) \cdot g \cdot (\rho_S - \rho) \tan \phi} \tag{2}$$

- van Rijn, 1993

$$ALT = 0.3 \cdot D_*^{0,7} \cdot \left(\frac{\tau_B - \tau_C}{\tau_B}\right)^{0,5} \cdot d_{50} \tag{3}$$

- Wong, 2006

$$ALT = 5 \cdot \left(\frac{\tau_B}{(\rho_S - \rho) \cdot g \cdot d} - 0{,}0549\right)^{0{,}56} \cdot d_{50} \qquad (4)$$

- Malcherek, 2003

$$ALT = \frac{d_{90}}{1-n} \max\left(1, \frac{\tau_B}{\tau_C}\right) \qquad (5)$$

Other parameters: ρ_S … density solid; ρ … density water; n … porosity; $\tan\phi$ … friction angle

The implementation of these formulae is possible for HR-VSP with very long morphological time steps. But it is limited, due to the smearing problem shown in Fig. 2. Especially in pulsating eddy zones the ALT changes by several 100% within few time steps instead of the above shown 0.0001%. This increases the smearing problem.

With the new C-VSP this problem is obsolete and the formulas for a dynamic ALT can be used over longer simulation periods in coupled morphodynamic and hydrodynamic models.

No further recommendation is given on these formulas, as their usability is strongly dependent to the project. Fig. 9 shows the strong variance of these formulas for the later described Guenter flume.

E. *Possible future extensions*

Another advantage of the separate bookkeeping method is the possibility to add other geotechnical algorithms like time dependent compacting, shrinking and changes of the porosity, as well. Furthermore we recommend the development of a vertical mixing algorithm which accounts for moving sediments without sedimentation or erosion.

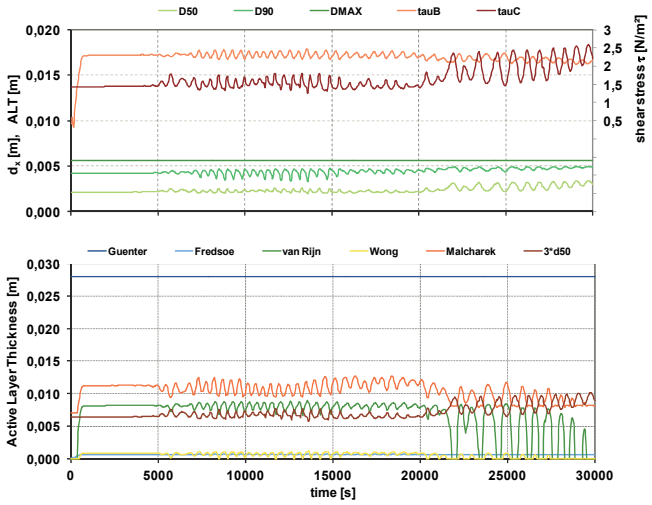

Figure 9. Development of the shear stress, the characteristic diameters and the active layer thicknesses for a random point in the middle of the Guenter flume, calculated with the five above mentioned formulas. Strong variations between the formulas force a careful selection.

III. VALIDATION OF THE NEW C-VSM

The capabilities of the C-VSM were tested against 3 laboratory flume experiments with a total of 25 different parameter combinations. Stability, usability and the bandwidth of the C-VSM is demonstrated in this chapter by picking demonstrative aspects of one suitable flume. Even though we did not calibrate all 25 setups, it is technically possible. The following examples show some new possibilities and the model behaviour.

A. *Validation case: BLOM FLUME*

1) Setup: Astrid Blom (2003a, 2003b, 2008a, 2008b) conducted flume experiments at Delft Hydraulic Laboratories in 1998 to investigate vertical sorting processes. She used the measured data to develop her own numerical vertical sorting model. The authors decided to use these experiments as validation cases as well.

This rectangular profile laboratory flume was 50m long, 1m wide and filled with an artificial 3 modal grain mixture (d_{50} = 0.00068 m, 0.0021 m and 0.0057 m, 33.3% each). Several flume configurations can be found in her publications, we calculated all with TELEMAC and the C-VSM, but want to focus on the "Series B" for this publication (see Fig. 10 for a picture).

For a discharge of 0.267 m^3/s a slope of 0.0018 produced a normal flow depth of 0.386 m for case "B2". The sediments were recirculated. Both, the physical and numerical experiments require the first half of the flume length to gain undisturbed hydro- and morphodynamic conditions, thus only the second half is used for comparison.

2) Results: Results of the C-VSM are shown in Fig. 12 (averaged) and Fig. 11 (2D top view). Bed forms occurred and fine material moved over coarse material.

The C-VSM clearly shows that the surface material has no coarse fraction any more as the fines move in form of dunes on top of them. This effect has been observed by Astrid Blom (see Fig. 12), but is clearly missing in the HR-VSM.

These results subsequently show a better grain and form roughness approximation for the C-VSM.

B. *Validation case: VIPARELLI FLUME*

1) Setup: Enrica Viparelli et al. setup a rectangular profile flume of 17 m length and 0.61 m width with a slope between 0.0046 and 0.0079. A sediment mixture between 1 and 10mm (d_{50}=7.8 mm) was filled in 18.5 cm strong. 9 Experiments were run with various discharge and duration configurations resulting in water depths H between 6.9 and 8.7 cm.

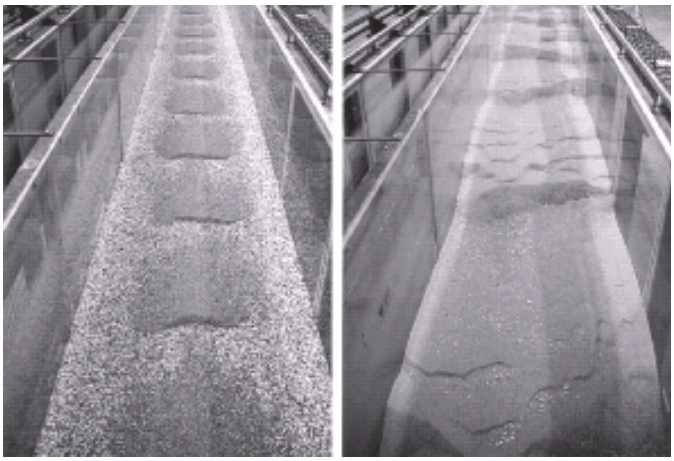

Figure 10. Pictures by Astrid Blom (2003) of flume experiment before (left) and after (right) experiment B2.

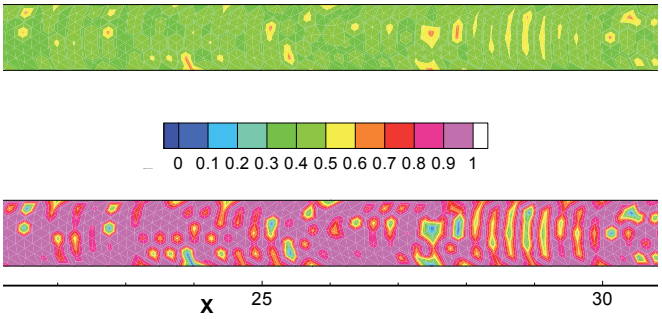

Figure 11. Top view a.k.a. flume surface. Development of the fine grain fraction after 4h. Initial values (t=0) for all grain fractions f and both models have been fi = 0.3333.

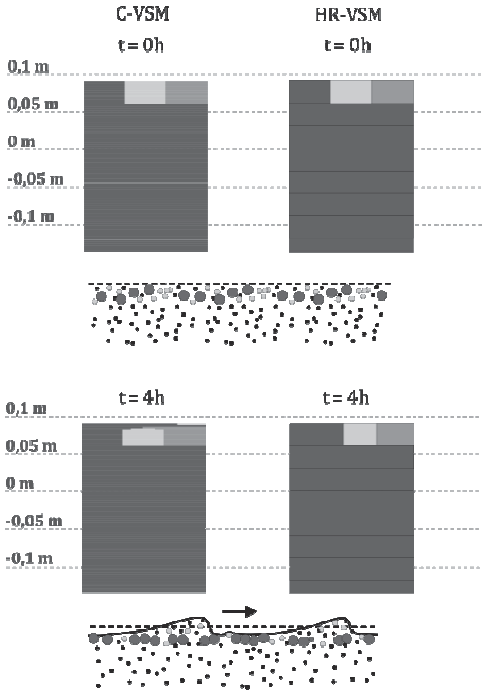

Figure 12. Development of bed form and grain sorting within 4h for the Blom series B. Calculated with TELEMAC / SISYPHE v6p1. C-VSM and HR-VSM show averaged values between flume stage 25 m to 47 m.

Transport rates, water depth, resulting slope and the shift of surface grading lines are documented well in Viparelli (2010). A TELEMAC-2D / SISYPHE v6p1 model with 3800 points was used to calculate the flume experiments. The initial grain mixture was set to 5 grain sizes with a fraction of 0.2 each.

2) Results: Viparelli describes the results of the flume as free from bed forms and lateral effects. This is the same for the C-VSM results. There is no clear trend of the grain sorting in neither direction, maybe due to the equilibrium conditions. But we have a strong variance on single points especially close to the inflow and outflow boundaries.

Fig. 13 shows 5 C-VSM profiles from probing points in the middle of the flume after 36000 hydraulic time steps of 0.1 s, what equals 1h. Due to an extended morphological time step this equals 720 calculations of the morphology. These 5 profiles with totally different character are selected because they show the capability of the bookkeeping system. Each of the shown profiles has its own development history out of erosion and sedimentation cycles and consists of 12 to 48 sections.

The black line marks the active part of the bed at the last time step, calculated with van Rijn formula. The active layer thickness varies between 2.5 and 4.5 cm as the shear stress varies and the different grain mixtures of the active zone have a different d_{50} value. An interesting fact is that the last 2 profiles are not mixed in as deep as the average active layer thickness reaches. This means that so far no erosion took the maximum of the available material. Maybe the dynamic ALT estimation according to van Rijn overestimates this case and one of the other formulas shown in Fig. 9 would perform better. This problem also inspires to develop a new formula for the ALT, dependent on the maximum impact thickness of the last time steps morphological processes.

3) Development of the C-VSM sections: Another important result proofs the robustness of the dynamic C-VSM data management. Initial fears that an uncontrolled fragmentation of the C-VSM might increase the memory demands significantly can be disarmed.

Starting with only 12 sections for the C-VSM in Fig. 14, sediment movements fragmented the profiles and the number of data points rises until a threshold of 80 is reached. Now the profile simplification algorithm merges neighbouring line sections in the profile while respecting a maximum fraction error which is user defined 10-12 here. The number of sections drops below 30. As the Viparelli flume is in

equilibrium state the cycle of growing and shrinking is in equilibrium as well.

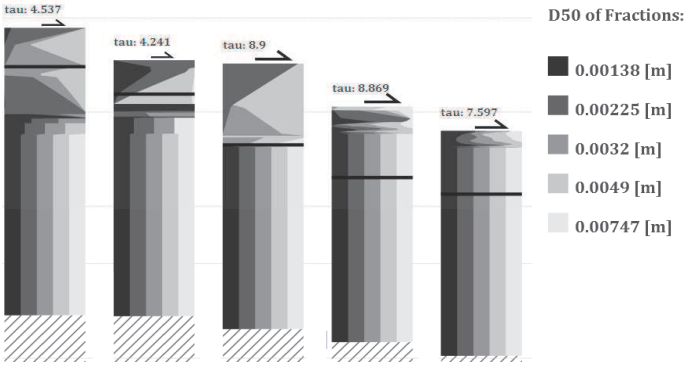

Figure 13. C-VSM profiles from 5 stations of the flume show a different morphological history, even though the surface mixture d_{50} is almost 3mm for all of them. Pulsating shear stress values τ_B(tau) of the last time steps are shown in N/m² and the resulting active layer thickness according to the van Rijn formula is marked as a thick black line.

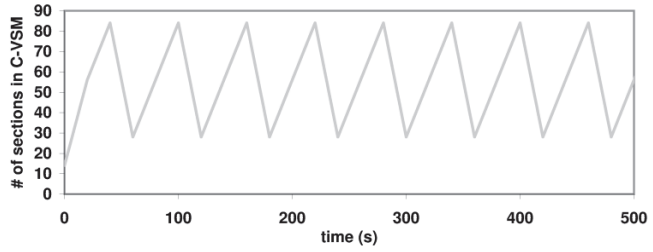

Figure 14. The number of sections in the C-VSM, averaged over all points in the middle of the flume, increases and decreases during changing erosion and sedimentation cycles. If the number of sections gets too high, recompression is performed, but an accuracy threshold is kept.

C. *Validation Case: GUENTER FLUME*

1) Setup: Arthur Guenter published his laboratory flume experiments at the ETH Zürich in 1971. The rectangular flume dimensions were X=40m / Y=1m / Ie~0.002 / H<0.1m. Different to the other 2 test cases he didn't use recirculation. Therefore this flume is especially useful to observe the development of armoring layers and the influence of turbulence on the critical shear stress.

We use a TELEMAC-2D + SISYPHE model based on a 5000 point irregular triangle mesh. All simulations are based on a 6 size fraction sieve line.

2) Results: Fig. 15 shows a longitudinal cut for d_{50} through the middle of the Guenter flume along the X axis and the corresponding C-VSM charts for X=55m; Y=0.5m.

Obviously only the 3 finer fractions are moving in higher percentage.

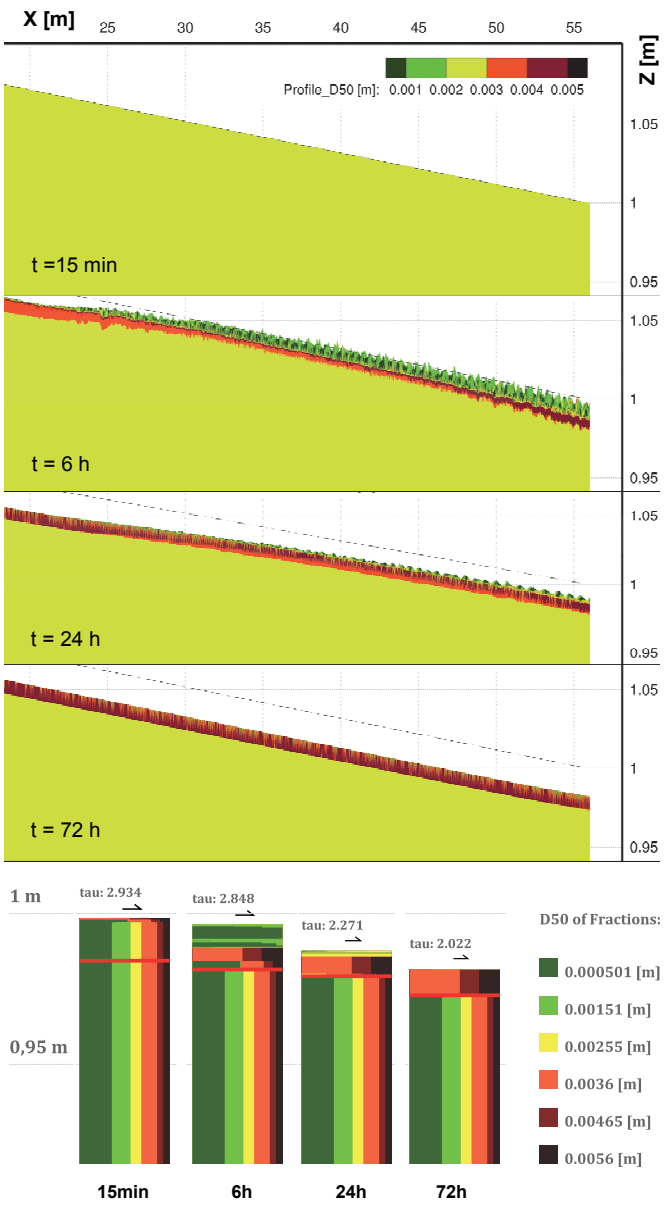

Figure 15. Top: d_{50} [m] - longitudinal cut through the Günther flume for T=15min; 6h; 24h; 72h. Bottom: According vertical sorting profiles of flume middle axis for x =55m.

After 6h most of the fine fractions are in motion on top of the coarser ones. A clear stratigraphy can be seen now. The available fine sediments are already getting less in the upper half of the flume. At the end of the flume the coarse intermediate layer is strongest, as all the fine material of this part has meanwhile been eroded and out of the flume. The fine material on top of this flume part is mainly originated from upper flume parts.

After 24h the upper part of the flume almost reached the final state. The lower part still has a small rest of fine sediments coming from the deeper zones below the coarse surface layer now sporadically reached by turbulent pulses.

After 72h the coarse zone nearly reached a constant strength, which equals almost the mean value over all points of the maximum estimated active layer thickness (here: Malcherek formula; option 5). Since even the shear stress peaks now do not reach deeper available fine sediments any more, erosion per time is very small now. An armouring layer has developed and protects the lower sediments.

We tried different formulas, which lead to a different strength of the armouring layer. And of course other parameters like hiding effects or the slope effect, estimation of the critical shear stress and others influence the resulting sieve lines and the time scales.

IV. Summary and Recommendation

The continuous vertical sorting model (C-VSM) overcomes many limitations of the classic layer implementation (HR-VSM).

Even though this paper shows a different way to manage the grain sorting, it is just another interpretation of Hiranos original idea with fewer simplifications. The new model doesn't overcome the need to carefully calibrate the same input parameters as all other models, but the new interpretation has the following advantages:

- It is possible to keep minor but prominent grain mixture variations even after a high number of time steps. Smearing effects and bookkeeping accuracy is defined by user defined thresholds or the computational resources, rather than through a fix value.
- A dynamic active layer thickness is not biased by these effects any more. Various functions for the impact depth of the shear stress can be chosen to the projects demands.
- The result is a much more accurate vertical grain sorting, which results in better prognoses for bed roughness, bed forms and erosion stability.

The modular implementation provides an interface for important future developments. Further validation in practical projects is in progress.

V. How to use it in SISYPHE v6p2

A couple of new keywords enables the C-VSM. Add the lines of Fig. 16 to your sis.cas file.

The full C-VSM output can be found in the Selafin files VSPRES & VSPHYD in the tmp-folders. As the higher resolution of the C-VSM needs resources, you can reduce the print output period, or suppress the output at all. The common SISYPHE result files only show the Hirano output. Even more disk space can be saved, if only few points are printed out as .VSP.CSV files in the subfolder /VSP/. We recommend using between 200 and 1000 vertical sections. More will not improve the accuracy much, and less will lead to increasing data management, as the profile compression algorithms are called more often.

```
/************************************************************************
/ New keywords for the Continuous VERTICAL SORTING MODEL by Uwe Merkel
/************************************************************************
/
VERTICAL GRAIN SORTING MODEL  = 1
/         0 = Layer = HR-VSM (HIRANO + RIBBERINK as until SISYPHE v6p1)
/         1 = C-VSM
C-VSM MAXIMUM SECTIONS        = 100
/         Should be at least 4 + 4x Number of fractions,
/         better > 100, tested up to 10000
C-VSM FULL PRINTOUT PERIOD    = 1000
/         0 => GRAPHIC PRINTOUT PERIOD
/         Anything greater 0 => Sets an own printout period for the CVSP
/         useful to save disk space!!!
C-VSM PRINTOUT SELECTION =
0|251|3514|1118|1750|2104|3316|1212|1280|2186|3187|1356|3027|1535|485
/        Add any 2D Mesh Point numbers for .CSV-Ascii output of the CVSP
/        Add 0 for full CVSP output as Selafin3D files
/            (called VSPRES + VSPHYD)
/            All files are saved to your working folder and
/            in /VSP & /LAY folders below
C-VSM DYNAMIC ALT MODEL       = 5
/        'MODEL FOR DYNMIC ACTIVE LAYER THICKNESS APROXIMATION'
/         0 = CONSTANT (Uses Keyword: ACTIVE LAYER THICKNESS)
/         1 = Hunziker & Guenther
/         2 = Fredsoe & Deigaard (1992)
/         3 = van RIJN (1993)
/         4 = Wong (2006)
/         5 = Malcharek (2003)
/         6 = 3*d50 within last time steps ALT'
```

Figure 16. Example configuration for Sisyphe v6p2.

Please feel free to report your experiences with our new development.

uwe.merkel@uwe-merkel.com
rebekka.kopmann@baw.de

ACKNOWLEDGEMENT

The authors thank Astrid Blom for the fruitful discussions.

REFERENCES

[1] G. Eason, B. Noble, and I. N. Sneddon, “On certain integrals of Lipschitz-Hankel type involving products of Bessel functions,” Phil. Trans. Roy. Soc. London, vol. A247, pp. 529–551, April 1955. (references)

[2] Blom, A. A vertical sorting model for rivers with non-uniform sediment and dunes. Ph.D. thesis. University of Twente (NL). 2003

[3] Blom, A. and Ribberink, J.S. and de Vriend, H.J. Vertical sorting in bed forms: Flume experiments with a natural and a trimodal sediment mixture. Water Resources Research. Vol.39. 2003

[4] Blom, A. Different approaches to handling vertical and streamwise sorting in modeling river morphodynamics. Water Resources Research. Vol.44. 2008

[5] Blom, A. and Ribberink, J.S. and Parker, G. Vertical sorting and the morphodynamics of bed form-dominated rivers: A sorting evolution model. J. Geophys. Res. Vol.113. 2008

[6] Enrica Viparelli, Robert Haydel, Martino Salvaro, Peter R. Wilcock & Gary Parker (2010): River morphodynamics with creation/consumption of grain size stratigraphy 1: laboratory experiments, Journal of Hydraulic Research, 48:6, 715-726

[7] Guenther, A. Die kritische mittlere Sohlenschubspannung bei Geschiebemischungen unter berücksichtigung der Dechschichtbildung und der turbulenzbedingten Sohlenschubspannungsschwankungen. Ph.D. thesis. ETH Zuerich (CH). 1971

[8] Hirano, M. River bed degradation with armouring. Proceedings Japan Society of Civil. Engineers 195. 1971

[9] Malcherek, A. Sedimenttransport und Morphodynamik, Scriptum Institut für Wasserwesen, Universität München, 2007

[10] Ribberink, JS. Mathematical modelling of one-dimensional morphological changes in rivers with non-uniform sediment. Delft University of Technology. 1987

[11] Villaret C. Sisyphe user manual, EDF R&D Report N° H-P73-2010-01219, www.systemtelemac.com. 2010

Dune simulation with TELEMAC-3D and SISYPHE: A parameter study.

Annalena Goll and Rebekka Kopmann
Federal Waterways Engineering and Research Institute (BAW)
Karlsruhe, Germany
annalena.goll@baw.de

***Abstract*—This paper presents results of RANS simulations of dunes in an open channel flume with TELEMAC-3D and SISYPHE. Three-dimensional sand dunes were produced, studied and compared to the physical dunes of a laboratory flume situated at the BAW, Karlsruhe. Aim of the study is to create a parameter set for TELEMAC-3D and SISYPHE with which it will be possible to conduct explicit simulations of bed forms for selected river stretches. For comparison the parameters of dune height and length are used. Additionally the mean deviation of the probability density function of the bed forms, the mean skewness and the mean kurtosis were computed and compared to the data of the physical data set. Three different bed load transport formulas and four different slope effect and deviation formulas were used. The deviation formula of Apsley & Stansby in combination with the slope effect formula of Koch & Flokstra and the transport formulas of Engelund & Hansen as well as Yang & Lim showed the best results. The study shows that even though the height, length and kurtosis of the dunes can be matched quite well with the dunes of the physical flume, the skewness is not in the same area. A possible explanation is that the produced dunes are not dune-shaped but have the form of ripples.**

I. Introduction

Most of the more-dimensional calculations in engineering practice are 2D-hydrodynamic simulations. More and more morphodynamic tasks and for this a coupling to morphodynamic simulations is needed. In this case bed forms are only accounted for by empiric formulations, e.g. by changing the roughness coefficient. The actual depth of the river with dune peaks and deepenings is not reproduced. Following this the correct prediction of the available shipping capacity must be assigned with a higher uncertainty. Explicitly modelling of dune movement and behaviour could help to solve this task.

There have been different approaches to tackle this lack in morphodynamic modelling. One is LES of bed forms, where [1], [2] used detailed hydrodynamics to model the coherent structures of turbulence that are responsible for dune sediment transport. Additionally the sediment model included pickup, transport and deposition. In another approach [3] used roughness predictors by Engelund [4] adapted for supply limited situations and could show good agreement between prediction and measurements. It is in between these two methods, highly resolved and implicit integration, the task of this research project of the Federal Waterways Engineering and Research Institute falls.

In previous papers the capacity of TELEMAC-3D and SISYPHE has been shown [5], [6]. This paper provides further evaluation and analyses of the results. The hydrodynamic and morphodynamic programs are described in detail in [7] and [8].

II. Flume Experiment

A. Experimental setup

The experimental flume is situated at the German Federal Waterways Engineering and Research Institute (BAW), Karlsruhe. It has been described in [9] and [10]. A stretch of 30m length and 2m width covered with nearly uniform sediment with a D50 of about 1mm provided the data for the comparisons presented here. Different runs without installation, groynes, slot groynes and partially fixed bed have been conducted.

B. Numerical Model

For the numerical computation, TELEMAC-3D and SISYPHE (version 6.1) were used (for a detailed model description please also refer to http://www.opentelemac.org and http://docs.opentelemac.org).

The computational grid spans the 30 x 2 m of the experimental flume. The horizontal mesh size is 6-16cm with a mean of 11cm. In total that gives 5750 nodes and 11000 elements. 10 layers are used in the vertical with a logarithmic distribution finer towards the bottom, which results in roughly 100.000 elements to be calculated.

At the inlet constant discharge and no sediment is given at the boundary. The sediment input is realised with the dredging and disposal module DredgeSim [11] coupled to SISYPHE to reproduce the conditions of the physical model. Like in the experimental flume the water level at the outlet is kept constant.

C. Statistical dune parameters

The common approach to evaluate dunes is the use of dune lengths and heights. Longitudinal cross sections every 1cm of the topography are extracted and for each the slope is deducted. Afterwards a partial regression line is plotted for

each profile and by the crossings of each of the profiles with these regression lines a mean dune length and a mean dune height is calculated.

Furthermore the skewness and kurtosis of these longitudinal cross sections can be calculated from the same dataset. Skewness and kurtosis give additional information about the dune field. They are the third- and fourth-order distribution moments normalised by the variance. Using distribution moments (as skewness and kurtosis) will imply that the results are independent of the mean of a series of bed-form profiles, as well as the resolution of the recording [12].

If the elevation of the bed surface is expressed as $\alpha(x,y,t=t1)$ then the variance σ^2 of this data set is the 2[nd] order momentum of a spatial series:

$$\sigma^2 = \int_{-\infty}^{\infty} \alpha'^2 f(\alpha) \mathrm{d}\alpha = \langle \alpha'^2 \rangle \quad (1)$$

The standard deviation (square root of the variance) represents a characteristic vertical roughness scale for the bed surface, even though the dune with its specific height is resolved [13].

The skewness is the 3[rd] order momentum divided by the cube of the standard deviation σ:

$$Sk = \langle \alpha'^3 \rangle / \sigma^3 \quad (2)$$

It is a measure for the symmetry of a spatial series relative to the normal distribution. If the skewness is zero, the distribution around a sample mean is symmetric. Data more spread to the right of the mean has a positive skewness value and vice versa [12]. The general shape or form of the bed surface can be taken from this skewness value. Dune fields are associated with a negative skewness, which might represent a flattened crests and steeper troughs [13]. A negative skewness also represents a long, convex upwards stoss-side slope and a relatively steep and short lee-side face which are characteristic for dunes [12].

The kurtosis is the 4[th] order momentum divided by the standard deviation to the power of 4:

$$Ku = \langle \alpha'^4 \rangle / \sigma^4 - 3 \quad (3)$$

It is the measure for the peakedness/tailedness of a spatial series distribution, as it is the variation of the variance. The kurtosis value of a normal distribution is 3, so here this value is corrected to get a value of zero for a normal distribution. A positive value means more extreme fluctuations of the data set, whereas a negative kurtosis is the result of flat data [12]. Bed waves that are widely spread on a flat bed have a large and positive kurtosis, and a train of triangular, identical waves following each other will have a negative kurtosis [13]. One mean parameter has been calculated for the whole flume.

D. New formulae in SISYPHE

Several parameter sets have been tested. The use of further slope effect and deviation formulas as well as new bed load formulas promised better results. The slope effect and deviation model proposed by Apsley and Stansby [14] and Stansby et al [15] is based on the concept of the "effective" shear stress, which is a modified shear stress that includes a bed slope contribution. This formula has already been presented by Nicolas Chini at the 2009 TELEMAC User Conference.

The change of the transport angle (deviation) in x and y direction, which is used in the following presented calculations, is calculated as:

$$\theta_x^* = \theta \cos(\delta) - \lambda \frac{\partial z}{\partial x} \cos^2(\beta)$$
$$\theta_y^* = \theta \cos(\delta) - \lambda \frac{\partial z}{\partial y} \cos^2(\beta) \quad (4)$$

with $\cos\beta$ calculated as:

$$\cos\beta = 1/\sqrt{1 + (\partial z/\partial x)^2 + (\partial z/\partial y)^2} \quad (5)$$

In notation conform to the SISYPHE User Manual the deviation change would have the following form:

$$\tan\alpha = \theta \tan\delta - T \frac{\partial Zf}{\partial n} \quad (6)$$

with

$$T = \frac{\theta_o \cos^2\beta}{\tan\phi} \quad (7)$$

A new bed-load formula has been implemented into SISYPHE: the formula of Yang & Lim [16]. The formula is a total bed load approach, based on the concept that in natural flow condition there is often no sharp distinction between suspended and bed load transport. Following this both types of load are computed together and expressed in a total load transport parameter T_T. The formula as presented in their paper reads as

$$\theta_s = k \left(\frac{\gamma_s}{\gamma_s - \gamma} \right) \tau_o \left(\frac{u_*'^2 - u_{*c}^2}{\omega} \right) = k\, T_T \quad (8)$$

with k being a constant of 12.5. u_{*c} is the critical shear velocity for sediment movement, u'_* is the effective shear velocity and ω the grain settling velocity as proposed by [17]:

$$\omega = \frac{\nu}{d} \left(\sqrt{25 + 1.2 d_*^2} - 5 \right)^{1.5} \quad (9)$$

In notation conform to the SISYPHE User Manual the transport formula would have the following form:

$$\Phi_b = 12.5 \frac{d}{\rho_o \omega} \tau \ (\Theta' - \Theta_c) \qquad (10)$$

depending on the grain diameter, density, settling velocity, bottom shear stress and as well effective and critical shear stress.

III. RESULTS

A. *Skewness and kurtosis*

Figs. 1 and 2 show the dune height and length of several configurations. In the diagrams it is not indicated which parameter configurations were used, as the diagrams are supposed to show only the variation of results that were gained with minor changes in TELEMAC-3D and SISYPHE. The used parameter variations are slope effect and deviation formula (where most runs used either Koch & Flokstra plus Apsley & Stansby or Soulsby plus Talmon as slope effect plus deviation formula) and variations in TELEMAC-3D (such as solvers and most importantly time step variation). For details about the used formulas see SISYPHE User Manual [18].

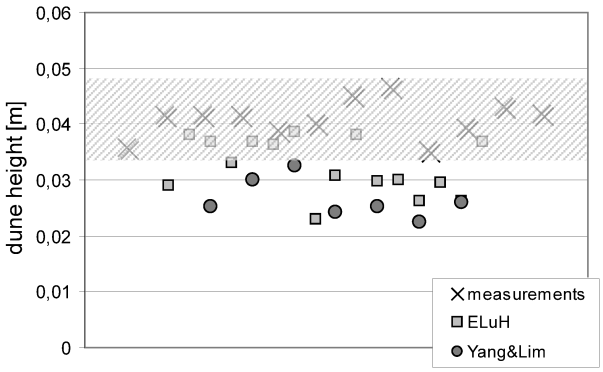

Figure 1. Dune length for different runs with Engelund & Hansen and Yang & Lim as transport formula compared to measurements.

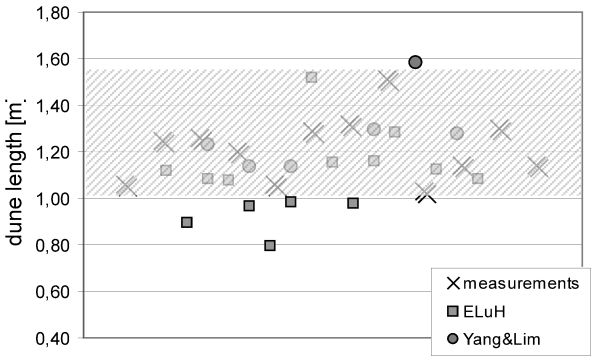

Figure 2. Dune heights for different runs with Engelund & Hansen and Yang & Lim as transport formula compared to measurements.

Additionally Figs. 3 and 4 show the skewness and kurtosis values of the same runs. In Fig. 5 the same data is plotted against a diagram taken from [12]. It can be seen that the kurtosis values can be matched for some runs, but that the skewness is off. Comparing it to the results from [12] it can be shown that the results of the simulations are mostly more similar to the ones of a riffle bed and that the skewness and kurtosis values of the experiments match the runs from fine sand dune runs presented by [12].

Ripples often have two sides that have the same length. This means that their stoss-side is much shorter as the one of dunes, which gives them a skewness that is much more close to zero. They will have less transport over their stoss-side and have no superposition. Due do this ripples can be even curved inwards instead upwards like dunes. This tends to results in a positive skewness for ripples whereas dunes will have a negative one [12].

In our numerical model we have obviously none or very limited existence of superposition due the limitations of the mesh size. Superpositioning ripples cannot be reproduced, as they are too small to be captured with our mesh. This might be a reason why it is not possible to reproduce the right curvature of our dunes and why most of the presented runs have a positive skewness. Due to this tests with finer resolutions will be conducted.

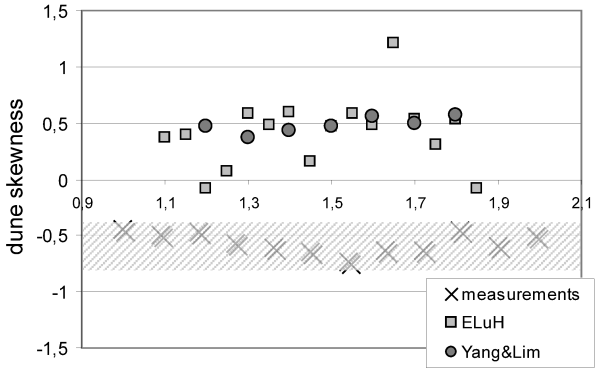

Figure 3. Dune skewness for different runs with Engelund & Hansen and Yang & Lim as transport formula compared to measurements.

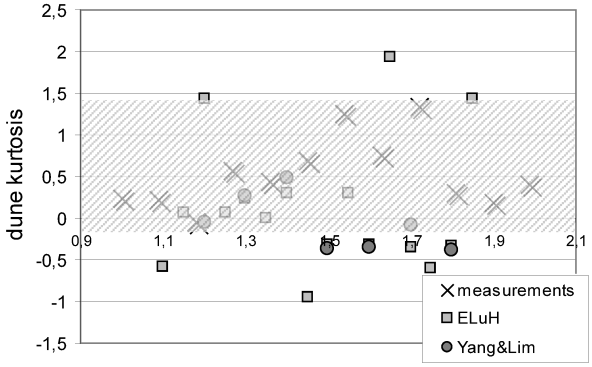

Figure 4. Dune kurtosis for different runs with Engelund & Hansen and Yang & Lim as transport formula compared to measurements.

Dunes have a flattened crest which will also result in a negative skewness value. As outlined by [13], this is due to the interaction of the dunes with the free surface and local flow acceleration. For ripples there is no flattening, as they do not interact with the free surface. Following this, the ripple-like form of our numerical dunes might be derived of a lacking reproduction of the flow field, namely the insufficient penetration of the dune influence towards the free surface.

For selected results the evaluated instant of area and time step has been varied (results not shown). From this it was possible to see that the results of skewness and kurtosis still slightly differed over time in the last hours of the run. A stable state of dune forms might not be reached yet. If a different area is chosen for evaluation, the values of skewness and kurtosis change. From this follows, that there are regions of different dune forms in the flume. The inflow is highly affected by the input measure and the output area as well might be disturbed by instabilities. The extent of the "undisturbed" area changes depending on the propagation speed of the newly added material, which changes with every bed load and slope effect formulation.

B. *Selected results*

Figs. 6 a), 6 b) and 7 show the overall best results compared to the measurements. They were gained with the bed load formulas of Engelund & Hansen and Yang & Lim. It can be seen, that even though the bottom topography matches the measurements quite well (Fig. 6 b), the values of skewness (and height as well) are not in the same range (Fig. 6 a).

C. *Time step dependency*

From Fig. 8 (a and b) we see very clearly that the time step influenced the results. The calculations have the same configuration but with time steps of 0.01s [1], 0.1s [2] and 0.5s [3]. On the left side runs of a setting with slope formula of Soulsby and deviation of Talmon are shown, whereas the runs on the right hand side have Koch & Flokstra as slope formula and the deviation formula of Stansby & Apsley. With a time step of 0.01s both settings result in a bottom formation that looks similar to the measurements of the physical flume (S10W1T2). In the graphs below (Fig. 8 b) the corresponding mean values of dune height and length, deviation, skewness and kurtosis are plotted against the time step. It can be seen that these mean values do not differ strongly between the 0.1s and 0.01s runs. The values of the 0.5s run on the other hand change in an obvious way. The same tendency can be observed in the plots of the bottom formation as well (Fig. 8 a).

For all runs the courant criterion is followed and the courant number ($c = ui\Delta t / \Delta x$) is below 1. This is checked even though this criterion is not a hard criterion for semi-implicit schemes. Further investigations will be done concerning this issue.

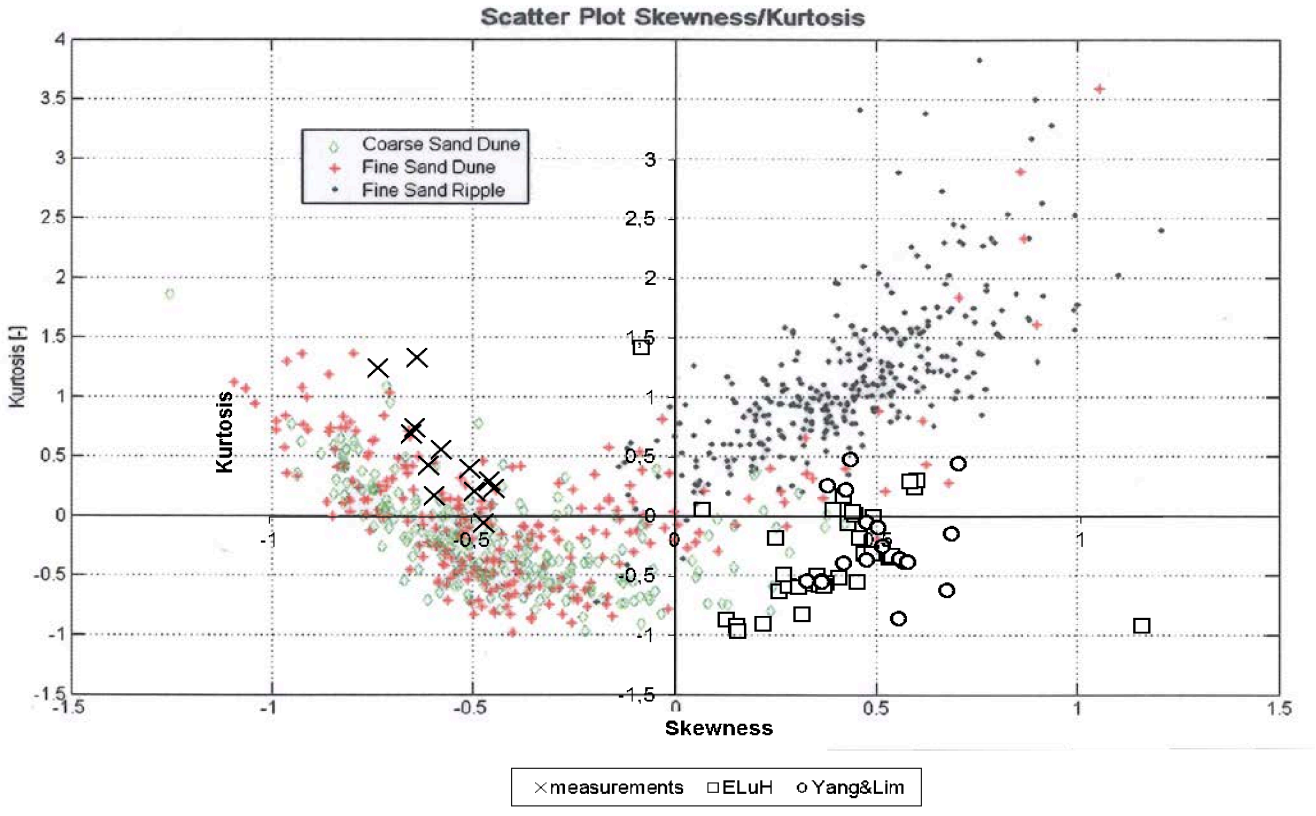

Figure 5. Dune skewness against kurtosis plotted against a diagram from [12].

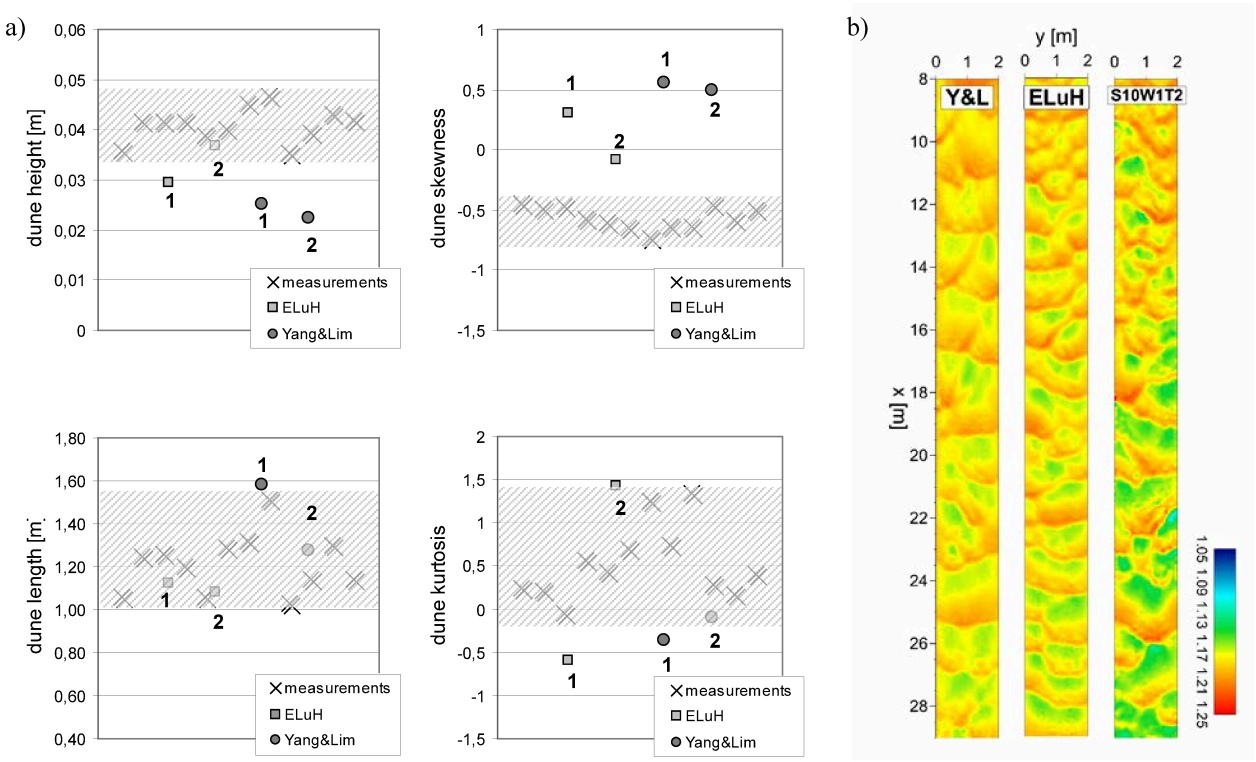

Figure 6. a) best runs in comparisons to measurements – 1: slope Koch&Flokstra and deviation Apsley&Stansby – 2: slope Soulsby and deviation Talmon. b) plots of bottom topography of run 1 for the two bed load transport formulas.

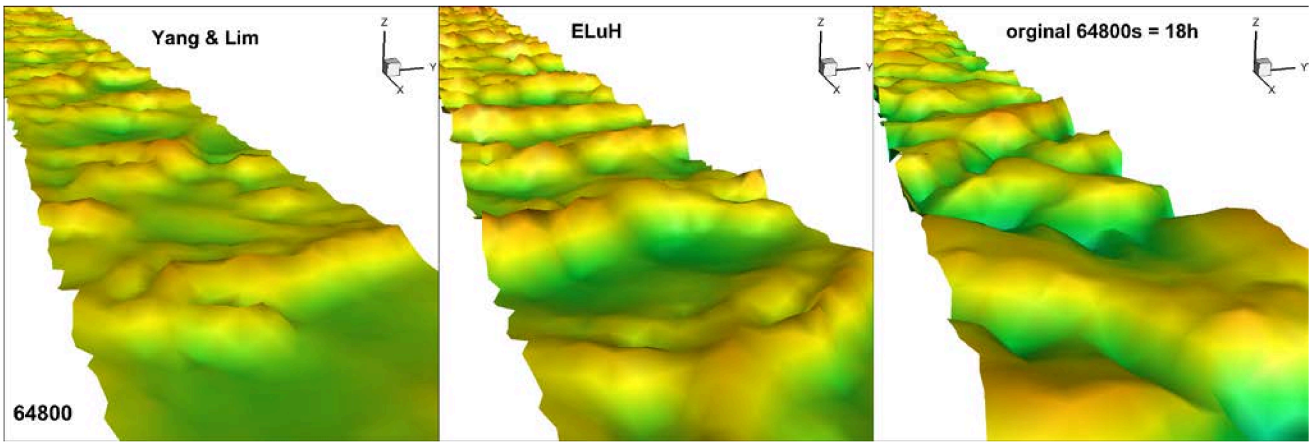

Figure 7. Comparison of simulated and physical flume bottom after 18h, 3D plot, same data set as figure 6 b)

D. Changed boundary conditions (input area)

The input of sediment still is one of the major challenges in this study. Even in the physical flume experiment the development of dunes was sensitive towards the sediment input method. In the numerical experiments this proved to be an even bigger issue. The dune form and also transport strongly depended on input volume and position. A reduced input volume (compared to the physical experiments) was chosen, which delivered better results due to the insufficient transport in the inflow area. Obviously the input method in the numerical model, being near to the boundary and subject to less developed flow conditions, created a fragile boundary condition. [19] states as well "…that even distant boundary conditions, which should normally be physically insignificant, may considerably influence numerical solution."

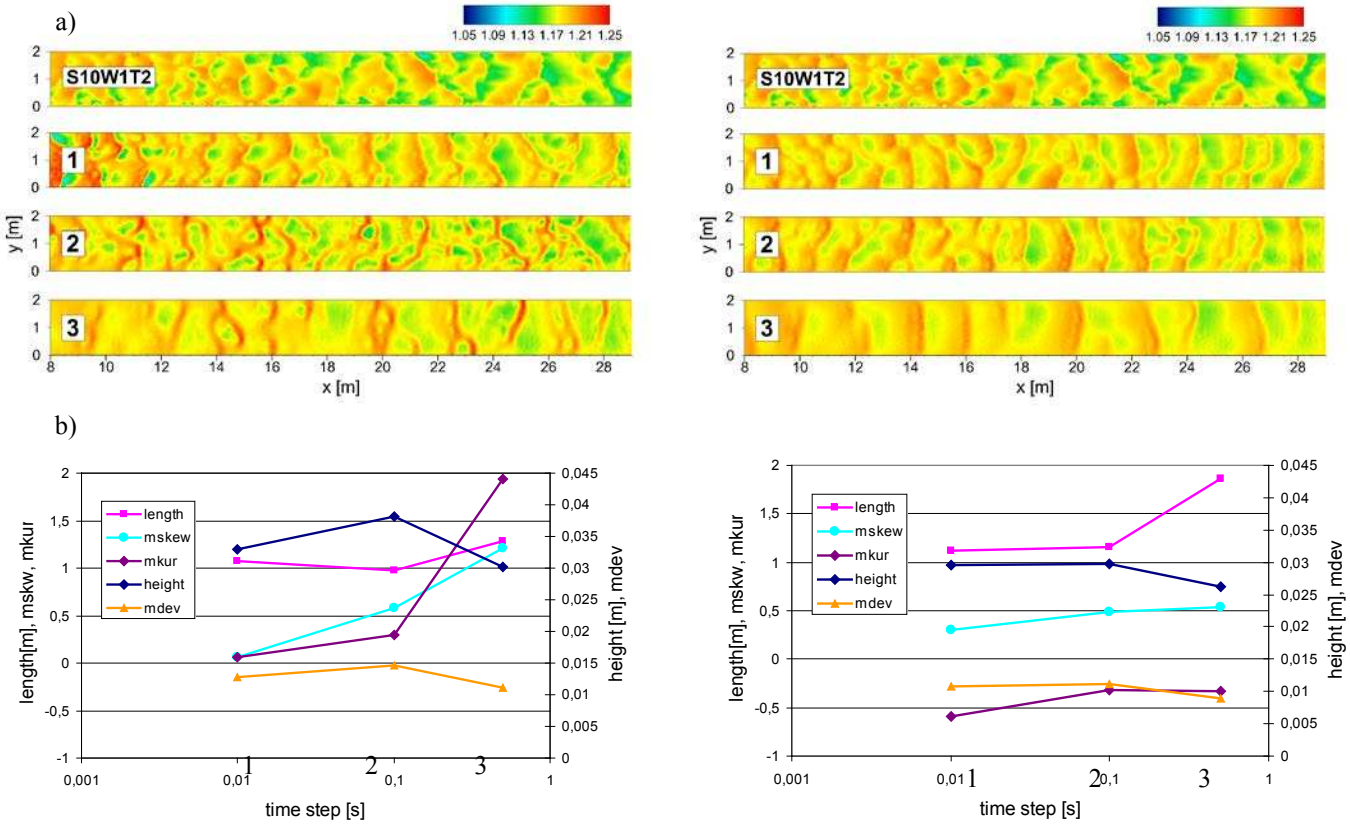

Figure 8. [1]: t=0.01, [2]: t=0.1 and [3]: t=0.5 – left side: slope effect formula of Soulsy and deviation of Talmon – right side: slope effect formula of Koch & Flokstra and deviation of Apsley and Stansby
a) bottom formations. b) mean values of dune height and length, deviation, skewness and kurtosis.

IV. CONCLUSIONS AND OUTLOOK

It was shown that explicit dune modelling with TELEMAC-3D and SISYPHE can be done. The correct shape parameters of these dunes are subject to several influencing factors such as bed load transport formula, slope effect and deviation formulas, morphodynamic time step as well as hydrodynamic parameters. A new transport formula by Yang & Lim [16] is presented for SISYPHE as well as the adaptation of the Apsley & Stansby [14] deviation formula for version 6.1. Both new formulas show good results for dune simulations.

Even though the presented results are promising, it is possible that they originated only from carefully calibrated numerical flaws and are not reproducible with other boundary condition or models. In their paper [20] state that dunes do not result from a linear instability of the code, whereas ripples can arise from such faults. Following this, the question would be if the here presented dunes are not dunes but ripples and the product of a linear instability, or if they are proper dunes with some faults in form and shape and that the correct shape can just not be reproduced in RANS. On the other hand there is research [21] that says that both ripples and dunes are the result of a primary instability (e.g. a linear instability of the code), which would make a linear stability analysis of the code interesting in both cases. But even this approach might have limitations: [22] state that "the complex evolution of bed forms is clearly a nonlinear process" which would conclude that a linear stability analysis could not asses this phenomenon. Nonetheless an analysis should bring further insights.

Other next steps will be further examination of flow parameters such as the turbulence model and the advection scheme of velocities, which are thought to be of major importance when modelling three-dimensional bed forms. So far the k-epsilon turbulence model and the SUPG advection scheme were found to deliver the best results. Further insights are expected from high resolution measurements which will be conducted over the fixed bed of a natural formed dune bottom. The calibration of the hydrodynamic model TELEMAC-3D with this new data set promises good results.

ACKNOWLEDGEMENT

We thank Martin Henning for the data of the experimental flume and fruitful discussions.

REFERENCES

[1] M. Nabi. Computational modelling of three dimensional bedform evolution. In Proceedings of River Flow 2010, 2010.

[2] M. Nabi. Computational modelling of small-scale river morphodynamics. PhD thesis, Delft University, Faculty of Civil Engineering and Geosciences, Department of Hydraulic Engineering, June 2012.

[3] A.P. Tuijnder and J.S. Ribberink. Development of supply-limited transport due to vertical sorting of a sand-gravel mixture. Proceedings of River Flow 2010, 2010.

[4] F. Engelund and E. Hansen. A monograph on sediment transport in alluvial streams. Technical University of Denmark, Denmark, 3rd edition, 1967.

[5] A. Goll, R. Kopmann, and T. Brudy-Zippelius. Numerical modelling of bed formes (dunes) with TELEMAC3D and SISYPHE. Proceedings of the 18th Telemac and Mascaret User Club, 19-21 October 2011, EDF, 2011.

[6] A. Goll and R. Kopmann. Numerical simulations of groyne influenced dunes. Proceedings of River Flow 2012, San José, Costa Rica. CRC Press, 2012.

[7] J.-M. Hervouet. Hydrodynamics of free surface flows: modelling with the finite element method. Wiley, Chichester, 2007.

[8] C. Villaret, J.-M. Hervouet, R. Kopmann, U. Merkel, and A. G. Davies. Morphodynamic modeling using the telemac finite-element system. Computers & Geosciences, 2011.

[9] A. Goll. Numerical modeling of bed load transport by dunes - Numerische Modellierung von Geschiebetransport durch Dünen. Master's thesis, Universitt Stuttgart, January 2011.

[10] K. Richter. Physikalische Modellversuche zur Auswirkung von Kerbbuhnen auf die Morphologie und den Geschiebetransport des Flussschlauchs. Master's thesis, Technical University Kaiserslautern, 2011.

[11] C. Maerker and A. Malcherek. Die Analyse von Baggern und Verklappen. Teil 1: Das Softwarepaket DREDGESIM. Korrespondenz Wasserwirtschaft, 2010.

[12] H. Friedrich, B.W. Melville, S.E. Coleman, T.M. Clunie, V.I. Nikora, and D.G. Goring. Three-dimensional properties of laboratory sand waves obtained from two-dimensional autocorrelation analysis, 2006.

[13] S. E. Coleman, V. I. Nikora, and J. Aberle. Interpretation of alluvial beds through bed-elevation distribution moments. Water Resources Research, November 2011.

[14] D. D. Apsley and P. K. Stansby. Bed-load sediment transport on large slopes: Model formulation and implementation within a RANS solver. Journal of Hydraulic Engineering, 2008.

[15] P.K. Stansby, J. Huang, D.D. Apsley, M.I. Garca-Hermosa, A.G.L. Borthwick, P.H. Taylor, and R.L. Soulsby. Fundamental study for morphodynamic modelling: Sand mounds in oscillatory flows. Coastal Engineering, 2009.

[16] S.-Q. Yang and S.-Y. Lim. Total load transport formula for flow in alluvial channels. Journal of Hydraulic Engineering, 2003.

[17] N.-S. Cheng. Simplied settling velocity formula for sediment mparticle. Journal of Hydraulic Engineering, 1997.

[18] C. Villaret, SlSYPHE USER MANUAL, Release 6.0. EDF R&D, 2010.

[19] J. Plešek, R. Kolman, and D. Gabriel. Estimation of the critical time step for explicit integration. 18th International Conference Engineering Mechanics 2012,2012.

[20] A. Fourriere, P. Claudin, and B. Andreotti. Bedforms in a turbulent stream: formation of ripples by primary linear instability and of dunes by nonlinear pattern coarsening. Journal of Fluid Mechanics, April 2010.

[21] M. Colombini and A. Stocchino. Ripple and dune formation in rivers. Journal of Fluid Mechanics, 2011.

[22] A. Singh, S. Lanzoni, P. R. Wilcock, and E. Foufoula-Georgiou. Multiscale statistical characterization of migrating bed forms in gravel and sand bed rivers. Water Resources Research, December 2011.

Morphological acceleration factor: usability, accuracy and run time reductions

Michiel. A.F. Knaapen
Coasts & Estuaries
HR Wallingford
Wallingford, United Kingdom
m.knaapen@hrwallingford.com

Rinse Joustra
Civil Engineering and Management
University of Twente
Enschede, the Netherlands

***Abstract*—Within SISYPHE 6.2, the option is created by BAW to use a morphological acceleration factor (MF) within the coupled TELEMAC2D-SISYPHE model. Multiplying both the evolution and the time by the same factor the model jumps forward in time, reducing the required computation time. This paper presents the usability of this approach, the gains in computation time and the loss of accuracy of this approach. Three different cases were used: a laboratory case of a trench in a constant flow, a river flood case and an estuarine test case. For the river flood case, a single event with varying water discharges, the approach is unsuitable. Using the MF implies that the water levels change too rapidly, altering the hydrodynamics. The same would be the case for tidal flow, but the morphological acceleration factor can still be used due to the repeating nature of the tide [1]. The downside is that strictly the results using a factor N are only valid after exactly N tides. For steady cases the approach can be used flexibly without limitations. Comparisons with the measured data the trench case show that the MF can be used with only limited loss of accuracy. The simulation time reduces rapidly, while the model skills only reduce marginally, up to the MF is 90. The simulation time initially reduces rapidly. For the larger model of an estuary, the gain using a MF of 20 reduced the run time by a factor 20. In this case however, the model does show some significant changes in the prediction.**

I. INTRODUCTION

Predicting long term morphology with a physical based model is still uncertain and a time consuming process. Several methods are available for reducing the computation time. These often used techniques are for example: Online method approach with morphological factor, Tide averaging approach, RAM, Continuity correction and parallel online approach. More information on each of these methods can be found in [2].

In version 6.2 of the TELEMAC suite, the morphological factor is available for us in SISYPHE. The morphological factor simply increases the depth change rates with a constant factor N. The new bed level represents a simulation period of N hydrodynamic time steps. For example, using 1 semi-diurnal tide (~12hours) and a morphological factor of 10 will result in an actual simulated time period of 120 hours.

In theory, assuming that the morphodynamic changes are small compared to the hydrodynamic changes, this approach reduces the computational effort without significant loss of model quality. In this paper, we describe efforts to quantify the effect of this morphological factor on the model performance, both in quality and speed.

II. APPROACH

The computational time on a dual core, single processor machine (details) without additional activity is used as a measure for speed.

To testing the reliability of the model runs with morphological factor objectively, the bias (mean error), and the Brier skill score [3] are calculated. The Brier skill score (BSS) compares the modelled morphological change $X_m(i)$-$X_0(i)$ to the observed changes ($X_1(i)$-$X_0(i)$):

$$BSS = 1 - \sum_i \frac{X_m(i) - X_0(i)}{X_1(i) - X_0(i)} \qquad (1)$$

This score was deemed the most suitable tool to assess the quality of morphological predictions [3], as it ignores model predictions in areas of little change ($X_m(i)=X_0(i)$). Downside is that it heavily penalizes small predicted changes where the measurement finds no change ($X_1(i)=X_0(i)$). The Brier skill score also allows to compare the model predictions with the no change prediction, which has a Brier skill score of 0.

TABLE I. BSS CLASSIFICATION FOLLOWING [3]

	BSS
Excellent	1.0-0.5
Good	0.5-0.2
Reasonable/faiar	0.2-0.1
Poor	0.1-0.0
Bad	< 0.0

Two test cases were chosen to test the approach to speed up morphological computations using a morphological factor: A stationary current case and a tidal current case.

III. TEST CASES

A. *Stationary current*

The first test case is based on the morphodynamic model of a trench flume experiment. The experiments were performed at Delft Hydraulics in a small flume with a length of 17 m, a width of 0.3 m and a depth of 0.5 m (Fig. 1). Sediment was used with D_{50} = 0.1 mm and D_{90} = 0.13 mm. Sand was supplied at constant rate at upstream section of flume to maintain equilibrium conditions. The channel had side slopes of 1 to 10 and a depth of 0.125 m.

Regular waves with a period of 1.5 s and height of 0.08 m were generated and a steady current following the waves was imposed. The water depth was 0.255 m and the current velocity was 0.18 m/s. The mobile bed consisted of well sorted sediment with 0.1 mm median diameter (D_{90} = 0.13 mm) and density 2650 kg/m^3. The mean fall velocity of the suspended sediment was 0.07 m/s.

To maintain equilibrium bed conditions away from the channel, 0.0167 kg/s/m sediment was fed into the flume at the inflow boundary.

The numerical model applied to simulate the dynamics in the flume experiment uses coupled TELEMAC-SISYPHE. It uses the SANDFLOW approach added to SISYPHE, using the lag function described in [4]. The model calculates the suspended sediment concentrations from the suspended transport predictor in the formula of Soulsby-van Rijn [7], while the bedload transport is calculated directly using the Soulsby-van Rijn formula (see [4] for more detailed information).

As Soulsby-van Rijn gives no sediment transport at all at these scales, the experiment is scaled up to field dimensions, multiplying the domain lengths by 10 and the time by √10. It was shown [4] that not scaling the sediment, assuming the morphology is bed-load dominated, gave the best model performance. After the simulation, the time and spatial dimensions are rescaled back to the scales of the flume experiment.

All other settings were the default SISYPHE settings. The calculation time without speed-up was 15 minutes and 7 seconds.

This model reproduces the flume experiments at Delft Hydraulics quite well (see Fig. 2 or refer to [5] for a more thorough analysis).

The model was run with a large range of range of morphological factors, and the results were compared with the measured bathymetry using the bias, root mean square error and the Brier skill score.

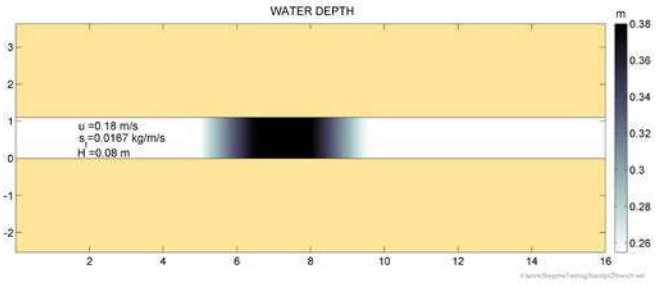

Figure 1. Layout, initial bathymetry (gray scales) and hydrodynamic conditions used in the flume experiments.

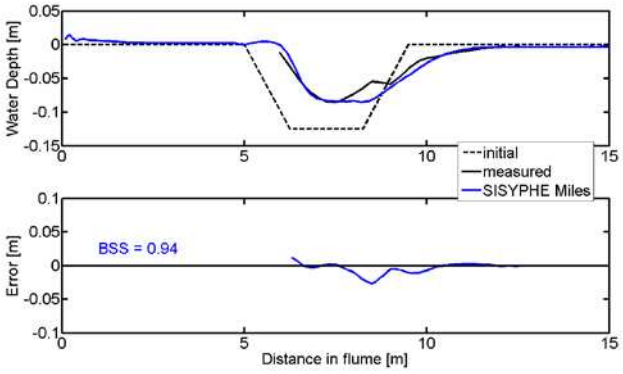

Figure 2. Comparison between the numerical model (blue) and the flume experiment (black) from the initial batymetry shown by the dashed line.

B. *Tidal current*

The second test case used was a model of the Dee Estuary in the northwest of England. The initial bathymetry is derived from LiDAR and swathe surveys (Fig. 3). All survey data are converted from Chart datum to ordinance datum.

The calculation is grid is a triangulated irregular mesh that covers the full estuary which is flooded during a spring neap tidal cycle. The maximum area of an element is 276595 m^2 the minimum element area is 22.9 m^2. The number of nodes and elements is respectively 21054 and 41386.

It is assumed that the main changes within the estuary are cause by tidal flow. The full spring neap tidal cycle at the estuary mouth is extracted from a calibrated hydrodynamic model of Liverpool bay (Fig. 4). The river discharge is neglected, because it has only minor contribution to the tidal prism over a tidal cycle (+/- 0.35%) [7].

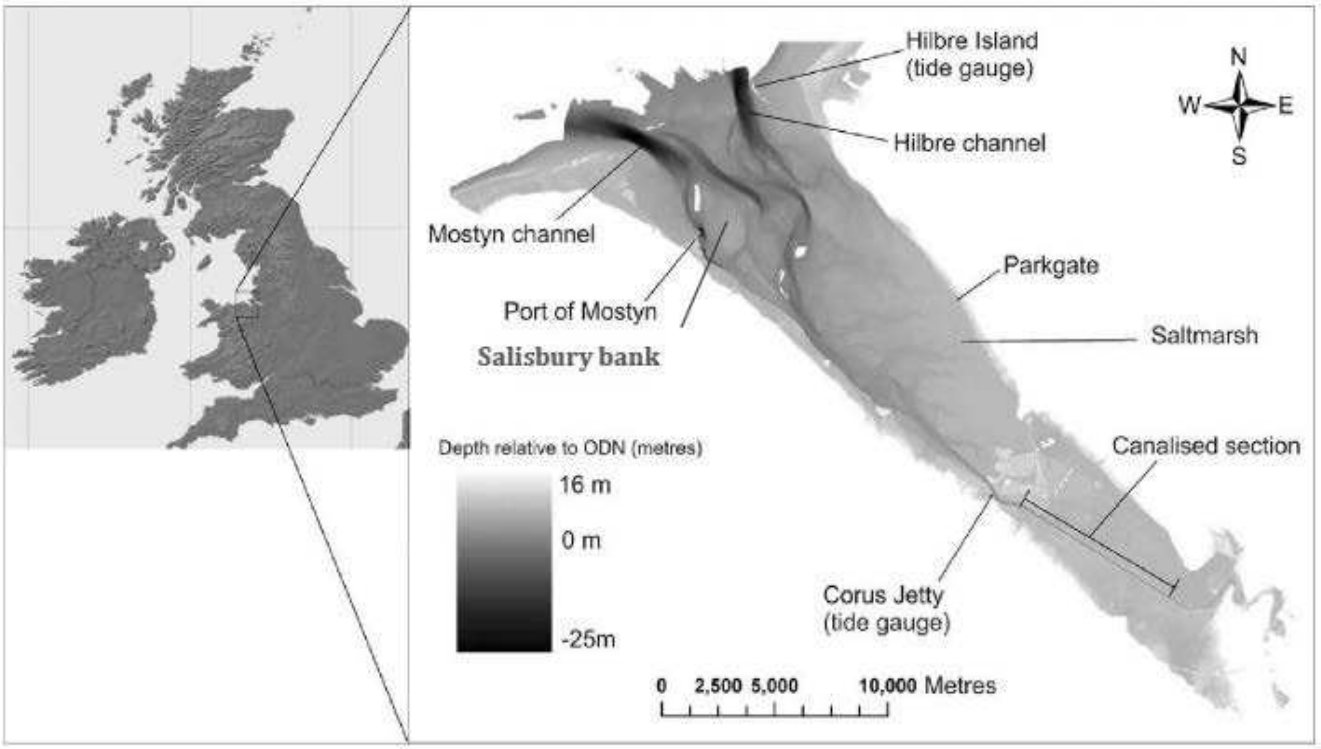

Figure 3. The Dee Estuary in the northwest of England.

Two grain size fractions (50-50%) of 0.09 mm and 0.2 mm, with each a respectively D_{90} of 1.0mm and 0.35 mm. Initially, grain sizes are constant through the domain of the estuary. Furthermore the sediment character is assumed as non-cohesive.

The other model settings were similar to those of the trench model, using the lag function described in [4]. The model calculates the suspended sediment concentrations from the suspended transport predictor in the formula of Soulsby-van Rijn [7], while the bedload transport is calculated directly using the Soulsby-van Rijn formula (see [4] for more detailed information).

Other model settings were kept at default values, slope effects are included, but no secondary current effects are used. As this model is still in development and not fully calibrated for morphodynamic predictions, the model compares poorly to the measured data (Fig. 5). The Brier skill score for example is negative, classifying the model as bad [3].

For this reason, the impact of the morphological factor is determined purely from the change between the model results with and without morphological speed-up.

IV. RESULTS

A. Stationary current

Fig. 6 shows that the largest rate of change of calculation time reduction occurs between the MF1 and approximately MF5. After approximately MF20 there is hardly any speed-up achieved. The reduction goes from 6% (MF20) to 2% at maximum MF of 130. This is caused by the time required to write the results to disc, which is already dominant with these morphological factors.

The Brier skill score reduces only marginally, from 0.93 with morphological factor 1 to 0.90 with morphological factor 130. With higher morphological factors the model became unstable. All results would classify as excellent according [3].

TABLE II. COMPUTATION TIME FOR THE RANGE OF MORPHOLOGICAL FACTORS USED TO MODEL THE DEE ESTUARY. IT SHOWS A LINEAR SPEED-UP WITH INCREASING MORPHOLOGICAL FACTORS

MF	Comp. Time (days)	Relative time
1	101.8	100%
5	20.1	20%
10	7.0	7%
20	3.7	4%

If we look at the bias (Fig. 7), however, the errors clearly increase with increasing morphological factor. The use of the morphological factor leads to an increased infill of the trench. The most relevant one, the median bias, increases with a factor 5 when using a morphological factor of 120.

The median bias is unchanged up to a morphological factor of 30, but then increases from about 1mm (less than

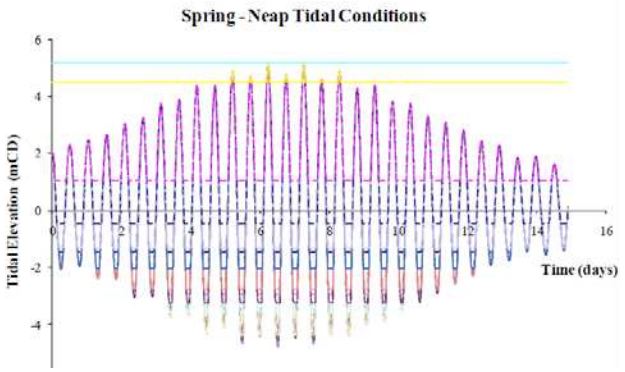

Figure 4. Tidal conditions at the boundary.

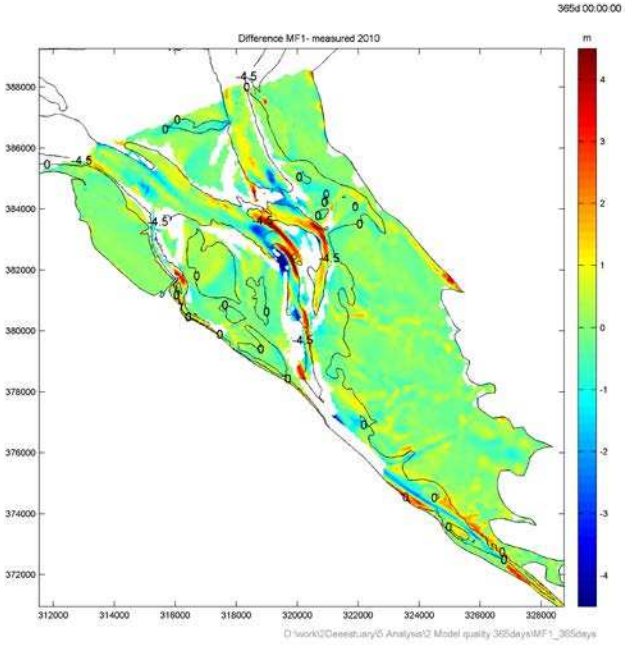

Figure 5. Differences between measured and model bathymetry after 1 year. The model tends to deepen and straighten the channels.

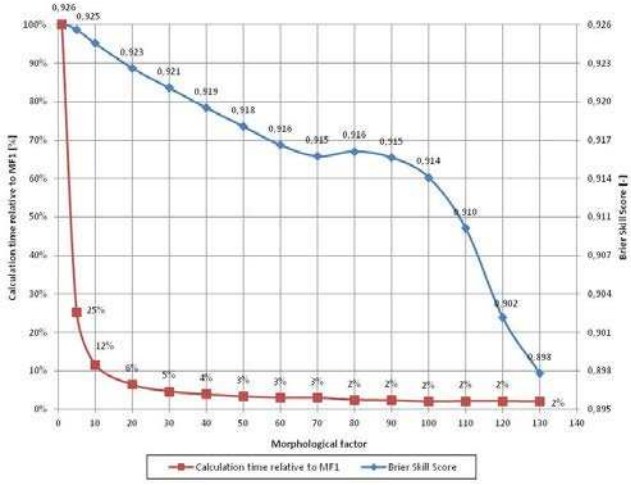

Figure 6. Results from the trench test case: Brier skill score (blue, right axis) and calculation time as percentage of the calculation time without speed-up (red, left axis) plotted against the morphological factor.

1% of the undisturbed water depth, or 2% of the observed bathymetric change) to 5 mm (4% of the undisturbed water depth, or 10% of the observed bathymetric change). Compared to a bathymetric change of about 5cm, that is not bad.

B. Tidal current

The tidal nature of the flows causes some issues using the morphological factor. Using a factor N means that a comparison of the results with and without morphological speed-up is only possible after a period of N tides. In the case of the Dee Estuary, the forcing contains a significant spring-neap cycle. Consequently, formal comparisons are only possible after N sping neap cycles.

Therefore, the test described here are limited to the factor 5, 10 and 20. The impact of the morphological speedup for this case is determined by the changes relative to the reference computation without morphological speedup (morphological factor 1).

For the Dee modelling, the morphological factor achieves a linear speed-up (The tidal nature of the flows causes some issues using the morphological factor. Using a factor N means that a comparison of the results with and without morphological speed-up is only possible after a period of N tides. In the case of the Dee Estuary, the forcing contains a significant spring-neap cycle. Consequently, formal comparisons are only possible after N sping neap cycles). The writing of the intermediate results can be neglected for the factors taking into consideration.

The predictive skill of the model deteriorates more for the Dee simulations then it did for the trench case (Fig. 8). With a 30% reduction in the skill for a morphological factor 20.

The bias in the model results (Fig. 9) shows that the use of the morphological factors leads to a overall bed lowering of up to an average 13 cm using a factor 20.

V. DISCUSSION

The results show that the use of a morphological factor does change the model results. The Brier skill score reduces with increasing morphological factor, while the bias increases.

The severity of these changes depends on the model specifics. In the trench case, with a uniform current and a short period being simulated, up to a morphological factor of 20, no discernible effects are visible. With higher factors the accuracy reduces linearly until the model becomes unstable.

In the case of the Dee Estuary, with a tidal forcing and a much longer period being simulated, already with lower morphological factors, the model results change significantly. At a morphological factor of 20, the Brier skill score using the morphological factor 1 run as ‘measured data’, is only 0.7, while the bias is several cms.

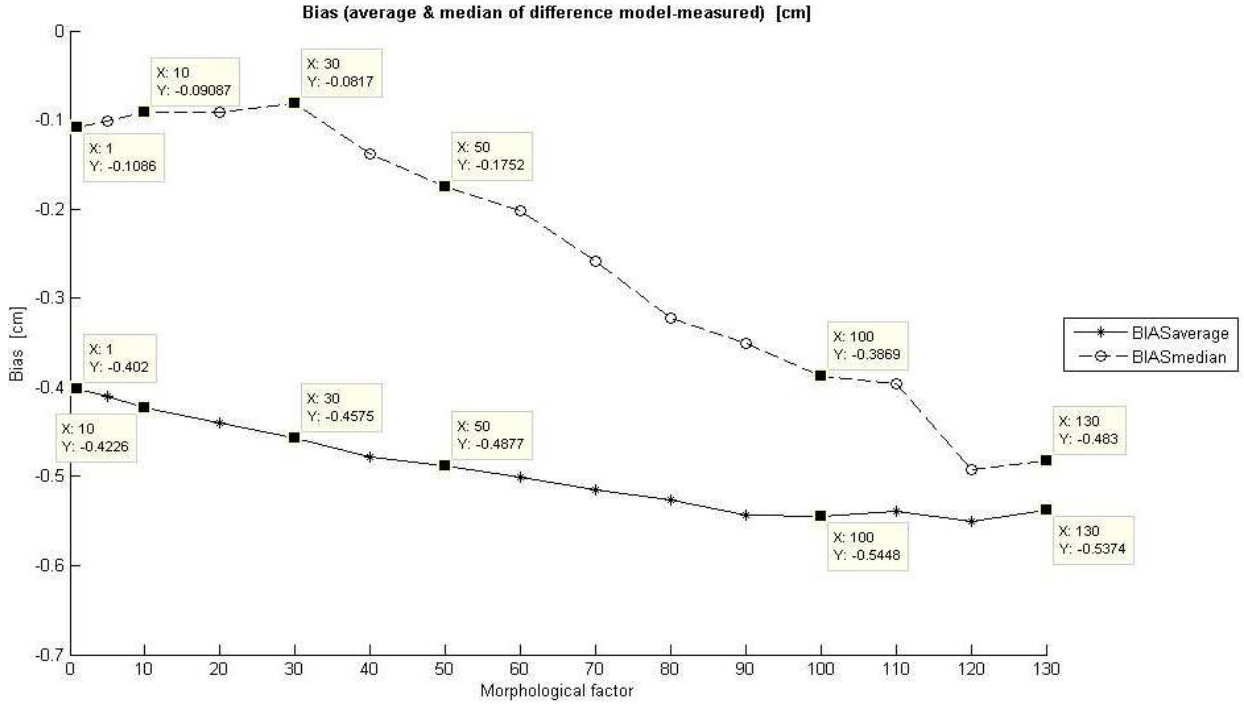

Figure 7. Median and average bias of the model as a function of the morphological factor for the trench test case.

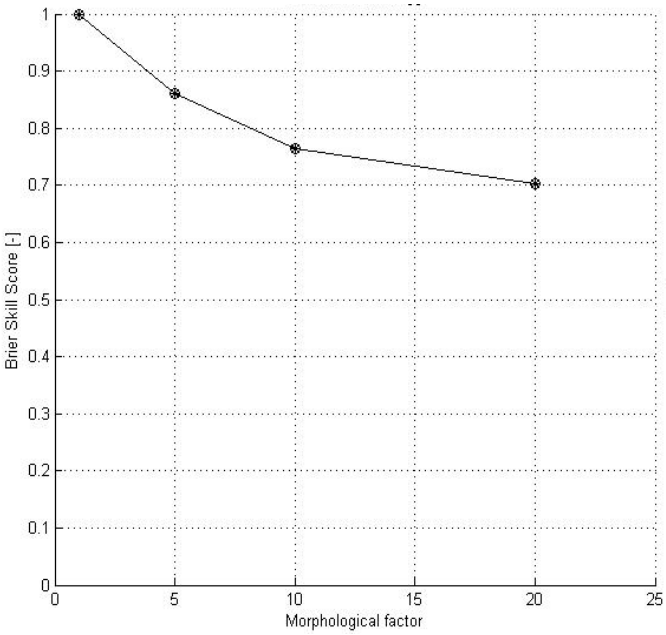

Figure 8. Brier skill score as function of the morphological factor used in the Dee simulations.

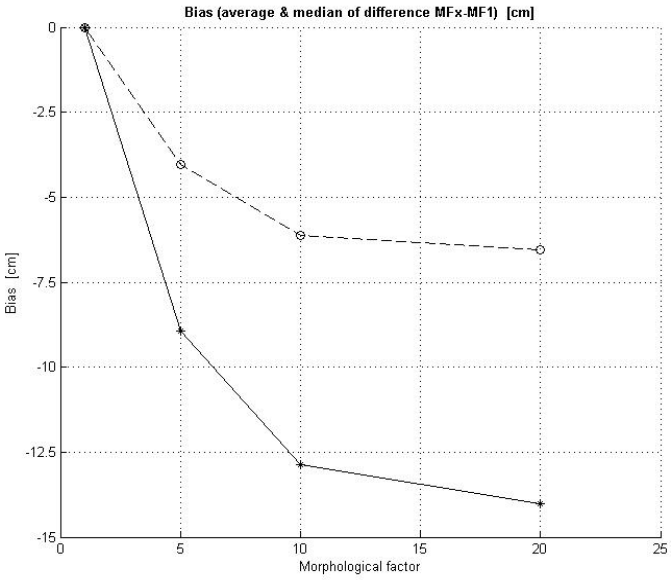

Figure 9. Average Bias (dots) and median bias (circles) in the model predictions as function of the morphological factor for the Dee Estuary simulations.

This bias in the Dee Estuary simulations might be related to an initialization issue, where initially sediment is being exported from the system. However, in general, the use of the morphological factor to speed up morphological simulations leads to an overshooting of the predicted dynamics, i.e. more deposition in case of infill and more erosion in erosion events.

VI. CONCLUSIONS

The morphological factor available to speed up morphodynamic simulations has been tested on two test cases. The first test uses measurements from a flume experiment on a trench; the second test is based on the Dee estuary.

The morphological speed-up available in SISYPHE works quite well, achieving linear gains in computation time for the large models. The results do, however, change adding additional errors to the prediction, reducing the model performance. The magnitude of these negative effects depends on the model specifics. For the short trench test, the added error is negligible, but for the larger Dee Estuary test case, the additional errors are significant.

Therefore, it is important to take care when using the morphological factor.

REFERENCES

[1] [1] D. McCain. “Long-term morphological modelling of tidal basins.” PhD thesis. Bangor University, 40pp, 2011.

[2] [2] D. Roelvink, and A. Reniers, “A guide to modelling coastal morphology,” Advances in coastal and ocean engineering. Volume12. pp.204-2014. World scientific, 2012.

[3] [3] J. Sutherland, D.J.R. Walstra, T.J. Chesher, L.C. van Rijn, and H.N. Southgate (2001). Evaluation of coastal area modelling systems at an estuary mouth. “Coastal Engineering”, 2004, pp.119-142.

[4] [4] M.A.F. Knaapen and D. Kelly, “Modelling sediment transport with hysteresis effects”, Proceedings XVIII TELEMAC-Mascaret User Conference, Chatou, 2011.

[5] [5] Van Rijn L. C. “Sedimentation of dredged channels by currents and waves”, Journal of Waterway, Port, Coastal and Ocean Engineering, ASCE. Vol. 112, 5, 1986.

[6] [6] Soulsby, R. “Dynamics of Marine Sands,” Thomas Telford. London, 1997.

[7] [7] R.D. Moore, J. Wolf, A.J. Souza and S.S. Flint.”Morphological evolution of the Dee estuary, Eastern Irish Sea, UK: A Tidal asymmetry approach”. Geomorphology vol. 103. p 588-596. 2009.

1D sediment transport modeling of reservoir operations

Test cases and application

Jodeau Magali, Lucie Guertault
LNHE
EDF R&D
Chatou, FRANCE
magali.jodeau@edf.fr

***Abstract*— COURLIS numerical code has been developed in order to calculate sediment transport, erosion and deposition. This numerical tool is used to simulate the effects of reservoir operations as emptying or flushing. COURLIS is based on a coupling between MASCARET (hydrodynamic) and a sediment component which allows calculation for sand and silt. Calculations with COURLIS on test cases are compared with experimental data. Eventually the capability of the code is illustrated with an example of reservoir emptying.**

I. INTRODUTION

Sediment transport and deposition in reservoirs is a worldwide subject of interest [1]. There may be impacts downstream and upstream of dams. In the French valleys, the filling of reservoirs depends on the production of sediment from the watersheds; it can be large and may be composed of gravel and/or silts. Hydroelectricity operators as EDF, have to take into account sediments when operating dams, therefore they need ways to predict the consequences of dam operations on sediment transport and reservoir morphology.

During emptying operations, one should avoid sediment erosion and downstream sediment output in order to mitigate water quality degradation. Reversely, flushing operations aim at eroding sediments from reservoirs to maintain or increase their storage capacity and/or prevent flooding upstream the dam. In such operations, the release of sediments to the downstream reach may be significant [1] and should be controlled [7]. There are different ways of predicting the downstream impacts of such operations, it often relies on experience, nevertheless numerical modeling could be used with relevant results.

This paper describes the use of a one dimensional sediment transport numerical model, COURLIS, to simulate reservoir operation or sediment transport in rivers. COURLIS is a one dimensional code for fine sediment transport modeling, it has been developed at EDF for more than 20 years, it is a component of the open-source TELEMAC-MASCARET system (www.opentelemac.org).

First, the basic principles of COURLIS are described. Then calculations with COURLIS on test cases are compared with experimental data. Eventually the capability of the code is illustrated with an example of reservoir emptying. The emptying of Tolla reservoir shows how numerical modeling can be used to assess the sediment release and to define an optimal emptying scenario.

II. COURLIS NUMERICAL CODE

A. *Overview of COURLIS*

COURLIS numerical code allows the computation of one dimensional flow and the sediment transport of mud and sand. COURLIS is based on a coupling between the hydraulic open-source component MASCARET which solves the 1D shallow water equations [3] and the sediment component which handles sediment processes. Both hydraulic and sediment components could be coupled at each time step, i.e. the hydraulic variables are calculated for a fixed bed then the bed evolution is calculated. If the hydrodynamic varies slowly, the user could define a less frequent coupling, for example coupling every ten or more hydraulic time steps. Details about the implemented equations can be found in previous papers [1] or [5], the following paragraphs give the main principles of the code.

B. *Sediment transport, erosion and deposition modeling*

Sand and cohesive sediment are dealt separately. For both type of sediments a one dimensional advection-dispersion equation is solved:

$$\frac{\partial A.C}{\partial t} + \frac{\partial Q.C}{\partial x} = \frac{\partial}{\partial x}\left(k.A.\frac{\partial C}{\partial x} \right) + Q_{erosion} - Q_{deposition} + Q_{bank} + S.q$$

Where : k dispersion coefficient (m^2/s)
q volumic sources ($kg/m^3/s$)
$Q_{erosion}$, … source terms for erosion, deposition and bank stability (kg/m/s)

For cohesive sediments, Partheniades (1961) and Krone (1962) empirical formulae are used to calculate erosion and deposition fluxes respectively:

Deposition $q_{deposition} = C.W_s.\left(1 - \frac{\tau}{\tau_{cd}}\right)$ if $\tau < \tau_{cd}$

Erosion $q_{erosion} = M.\left(\frac{\tau}{\tau_{ce}} - 1\right)$ if $\tau > \tau_{ce}$

Where τ_{ce} and τ_{cd} are respectively critical shear stresses for erosion and deposition.

For sand, i.e. non cohesive sediments, the transport capacity, q_s, is calculated with the Engelund Hansen formula (1967). An equilibrium concentration, C_{eq}, is obtained:

$$q_s = 0.05\sqrt{\frac{\delta d^3}{g}}\frac{K^2 R_h^{1/3}\tau_{eff}}{(\rho_s-\rho)gd} \quad C_{eq} = \frac{\rho_s q_s}{Q}$$

Deposition and erosion fluxes depend on the difference between concentration in the flow, C_{sand}, and equilibrium concentration:

$$\begin{cases} \text{if } C_{sand} \geq C_{eq} \text{ deposition} & D = w_s\,(C_{sand} - C_{eq}) \\ \text{if } C_{sand} \leq C_{eq} \text{ erosion} & E = w_s\,(C_{eq} - C_{sand}) \end{cases}$$

$$\frac{\partial Zb}{\partial t} = \frac{D}{C_{deposition}} - \frac{E}{C_{layer}}$$

Besides, the bank deformation is taken into account using a simple model, the bank slope is compared to a stability slope (submerged or emerged). If the critical slope is exceeded, sediment deposit is supposed to collapse immediately.

COURLIS numerical code has already been used to define efficient sediment management for various French reservoirs: the flushing of Genissiat and Saint Egrève reservoirs, [1] and [8], the emptying of Grangent and Tolla reservoirs, [5] and [4].

III. TEST CASES: COMPARISON WITH EXPERIMENTAL DATA

The following comparisons between numerical calculations and laboratory experiments show the capability of COURLIS to well calculate sand transport.

A. *Erosion : Newton experiment*

The Newton laboratory experiment [7] gives data to test erosion process. A flume is fed with sediment at equilibrium concentration. Measurements were performed in the flume after the stop of the upstream sediment input. Bed erosion is observed. The experiment parameters are given in TABLE I.

TABLE I. NEWTON EXPERIMENT, PARAMETERS

Flume length	L	9.14	(m)
Flume width	w	0.3048	(m)
Slope	S	0.00416	
discharge		0.00566	(m3/s)
Downstream water depth	Hd	0.041	(m)
Upstream concentration	Cu	0.88	(g/l)
Median grain size	d50	0.68	(mm)

In order to model this experiment, COURLIS is tested. The mesh size is 25cm, Strickler coefficient value is 67$m^{1/3}s^{-1}$ and dispersion coefficient is 1.0 m^2s^{-1} . The calculation gives very good results, Figure 1 . For the three measurement times, calculated values of bed evolution are very near from the measurements. The Meyer Peter Formula is also tested and gives even better results, in particular in the upstream part of the flume, Figure 2.

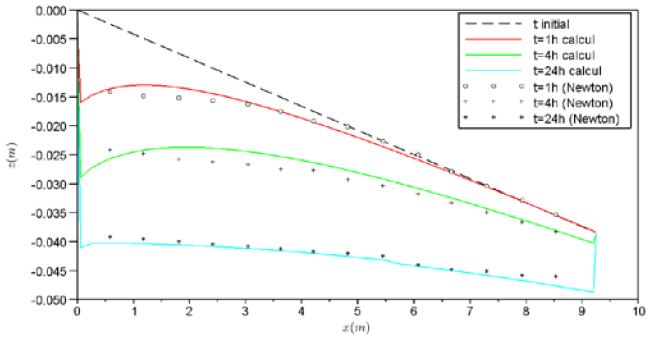

Figure 1. Newton experiment, calculation with Engelund Hansen formula.

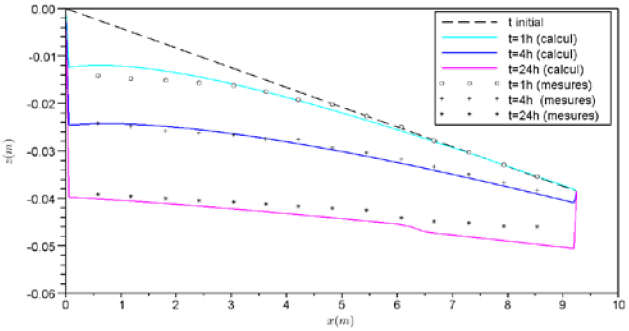

Figure 2. Newton experiment, calculation with Meyer Peter and Muller formula.

B. *Deposition : Soni experiment*

The Soni experiment [9] provides experimental data to test deposition process. A flume was fed with sediment at equilibrium concentration. Measurements were performed in the flume after an increase of the upstream sediment input. Bed deposition is measured. The experiment parameters are given in TABLE II.

TABLE II. SONI EXPERIMENT, PARAMETERS

Flume length	L	30	(m)
Flume width	w	0.2	(m)
Slope	S	0.00427	
discharge		0.0071	(m3/s)
Downstream water depth	Hd	0.072	(m)
Upstream concentration	Cu	4.88	(g/l)
Median grain size	d50	0.32	(mm)

In this calculation the mesh size is 25cm, Strickler coefficient is 45$m^{1/3}s^{-1}$ and dispersion coefficient is

$0.025 m^2 s^{-1}$. A non equilibrium coefficient [3] is used in the deposition law in order to better represent the dynamic of deposition. The value of this coefficient is set to 0.54.

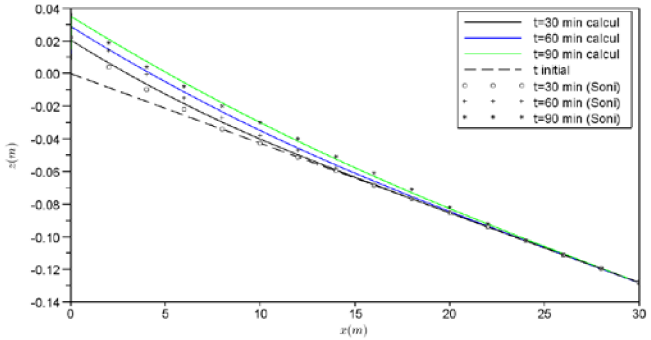

Figure 3. Soni experiment, calculation with COURLIS.

Results of deposition calculations well reproduce the experiment, Figure 3. There is a small over estimation of deposition in the upstream part of the flume.

IV. MODELLING RESERVOIR EMPTYING

COURLIS has been developed in order to model reservoir operations. It allows calculation of flushing flows but also simulation of reservoir emptying.

A. Tolla Reservoir

Tolla reservoir is located in South Corsica (France), the upstream watershed (132 km^2) is made of granite and covered by dense vegetation. Therefore sediment inputs are sand and organic matter. The dam, 90m height, was put in operation in 1965, Figure 1. The reservoir has a volume of 35 10^6 m^3 and a surface of 1.18 km^2. An emptying of the reservoir has to be done in the next years. One way to achieve mitigation of water quality degradation during operations is to control sediment output through the reservoir. Numerical modelling is performed to compare drawdown scenarios and to identify the less downstream impacting scenario. One dimensional modelling is well suited because of the large size of the reservoir (5km long), but also because we focus on the output concentration and we don't need details on three dimensional patterns in the reservoir.

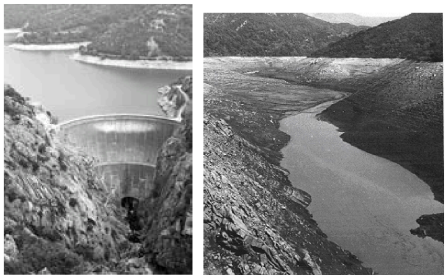

(a) (b)

Figure 4. (a) Tolla dam; (b) Picture of the reservoir during the 1981 emptying;

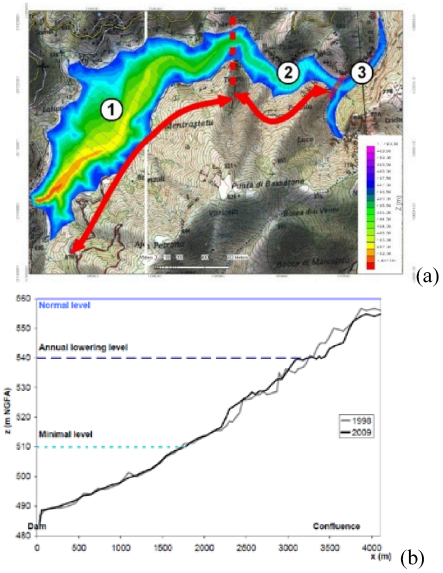

Figure 5. (a) reservoir bathymetry, definition of the three sediment specific area of the reservoir; (b) longitudinal profile.

In order to quantify sedimentation in the reservoir and estimate sediment properties, measurements were performed. Two bathymetries, 1998 and 2009, indicate that the reservoir shows three specific areas, Figure 5. . In addition, 15 sediment cores have been sampled using an Uwitech sampler to characterise the reservoir bed. Cores were located along the thalweg from the dam to the upstream part. The composition of the bed differs in the three areas: **(i) the downstream area**, from the dam to 2.1km upstream, is a deposition area where the sediment bed rises of 4.5cm per year. Low concentrated cohesive sediments are sampled; 1m layer of mud is implemented in the model. Some layers of tree leaves are squeezed in the sediments; **(ii) the middle area**, from 2.1km to 3.2km, is a delta deposit due to annual level lowering. The bed is made of a surface layer of silt (30cm) and a sub layer of sand (1m), leaves layers are also observed; **(iii) the upstream area**, from 3.2km, is an erosion area. Boulders, gravels, and layers of tree leaves fill the bed. Due to a lack of previous monitored emptying, there is not any calibration data to validate the model. Therefore the model is built upon the available measured data, analogy with sediment from other reservoirs is performed [7][6][1].A parametric analysis is used in order (i) to assess the weight of each parameter and (ii) to model the emptying with the most pessimistic (but still realistic) set of parameters.

B. Hydraulic and sediment boundary conditions

The emptying of the reservoir is controlled by the opening of the bottom gate and by the upstream discharge. Therefore (i) the upstream boundary condition is the assessed upstream discharge; in a first step, calculations were based on monthly averaged discharges and (ii) the downstream boundary condition is a water level calculated from the opening of the dam gates. Based on input discharge and gate opening, a reference emptying scenario is established from September to mid-February. In the beginning of the period,

the level lowering is slow (1.4cm/h from level 558 to 520mNGF and 2.36cm/h, from 520 to 490mNGF), then, due to the smaller amount of water, the lowering is greatly increased to 20cm/h for the last 5m.Upstream sediment concentration is assumed to be almost zero, and downstream boundary condition is a free output (i.e.$\frac{\partial C}{\partial x} = 0$).

C. *Numerical parameters*

The numerical parameters (vertical and longitudinal meshes, numerical schemes, coupling time step) are chosen in order to obtain reliable results with the shortest calculation times. An explicit scheme is used for the resolution of the hydraulic equation, thus the Courant-Friedrich-Lewy stability condition sets $\left(u + \sqrt{gh}\right)\frac{dt}{dx} < 1$. During the emptying, the low discharge and the high slope in the upstream part lead to supercritical flows and high Froude numbers in the backwater limit zone. Thus a fine mesh must be chosen there. Downstream the backwater limit, water-depth increases to reach 60m at the dam. Thereby, fine meshes lead to small time steps, smaller than 1s. The duration of the emptying is long; it takes 3 months to reach the lowest level, i.e. 1.4 10^7s. The best way to deal with this issue would have been to use a mesh adaptation, that is to say a fine mesh upstream the backwater limit and a large mesh downstream.

The coupling between the hydraulic and the sediment components is time consuming, so we tested different coupling frequencies and chose the one that leads to the smaller calculation time and gives results with small difference to the 1/1 coupling calculation. The coupling frequency has to be fitted to the characteristic time of hydrodynamic variations, i.e. to the speed of the level lowering. In the case of a slow level lowering (2.36cm/h), it highlights the relevant results of some low frequency couplings, below 1000 the results are similar to the 1/1 coupling. Calculation time for a 1000/1000 is 100 times faster than a 1/1 coupling meanwhile results are near from 1/1 results. The same comparisons are performed for a faster lowering (20cm/h), results indicate that a 100/100 coupling should be used.

The size of the vertical mesh (number of points to describe a cross section) is also investigated. The same issue as longitudinal mesh arises. Due to low discharges during the emptying (~4m^3/s), the modifications of the bed are located in the lowest parts of the section, which therefore require a fine discretization where there is erosion. For large meshes (50 points per a 150m large section), erosion is not well represented. We tested different meshes and we eventually selected the one given identical results as a very fine discretization (400 points per section) while leading to the smallest calculation time. In the following, lateral mesh is 200 points per section, i.e. Δx= 0.75m.

D. *Parametric Analysis*

The lack of calibration data to model reservoir emptying often occurs if there has not been any previous monitored operation. Therefore, the user of a numerical model may follow different means to estimate sediment output. Sensitivity analysis is a way to assess the weight of calculation parameters. Due to large calculation times, the Tolla model does not allow to perform a sensitivity analysis using Monte Carlo simulations. Notwithstanding, we perform sample runs to identify the impact of each parameter on the results. In this emptying calculation, the goal of the calculation is to give an assessment of the masses of sediment eroded from the reservoir (M_{silt} and M_{sand}) and assess the downstream maximal reached concentrations ($C_{max\ silt}$ and $C_{max\ sand}$). Therefore both criteria on mass and maximal concentration were used to identify the set of physical parameters which, in a relevant range, leads to the maximal value, i.e. the worst for the downstream hydro system. We start with common values previously used on this type of reservoir and explore limited ranges below and above these reference parameters. These parameters will be called *default parameters* in the following.

Some parameter variation effects are predictable. But the consequences on maximal output concentrations of sand or silt are not straightforward and effects of some parameters are not easy to foresee. Consequently, each parameter is tested while the others remain constant and equal to their default values. Table 1 shows the whole results. It highlights the small effect of some of the parameters (for example silt Dispersion coefficient) and the weight of others on the results (Parteniades coefficient, for example). In some cases, there is no obvious trend tendency in the effect of an increase of the coefficient on the results, one is able to identify maximising value (for example, Strickler coefficient Ks=30m$^{1/3}$s^{-1}). Parameters of sediment erosion and deposition laws lead to foreseeable results: (i) an increase of Parteniades coefficient, M, or a decrease of the erosion critical shear stress, τ_{ce}, give an increase of silt erosion and consequently of concentration; (ii) an increase of deposition critical shear stress, τ_{cd}, or a decrease of settling velocity lead to a decrease of silt deposition and therefore an increase of output masses. This analysis allows us to identify the set of realistic parameters that provide maximal output concentrations and masses.

E. *Emptying scenario*

The model is used to compare the reference scenario to different kind of emptying. The velocity of level lowering is increased to 10cm/h and 20cm/h instead of 2.5cm/h in the beginning of the emptying, and 20cm/h is kept in the end of the operation. It would be a way to reduce the duration of the operation. Results on Figure 6. show that the increase of the lowering speed in the first part of the emptying does not affect the value of the maximal output concentration, around 10g/l, as well as the total output mass which is around 6000t. But the duration of concentration exceeding 1g/l varies from 58 to 111h depending on the lowering speed. A longest duration may affect more the downstream fishes. In the case of a large increase of the lowering speed during the end of the emptying, the maximal concentration is strongly affected; it reaches the high value of 25g/l.

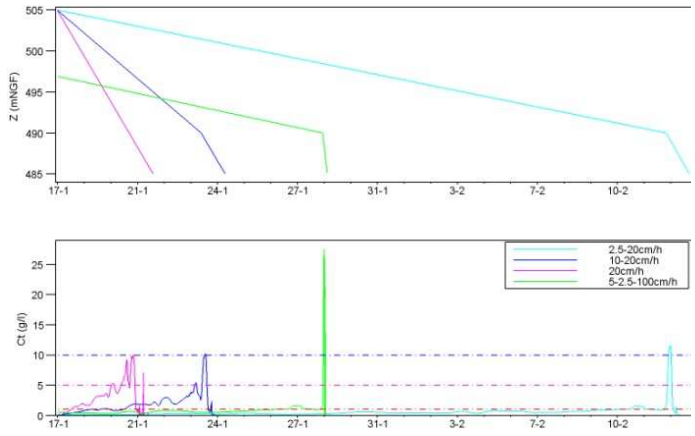

Figure 6. Emptying scenario: (scenarii A, B, C : 2.36, 10 and 20cm/h in the beginning and then 20cm/h of the lowering ; scenario D : first 10cm/h and then 50cm/h), (a) level variations and (b) output concentrations.

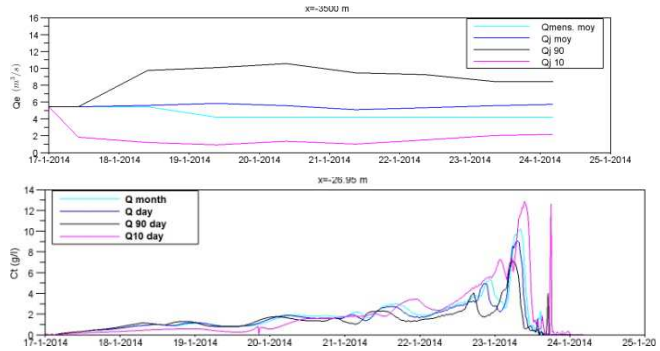

Figure 7. Emptying calculations (10cm/h) for different upstream discharges.

As the upstream discharge remains a source of uncertainty (there is no way of controlling it during the operation), we investigated the effect of the upstream discharge. Calculations were performed with mean monthly and daily discharges, and quartiles 10 and 90 of daily discharges, Q_{10} and Q_{90}, Figure 7. The value of the upstream discharge clearly affects the results: the lower the discharge, the lower the total eroded mass and the higher the maximal output concentration. The calculation with Q_{10} induces a maximal output concentration of 13g/l and an output total mass of 2600t whereas the calculation with Q_{90} leads to a maximal concentration of 7.2g/l and an output mass of 9000t. Even if a higher discharge increases the quantity of eroded sediments, the dilution effect induces a smaller output concentration.

V. CONCLUSION AND PERSPECTIVES

The cases presented in this paper illustrate how numerical modeling of sediment transport with COURLIS is used as a reliable tool to predict the effects of dam operations on sediment transport. Besides, these cases highlight the need of good quality field data sets to perform numerical modeling. Measurements made during dam operation and comparisons with calculated values would have improved the reliability of the numerical results. Unfortunately, no data are available so the numerical results must be analysed with cautiousness. They only allow a qualitative comparison of the scenarios.

REFERENCES

[1] C.Bertier, J.-P. Bouchard, & L. Dumond, " One dimensional model for reservoir sedimentation management". River Flow Conference, 2002

[2] S.A. Brandt, "Reservoir desiltation by means of hydraulic flushing: sedimentological and geomorphological effects in reservoir and downstream reaches as illustrated by the Cachi Reservoir and the Reventazon river, Costa Rica" PhD Thesis Institute of geography, University of Copenhagen 1999

[3] D. Chen,; K. Acharya, & M. Stone, "Sensitivity analysis of nonequilibrium adaptation parameters for modeling mining-pit migration" *Journal of Hydraulic Engineering,* 806-811, 2010

[4] N. Goutal & F. Maurel, " A finite volume solver for 1D shallow-water equations applied to an actual river". Int. J. Numer. Meth. Fluids, 38: 1-19, 2002

[5] M. Jodeau & S. Menu, ,"Sediment transport modelling of a reservoir drawdown, example of Tolla reservoir" *River Flow Conference,* 2012

[6] D. Marot, J.-P. Bouchard & A. Alexis, "Reservoir bank deformation modeling: application to Grangent reservoir". Journal of Hydraulic Engineering, 586-595, 2005

[7] G. L. Morris & J. Fan, "Reservoir sedimentation handbook McGraw-Hill", 1997.

[8] C. Newton, "An experimental investigation of bed degradation in an open channel"*Trans., Boston Society of Civil Engineers*, 28-60 , 1951

[9] H. Shen, "Flushing sediment through reservoirs". *Journal of Hydraulic Research*, 37-6, p.743-757, 1999

[10] J. Soni, "Laboratory study of aggradation in alluvial channels" *Journal of Hydrology, 49*, 87-106 , 1981

[11] E. Valette, & M. Jodeau, "How to predict the sedimentological impacts of reservoir operations?" International Conference on scour and erosion, 2012

Development of a long-term morphodynamic model for the German Bight

Bert Putzar, Research Assistant
Institute of Hydro Sciences
University of the German Armed Forces Munich
Munich, Germany
bert.putzar@unibw.de

Andreas Malcherek, Professor
Institute of Hydro Sciences
University of the German Armed Forces Munich
Munich, Germany
andreas.malcherek@unibw.de

***Abstract*—Located in the South-East of the North Sea, the German Bight is strongly influenced by high anthropogenic impacts like commercial fishing, offshore wind farms, shipping, dredging and disposal activities and tourism. The intensified use and the commercial exploitation will make it essential to predict the evolution of the sea bed for decades. Numerical models can be a powerful tool to contribute to this challenging issue and to provide a basis for decision-making. This article introduces a coupled numerical model based on the TELEMAC system for the German Bight to predict the long term and large scale morphodynamic development.**

I. THE GERMAN BIGHT

The German Bight is a large bay located in the South-East of the North Sea, bounded by the Dutch, the German and the Danish coastline. The morphology is characterised by the barrier island systems of the Frisian Islands, the intertidal area of the Wadden Sea, and three main estuaries of the Elbe River, the Weser River and the Ems River (Fig. 1).

With an average water depth of approximately 30 m, the German Bight is relatively shallow in contrast to the North Sea, which has an average water depth of about 100 m and a maximum value in the Norwegian Trench of about 725 m. Larger areas with maximum depths up to 60 m are located in the central part (Fig. 1). The Dogger Bank, a large shallow area, is a natural boundary to the adjacent part of the North Sea in the north-westerly and westerly direction. The water depths in this area are between 20 m and 30 m.

The tidal wave enters through the English Channel and the northern connection to the Atlantic Ocean, causing a tidal range between three and four meters. The semidiurnal M2-tide dominates and induces a 12.25-hour rhythm of ebb and flow. Exposed to the prevailing westerlies, storm surges and high waves contribute to the morphodynamic evolution of the coastal area.

Fig. 2 shows the sediment distribution of the upper stratum of the sea floor. The classification used here is based on the Udden-Wentworth scale and the median grain diameter d_{50}. The sediment distribution is a result of deposition during the Quaternary, the geological youngest period of Earth's formation, and relocation of these sediments by tide and wind-induced waves. Very fine sand and Medium sand predominate in the upper stratum. Sediments with a larger d_{50} do not occur significantly in the German Bight. In contrast, one can find partially wide areas with cohesive sediments, summarised in one sediment class denoted as Coarse silt in Fig. 2. Examples are the area south-east of the Island of Heligoland or the Wadden Sea.

Due to the geological development, the sediment available for sediment transport is in general limited by a non-erodible horizon, the basis of Holocene sediments. The sediment thickness varies between a few meters around the East Frisian Islands and approximately 15 m in the south-easterly part of the German Bight and the area of the North Frisian Islands [1].

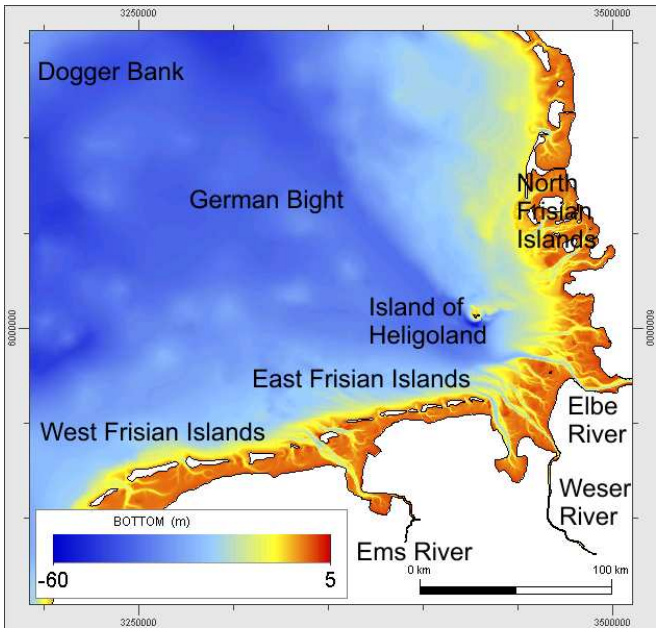

Figure 1. Overview of the German Bight.

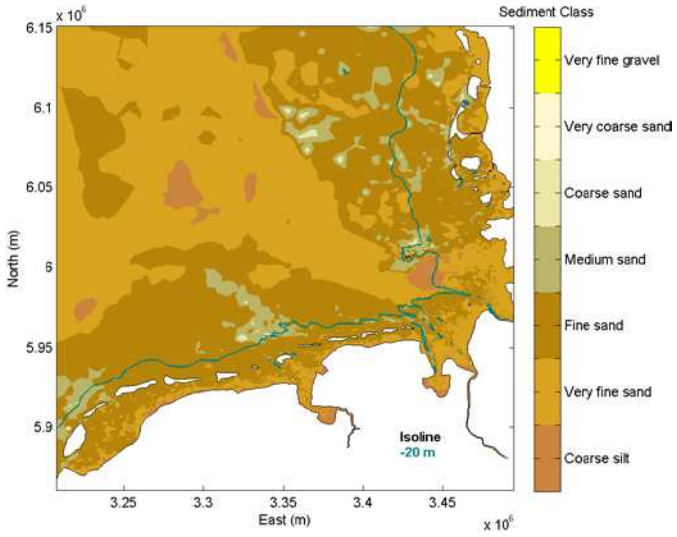

Figure 2. Sediment distribution in the German Bight.

II. SIMULATION MODEL

To simulate the long-term morphodynamic evolution of the German Bight, a coupled numerical model was developed based on the Finite-Element system TELEMAC [2]. The models used are the hydrodynamic model TELEMAC-2D [3] for calculating depth-averaged flow, the third generation wave model TOMAWAC [4] to obtain sea state parameters and the morphodynamic model SISYPHE [5].

The simulation model can take into account the tide-induced and wind-induced forces on the hydrodynamics to calculate depth-averaged velocities in the model domain. Based on two-dimensional velocities, fractionated sediment transport as bed load and as suspended load is modelled. The Exner equation is solved iteratively to update the bed morphology. The effect of waves is considered by calculating the wave-induced bed shear stress. According to the integrated modelling approach of the TELEMAC system, all models use the same Finite Element grid.

The hydrodynamic model TELEMAC-2D and the morphodynamic model SISYPHE are coupled in a direct way. At each simulation time step, the hydrodynamic model calculates the depth-averaged flow field and the water depth. These results are passed to SISYPHE. After calculating sediment transport and the resulting bed evolution, the updated bed level and the new bed roughness are passed back to TELEMAC-2D. The mean period, peak frequency and mean direction are calculated a priori with the TOMAWAC model and saved as a binary file. For simulations with wind and wave influence, the TOMAWAC file is read and the sea state is interpolated at every time step according to the actual simulation time to match the wind field from TELEMAC-2D.

For accelerating the simulations, the parallel version of TELEMAC is applied that uses a Message Passing Interface (MPI) implementation to take advantage of parallel computing power. With a number of 16 processors and a time step of 200 s, which is used for all the results presented in this paper, and taking into account tide, wind and wave forcing a simulation for 100 years requires approximately 25 days of real simulation time on the mesh with 70.000 elements.

III. GRID, BOUNDARY AND INITIAL CONDITIONS

The simulation domain covers the North Sea, the English Channel and the adjoining area to the Baltic Sea. The unstructured finite element mesh consists of nearly 70.000 triangular elements and is applied to all simulation models. For detailed simulations, a high resolution mesh with approximately 2 million elements is used.

At the open boundaries to the Atlantic Ocean tidal elevations are imposed. 14 harmonics extracted from the FES2004 [6] tidal data are applied. Hourly wind field data is obtained from the German Weather Service for the years from 1996 until 2006. The whole structured data is interpolated on the unstructured simulation grid. Fresh water inflow is considered for the Elbe River with 870.0 m^3/s [7], the Ems River with 80.1 m^3/s [8] and the Weser River with 324.0 m^3/s [8]. These values represent the multi-annual mean discharge. In case of simulations with wave influence, the sea state computed a priori by TOMAWAC is used to calculate the wave orbital velocity within the morphodynamic model SISYPHE.

The bed composition of the sea floor is modelled by one cohesive fraction and six non-cohesive fractions. For each sediment fraction a characteristic grain diameter was defined as followed: Coarse silt (d = 4.7 x 10^{-5} m), Very fine sand (d = 9.4 x 10^{-5} m), Fine sand (d = 1.875 x 10^{-4} m), Medium sand (d = 7.5 x 10^{-4} m), Coarse sand (d = 1.5 x 10^{-3} m) and Very fine gravel (d = 3 x 10^{-3} m). Fig. 2 shows the initial sediment distribution in term of sediment classes. The active layer thickness was calculated as three times the mean grain diameter and the initial thickness of available sediment is set to a fixed value of 20 m.

The long term simulations were carried out over a period of 100 years with the initial bathymetry from 2006 and the wind- and wave forcing of the calendar year 2006. For the medium term sensitivity analysis the period from 1998 to 2006 was simulated with tide, wind and wave forcing. To compare the influence of the grid size, the year 2006 with tide forcing only was chosen. The initial bathymetries and the sediment distribution are obtained from an advanced data-based model, providing high-resolution data for every node of the computational grid. Initial values for the velocities and the free surface elevation are set to zero for each simulation. The Bijker formula was chosen for the long term simulations over 100 years and for simulations over 1 year to account for current and combined current-wave induced bed load transport. The Bailard formula was applied for 10-year simulations to appraise the sensitivity of the results in terms of the bed load formula.

IV. RESULTS

A. *Tide-driven morphodynamics*

The results for the bed level and bed evolution are illustrated in Figs. 3 and 4. During the simulation period the large scale morphology does not change much. Comparing the initial state (Fig. 3, top) and the bed level after 100 years (Fig. 3, bottom), one can recognise that the deeper parts in the central German Bight show no significant change and the morphological most active area is between the –20 m isobath and the coastline.

Around the East and West Frisian Islands significant deposition and erosion patterns occur at the ebb tidal deltas and in tidal inlets (Fig. 4, top). In the area of the mouths of Elbe River and Weser River some tidal channels show a migration eastwards ("+" in Fig. 4, top) whereas some channels are only deepened. The largest erosion and deposition patterns are located around 6 x 106 m North and 3.45 x 106 m East, which is the area east of the Island of Heligoland. Fig. 4 (top) shows that the sediment is eroded at a wide area, transported in eastern direction and deposited more closed to the coast. As a result, after 100 years a channel has developed, marked with an "X" in Fig. 4 (top).

Mainly deposition occurs at the tidal flats, which are located approximately between the –2 m and the 2 m isobaths, in the whole model domain. The development of the tidal flat area shows Fig. 4 (bottom). After a simulation time of 100 years the area remains nearly constant with a small loss of 53 x 10^6 m^2. The volume increased by 7.28 x 10^8 m^3, which is an average accumulation of approximately 18.22 cm. Even if this result sounds reasonable, one should bear in mind that consolidation of cohesive sediments is not accounted for in the simulation model presented in this article.

B. *Morphodynamic evolution under the influence of tide, wind and wave*

Fig. 5 (top) shows the bed level after a simulation period of 100 years with the influence of tide, wind and wind-induced waves. The bed level is very similar to the simulation with tide forcing only. Large scale morphological changes, e.g. development of a new channel system or removal of outer sand banks, do not occur. But the analysis of the difference between this simulation and the simulation with tide forcing only shows that due to wave-induced wave shear stress, the morphodynamics increases between the –5 m and the –20 m isobaths (Fig. 5, bottom). The tidal flat area remains nearly unchanged with a loss of 67 x 10^6 m^2 and an increased volume of 7.16 x 10^8 m^3. The average accumulation is approximately 17.97 cm, which is similar to the simulation with tide forcing only.

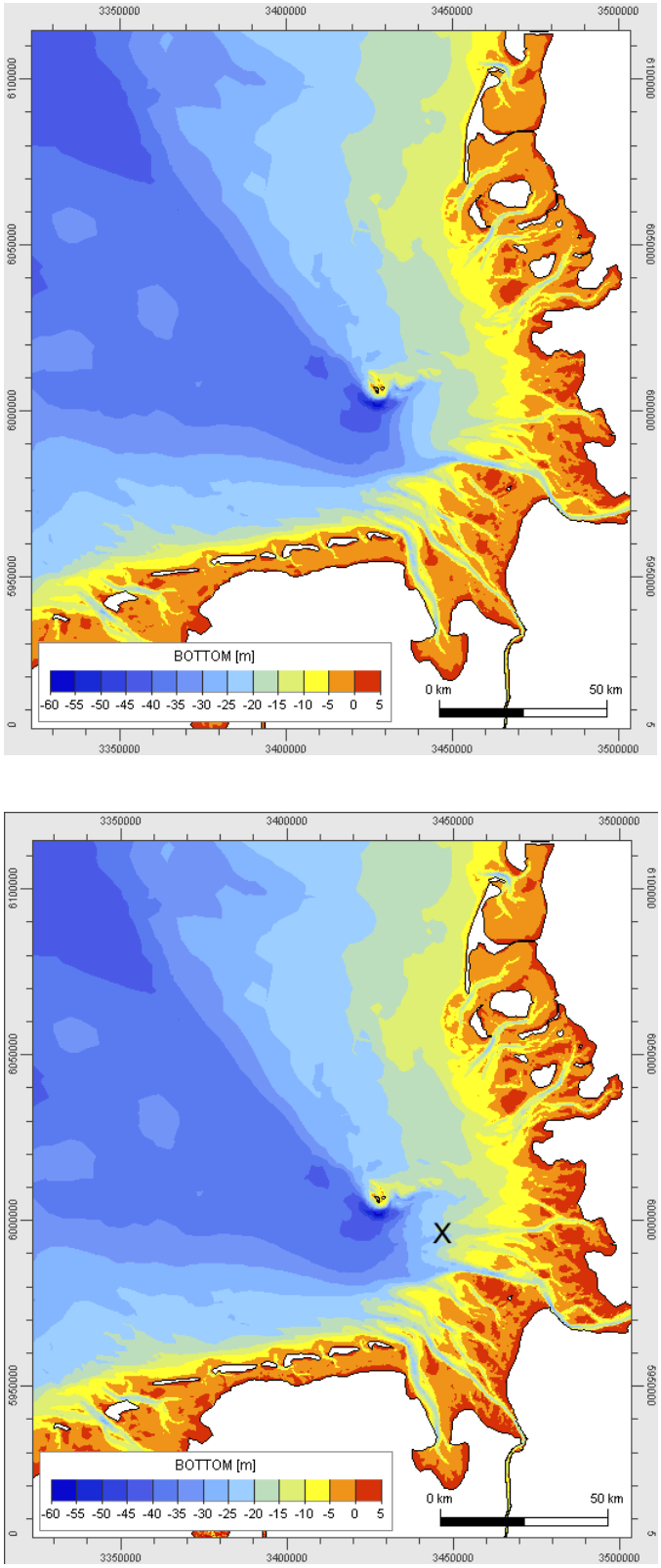

Figure 3. Long-term simulation results with tide forcing only. Top: Initial bed level. Bottom: Bed level after 100 years.

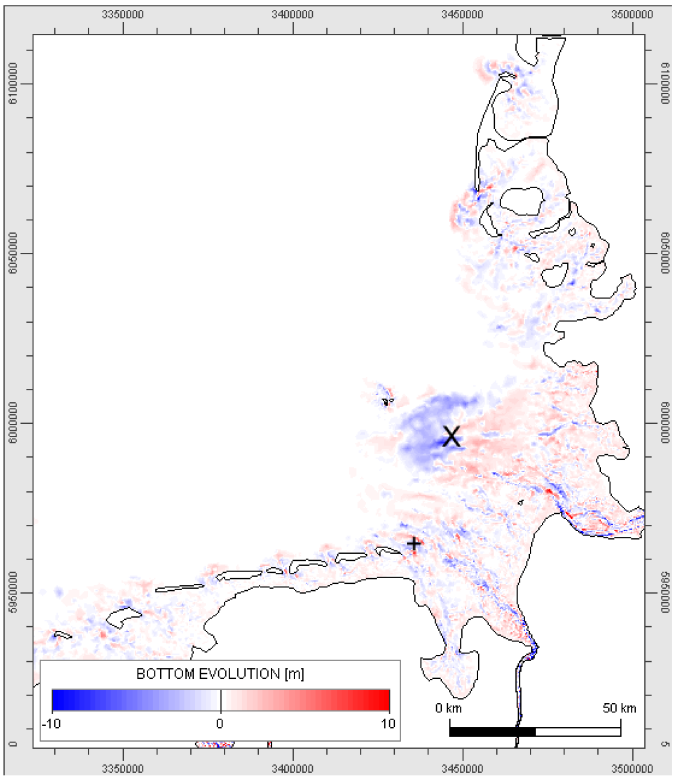

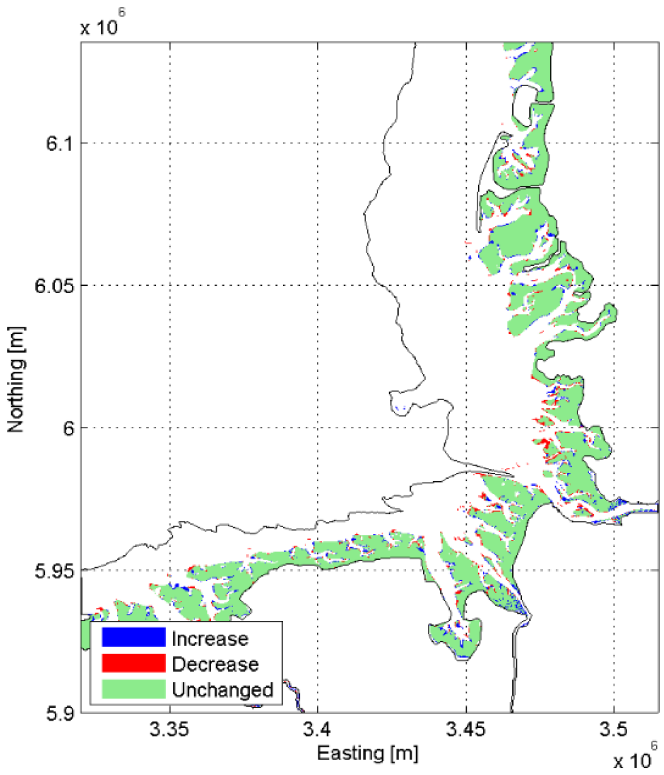

Figure 4. Long-term simulation results with tide forcing only. Top: Bed evolution after 100 years; X indicates the development of a new channel, + indicates an example for channel migration. Bottom: Development of tidal flat areas.

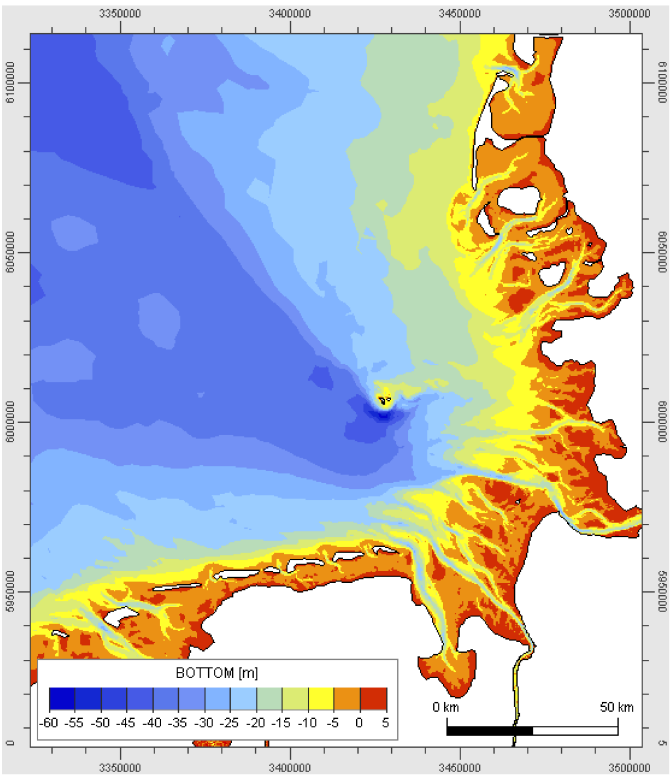

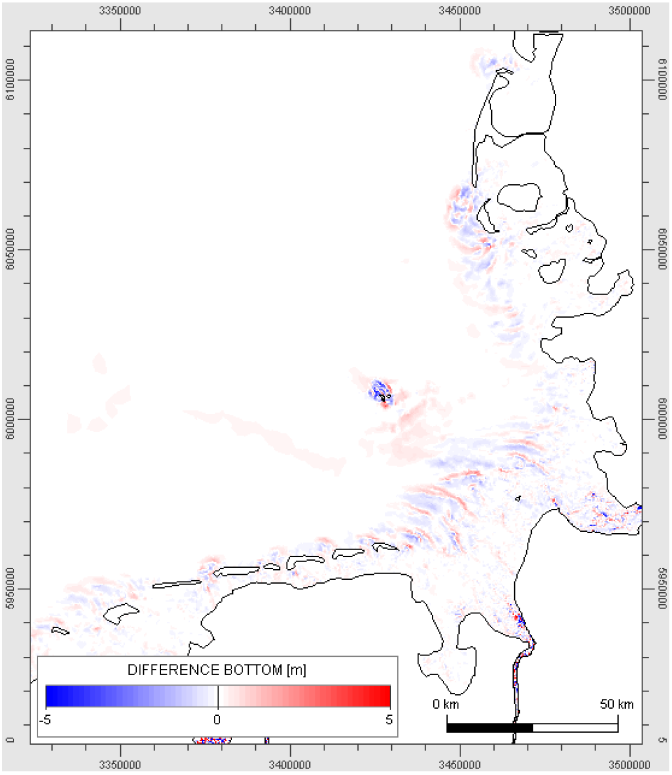

Figure 5. Long-term simulation results with tide, wind and wave forcing. Top: Bed level after 100 years. Bottom: Difference in bed level to the simulation with tide forcing only.

C. *Ongoing parameter studies*

Although the simulation results with different forcing for a period over 100 years show that reasonable bed evolutions can be computed, there are important parameters that require further investigation. First results for the influence of the active layer thickness on the tidal flat volume and the bed evolution computed with two different grid resolutions are described hereinafter.

1) *Development of tidal flat volume:* In general, sediment transport takes place within a specific sediment layer at the bed surface and the total amount of sediment is restricted by a non-erodible bottom. As a result, when solving the bed evolution equation numerically, these two parameters restrict the amount of sediment that is available for transport each time step. Therefore, and with respect to a wave-influenced model domain, parameter studies with different active layer models (constant, as a function of mean grain diameter, as a function of the grain diameter and the predicted wave-induced ripple height) are currently executed.

First results for a simulation period of 10 years with tide, wind and wave influence using the Bailard and the Bijker transport formulas show Fig. 6. Herein, the development of the tidal flat volume is illustrated for global constant values and as a function of the mean grain diameter at each node. The constant active layer thickness was set to 1.0 x 10^{-4} m, 1.0 x 10^{-3} m and 1.0 x 10^{-2} m. These values correspond to dimensions in a range of the mean grain diameter up to wave-induced ripple heights.

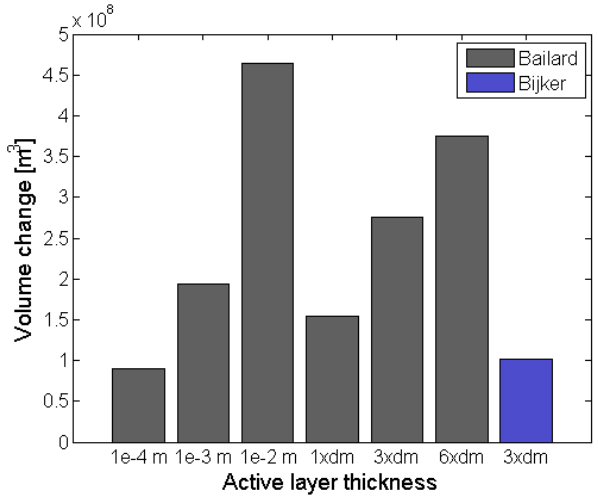

Figure 6. Development of tidal flat volume for different active layer thicknesses for the period 1998 to 2006 with tide, wind and wave forcing.

As expected, the tidal flat volume shows a strong dependence on the chosen thickness. When the active layer thickness increases, more sediment is deposited at the tidal flats. Nearly the same volume change can be obtained with a constant value as well as with an active layer thickness calculated from the local sediment distribution. For evaluating the model performance with respect to the global volume balance a constant value seems to be sufficient, but indeed the morphological development is different. On the other hand, an active layer thickness equal three times the mean grain diameter combined with the Bijker formula results in a smaller volume change compared to that calculated with the Bailard formula. Since the later formula predicts in general higher bed load sediment transport capacities in our simulation model, it is more sensitive to the active layer thickness, which can act as a limiting factor. Therefore, the quality of simulation results in comparison to measurements has to be estimated to identify the appropriate active layer model with respect to the transport formula for the German Bight model.

2) *Influence of grid resolution:* The results presented in the previous sections where obtained with a grid resolution that is – compared to small and medium scale morphological features – relatively coarse. Especially tidal channels and tidal creeks are in some cases represented just by a few grid points. The coarse grid seems to be sufficient to investigate the large scale, long term sediment transport and morphodynamics in the German Bight, but it is important to know how large the influence of grid resolution on the simulation results is. For that reason a refined mesh based on the coarse grid was constructed with a constant edge length of 100 m in the coastal zone and a total of 2 million elements.

The bed evolution for a 1 year simulation period (calendar year 2006) with the Bijker formula and tide forcing only is illustrated in Fig. 7. The coarse model (Fig. 7, top) shows well-defined deposition-erosions pattern (e.g. at “A”), while at the same time in some areas clear structures are hard to identify. The edge length varies in the depicted area between 450 m and 950 m. In contrast, the fine model (Fig. 7, bottom) calculates a bed evolution that makes it even on small scales easy to recognize a morphodynamic trend, for example were dunes are present. Concerning the large scale bed evolution pattern, with both grids more or less matching results are obtained, for example at positions “A” and “B”. Note that the value of the bed evolution at a certain location cannot be the same since the element size is very different.

These results indicate that the large scale morphodynamic behaviour can be represented quite well with a coarse grid. Below a certain scale level, only the fine model is able to produce plausible bed evolutions for small scale features. Subgrid models need to be implemented into the coarse grid model to simulate small scale morphodynamics and to take advantage of the smaller computational time.

V. CONCLUSIONS

This article introduces a numerical model for long-term morphodynamic simulations for the German Bight, with the aim to provide a tool for sustainable coastal management. First test cases with tide forcing and with tide, wind and wave influence show reasonable results and provide a first insight into the system behaviour of the German Bight. In the next stage further calibration and validation of the model as well as parameter studies, like for the active layer and the grid resolution as shown, are necessary to obtain more

reliable results. Furthermore, simulations with dredging and disposal activities over a period of 100 years should be carried out.

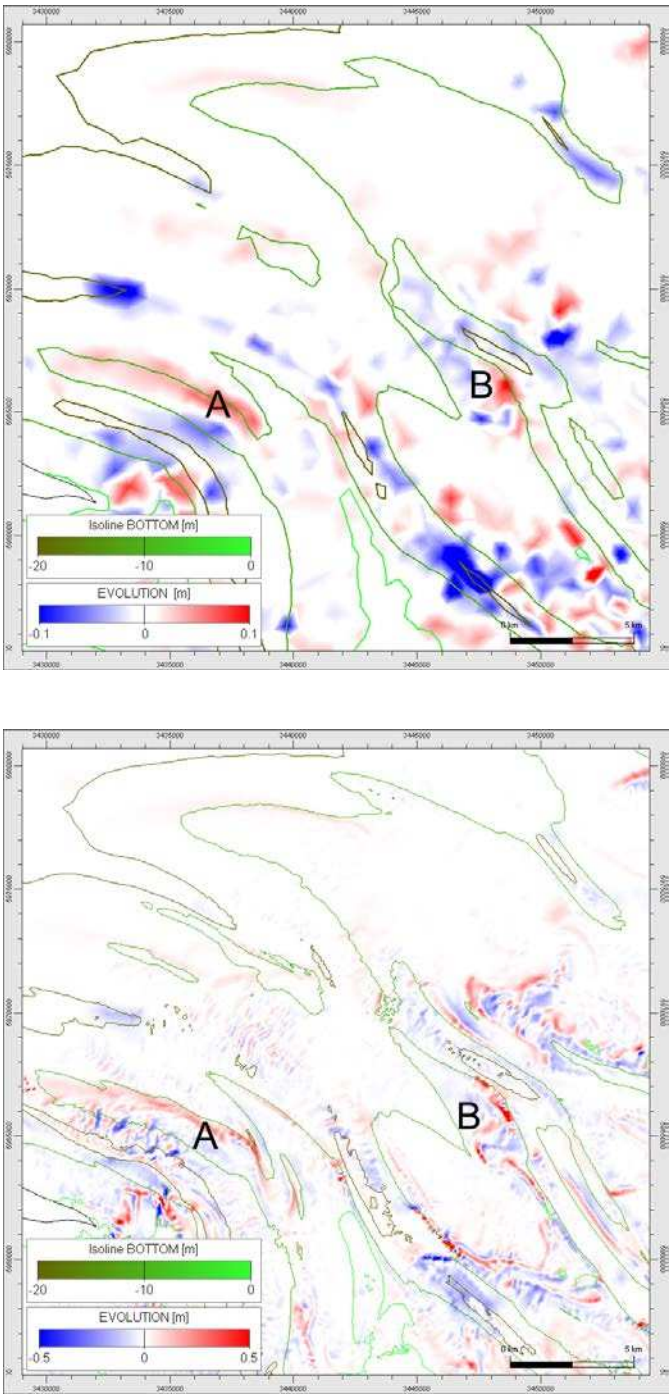

Figure 7. Bed evolution after 1 year (calendar year 2006) with tide forcing only. Top: Coarse model with 70.000 elements. Bottom: Fine mesh with about 2 million elements.

ACKNOWLEDGEMENTS

The presented work was conducted within the research project "AufMod" (Development of an integrated model system for analysing the long-term morphodynamics in the German Bight), which is a project of the Association for Research in Coastal Engineering (grant number 03KIS085), financially supported by the German Ministry of Education and Research. We would like to thank the Federal Waterways Engineering and Research Institute, Karlsruhe, Germany, for the support in running TELEMAC simulations on their high performance computer. We also would like to acknowledge Dr. Sandra Wappelhorst for double checking this article and improving the layout.

REFERENCES

[1] M. Zeiler, K. Schwarzer, and K. Ricklefs, "Seabed morphology and sediment dynamics," in Die Küste, vol. 74, 2008, pp. 31–44.

[2] J.M. Hervouet and P. Bates, P., "The TELEMAC Modelling System," Special Issue of Hydrological Processes, vol. 14, 2000.

[3] Electricité de France, "TELEMAC User Manual Version 6.0," Note technique, Electricité de France, Direction des Etudes et Recherches, Chatou Cedex, 2010.

[4] Electricité de France, "TOMAWAC User Manual Version 6.1," Note technique, Electricité de France, Direction des Etudes et Recherches, Chatou Cedex, 2011.

[5] Electricité de France, "SISYPHE User Manual Version 6.0," Note technique, Electricité de France, Direction des Etudes et Recherches, Chatou Cedex, 2010.

[6] F. Lyard, F. Lefevre, T. Letellier, F. Thierry, O. Francis, "Modelling the global ocean tides: modern insights from FES2004," in Ocean Dynamics, vol. 56(5-6), 2006, pp. 394–415.

[7] Wasser- und Schifffartsamt Cuxhaven, "Elbe", website, url: *http://www.wsa-cuxhaven.de/wasserstrassen/Elbe/index.html*, 2012.

[8] Niedersächsischer Landesbetrieb für Wasserwirtschaft, Küsten- und Naturschutz, "Deutsches Gewässerkundliches Jahrbuch – Weser- und Emsgebiet," Norden, 2006.

Simulation of hydrodynamic and sediment transport processes – Two Austrian case studies

Clemens Dorfmann, Gabriele Harb, Gerald Zenz
Institute of Hydraulic Engineering and Water Resources
Graz University of Technology
Graz, Austria
clemens.dorfmann@tugraz.at

***Abstract*—In this paper two Austrian case studies will be presented and discussed. The first case study deals with a geometrically complicated sand trap. After alteration works massive water surface and flow oscillations occurred. The oscillation was investigated with hydrodynamic simulations using TELEMAC-2D and measures proposed to prevent those oscillations. The second case study focus on sediment transport simulations of flushing processes in an alpine reservoir of a hydro power plant. Sediment transport processes are an important topic in Austrian rivers and reservoirs. On one side existing reservoirs built decades ago have severe sedimentation problems now. On the other side the construction of new hydro power projects is connected with stringent conditions imposed by the public authorities due to the water framework directive. TELEMAC-3D internally coupled with SISYPHE was used. The calibration of the morphological part of the model (SISYPHE) was very difficult because of the complex reservoir geometry.**

I. CASE STUDY: SAND TRAP

In this case study hydrodynamic simulations with TELEMAC-2D are performed to investigate the flow behaviour in a sand trap. After alteration works at the prototype massive water surface and flow oscillations occurred. Purpose of the 2D numerical simulations was the investigation of the original state, to reproduce the unsteady flow behavior of the modified sand trap and to propose measures to prevent those oscillations.

A. Overview

The sand trap is part of a high head hydro power plant which is located in the province Salzburg in Austria. After years of operational experience – very low sediment input observed during the last years –, the owner decided to decommission the sand trap by closing three of the 15 sand trap chambers - the first and the last two chambers. The outlet sills were removed which were located downstream of every chamber. Originally they had the function to decrease the flow velocities in the chambers for a better siltation efficiency of suspended load material. Figs. 1 and 2 show the original sand trap and the modified sand trap (status quo) respectively.

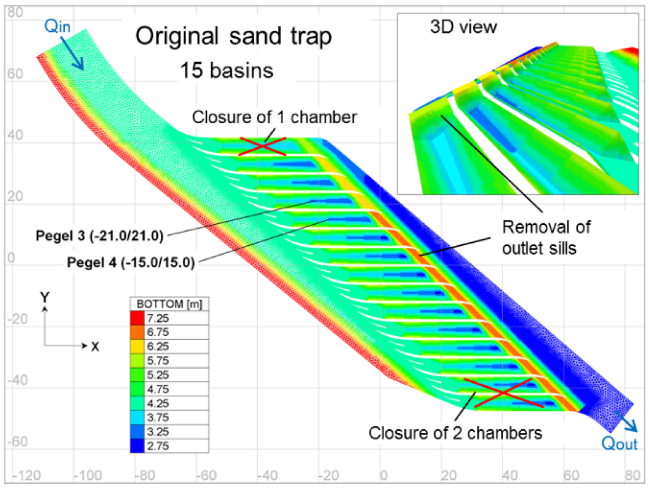

Figure 1. Plan view of the original sand trap.

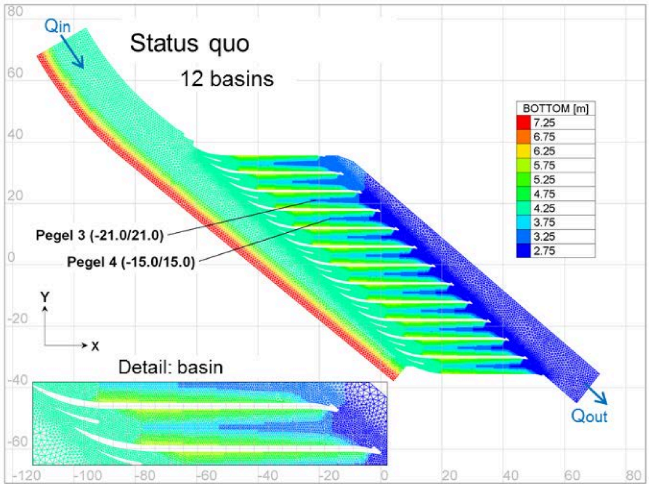

Figure 2. Plan view of the modified sand trap (Status quo).

After the structural alteration works in the modified sand trap (status quo) unsteady flow behaviour occurred even under hydraulic steady inlet and outlet conditions. Measurements of the water surface elevation showed the swinging up and down of the water surface with amplitudes of around 40 cm (Fig. 3).

Figure 3. Prototype with water surface swinging up and down.

B. *Geometry of the sand trap and mesh generation*

The original sand trap consists of 15 chambers, each with a length of around 30 m and a trapezoidal cross section with a crest width of 5.0 m and a bottom width of 0.5 m. The upstream zone of the sand trap has a width of 17 m, the outflow zone a width of 12 m. The average flow path length of the whole project area is 230 m, the elevation difference between inlet and outlet is 1.45 m. The original sand trap was designed with downstream sills at the outlets of the chambers. The differences between original and modified sand trap are the closing of 3 chambers and the removal of the downstream sills. The meshes are triangulated with the free software BlueKenue [1] using edge lengths from 25 to 80 cm, whereas the chambers and the zone around have a denser mesh with 25 cm edge lengths. The guide walls and boundary walls are modelled as vertical impermeable walls. The mesh of the original state consists of 106000 elements, whereas the mesh of the modified sand trap has 75000 elements.

C. *Numerical simulations of original state and status quo*

In the TELEMAC-2D simulations most of the default numerical parameters (keywords) were used. For the advection of the velocities generally the method of characteristics was used in combination with the wave equation. For the advection of depth (continuity equation) a conservative scheme was applied with the Streamline Upwind Petrov-Galerkin (SUPG) upwinding turned off. For the bottom friction a Strickler roughness value of 65 $m^{1/3}/s$ was chosen and the wall roughness was set to a Strickler value of 80 $m^{1/3}/s$. For turbulence closure the depth averaged k-e turbulence model was used. Details of the different methods and schemes employed in the TELEMAC System can be found in [2]. A time step of 0.05 seconds was used. The simulations were run until a theoretical steady state in the prototype. As hydraulic boundary conditions a constant inflow discharge of 80 m^3/s and a constant water depth of 4.7 m at the outlet were applied.

Fig. 4 shows the results of the original state in terms of flow velocity magnitudes. The flow pattern is at steady state and the chambers have nearly equal flow rates. No problem with reaching a steady state was encountered. This hydrodynamic result obviously indicates a good hypothetical siltation efficiency of the original sand trap.

The simulation results of the modified sand trap shown in Figs. 5 - 7 reveal completely other flow pattern conditions compared to the original state. The flow velocities show an oscillating behaviour in the chambers with swinging up and down of the water surface with amplitude of around 7 cm. Three to five chambers are charged sequentially with flow in the downstream direction whereas the flow in the three chambers downstream synchronously emerges in the opposite direction (Fig. 6). This process evolves repeatedly in time with no attenuation of the oscillations. The results are in qualitatively good agreement with the oscillations observed in the prototype; however the measured water surface amplitudes in the prototype cannot be reached.

An interesting remark is that the 2D numerical simulation of the original state with 15 chambers but without downstream sill at the outlets of the chambers yields also unsteady flow behaviour with water surface oscillations.

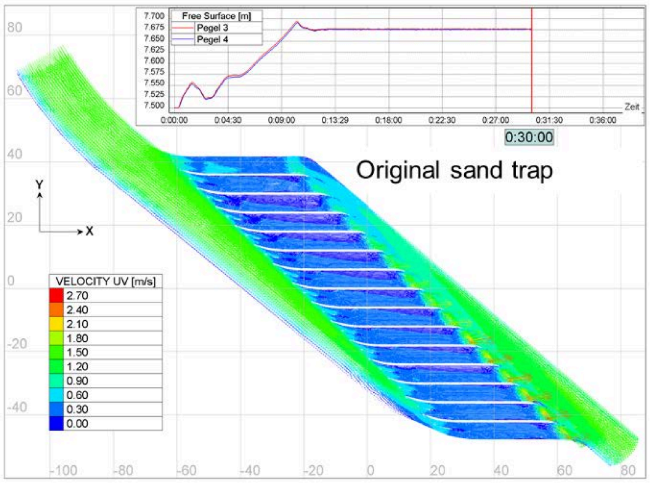

Figure 4. Original sand trap, plan view:
flow velocitiy magnitudes and water surface at steady state.

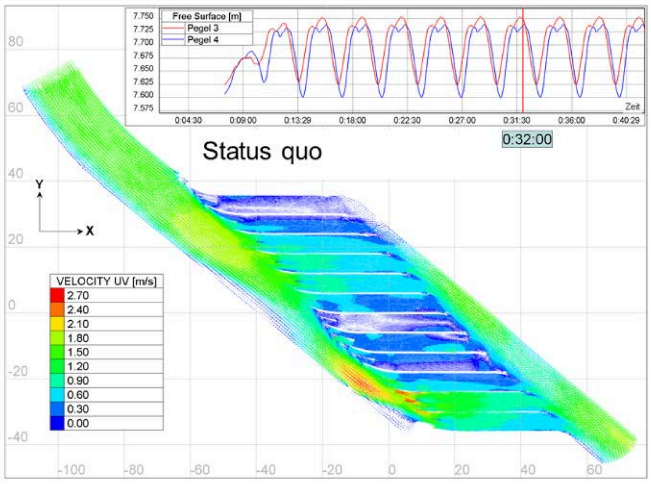

Figure 5. Modified sand trap, plan view:
oscillating flow velocitiy magnitudes and water surface.

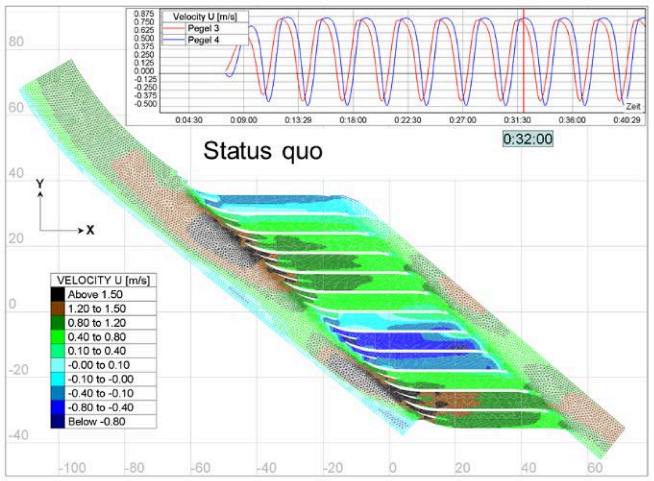

Figure 6. Modified sand trap, plan view: oscillating flow velocities in x-direction.

For the modified sand trap a numerical sensitivity analysis was performed, first to verify the preceding results and second to attempt to simulate higher water surface amplitudes to achieve a better agreement with the amplitudes observed in the prototype. The variation included the following numerical parameters:

- Time step
- Primitive equation (coupled)
- SUPG upwinding, classic and Courant number based
- Fine mesh with constant edge length 30 cm
- Constant eddy viscosity from 1.E-6 to 0.5 m²/s
- Roughness variation
- Finite Volume method: kinetic scheme of 1[st] order

The results of the numerical parameter variation are that the use of wave equation (default) or primitive equation (coupled), the chosen time step, the choice of SUPG upwinding, the use of a finer mesh or the variation of roughness gives no significant differences in the computed flow pattern and water surface amplitudes. Simulations using the constant eddy viscosity model with values from 1.E-6 to 1.E-3 m²/s show nearly the same flow pattern as the default result with the k-e turbulence model. By increasing the eddy viscosity to 0.1 and 0.5 m²/s the oscillations show a remarkable attenuation with a steady state flow field using the latter value. However an eddy viscosity value of 0.5 m²/s is not real physical in combination with the chosen cell sizes and expected flow velocities. The use of the Finite Volume Kinetic scheme of 1[st] order gives a steady state flow pattern in the entire model. With the kinetic scheme the maximum Courant numbers are around 0.1 which, maybe, indicates high numerical diffusion and thus the damping out of the oscillations. This assumption would correspond also to the findings of Cooper [3]. Fig. 7 shows the results of some parameter variations in terms of water surface elevation over time at Pegel 3.

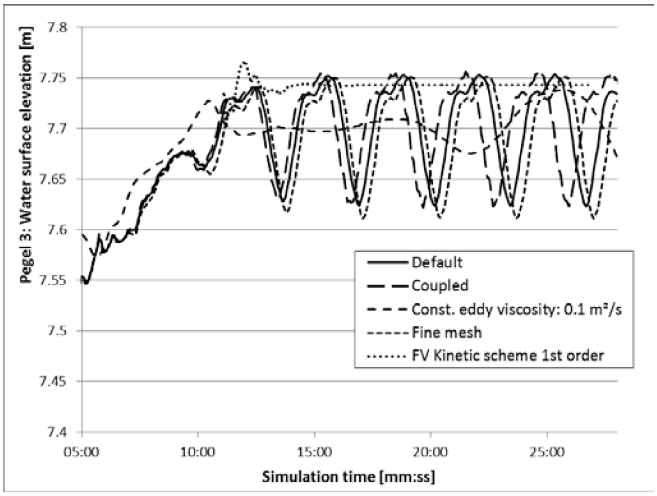

Figure 7. Parameter variation: calculated water surface elevation over time at Pegel 3.

D. *Investigations of variants*

The primary aim of the numerical investigation of variants was the elimination of the oscillation in the sand trap by implementing various constructional measures.

Fig. 8a shows such a proposed measure by installing submerged stop-logs at the inlets of the chambers. With this exemplary method a steady state flow pattern could be realized. Other simulated measures included e.g. the opening of some chambers by removing the guide walls in between and closing of various chambers (Fig. 8b). The resulting steady flow pattern is shown in Fig. 9 representing the (not much exciting) velocity distribution in the model.

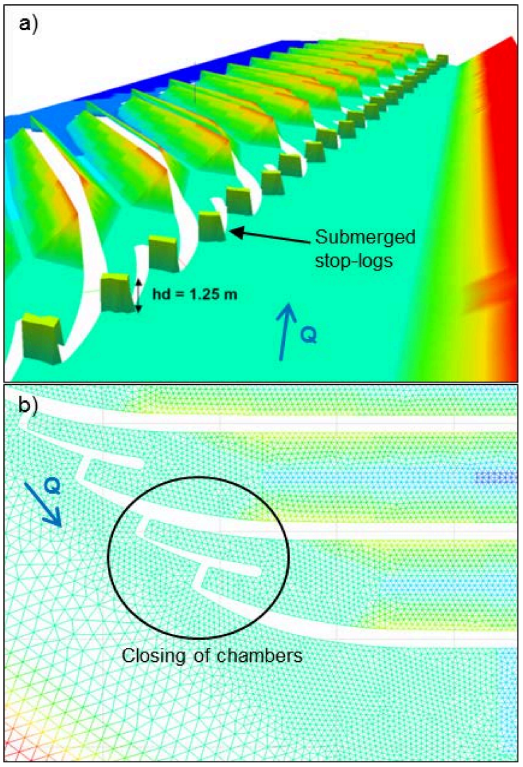

Figure 8. Two examples of investigated variants.

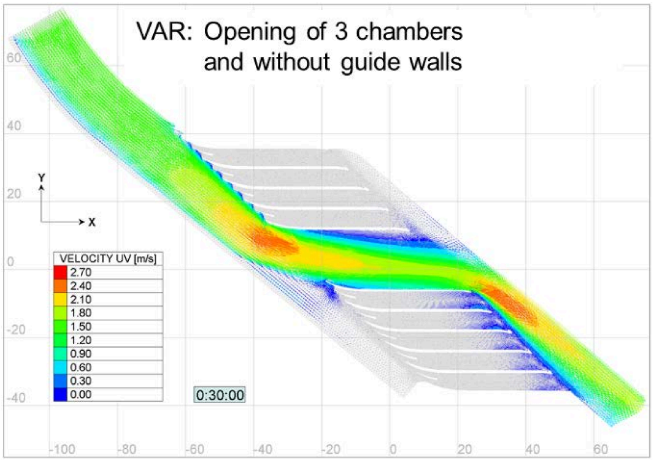

Figure 9. Calculated flow velocities magnitudes for a variant with opening of 3 chambers and removed guide walls.

E. *Discussion*

This contribution highlights hydrodynamic depth averaged simulations of a sand trap using TELEMAC-2D. The alteration works at the discussed sand trap led to considerable water surface oscillations and unsteady flow behaviour. Measurements of the water surface elevation in the prototype showed the swinging up and down of the water surface with amplitudes of around 40 cm.

Purpose of the 2D numerical studies is the reproducing of the unsteady flow oscillations and to propose measures against this undesired behaviour. The simulation results of the original state show the expected steady flow field. The simulation of the modified sand trap using most of the default parameters (keywords) demonstrates the ability of TELEMAC-2D to reproduce the unsteady flow behaviour in the chambers. However the measured water surface amplitudes in the prototype cannot be reached in the simulation. A large sensitivity analysis has been carried out to validate the results and to attempt to achieve numerically the water surface amplitudes observed in the prototype. The parameter analysis included the variation of time step, use of the primitive equation, SUPG upwinding, turbulence model, roughness, mesh size and the use of the 1st order Finite Volume kinetic scheme. The sensitivity analysis reveals the general reliability of the results obtained with the default parameters in TELEMAC-2D. So merely the variation of the constant eddy viscosity to higher, for the employed configuration unphysical, values causes the oscillations to be partially or fully attenuated. By use of the 1st order Finite Volume kinetic scheme not any flow oscillations arise and a steady flow field is calculated in the entire model, which possibly indicates considerable numerical diffusion of this in TELEMAC-2D implemented scheme. In addition to the sensitivity analysis it should be noted that the non-achievement of the observed water surface amplitudes with the TELEMAC-2D simulations can be also attributable to non-hydrostatic flow effects in the prototype and also to the hydraulic boundary conditions. The applied constant water depth at the outlet of the 2D model doesn't allow any water surface variations respectively dampens possible water surface oscillations in its vicinity which in the prototype certainly occur in this area.

For practical benefits the numerical investigations reveal that the removal of the downstream sills at the outlet of the chambers is responsible for the flow oscillations in the modified sand trap. However the question why these oscillations appear is still not answered. Numerical variation studies to prevent the unsteady flow behaviour in the chambers, e.g. the installation of submerged stop-logs or the closing of chambers, indicate some cost-efficient solutions.

II. CASE STUDY: RESERVOIR FLUSHING

In this case study a numerical analysis is carried out to investigate the sediment transport processes in a reservoir during flushing events in case of floods. TELEMAC-3D internally coupled with SISYPHE was used to perform the simulation of the flushing event.

A. *Background*

The project area is a reservoir at the river Mur in Styria, Austria (Fig. 10). The run-of-river hydropower plant forming the reservoir was built in 1994. The reservoir is approximately 4.5 km long with an initial storage volume of about 1.4 Mio. m^3. Annually around 85000 m^3 of sediments deposit in the reservoir. A small amount of the deposited sediments has been eroded and transported through the reservoir in former flushing events. However, echosoundings performed in 2007 showed that approximately 890000 m^3 of sediments are already deposited in the reservoir. This represents an annual sedimentation rate of about 6.1 % of the initial reservoir volume. Due to this fact, the present flushing strategy has to be adapted and optimized.

B. *Mesh and input data for the simulation*

Based on the existing bathymetry data, a three-dimensional digital elevation model was generated. The mesh with 46300 triangular cells and an average edge length of 4.5 m was mapped on the digital elevation model using the free software Blue Kenue [1]. Fig. 11 shows a 3D view of a part of the generated mesh with the conserved break lines of the river banks.

For the numerical simulation a time step of 1.0 seconds was chosen. The flushing process during a nearly 1-year flood in May 2009 was simulated and the calculated erosion pattern was compared with the measured erosion pattern. The stage hydrograph as downstream boundary condition and the inflow hydrograph for the upstream boundary for the flushing event 2009 are shown in Fig. 12.

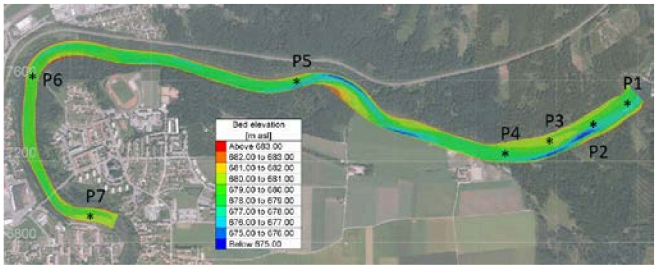

Figure 10. Overview of the reservoir with bathymetry data before the flushing event (March 2009) and indicated freeze core sampling points.

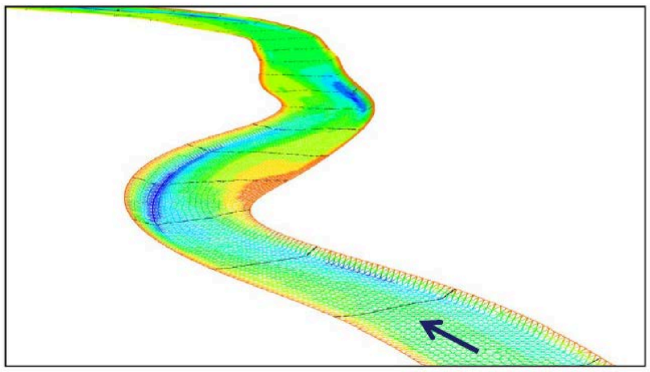

Figure 11. Sketch of the generated mesh with the conserved break lines of the river banks, 3D view superelevated.

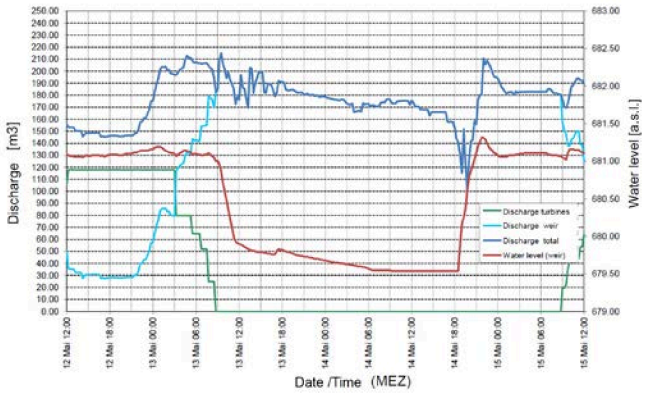

Figure 12. Inflow and stage hydrograph for the flushing event 2009.

C. *Sediment analysis*

In December 2008 seven representative sediment samples were taken from the reservoir and sieved according to the Austrian Standard ÖNORM B4412. The freeze-core method was used for taking the sediment samples, starting from the weir (sample 1) to the head of the reservoir (sample 7).

Table I presents some characteristics diameters of the sediments samples.

TABLE I. SEDIMENT CHARACTERISTICS

Sediment characteristics		
Sediment Sample	***d_{90}[mm]***	***d_{50}[mm]***
Sample 1	0.15	0.10
Sample 2	0.2	0.11
Sample 3	0.2	0.07
Sample 4	0.25	0.16
Sample 5	0.5	0.22
Sample 6	16.0	3.8
Sample 7	32.0	17.0

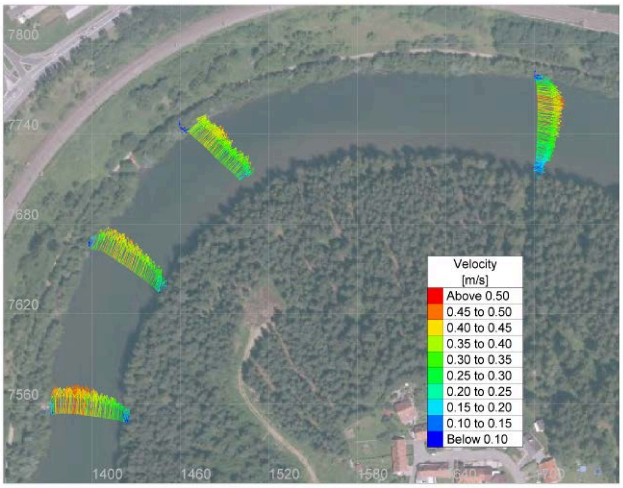

Figure 13. Measured depth averaged velocities in the reservoir.

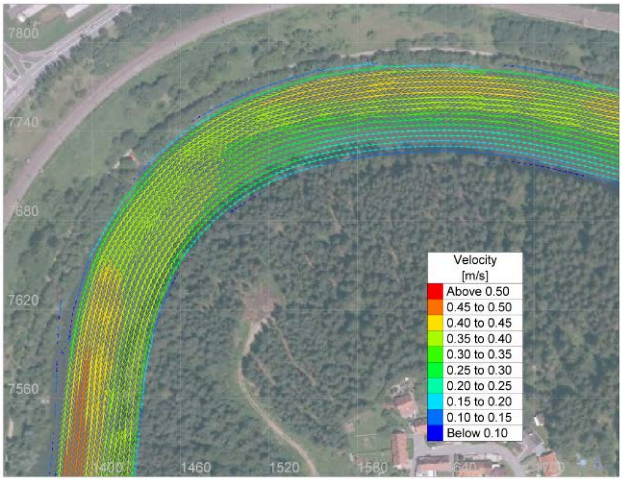

Figure 14. Calculated depth averaged velocities in the reservoir.

D. *Calibration of the numerical model*

The calibration of the hydrodynamic model was done using ACDP measurements performed at the prototype to calibrate the roughness at the river bed and at the banks.

E. Sediment transport - Results and Discussion

The measured bed changes (Fig. 15) of the flushing event 2009 were used for validation of the numerical model. These measurements are very interesting, because in this case most of the erosion took place at the inner site of the river bends and not on the outer side as expected. This may result from the complex meandering geometry of the reservoir (Fig.10). The massive depositions at the inner site of the river bend are eroded in case of higher discharges and sand slides and instabilities at the river banks lead to the erosion on the inner site and deposition on the outer site of the river bend. The complex geometry and the various sediment transport processes were difficult to handle in the numerical model.

Several parameters were tested and validated in a sensitivity analysis:

- different sediment transport formula (Meyer-Peter-Müller, Engelund-Hansen, Van Rijn)
- skin friction correction
- hiding / exposure factor
- slope effect formula and deviation formula
- number of layers (2 layer – 5 layer – 8 layer)
- non erodible bed subroutine.

The sensitivity analysis showed that the skin friction correction and the deviation formula affect the results significantly. Without the deviation formula the erosion pattern is inverted due to the secondary currents effect and the direction of the shear stress vectors. The calculated sediment transport rates with skin friction correction are in the areas with very fine sediments quite low (approximately 20% of the total shear stresses) and therefore the calculated bed changes were too low. Otherwise, without skin friction correction, the calculated sediment transport rates are much too high.

The sediment transport formula derived by Meyer-Peter-Müller underestimates and the formula by Engelund-Hansen overestimates the sediment transport rate in case of the flushing 2009. The formula of Van Rijn showed the best agreement. Fig. 5 illustrate the measured bed changes derived from echosoundings before the flushing event (March 2009) and after the flushing event (May 2009). The erosion pattern of the calculated bed changes (Fig. 16) compare well with the measured ones but the erosion depths in the middle of the reservoir are too high and at the weir too low. This may be a result of the very low effective shear stresses at the weir due to the skin friction correction. The different hiding and exposure formulas showed only marginal differences.

F. Conclusion

The calibration of the morphological part of the model (SISYPHE) was very difficult because of the complex reservoir geometry and maybe also some numerical limitations. The sediment transport processes which lead to the measured erosion pattern of the flushing event 2009 were mainly determined by the modification of the effective bed shear stresses due to slope effect and by the correction of the direction of the sediment transport due to steep transverse slopes in the cross sections.

In some simulations “furrows” occurred in direction of the main velocities and parallel to the mesh. In this case, with lots of break lines in the geometry, it was very difficult to handle these “mesh effects” of SISYPHE. We had also some problems with the layer subroutine. Because of the big variation of the grains sizes in the model area, some simulations with a small active layer thickness ($3d_m$) stopped after an error in layer.

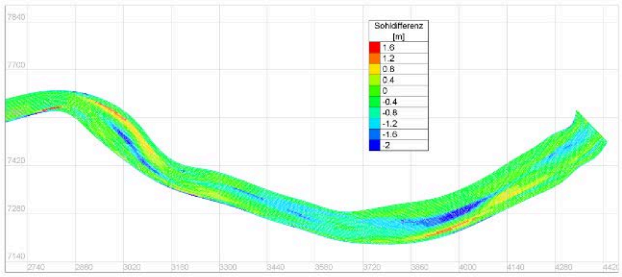

Figure 15. Measured bed changes after the flushing event, derived from echosoundings before (March 2009) and after (May 2009).

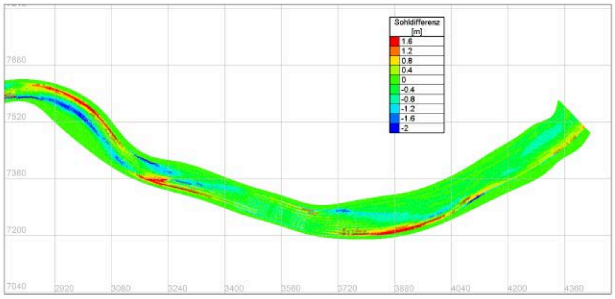

Figure 16. Calculated bed changes for the flushing event 2009 using the sediment transport formula derived by Van Rijn [3].

In summary, TELEMAC-3D internally coupled with SISYPHE was able to simulate the flushing process. The simulated flushing event reproduced the routing of sediments from the upstream free flowing area through the reservoir and of remobilization of the deposited sediments.

The numerical simulation of sediment transport processes and of flushing events is still a research topic and under development. Further studies and field measurements are required to enhance the knowledge of sediment transport processes.

REFERENCES

[1] CHC - Canadian Hydraulics Centre, National Research Council,. Blue Kenue, Reference Manual, August 2010.

[2] J-M. Hervoeut, “Hydrodynamics of free surface flows: modelling with the finite element method”, 2007, Wiley.

[3] A. Cooper, “Comparison of TELEMAC2D Finite Element and Kinetic Schemes”, Telemac User Club 2010, La Rochelle, France

[4] L. C. Van Rijn, “Sediment Transport. Part I: Bed load transport. Journal of Hydraulic Engineering”, 110(10), pp. 1431-1456, 1984.

Drivers of Sediment Transport Across the Entrance to the Gippsland Lakes, Australia

Julian G. O'Grady, Kathleen L. McInnes
CMAR, SLRC
CSIRO
Melbourne, Australia
Julian.O'Grady@csiro.au

Alexander Babanin
COEST
Swinburne University
Melbourne, Australia

***Abstract*—This paper describes the application of the TELEMAC suite of models to provide evidence of the movement of sediments in the nearshore region of the Gippsland Lakes. The longshore directional wave climate variability is investigated to show a decadal trend. Reasonable validation of the modelled wind and wave on the ocean side of the domain is achieved in this study, however improved hydrodynamic modelling requires improved bathymetry within the Gippsland Lakes system. Three simulations testing different components of the hydrodynamics highlight the sensitivity of the model setup to move sediments offshore during stormy conditions.**

I. Introduction

Lakes Entrance, a township located in south-eastern Australia (Fig. 1), is the largest fishing port in Victoria and is situated at the entrance to a man made channel connecting the Gippsland Lakes to Bass Strait. The channel was first opened in 1889 and requires ongoing dredging to maintain the passage of fishing vessels. The channel sits at the northern end of a 151km high energy beach "Ninety Mile Beach" where the region is subject to large fluctuations in the sediment budget.

Various studies have documented the severe weather patterns that drive storm surges over southeastern Australia (e.g. [1,2,3]). Of particular relevance to local authorities is how effective these storm events move sediment and how the system recovers between storm events.

The climate of significant wave height over the southern ocean has been found to be increasing (e.g. [4,5,6]) in conjunction with an increasing Southern Annular Mode, which is associated with sea level pressure reductions over the pole and a general poleward shift of the mid-latitude storm tracks. Furthermore, a significant proportion of the ensemble of GCM projections from the IPCC fourth assessment report suggest this trend will continue in the future [7] and that the subtropical ridge, which affects wind and weather regimes in the study region, will also undergo a southerly shift, (e.g. [8,9,10]). Such a change could lead to a regime shift in sediment movement along this coast. This talk will discuss a project aimed towards understanding changes in sediment transport budgets that may influence this region in the future.

Investigation into the sediment system at Lakes Entrance has mostly focused on the flood-tide delta inside the channel [11], where the accumulation of sediments inside the channel over the last century is reportedly due to a progressive reduction in catchment runoff flowing out through the channel to the sea. The focus of this paper is on the modeling of the longshore transport within the nearshore littoral zone on the seaward side of the channel under current climate conditions. A one month hindcast of the sediment transport along the coast is undertaken to understand how the atmospheric drivers and remotely generated swell influence sediment transport in the region. For this purpose, the open TELEMAC suite of tools is employed to model the coupled spectral waves, 2D hydrodynamics and morphodynamics.

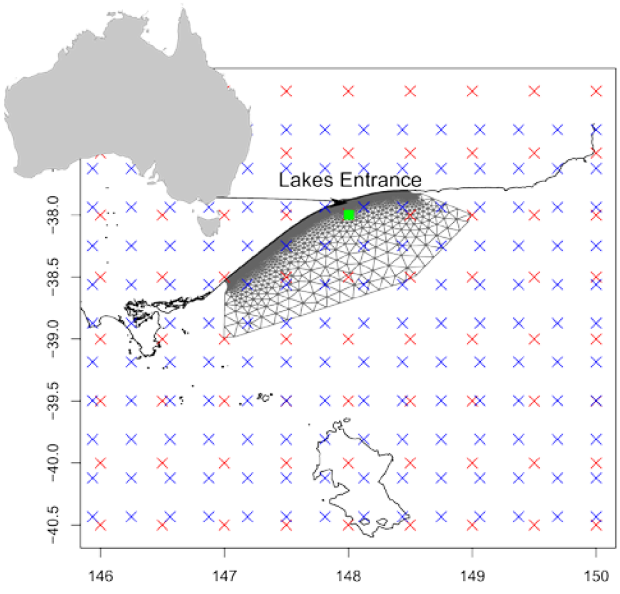

Figure 1. Map of the Gippsland coastal region relative to its location in Australia and gridded global hindcast points. Green 'q' are ½ degree CFSR MSLP and nWW3 data points and blue dots are 1/3 degree CFSR 10m wind vectors. Grey triangles are the computational grid domain of model simulations. Green square indicates location of NWW3 comparison point.

The particular month is selected on the basis that it contains both active storm events and there are field observations available to validate the model simulation. This will set the scene for the longer term goal of the study, which will be to understand how changes in wind regime may affect sediment transport along this coastline in the future.

II. DATA SOURCES

Observations of several variables are available at Lakes Entrance for the validation of the wave and hydrodynamic simulations in this study. A tide gauge monitoring station located at Bullock Island (see Fig. 5) provides measurements of sea level, water at atmospheric temperatures and atmospheric pressure. A seafloor mounted ADCP located with the entrance channel records current data and provides a second location for tide measurements with data availability from mid-2008 to present.

Integrated wave parameters of significant wave height (Hs), peak wave period (Tp) and peak wave direction Dp are available from a wave rider buoy which is located in about 22 m depth of water 2.6km off the coast at 37°54'48"S 147°58'55"E (WGS84) over the period from August 2007 to present.

The wind speed and direction observations are provided from a anemometer located at the end of the eastern pier at the entrance at 37°53'25"S 147°58'25"E (WGS84)

Gridded global hindcasts of winds (CFSR; [12]) and waves (NWW3; [13]) are used to force the model boundaries. A regional 5 km resolution hindcast of storm tide around Australia [14] is use to force the ocean boundary provided ocean velocities and water levels for the open boundaries.

Bathymetric data is sourced from a recent Light Detection And Ranging (LiDAR) survey of the coastline from a depth of 20 m to an elevation of 10 m [15]).

III. LONGSHORE WAVE CLIMATE OF GIPPSLAND

Frontal systems dominate the atmospheric weather patterns that cross the region, driving winds and waves from the west while midlatitude low pressure systems known as “east coast lows”, less frequently develop to the east in the Tasman Sea and produce severe easterly winds over the region [17]. Both systems occur most commonly during the winter half-year (April-September). Ocean currents generated by these systems generally transport sediments from west to east, however it is the waves that cause the significant effect on bed evolution.

With land to the north and west, the dominant direction of the waves approaching l Lakes Entrance (that entrain sediment into the water column) generally come from the east and southeast with some waves generated from the southwest. Long period swell that affects much of the southern coastline of Australia originates from storms in the southern ocean. In northeastern Bass Strait this swell is mostly blocked by Tasmania although some swell propagates from the southern ocean into the region from southeast.

As an indicator of the variability in the longshore wave component of the wave climate at Lakes Entrance, we consider just the zonal component of the wave direction (Fig. 2). The 30-year NWW3 wave hindcast, filtered to remove seasonal and short term variations, is used to explore the longshore wave component (Fig. 2a). There is evidence of inter-annual variability with, for example, greater frequency of westerly-component waves during the mid-2000s compared to the decade as a whole.

The monthly climatology of the mean monthly longshore wave component (Fig. 2b) shows in September the most westerly component for incoming waves occur, while in February the most easterly waves occur.

To demonstrate the weather signal of the longshore wave component, a time series of the wave component for September 2009 is plotted in Fig. 2c along with the Hs (top axis), in which several strong westerly events occurred, corresponding to the synoptic events in Fig. 3. We use part of this month as the basis of sediment transport modeling in the paper. During this month (Fig. 2c) waves tend to have an easterly component, which shifts to a more westerly component during strong south-westerly wind shifts (Fig. 3, [16]).

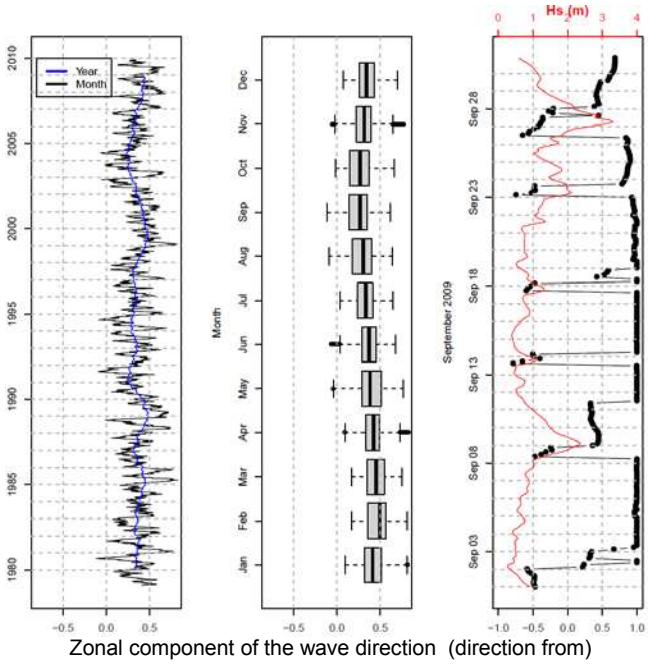

Figure 2. NWW3 wave reanalysis (a) 30 years of mean annual (blue line) and mean monthly (black) zonal wave components (b) Monthly W-E mean wave component climatology (c) Three hourly W-E wave component and significant wave height (red line corresponding to the top axis) for September 2009. Note that westerly (easterly) waves are indicated by negative (positive) values on the horizontal axis.

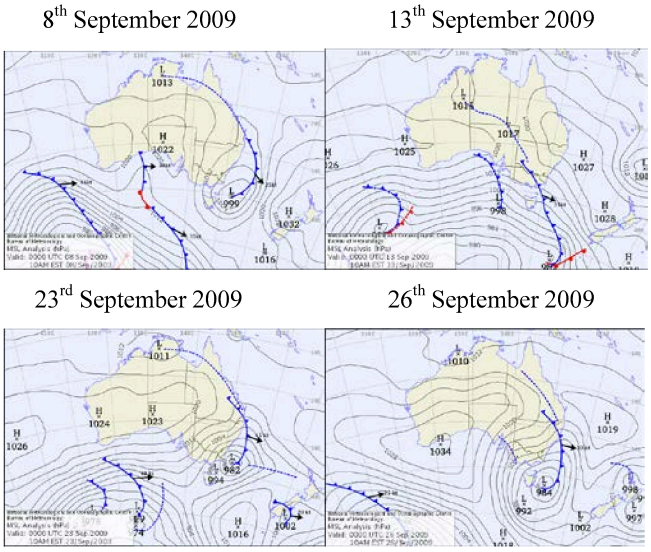

Figure 3. Synoptic maps for 4 key times in September 2009 [15].

IV. Model Setup

To investigate how well the model is able to simulate weather-driven variations in currents, waves, sea levels and sediment transport, a model simulation of a selected month (September, 2009) is undertaken. This month was selected because it feature active storm events and field observations were available to validate the model.

The global and regional gridded hindcast datasets described in section II were used to force the coupled simulations, with the different model components laid out in a flowchart (Fig. 4). All three modelling components are run on the same computational grid (see Figs. 1 and 5) with 10 km grid spacing at the open ocean boundary, contracting to 250 m resolution at the 12 m depth contour and then 30 m in the vicinity of the channel.

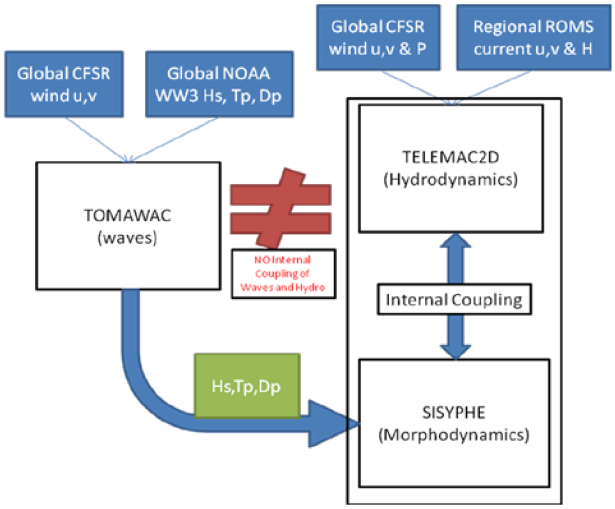

Figure 4. Modelling flowchart of model coupling and data inputs.

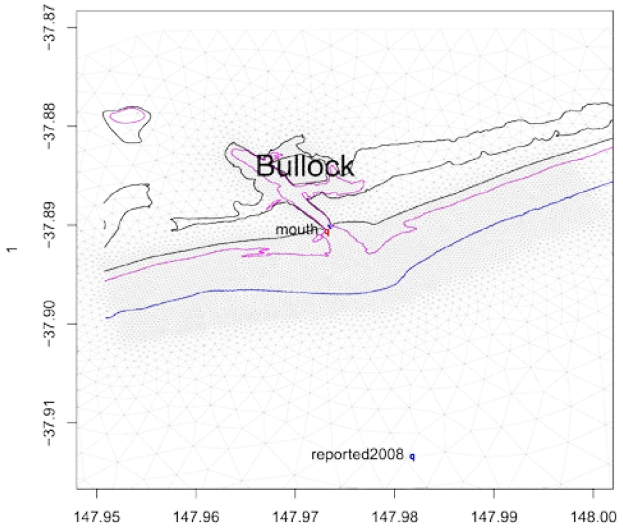

Figure 5. Computation grid in the nearshore zone. Grid points are separated by 320m at the directional wave rider buoy, 250m at the 12m depth contour and 30m within the area of interest, grid expand to 10km for outer ocean boundary. Blue line is the 12m depth contour, magenta line is 3m depth contour and the black line is the coastline.

A. *Waves*

The 2D spectral wave model TOMAWAC was forced at the open sea boundary by a bilinear interpolated NWW3 three-hourly ½-degree gridded (see Fig. 1) global wave hindcast. The integrated parameters of Hs, Tp and Dp from NWW3 were fed into a JONSWAP spectrum divided into 18 directions and 26 frequency bins. The model was run at 1 hour time steps for 30 days on the unstructured triangle grid shown in Fig. 1. The modelled integrated parameters of Hs, Tp and Dp were stored for later use by the morphodynamic model SISYPHE. Note: in these simulations the waves do not take into account the tide interactions.

B. *Hydrodynamics*

The hydrodynamics (currents and sea levels) were generated by TELEMAC-2D. Boundary conditions of water levels and currents where sourced from a five-kilometre-resolution regional hindcast of storm tides around Australia [13]. A tide-only validation run was performed as well as an internally coupled simulation with the morphodynamic module/model, SISYPHE. TELEMAC-2D was set with a timestep of 30 seconds and output every 15 minutes for the 30 days. Strickler's law for friction was used with the friction coefficient set at 50. The equations for the Saint-Venant Finite Element solution with the default turbulence model were used, where turbulent viscosity is constant throughout the domain.

C. *Morphodynamics*

The mophodynamics were modelled with SISYPHE run internally coupled to TELEMAC-2D. Bijker's formula for the sediment load transport to include the effect of waves was employed. A control run was investigated, with suspended

transport switched off, in order to examine the bed load transport. A tide-only simulation was also performed to isolate the role of the waves on the sediment transport. SISYPHE is run with the same time step as TELEMAC-2D and the waves are input hourly and interpolated linearly to the 30 s timesteps of SISYPHE.

V. VALIDATION

TOMAWAC modelled waves are compared with observations in Figs. 6a and 6b. A comparison of the CFSR wind and pressure forcing, used to force the TOMAWAC and TELEMAC-2D models, with observations is given in Fig. 6c.

The global hindcast NWW3 matches well with the observed Hs and Dp (Fig. 6a), the simulation with TOMAWAC (forced by NWW3) improves in capturing the peak values and wave directions but seems to underestimate lower wave conditions. The TOMAWAC modelled Tp (Fig. 6b) matches the observed quite well. The wind speeds from the CFSR reanalysis (Fig. 6c) slightly underestimate the observations, however the MSLP is well captured.

A comparison of the water levels and currents, simulated by the TELEMAC-2D model, with measured sea levels and currents at the mouth of the entrance is shown in Fig. 7.

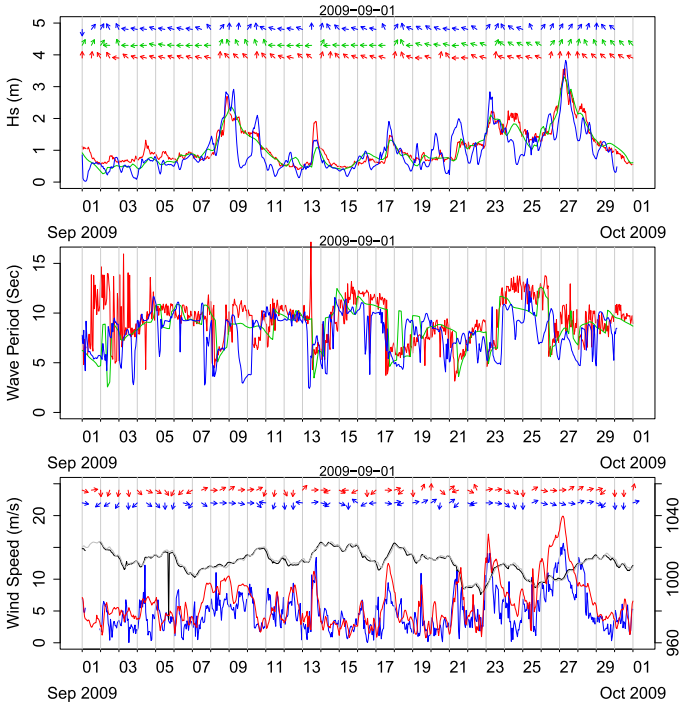

Figure 6. (a) Hs (curves) and Dp (vectors) and (b) Tp for observed (red), NWW3 (green) and TOMAWAC (blue). (c) Wind speed (curves) and directions (vectors) for CFSR (blue), observed (red), and MSLP (hPa), CSFR (black), observed (grey).

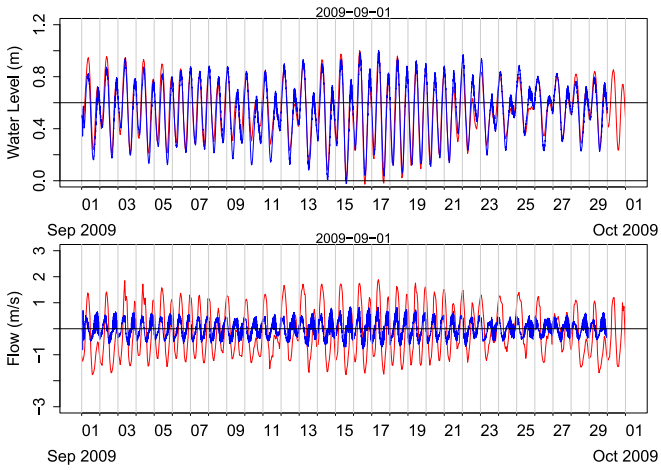

Figure 7. Water level and currents validation plot. (a) Total water level (AHD) observed (red), TELEMAC-2D scaled down by 1/3 (blue). (b) Water flow in the direction into the channel (same colours as (a)).

TELEMAC-2D modelled water levels in the channel were found to overestimate the observed values by a factor of 4/3, in Fig. 7a. Note the modelled values shown in Fig. 7a have been scaled down by 1/3 to facilitate the comparison of the phase of the modelled tides, which are in good agreement with the measured tides. The poor agreement in the tidal amplitudes and currents (Fig. 7b) is likely to relate to the fact that the Gippsland Lakes were not entirely resolved in the coastal LIDAR survey used to define the bathymetry in the model. Efforts are underway to source additional information on the bathymetry within the Lakes to improve the hydrodynamic simulations.

VI. RESULTS

Results so far focus on 3 SISYPHE simulations that were undertaken to compute the bed-evolution after 9 days (1) with bed-load transport but without waves or suspended transport (Fig. 8), (2) with bed-load transport and waves but no suspended transport (Fig. 9) and (3) with bed-load transport, waves and suspended transport (Fig. 10). The bed evolution, mapped in Figs. 8-10, is at 00 UTM on the 10[th] of September.

Very little bed evolution is evident for the simulations without the influence of waves or suspended sediment transport (Fig. 8). When waves are included (Fig. 9), the storm that occurs on the 8th September leads to the movement of sediments offshore in relatively uniform longshore sand bar and trough pattern. With the inclusion of suspended sediment transport (Fig. 10), the bed evolution is balance and less sediment is transported sea ward.

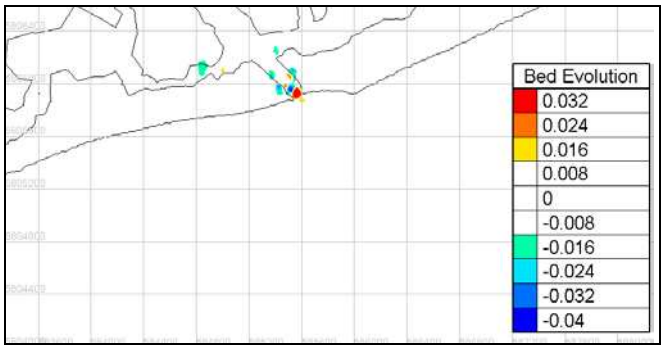

Figure 8. Bed evolution (m) from the tide forced run without waves or suspended sediment transport. 00z Hr (UTM) on the 10th of September 2009.

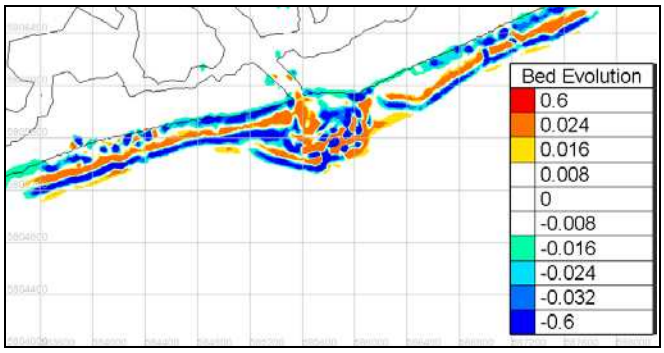

Figure 9. Bed evolution (m) from the tide and wave forced run without suspended sediment transport. 00z Hr (UTM) on the 10th of September 2009.

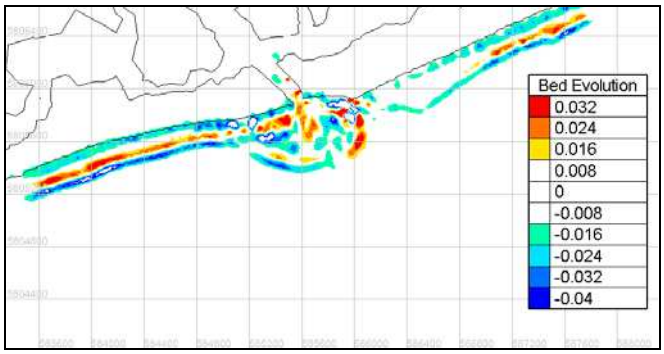

Figure 10. Bed evolution (m) difference between a wave forced run with suspended sediments less a wave run without suspended sediments. 00z hr (UTM) on the 10th of September 2009.

VII. Discussion

Preliminary calibration of the suite of models has been demonstrated for its application in the region. Future work will include better refining of the bathymetry in the Gippsland Lakes system and further testing of the sensitivity of the model setup with different equations, parameters and inputs to provide improved validation of the modeled waves and hydrodynamics. The range of uncertainty of the results will be addressed by modeling the morphodynamics under multiple scenarios to test the possible ranges of outcomes. It is intended that this model will then be used to investigate the coastal sediment response to climate forcing under current and future climate conditions.

Acknowledgement

The authors are thankful to Mark Spykers from Gippsland Ports for the supply of the observational datasets and Dr Frank Colberg for the provision of modelled currents and tides used as boundary forcing.

References

[1] McInnes, K.L. and Hubbert, G.D. 2003: A numerical modeling study of storm surges in Bass Strait. Aust. Met. Mag. 52. 143-156.

[2] McInnes, K.L., Macadam, I., Hubbert, G.D. and O'Grady, J.G. 2009: A Modelling Approach for Estimating the Frequency of Sea Level Extremes and the Impact of Climate Change in Southeast Australia. Natural Hazards 51 115–137.

[3] McInnes, K. L., D. J. Abbs, & J. A. Bathols 2005: Climate Change in Eastern Victoria. Stage 1 Report: The effect of climate change on coastal wind and weather patterns. Report to Gippsland Coastal Board. 26pp.

[4] Young, I.R., S. Zieger, and A.V. Babanin, 2011: Global trends in wind speed and wave height. Science, 32(6028), 451-455.

[5] Bosserell, C., Pattiaratchi, C. and Haigh, I. 2011: Inter-annual variability and longer-term changes in the wave climate of Western Australia between 1970 and 2009. Ocean Dynamics DOI 10.1007/s10236-011-0487-3

[6] Hemer, M.A., J.A. Church, and J.R. Hunter, 2010: Variability and trends in the directional wave climate of the Southern Hemisphere. International Journal of Climatology, 30(4), 475-491.

[7] Meehl, G.A., T.F. Stocker, W.D. Collins, P. Friedlingstein, A.T. Gaye, J.M. Gregory, A. Kitoh, R. Knutti, J.M. Murphy, A. Noda, S.C.B. Raper, I.G. Watterson, A.J. Weaver, and Z.C. Zhao, 2007b: Global climate projections. In: Climate Change 2007: The Physical Science Basis. Contribution of Working Group I to the Fourth Assessment Report of the Intergovernmental Panel on Climate Change [Solomon, S., D. Qin, M. Manning, Z. Chen, M. Marquis, K.B. Averyt, M. Tignor and H.L. Miller (eds.)]. Cambridge University Press, Cambridge, UK, and New York, NY, pp. 747-845.

[8] McInnes, K.L., Erwin, T.A. and Bathols, J.M. 2011: Global Climate Model projected changes in 10 m wind due to anthropogenic climate change. Atmos. Sci. Letters, 12: 325–333. DOI: 10.1002/asl.341.

[9] Hemer, M.A, McInnes, K.L. and Ranasinghe, R. 2011: Investigation of uncertainty in regional east Australian wave climate projections. Int. J. Clim. DOI: 10.1002/joc.3537

[10] Perkins, S. E., D. B. Irving, J. R. Brown, S. B. Power, A. F. Moise, R. A. Colman, and I. Smith (2012), CMIP3 ensemble climate projections over the western tropical Pacific based on model skill, Clim. Res., 51, 35–58, doi:10.3354/cr01046.

[11] Wheeler P. J, Peterson J. A., Gordon-Brown L. N. (2010) Flood-tide Delta Morphological Change at the Gippsland Lakes Artificial Entrance, Australia (1889–2009), Australian Geographer Vol. 41, Iss. 2

[12] Saha, Suranjana, et. al., 2010: The NCEP Climate Forecast System Reanalysis. Bull. Amer. Meteor. Soc., In Press (DOI: 10.1175/2010BAMS3001.1).

[13] Chawlaa, A., Spindlerb D. M. and Tolmana H. L. (2012), Validation of a thirty year wave hindcast using the Climate Forecast System Reanalysis winds, Ocean Modelling, in press.

[14] Colberg, F., and K. L. McInnes (2012), The impact of future changes in weather patterns on extreme sea levels over southern Australia, J. Geophys. Res., 117, C08001, doi:10.1029/2012JC00791

[15] http://www.climatechange.vic.gov.au/adapting-to-climate-change/future-coasts

[16] http://www.bom.gov.au/climate/mwr/vic/mwr-vic-200909.pdf

[17] O'Grady, J.G. and McInnes, K.L. 2010: Extreme wind waves and their relationship to storm surges in northeastern Bass Strait. Australian Meteorology and Oceanography Journal, 60: 265-275.

Adaptation of TELEMAC-2D to the regulation of a CNR development during floods

Sophie TROSSAT, Jean-Paul BARD
Enginering department
Compagnie Nationale du Rhône
Lyon, France
s.trossat@cnr.tm.fr

Pierre LANG
Expertise et structure
INGEROP
Grenoble, France
pierre.lang@ingerop.com

Abstract — **On the Rhône River, Donzère-Mondragon is the second oldest CNR development and the most productive one with a total installed capacity of almost 2100 MW. It follows the typical CNR development scheme. It is composed of a reservoir, a barrage, a diversion channel leading to a hydropower plant and a lock. When there is no flood, water is diverted to the hydropower plant. During floods, water passes mainly through the barrage. Donzère-Mondragon specificity is its 17.3 km long headrace channel. Three specific structures were built at the diversion channel entrance to prevent water level from rising in the channel during floods and to allow navigation when there is no flood. Operating rules are established to manage water levels and hydropower plant discharges from lowest discharge to the design flood.**

A 2D-model of the whole development is built using TELEMAC system. The model is 68 km long and integrates 115 km² of flooding area. A 141 500 elements mesh has been generated and calibrated. Specific programs are implemented in TELEMAC-2D so as to represent Donzère-Mondragon development behaviour in flood period. For the hydropower plant, the regulation managing upstream water level and outflow is simulated. A specific program based on energy equation is applied for the CNR structures. The subroutine allows manual water level management. The barrage management also requires a specific implementation depending on upstream discharge. Those specific programs are gathered to perform computation during high floods in steady and unsteady mode.

Opening structures calibration is detailed. Results focus on hydropower plant and barrage discharges to check flow conservation. Reservoir and channel water levels are analysed to ensure operating rules are respected for various discharges in steady mode. In unsteady mode, program limits connected water level operating managements are identified. Computation stability problems are encountered. Part of them is fixed by adapting mesh density. Solutions found in the studies to get round of the other difficulties are mentioned. Improvements are needed to avoid instabilities due to flow calculations at a specific section.

I. INTRODUCTION

Modelling of widespread floodplains and complex structures with regulation have been carried out for a long time with mono-dimensional software. The progresses in computing performances, the densification of topographic and bathymetric data, and the capitalisation of experiences in TELEMAC-2D have made possible the bi-modelling of a complex development. The article presents the modelling of Donzère-Mondragon development.

Donzère-Mondragon is one of the eighteen developments managed by the Compagnie Nationale du Rhône (CNR). CNR holds the concession of Rhône valley from Swiss border to Mediterranean Sea. Its three main missions are electric production, navigation and irrigation. CNR engineering team develops mathematical modelling to answer operating needs, to check the concessionary obligations and for engineering as well. Modelling was mainly mono-dimensional and now very often bi-dimensional.

The bi-dimensional modelling of Donzère-Mondragon development answers the issues of dike overflows and flow propagation in Pierrelatte plain. As a first approach, the simulations are focused on flood. This article describes the methodology carried out to integrate CNR development regulation using TELEMAC-2D.

The approach is divided in four steps. Firstly, the Donzère-Mondragon development features are explained. Secondly, the TELEMAC modelling is detailed. Thirdly, the article describes programs implemented within TELEMAC-2D to integrate regulation. Finally, modelling results are analysed, limits of developed programs are listed and improvements are proposed.

II. DONZÈRE-MONDRAGON DEVELOPMENT

A. A typical CNR development

Donzère- Mondragon (DM) development is located in the Rhône River valley (south east of France), north of the city of Orange and south of Montelimar. It was built in 1953. The development includes Pierrelatte floodplain. Caderousse (CA) is situated downstream Donzère-Mondragon development.

Donzère-Mondragon follows the typical CNR development scheme (Fig. 1). Indeed, it is composed of:

- A hydropower plant (Usine de Bollène: USB) with a total installed capacity of around 2 100 MW. It comprises six Kaplan units with a maximum power station discharge of 1 980 m3/s. The power station units do not include sluicing operation capabilities. Thus, two surface gates and six gates were designed. Their aim is to prevent surge waves in case of full load rejection. Moreover, during big floods, around half of the diverted discharge passes through the gates.
- A barrage (BarraGe de ReTenue de Donzère: BGRT). It is composed of six gates. When upstream discharge is higher than the turbines maximal discharge, gates start opening. During big floods, the gates cannot regulate water level as they are totally opened.
- A lock for navigation purposes.
- A reservoir (retenue RE). It is 4 km long and its normal water level is 58.5 m NGF.
- A headrace channel (Canal d'amenée: CdA). It is 17.3 km long and the longest of CNR ones.
- A tailrace channel (Canal de Fuite: CF) which is 11 km long.
- The natural river course (Vieux Rhône :VR). A minimal discharge is always maintained during dry season. During floods most of the flow goes through this natural river. The famous cevenol tributary Ardèche converges into this part of the natural river course.

Figure 1. Typical low-head development scheme.

B. *Donzère-Mondragon deveplopment features*

Donzère-Mondragon uniqueness is its headrace channel which is very long. In case of flood, water levels upstream the barrage rise and this rising can be propagated in the headrace channel. Specific structures were built at the headrace entrance to minimise this effect, to reduce dykes height and to prevent solid transportation from entering the headrace channel. They are called "protecting gates".

On the right bank, the old navigable gates (Ancienne Passe Navigable: APN) were originally built for paddle boat passage. The two 45 m long gates are closed during flood. No vulnerability has been identified for flood bigger than the design one concerning this structure.

The changing characteristics of convoys and the transit difficulty through the APN required building a new gate. This new navigable gate (Nouvelle Passe Navigable: NPN) was commissioned in 1986. In case of flood; this gate is closed. In extreme conditions (discharge higher than the design flood) the NPN may break depending on upstream hydraulic head.

On the left bank, the hydropower barrage (BarraGe Usinier: BGU) was designed to limit headrace water level for high discharges.

C. *Operating rules*

So as to combine hydroelectricity optimisation, navigation and overflow prevention in headrace channel, operating rules were set. Operating rules manage the water level at a specific location (Regulating Point – Point de Réglage: PR) in the reservoir or in the headrace channel depending on the input discharge. They also assign power plant discharge vs. the total input discharge. These rules have to be observed from the lowest discharge to the design flood.

Three regulating points (Fig. 2) are used to manage the water levels of the Donzère-Mondragon development: PR1 at SNCF bridge for low discharges, PR2 upstream the barrage for middle discharges and PR3 downstream the "keeping structures" at KM 171.5 for high discharges.

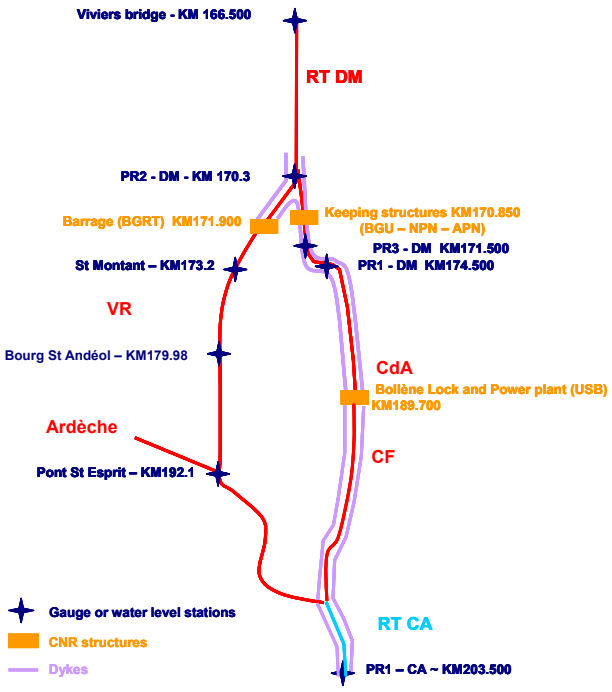

Figure 2. Location of Donzère-Mondragon structures, dykes and stations.

As the study focuses on high discharges, only rules at PR3 are considered. The water level is managed by the BGU with a 50 cm allowed variation.

III. TELEMAC MODELLING

A. Computational domain

The whole stretch of the modelling is 68 km long, integrating downstream part of the Ardèche tributary and 2 km of the Caderousse downstream reservoir. Piers of the sixteen bridges situated in the modelling footprint are represented as islands within the mesh. This modelling is considered acceptable given the study purposes. Indeed, results are not focused on local phenomenon at the immediate vicinity of bridge piers. Hard lines have been built to represent CNR and other dykes. The mesh segment size varies from 40 m close to the CNR structures, as instabilities are liable to occur, to 100 m in the low-water bed of the natural watercourse. The grid (Fig. 3) comprises more than 71,500 nodes and 141,500 elements. This mesh has been generated with Matisse. The time step is 2s.

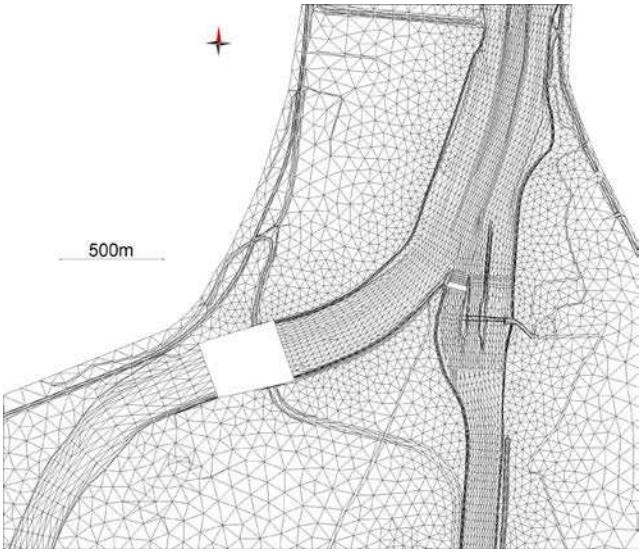

Figure 3. Bi-dimensional grid of the headrace entrance and BGRT.

B. Calibration

The modelling of turbulence is constant viscosity with an overall viscosity coefficient equal to 0.1.

Then, the calibration is focused on bottom friction coefficient, which is computed following Strickler's law [1]. A high variation in initial water levels is observed between upstream and downstream boundary conditions (more than 20 m high).This variation makes complex the model initialisation. To avoid this problem and since there is a hydraulic disconnection at BGRT and USB, it has been possible to subdivide the grid in two sub-grids. The upstream sub-model spreads from Viviers bridge to Donzère-Mondragon barrage and hydropower plant. The downstream sub-model starts from BGRT and USB to KM 203.500. The low-water bed is calibrated in steady state (Fig. 4) and the calibration of the high-water bed friction coefficient is carried out in unsteady state (Fig. 5). The low-water bed is calibrated with stationary boundary conditions for a large range of input discharges. The comparison of water level computed (lines in Fig. 4) and profiles water level measurements (points in Fig. 4) highlights an average difference lower than 10 cm. Simulations of 2002 [2] and 2003 [3] floods enable to check the calibration of low-water bed bottom frictions and to adjust high-water bed bottom frictions. The comparison of water levels calculated (lines in Fig. 5) and recorded (points in Fig. 5) exhibits a maximum difference of 15 cm at flood peak. In the floodplain, the comparison between water levels and flood marks shows an average difference of 25 cm. Consequently, the sub-models accurately represent observed water levels.

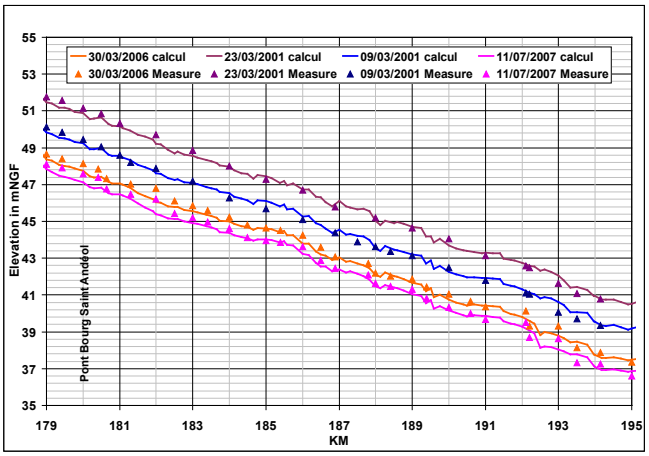

Figure 4. Calibration of low-water bed bottom friction – Downstream sub-model.

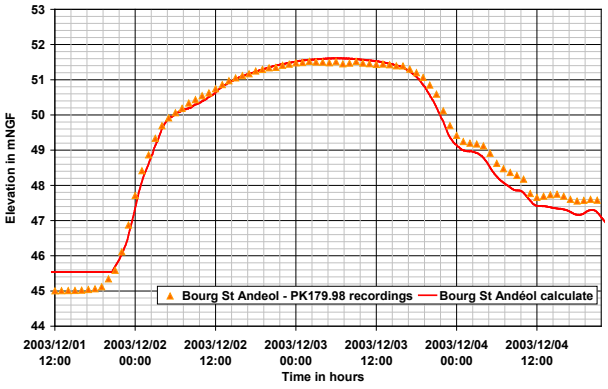

Figure 5. Checking of bottom friction low-water bed calibration for the 2003 flood at Bourg Saint Andéol hydrometric station – Downstream sub-model.

IV. SUBROUTINE

A. Equations

A Specific subroutine is carried out on TELEMAC-2D version V5P9 to calculate flow rate passing through, or water level upstream, CNR structures. The subroutine comprises three main options: weir, gate and regulation. The first two

options solve equations based on energy conservation. To expose then, two variables are defined: the vertical coordinate:

$$y = z - z_c \quad (1)$$

where z is an average of water level in the section defined by the user and z_c the weir crest elevation, and the specific energy E [4]:

$$E = y + \frac{V^2}{2g} \quad (2)$$

where g is the acceleration of gravity and V is an average of scalar velocities in a section defined by the user.

The weir equations are obtained applying Bernoulli equation between upstream and downstream weir crest and considering a rectangular weir. The unsubmerged weir equation is:

$$Q = C.L.\sqrt{2g}.\sqrt{1/3}.\frac{2}{3}.\left(E_{upstream}.\right)^{\frac{3}{2}} \quad (3)$$

and the submerged weir equation is:

$$Q = C.L.y_{downstream}\sqrt{2g}.\sqrt{E_{upstream} - y_{downstream}} \quad (4)$$

where L is the weir crest width and C corresponds to the weir conveyance coefficient.

In addition, gate conveyance equations are implemented applying Bernoulli formula and considering a rectangular gate opening. The unsubmerged gate equation is:

$$Q = C_{ctr} \cdot C \cdot L \cdot \sqrt{2g} \cdot O \cdot \sqrt{E_{upstream} - O} \quad (5)$$

and the submerged one is:

$$Q = C_{ctr} \cdot C \cdot L \cdot \sqrt{2g} \cdot O \cdot \sqrt{E_{upstream} - y_{downstream}} \quad (6)$$

where L is the gate width, C_{ctr} is the coefficient of the streamline contraction, C corresponds to the gate coefficient and O is the gate opening (in meters). The gate opening can vary with time following operator instructions.

To comply gate operating rules, the regulation option calculates the flow rate to be prescribed downstream in order to respect the appropriate water level at the regulating point.

B. Description

Within the mesh, a structure is materialised as a rectangular island. The island is delimited with four boundary conditions: two liquid boundary conditions (upstream and downstream) in the mainstream direction and two solid boundary conditions corresponding to the lateral structure ends. The liquid boundary conditions (mainly prescribe discharge) are managed by Fortran programming.

C. Adaptation to Donzère-Mondragon development

Five structures have to be considered in the modelling of Donzère-Mondragon development. As the simulation starts with a high flow rate, the following configuration is chosen:

- BGRT: opened so weir equations ((3) if unsubmerged weir and (4) if submerged weir);
- BGU: gate equations with opening law to be determined;
- USB: regulation option with water level law vs. upstream discharge to be determined;
- NPN: closed so modelled by dyke that breaks in case of overflow,
- APN: closed so modelled by dyke without break possibility.

V. SIMULATIONS

A. Stationary discharge conditions

Prior simulating the extreme flood in unsteady mode, the model has to be initialised. In order to reduce water level instabilities at the immediate vicinity of the structures, a first calculation is launched with the sub-models generated in the calibration phase. The water level and flow resulting from this calculation are interpolated thanks to Fudaa PrePro software and an initial "Selafin" file of the whole model is generated.

Subsequently, the law of BGU opening vs. input discharge (at Viviers bridge station) is determined iteratively so as to respect water level at PR3 for various input discharges. It has been done in steady mode.

The USB law of water level vs. discharge, immediately upstream the power plant, is calculated for input discharges higher than the design flood. During flood, around half of the discharge (and more for extreme flood) pass through the six gates and the two surface gates. The law is determined using unsubmerged equations: (3) for surface gates and (5) for gates. The gate and weir coefficients are calibrated. The accuracy of the weir coefficient calibration is shown in Fig. 6 where calculations (blue line) and physical modelling measurements (pink squares) are compared.

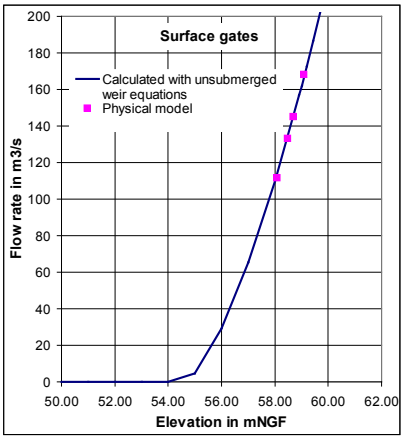

Figure 6. Calibration of weir coefficients for USB surface gates.

B. *Unsteady state*

As BGU opening law is calibrated with stationary boundary conditions, it has to be checked in unsteady mode. In Fig. 7,the PR3 water level, orange dashed line, is lower than the maximum authorised elevation, with a 50 cm toleration, as long as the input flow rate at Viviers station (dark blue line) is lower than the design flow (time is lower than t1 where t1 corresponds to the latest time when development is in operation). Thus, BGU opening is well calibrated.

Prior to flood peak and immediately upstream the NPN, the water level overreaches the maximal head tolerated by the NPN structure. Consequently a break is created [5] and launched at t2.

The discharge passing through the BGU is a relevant indicator of the development behaviour representativeness. Indeed, as long as the BGU opening is manoeuvred, its flow rate (light blue line) is stationary. Afterward, the flow rate increases following the input discharge rising (at Viviers) and since gate opening is fixed. When NPN break occurs, BGU flow rate suddenly decreases given that most of the discharge passing through the BGU is diverted into the NPN wide opening.

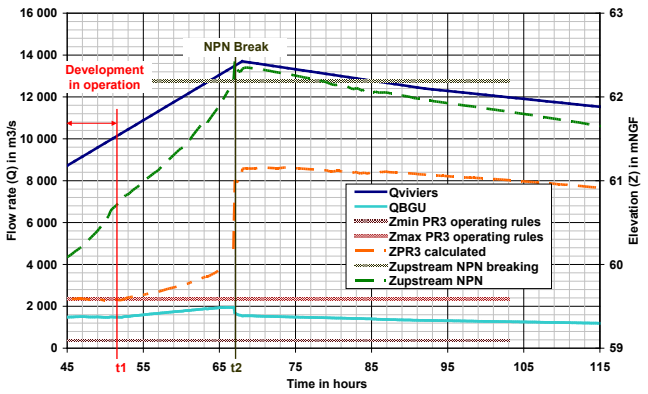

Figure 7. Flow rates and water levels evolution for the extreme flood.

In case of extreme flood, almost the whole Pierrelatte plain is flooded (Fig. 8). Water depths can reach 6 meters in gravel-pits (downstream part of the model). Inundations occur on the left bank of the headrace channel. The velocities (red arrows in Fig. 9) exhibit overflows within the headrace channel due to NPN break. They are located predominantly upstream the SNCF bridge.

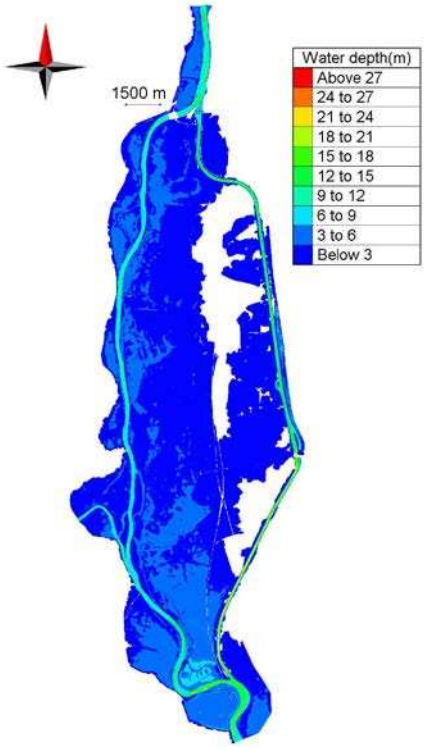

Figure 8. Map of the maximum water depths in case of extreme flood within Donzère-Mondragon developments.

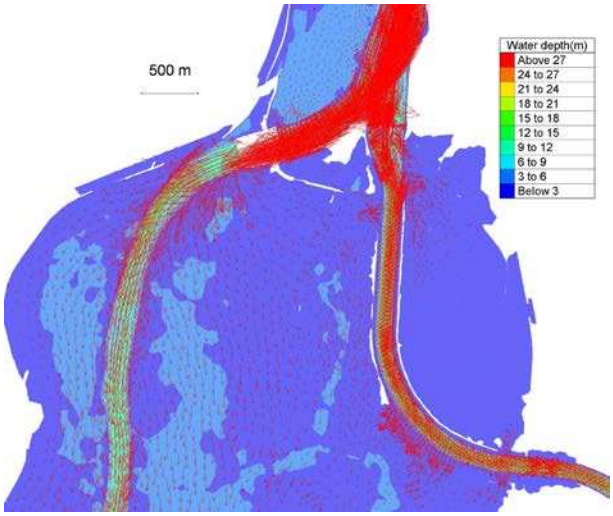

Figure 9. Map of the maximum velocites UV in case of extreme flood at the upstream part of headrace channel.

C. *Technical problems and improvments*

The problems encountered concern:

- mesh distortion: it is noticed that the water levels and velocities analysis is sensitive to strong distortions. A solution is to create a utility program giving every element distortion so as to modify the mesh. N.B. Distortion maps generated by Matisse don't seem to be exploitable;
- flow rate variation: a small variation in water levels can induce a high variation in flow rates, especially at the initialisation. The solution was to add a relaxation variable Q correction ;
- In TELEMAC V5P9 version, it was not possible to prescribe at a boundary condition depending on the discharge passing through a selected section. A programming was attended but didn't succeed due to discharge calculation instabilities. The upgrading of V5P9 in V6P1 could solve this problem.

VI. CONCLUSIONS

A hydrodynamic 2D modelling of Donzère-Mondragon development has been built and calibrated with TELEMAC-2D. Specific subroutines have been implemented within the model to consider CNR structures during extreme flood. The main outcomes of the article are as follows:

(1) The development behaviour is successfully represented and operating rules are complied.

(2) In case of an extreme flood, high water levels are calculated in Pierrelatte floodplain and overflows are noticed in the headrace channel.

(3) Program limitations are identified: the subroutine only answers to flood issues. Furthermore, instabilities in flow rate calculation prevent regulation from running at a specific section.

The present results consider all CNR structures are in operation. The next step of the study will be to change CNR structures configuration: USB units out of order or a BGRT gate closed for maintenance and observe water levels evolution. Considering subroutine improvements, prospective is to implement a complete regulation of each barrage gate to ensure fulfilment of the operating rules from low flow to floods.

REFERENCES

[1] J.-M. Hervouet, Hydrodynamique des écoulements à surface libre, Modélisation numérique avec la méthode des éléments finis, Presse de l'école nationale des Points et chaussées, 2003

[2] S.Raimondo, S.Reynaud, E.Divet, Vallée du Rhône, Rapport de crue de novembre 2002, CNR, unpublished

[3] S.Reynaud, Vallée du Rhône, Rapport de crue de décembre 2003, CNR and Météo France, unpublished

[4] Richard H.French, Open Channel Hydraulics, Water Resources Publications, LLC, 2007, p53-p55

[5] M. Pochat, S.Trossat, Dykes break modelling, Presentation at the 2009 Telemac User Club, CNR, unpublished

Feasibility of a flash flood forecasting service

T.Godfroy, C.Girard, A.Levasseur, M.Erlich, E.David
ARTELIA Eau et Environnement
Echirolles, France
thomas.godfroy@arteliagroup.com

C.Sorbet, V.Pourret, M.Veysseire, B.Vicendon
METEO FRANCE
Toulouse, France

***Abstract*— The feasibility of a flash flood forecasting service has been investigated for the Gardon river. This mission is part of the FP7 project SAFER [1] (Services and Application For Emergency Response) and consists in integrating real-time meteorological data such as rainfall and runoff into a numerical model of river flow. Aim of this mission is to create forecasting inundation maps to make easier decisions and intervention of civil protection.**

The methodology developed has to be easily transposable from one watershed to another and has to deliver a final product operational.

Thus, we present here general functioning of forecasting service and the new methodology with TELEMAC-2D to answer at mission needs.

I. INTRODUCTION

In some areas such as the Cevennes in France (Fig. 1), intense rain events and the specific configuration of watersheds create the phenomenon of flash flood. In France, especially during the flood of the Gardon River in September, 2002 [2], more than 800mm have been measured in two days in some place. This event has caused important damages:

- 13 deaths,
- an economic damage of 1.2 billion euros.

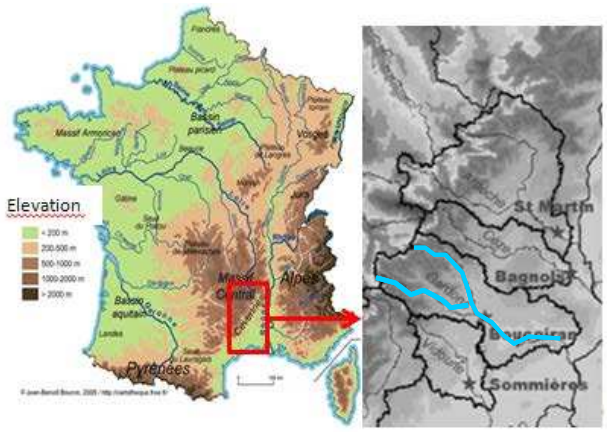

Figure 1. Gardon river location.

To protect the area against this terrible phenomenon, a feasibility of a flash flood forecasting chain has been implemented and validated on the Gardon river. This chain aims at creating inundation maps (Fig. 2) to assist final users (civil protection organisms, NGO...) in making decisions and in making easier interventions.

Figure 2. Example inundation map.

To carry out this mission, a partnership with Météo France (French meteorological service) and Spot Image (satellite picture and map making service) was established. Météo France was responsible for providing rainfall and runoff data which can be downloaded from a website created by Spot image. Spot image was responsible for publishing forecasting maps of the inundation areas.

This paper presents the different steps which have conducted to realize forecasting inundation maps since the reception of data from Météo France forecasting chain [3]. These tasks were performed with TELEMAC-2D and especially with the hydraulic model of the Gardonnenque plain of the Gardon River [4]. The lateral watershed was added to this model, to predict flow coming out from the watersheds as Meteo France forecasting chain cannot provide flow in the outlets of the watersheds. The final mesh covers the whole Gardonnenque plain (Fig. 3).

Figure 3. Presentation of the Gardonnenque plain and the lateral watersheds.

The final model is a mesh containing 19589 nodes. The mesh size varies from 40 meters in stream to 300m in lateral watersheds (Fig. 4).

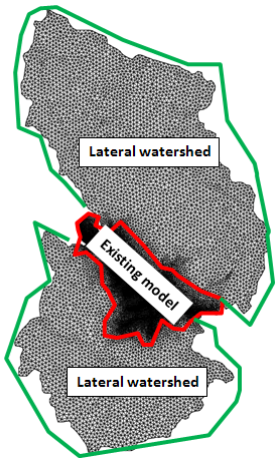

Figure 4. Gardonnenque plain model.

To take into account the contributions of the lateral watersheds it was necessary to perform rainfall/runoff transformations. That is why we decided to use TELEMAC-2D. This choice is explained in the third paragraph.

The development of a forecasting service with TELEMAC-2D implies two main challenges:

- integration of data from Météo France forecasting chain, and
- completion of rainfall/runoff transformation inside TELEMAC -2D.

This paper presents the approach used for both points.

II. INTEGRATION OF REAL-TIME DATA

A. *General presentation*

The first element used to perform integration of real-time data is a program which runs all the time and tests the FTP site (exchange data site) to check if new data are uploaded by Météo France (1, Fig. 5). If in the forecasted data the script detects an important value of runoff, then:

- Data are duplicated in a directory (2, Fig. 5) and used to launch a TELEMAC-2D simulation.
- A hydraulic model is launched automatically by the script (3, Fig. 5).

Then TELEMAC-2D [5] is used to calculate depths and vertically-averaged horizontal velocites in the Gardonnenque plain. At the end of each hour simulated, we provide a result as TELEMAC-2D (4, Fig. 5). Only depths and vertically-averaged horizontal velocities are in the result file. This file is then treated to realise inundation maps.

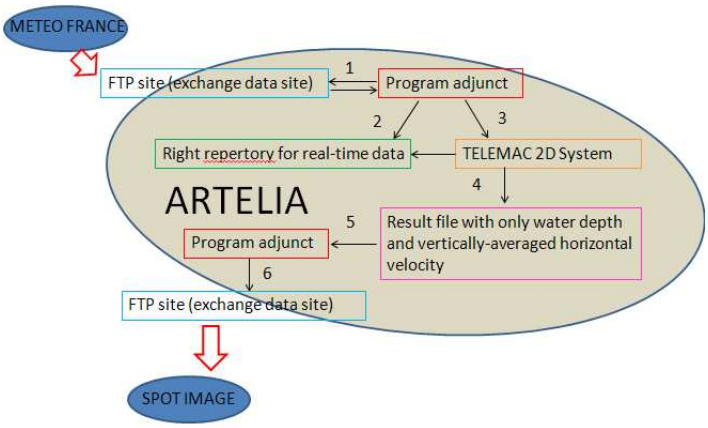

Figure 5. Description of real-time forecasting chain.

The integration of data in real time asked a significant modification of TELEMAC-2D programs such as the creation of the final file each hour simulated. The program designed to launch simulation is also used to publish result file on the FTP site. (5 and 6, Fig. 5).

B. *Integration of forcasted runoff and rainfall*

1) Integration of forecasted runoff: Integration of runoff is made using an existing program of liquid boundaries file. In our case, one simulation models 30 hours of runoff. Runoff is updated every 6 hours and flood may last several days. It means that 4 simulations are run per day. Generally flow lasts between 2 and 4 days. Thus we have to anticipate c. 16 successive simulations.

Most of the time forecasted flow data from Météo France are very different for the same date from one simulation to the next (examples in Figs. 6 and 7).

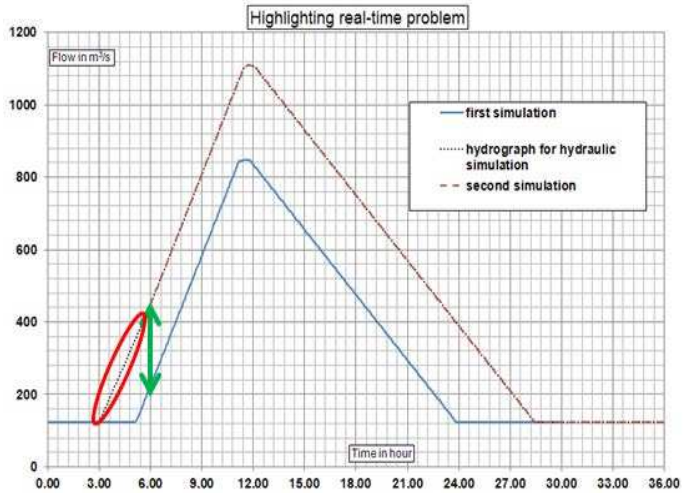

Figure 6. Flow data from Météo France for two different simulations.

Forecasted flow for hydraulic simulation has the most important part concerning calculation of water level in the Gardonennque plain. It causes problem particularly when the initial flow of the next simulation (Simulation 2 in Fig. 7) is different of the sixth flow of the previous simulation (Simulation 1 in Fig. 7) for the same date. Indeed there is an important gap of flow (green arrow Fig. 6) and consequently of volume. Volume variable is very important in our case to make inundation map.

In order to avoid comitting this error we have chosen making a linear interpolation between the third flow of previous simulation and the first flow of next simulation (red circle Fig. 6). The third flow of the first simulation was selected because this flow comes from observed rainfall and first flow of second simulation two.

Simulation 1 11/03/2011 18:00		Simulation 2 11/04/2011 00:00		
Time	Flow (m3/s)	Time	Flow (m3/s)	
03/11/2011 18:00	189.034	**04/11/2011 00:00**	**398.01**	Flow from observed rainfall
03/11/2011 19:00	231.494	04/11/2011 01:00	511.46	
03/11/2011 20:00	269.861	04/11/2011 02:00	586.084	
03/11/2011 21:00	289.986	04/11/2011 03:00	584.847	Flow from forecasted rainfall
03/11/2011 22:00	305.711	04/11/2011 04:00	496.567	
03/11/2011 23:00	334.301	04/11/2011 05:00	375.848	
04/11/2011 00:00	**370.151**	04/11/2011 06:00	322.406	
04/11/2011 01:00	488.855	04/11/2011 07:00	310.087	
04/11/2011 02:00	542.69	04/11/2011 08:00	284.857	
04/11/2011 03:00	471.576	04/11/2011 09:00	273.162	
04/11/2011 04:00	388.304	04/11/2011 10:00	227.973	
04/11/2011 05:00	316.569	04/11/2011 11:00	221.879	
04/11/2011 06:00	288.304	04/11/2011 12:00	237.913	

Figure 7. Flow data values from Météo France for November 2011 event.

2) Integration of forecasted rainfall: Forecasted rainfall has been modelled like source point. Rainfall data is in the form of a grid in which each value is a georeferenced data of rain. The five first lines of data file give information for geo-referencing.

Rainfall data are provided on a regular grid and are interpolated over the irregular TELEMAC grid. Formula used for interpolation is based on the inverse of distance. Interpolation has been restricted to four rainfall data. Thus the formula used is the following (1):

$$R_{mesh} = \frac{\left(\frac{R_{data1}}{D_{data1 \to mesh}} + \frac{R_{data2}}{D_{data2 \to mesh}} + \frac{R_{data3}}{D_{data3 \to mesh}} + \frac{R_{data4}}{D_{data4 \to mesh}}\right)}{\left(\frac{1}{D_{data1 \to mesh}} + \frac{1}{D_{data2 \to mesh}} + \frac{1}{D_{data3 \to mesh}} + \frac{1}{D_{data4 \to mesh}}\right)} \quad (1)$$

R is the abbreviation for rainfall. R_{mesh} is rainfall to apply to one node of model. R_{datai} represents the four rainfall data nearest to one computation node. D is the abbreviation for distance between considered computation node and the four rainfall data nearest.

This formula is applied to give rainfall data for each computation node. Soil conservation Service (SCS) Methodology [6] has been used to perform transformation between rainfall and rain which contributes to runoff. Rainfall data are also updated every 6 hours. Météo France forecasting chain simulate 30 hours rainfall for one simulation. Meteo France also provides rainfall data recorded by a network of rain gauges 15 minutes after the hour which just happened. Fig. 8 shows the location of different input data in the Gardonnenque plain.

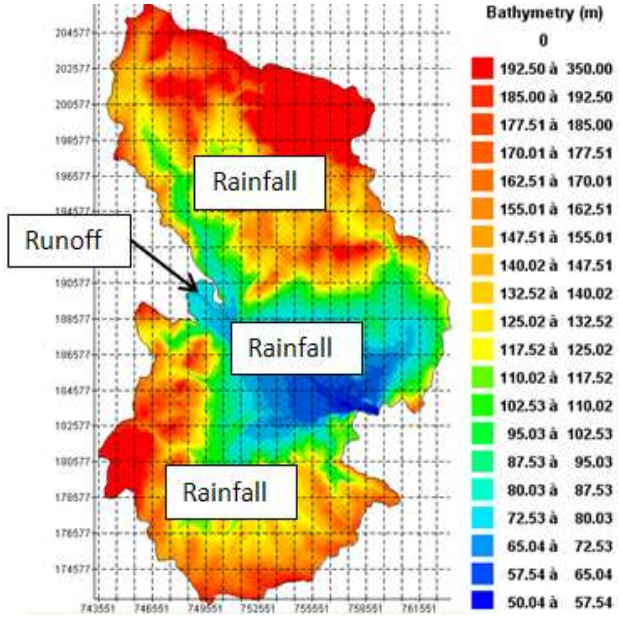

Figure 8. Localisation of flow and rainfall injection.

III. RAINFALL/RUNOFF TRANSFORMATION

A. *Choice of TELEMAC-2D*

Several possibilities have been considered to perform rainfall/runoff transformation. The aim of this study is to find a methodology which can be transposed from one watershed to another. That's why using of classic hydrological model is not interesting. Indeed, these models often take a long time to be calibrated because they depend on too many parameters. TELEMAC-2D depends only on two parameters:

- 1 hydraulic parameter: Strickler coefficient which represents soil roughness, and
- Curve Number (CN) which is the rainfall/runoff transformation of SCS methodology.

The new concept is to use TELEMAC-2D to make rainfall/runoff transformation. Alès watershed has been defined to perform tests. Two past events have been chosen to calibrate and validate the new methodology.

B. *Preliminary tests*

1) Mass conservation: We have tested two different options of tidal flats to see if rain volume was conserved in the model.

First option solves Barré-De-Saint-Venant equations everywhere and applies a correction for element considered as tidal flats.

In the second option, processing is done in the same way as in the first case, but a porosity term is added to half-dry elements. Tests consist to inject rainfall in Alès watershed divided into 6 subwatersheds.

Then, we compared rain injected and volume collected at each red point (Fig. 9) for both option. Volume takes into account the flow that has passed through the outlets (red dots) and standing water in the sub-watersheds (Fig. 9).

Results are given Table I. The first option gives the smallest error on mass conservation. This option will be kept for the other simulations.

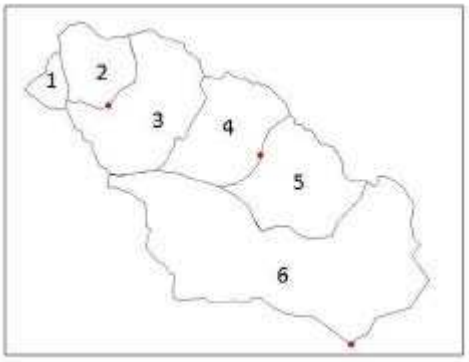

Figure 9. Outlets (red dots) for mass conservation test.

TABLE I. RESULTS SYNTHESIS FOR MASS CONSERVATION TEST

	Subwatersheds 1 and 2		
	rainfall volume injected	volume calculated at outlet	errors in percent
Option 1	**4.91 Mm3**	**5.35 Mm3**	**8.90%**
Option 2	**4.91 Mm3**	**0.78 Mm3**	**84.00%**
	Subwatersheds 1,2,3 and 4		
	rainfall volume injected	volume calculated at outlet	errors in percent
Option 1	**20.49 Mm3**	**21.11 Mm3**	**3.00%**
Option 2	**20.49 Mm3**	**10.47 Mm3**	**49.00%**
	Whole Alès watershed		
	rainfall volume injected	volume calculated at outlet	errors in percent
Option 1	**55.42 Mm3**	**53.95 Mm3**	**2.70%**
Option 2	**55.42 Mm3**	**42.90 Mm3**	**22.60%**

2) Mesh and hydrograph propagation: We defined several meshes to define a compromise between accuracy and computational speed. Tests have been done to see if a simplified geometry (Fig. 10) can properly propagate the flood wave. Indeed, generally the hydrograph propagation is better when the stream geometry is the closest to the reality (Fig. 10).

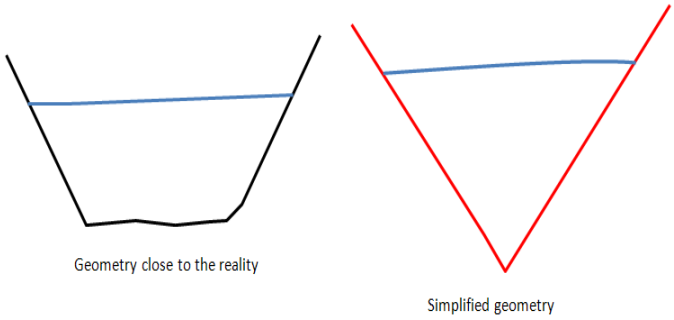

Figure 10. Geometry used for simulation.

We have compared TELEMAC-2D propagation time with MASCARET 1D [7] model for the simplified geometry. Triangular mesh of TELEMAC-2D is done with only one wet node in a cross section (Fig. 11). The propagation test is done in a channel of 3700m long and the slope is 0.006.

Results of this comparison show that TELEMAC-2D can correctly propagate with a simplified geometry (Fig. 12).

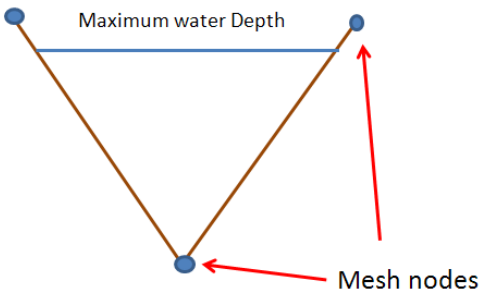

Figure 11. Triangular cross section used.

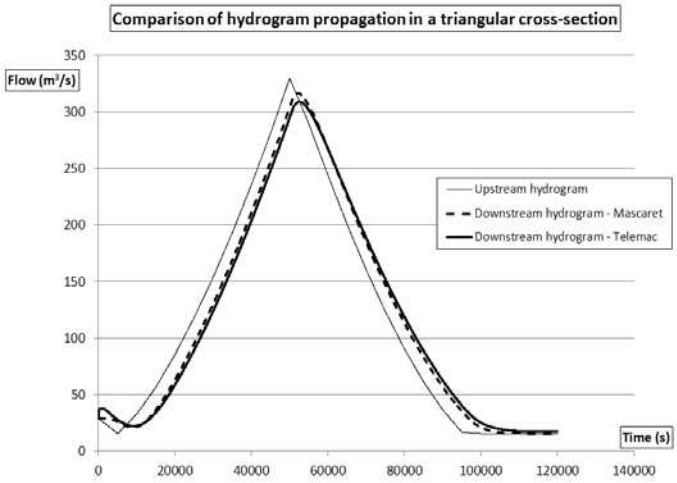

Figure 12. Comparison of propagation time between TELEMAC-2D and MASCARET 1D.

The second test for propagation permits to evaluate if simplification of geometry leads to important errors concerning propagation time. We have compared propagation time with TELEMAC-2D between a real geometry and a very simplified geometry. Test has been performed with the same channel length than in the previous test. Cross sections are obviously the same as the cross sections on Alès stream. Several hydrographs with different peak flow were tested and the channel slope was changed.

We can observe (Fig. 13) that time propagation is quite different for flows non-overflowing (until 40% of lateness). Fortunately for high flow the error is considerably reduced (10% early). The methodology developed here is used for very high flows, which explains this result. Moreover, steeper is the slope, the less significant is the difference in propagation time.

In Alès and lateral Gardonnenque watersheds slopes are steep and flows are high.

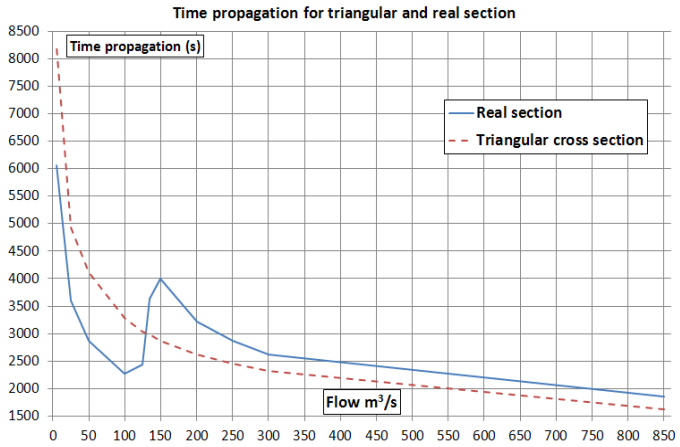

Figure 13. Comparison of propagation time between real geometry and simplified geometry.

Tests have shown that TELEMAC can perform correctly rainfall/runoff transformations. Simplification of geometry for watersheds with steep slopes allows having good propagation of peak flow compared to real cross section. However the flow studied must be overflowed. This methodology can be applied on the Alès watershed.

C. *Calibration and validation on Alès watershed*

1) Calibration: Simplified stream geometry is applied to the Alès watershed. Mesh size is 300m to reduce computational time. Calibration was done according to:

- Hydrograph volume
- Peak flow value
- Peak flow time

Then, we have compared these 3 points between observed values and simulated values.

To obtain the final calibration (Fig. 14), the parameter used to perform rainfall/runoff (CN) wad set at 35. This value means that soil was dry before rainfall event.

The only hydraulic parameter is the Strickler coefficient (which represents soil roughness). To manage calibration, values were set to 50 for overland flow and 35 for stream flow. We have used a high value of Strickler coefficient to represent small drains and gullies that are not represented mesh size of 300m.

A comparison between measurement and modelled flows shows a good agreement (Table II).

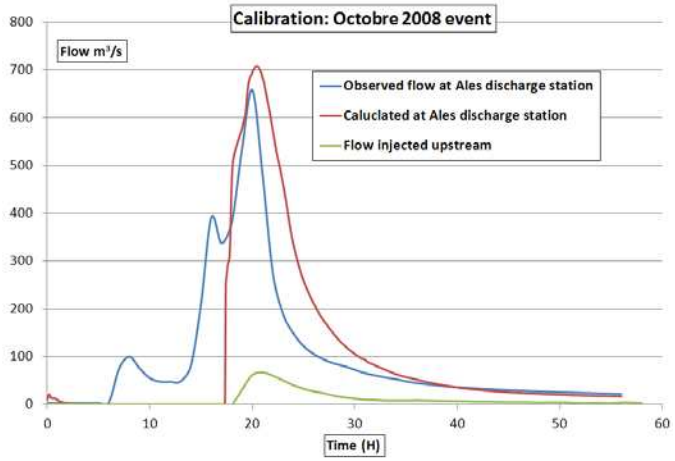

Figure 14. Calibration results.

TABLE II. CALIBRATION RESULTS

	Measured	Calculated	Error (%)
Hydrograph volume	20.3	20.7	2
Peak flow (m³/s)	658	708	8

	Measured	Calculated	Error (%)
Peak flow time (h)	20	20.5	<1

Next step is the validation for two different events.

2) Validation

a) November 2008 event : Validation on Alès watershed: This event happens just after the calibration event and consequently the soil was wet. According to the formula from SCS methodology with humid conditions CN was set up to 56. Hydraulic parameters were kept equal to the calibration parameters.

Concerning the hydrograph volume, 77.3 Mm^3 were measured and simulation give 76.4 Mm^3. The error made is 1%.

T the time of peak flow (Fig. 15), 493 m^3/s were observed compared to 441 m^3/s for the model (Error made =11%).

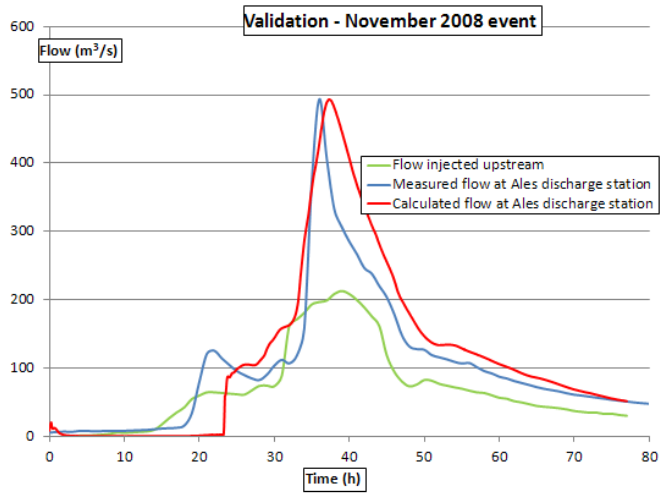

Figure 15. Validation results.

Peak flow time is also well respected. The error made is only 3% (37.00h measured against 38.25h calculated).

Results from first validation are very satisfactory and encouraging. Moreover calculation time is very low. A simulation of 50hours on the Alès watershed takes 1 hour.

b) September 2002 event: validation on the whole Gardon watershed: September 2002 is a historical event because the surface of impact was approximatively 5000 km². Small rainy event happened before the studied event. According to the SCS methodology, soil was humid. CN was set up to 56.

Results from this validation are also very good for this bigger area (Fig. 16). The rainfall/ runoff transformation and the flood propagation runs well with TELEMAC-2D.

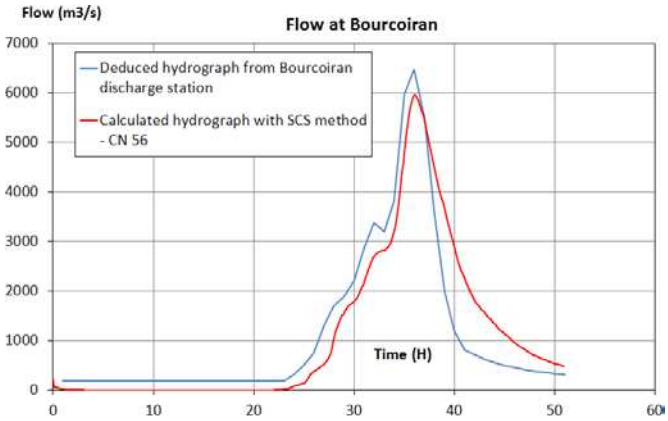

Figure 16. Validation on the whole Gardon watershed.

IV. REAL-LIFE TEST FOR THE FLASH FOOD FORECASTING CHAIN

At the time of November 2011 event (1-7 November) we had possibility to test the whole forecasting chain service.

Indeed, during these 6 days rainfall reached from 600 to 700mm and even more (until 900 mm) in some location. This event engendered a flash flood and caused some damage.

Test has been realized since 3[rd] of November at 18 hours until 4[th] of November at 18 hours. Forecasted rainfall and runoff were updated every 6 hours. Consequently 5 simulations with TELEMAC were performed (Fig. 17).

We can observe (Fig. 17) that from simulation to simulation there is an important difference. Curve with continuous black line represents flow obtained with observed rainfall until 4[th] of November at 18 hour and later it is only prediction.

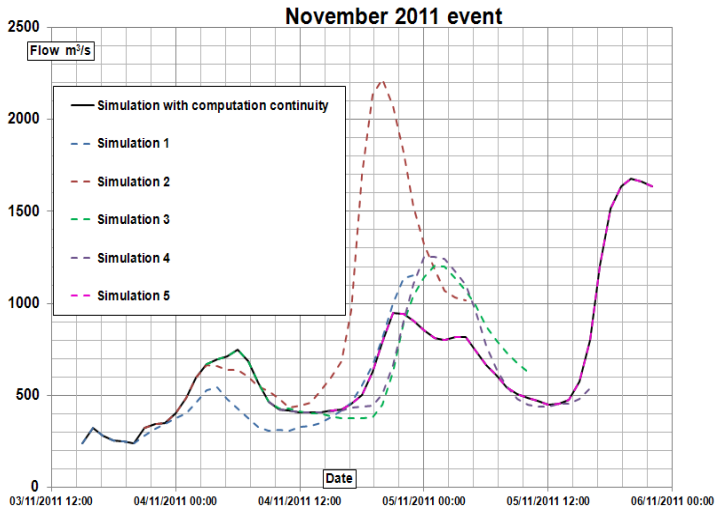

Figure 17. Simulation of November 2011 event.

During this test, beyond results, the main preoccupation was to observe if all the flash food forecasting chain runs and specially the transition between the three partners.

However, the main problem is the calculation time of forecasting chain. Indeed Météo France needs 5h30 of calculation to supply us with hydro meteorological data. Then 2h are necessary to simulated 33h of simulation with TELEMAC-2D.

Thus, computation time lasts about 8 hours. Consequently 8 hours have already happened and we can predict for only 22 hours. It means that we have to begin calculation 1 or 2 days before rainy events to be sure to cover the rise of water level.

V. CONCLUSION

Realisation of a flash flood forecasting chain is now operational.

During SAFER project, improvements concerning tools used by all the partners have been performed. These improvements were crucial to manage this project. Concerning TELEMAC-2D, adaptations and conception of new methodology for rainfall/runoff transformation have allowed integrating TELEMAC-2D to the forecasting chain.

The Methodology developed here can be easily transposed to other watershed prone to flash food where spatial rainfall is available.

Several improvements could be done in order to optimize computation time. Especially with TELEMAC-2D, it will be interesting to parallelise the computational code to reduce the calculation time.

However, we have seen in the previous paragraph that from simulation to simulation results can be quite different. To avoid false alarm and make easier decisions of final users, it will be certainly interesting to do for each Météo France rain forecast a spatial statistic analysis to estimate the probability that forecasting occurs at a given area.

ACKNOWLEDGEMENT

Thanks to CVMHO (Cévennes-Vivarais Mediterranean Hydro-meteorological) for rainfall and runoff data. We also acknowledge Spot Image for its contribution for this project.

REFERENCES

[1] RISKEOS, 2007. A European service network in Support to natural disaster reduction in EU27 countries, ENVSAT Symposium, Montreux, 26 April, http://www.riskeos.com

[2] Le Lay, M. & Saulnier, G.M. 2007. Exploring the signature of spatial varibalilities in flash flood events: case of the 8-9 september 2002 Cévennes-Vivarais catastrophic event. *Geophysical Research Letters 34 (L13401)*

[3] Bouilloud,L. Chancibault, K. Vincendon, B. Ducrocq, V. Habets, F. Saulnier, G Anquetin, S. Martin, E. Noilhan, J. 2010. Coupling the ISBA Land Surface Model and the TOPMODEL Hydrological Model for Mediterranean Flash-Flood Forecasting: Description, Calibration, and Validation. *Journal of Hydrometeorology* 11: 315-333

[4] Artelia. 2001. RN106 – Aménagement à 2x2 voies entre Bourcoiran et La Calmette –Etude d'optimisation et d'impact des ouvrages hydrauliques. Client : DDE Gard

[5] J.M. Hervouet. 2007. Hydrodynamics of free surface flows modeling with the finite element method. Wiley.

[6] USDA. 1986. Urban hydrology for small watersheds – TR-55

[7] Cheviet, C. Duvivier, G., Goutal, N. 2006. Chapter 43. 1D complex modelling with lateral exchanges coupling two reaches, in : River Flow 2006, Two Volume Set Proceedings of the International Conference on Fluvial Hydraulics, Lisbon, Portugal, 6-8 September 2006, Taylor & Francis.

Determination of marine risk by hydraulic coastal modelling – Application to Charente-Maritime coast

Christophe COULET, Yvon MENSENCAL
Hydraulic Modelling and Software team
ARTELIA Water & Environment
Merignac, France
christophe.coulet@arteliagroup.com
yvon.mensencal@arteliagroup.com

***Abstract*— In 2010, on February 28th, Storm Xynthia strikes Europe causing the death of 53 people in France and €1,4 billion damages mainly on the Atlantic coast. Charente-Maritime was highly impacted by this event, which covered 300 km of coasts. In this region alone, Xynthia caused 12 deaths, 4 800 flooded houses, 900 shellfish industries injured and 793 firms in trouble after the storm, 120 km of dikes damaged, 40 km of flooded roads and 232 km² of flooded area on the continent and on the islands of Oléron, Ré and Aix.**

Despite, it has been demonstrate that the storm in itself was not a statistically exceptional event. The dramatic context is induced by the concomitant phenomenon of high spring tide and surge of sea level due to meteorological conditions.

In order to anticipate and assist stakeholders for the management of this kind of risk, including a potential increase due to climate change and sea level rise, we have built an efficient operational model of surge propagation on the Atlantic Ocean up to the coastal area and inland area. The exchanges at the coast are managed at the dikes scale and can take in account the breaches and the overtopping of waves. The methodology and the first results will be presented and discussed in regards of potential requirements for the needs in crisis preparedness and management of the Stakeholders.

I. INTRODUCTION

The events over the last decade (Martin in 1999, Klaus in 2000 and Xynthia in 2010) and the consequences of climate change on these phenomena lead decision makers to examine accurately the risk of marine submersion.

Marine or coastal flooding are generated by a combination of different factors linked for some and independent for others. Thus we could consider that these submersions are derived from the crossing of the statistical level to the coast, the swell at the coast and coastal protection system.

The water level at the coast consists of:

- The evolution of the astronomical tide.
- A chronicle of positive and negative surges off the coast, mainly generated by the anticyclones and depressions.
- The action of wind on the water.
- The action of the swell on tidal currents (set-up phenomenon).

The combination of all these parameters generates static water level at the coast. If this level is higher than the crest level of protections, a flooding by overflow protection is observed. This phenomenon is similar to the River overflow over the dikes of a river. The protections structures even not initially designed for this, are submitted to high stress, which often results in the appearance of breaches, or sometimes the complete destruction of an important linear of protection.

The swell at the coast is the result of the influence of:

- The swell offshore,
- The action of wind on the water.
- The influence of the water level (and associated water Heights) and tidal currents.

The swell at the Coast causes overflows above protections, without the static water level not necessarily above the crest level of the protection. This overflow by "packet of sea" is also called "overtopping".

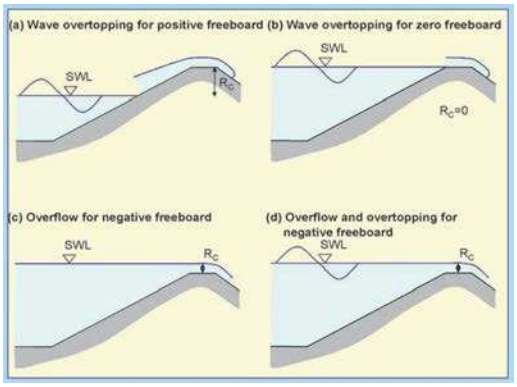

Figure 1. Visualization of the modes of crossing of a dike (sources [2]).

Fine representation of the phenomena of flooding using a modeling tool therefore requires the perfect representation of all of the factors described earlier to approach to the best of the physical reality of the phenomenon to study.

The extent of these territories and the complexity resulting from road networks and drainage networks as well as the protective devices make 2D models the best suited tools for the study these territories in the event of flooding.

TELEMAC-2D allows the calculation of free surface flows in such configurations [1] spread the flood initially dry areas corresponding to the terrestrial part of the study located behind the protection systems. In addition, the fact that it is based on a non-structured triangular mesh to represent all the structures (roads, ditches, dikes,...) by local refinement without forcing the size of mesh in the other sectors (in particular the marine area) and so therefore without increasing significantly the number of nodes. Finally, for some cases that require too great refinement of the mesh in relation to the problem posed (it is the case of dikes located in the interface of marine part and the terrestrial part), access to the sources allows the development of specific features such as:

- The computation of the flow in the drainage networks with the possibility to represent the valves and the sluice gates;
- The computation of the overflow on dikes (taken into account faithfully in the form of an exchange flow calculated at the scale of topographic survey);
- The wave overtopping on the dikes (with the same finesse of description).

Charente-Maritime coast located on the west coast of France, face to the Atlantic Ocean has largely been affected during the recent storms and Xynthia particularly in February 2010 (53 deaths and 1.4 billion € of damages in France). The consequences of this storm in this region (12 deaths, 4 800 flooded houses, 900 shellfish industries injured and 793 firm in trouble after the storm, 120 km of dikes damaged, 40 km of flooded roads and 232 km2 of flooded area) led the Greater La Rochelle (CDA) and the Territorial Collectivities of the Charente-Maritime (DDTM 17) to launch a study to determine the risk of marine submersion on a part of its territory.

II. AREA MODELLED

The modelled area is defined by hydraulic criteria (topographic for the land part). All the territory of the CDA potentially flooded for the most pessimistic configuration to study is integrated in the model.

A. Marine area

The outline is located about 80 km off the coast from the mouth of the Charente, beyond the bathymetric level - 50.0 m NGF IGN69.

The northern boundary is located at the level of the Sables D'olonne in Vendée and the southern boundary at the level of Vendays-Montalivet, along the Aquitaine coast, in Gironde.

All the ocean coast of the Poitou-Charentes region is thus covered by this model.

The main rivers are integrated in the model. It's the Lay, the Sèvre Niortaise, the Charente, the Seudre, the Garonne and the Dordogne which form the Gironde estuary just below Ambès.

This choice ensures that the various hydrodynamic phenomena are properly represented by the model and in particular the influence of fluctuating volumes of these rivers on the hydrodynamics of the Pertuis.

B. Land area

This area is essentially based on the level 6.0 m NGF in order to integrate all the places under the maximum water level potentially reached by an event.

Taking into account this limit involves a mesh on very large areas, especially on the North and South of the territory of the CDA. These areas, bordering the Charente and Sèvre Niortaise estuaries are large marsh areas which were in the past the outlets of these rivers.

Fig. 2 illustrates the model area.

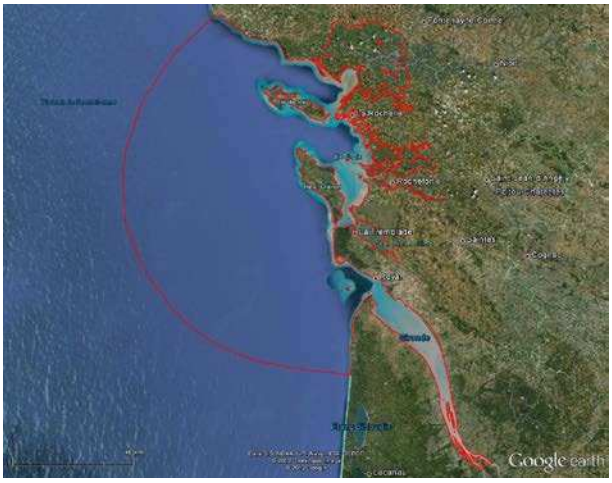

Figure 2. The modelled area.

C. The mesh: schematic representation of reality

The mesh is a schematic representation of reality. Because of this mapping, its construction is an essential step in the realization of a hydraulic model study. It is essential that the mesh incorporates and represents the most accurately the reality of the land, and specifically at the level of structuring elements. These elements consist of particularities which have locally an influence on the behaviour of flows. On the area of study, structuring elements are many and various. Their treatment and how to represent them in the models are detailed in the following paragraphs.

1) Embankments and dykes: The representation of embankments and dykes requires good representation of the role of obstruction to the flow and their possibly submersible character. To do this, it is necessary to represent properly and jointly the altimetry of the foot of dikes and the top (crest).

Two principles are used to this, depending on the size of the obstacle and the vertical heterogeneity of its crest:

- The first is to integrate the obstacle in the mesh,
- The second is to represent the obstacle in the form of two boundaries of the model and to calculate the flow eventually overflowing on the obstacle with the "classics" hydraulics laws (weir law). For coastal levees, the calculation of those overflows also integrates the characteristics of wave to determine the flow generated by the phenomenon of overtopping.

This second method was chosen to represent the whole coastal dikes on the modelled area. It has the advantage to be able to integrate the vertical representation of the crest of the embankment at a small than the mesh size.

For example, topographic survey of the protections dikes has an average spacing between the points identified in 50 m approximately. It was fully taken into account in the model. This method allows representing the flow that passes on a low point of protection, whatever its width, without requiring the refinement of the mesh on this particular sector.

Note that the walls in the floodplain were not represented in the model; these elements have no vocation to protect against overflows.

2) Buildings: It was the choice for this study to not represent buildings existing in the study area.

It should however be noticed that buildings can play a role of barrier for the local progression of flows in dense urban areas. This detailed analysis is not compatible with the study area and thus with the resolution of the model scale implemented here.

3) Lakes and gravel pits: Large gravel pits and lakes were represented in the models. However, there is not always information on the bathymetry of these areas. Therefore, the bottom level in these sectors was assumed from our land investigations and our knowledge of the sector.

4) Drying network and hydraulic works: The main drying system (ditches, canals...) is integrated in the model.

The lack of bathymetric information on these sectors has led us to use standard hydraulic sections and to impose an assumed bottom level for this network. The bottom level has been selected based on our expertise combined with the survey available on the hydraulic works of this network.

An initial water level is imposed in the drying system, level which is lower than the overflow level of these rivers and which can be locally depending on reports made by people met during the on-site visit.

Main hydraulic works, and particularly works downstream of this network, have been incorporated in the model. The functioning of specific works (valves, sluice gate...) is also integrated in the computations.

The secondary network (ditches...) is not include in the model, but its outlets are however integrated. The outlet works is connected to the low point behind the protection, which means that the transfer of water from the low area to the sea is not represented by the model but the emptying of low points is achieved through those outlets.

The storm network is not represented in the model. The main existing outfalls on the urban area are however integrated to represent the drain from the low areas of the floodplain.

The model should determine the water hazards (levels and maximum heights of water). However, the methodology used to build the model allows the representation of the post-event period and the emptying of the flooded areas.

5) Characteristics of the mesh: The mesh of the model consists of 163 200 nodes and 315 500 triangular elements.

The maritime part is composed of approximately 23 600 nodes and 44 360 elements.

For the terrestrial part, the mesh sizes range from 25 m along the coast up to 100-250 m in the distant marshes. It can reach 800 m in the marshes of Vendée (North of the Sèvre Niortaise), areas that were simply modelled to dispose of the potential interactions over the dike of the “Canal des 5 Abbés”.

The maritime mesh size varies from 5 km off within 300 m between the Islands and the coast. At the level of the Pertuis Breton and Maumusson, the mesh size is around 100 m, Fig. 3.

The maritime mesh has been forced to properly represent the hydraulic sections of numerous channels and banks existing on this sector. This method allows the perfect representation of the effect of channel flows observed at the level of the Pertuis.

6) Bathymetry and topography: The bathymetry of the maritime part of the model is taken from SHOM maps available on the sector.

The topography of the land part of the model is the interpretation and the exploitation of a recent LIDAR survey of study. The topography of the crest of protection dikes comes from a topographic survey achieved after Storm Xynthia. These data have been changed during the calibration to best match to the altimetry of existing dikes during Storm Xynthia, which were for the most part lower than present because of the emergency work made after the event.

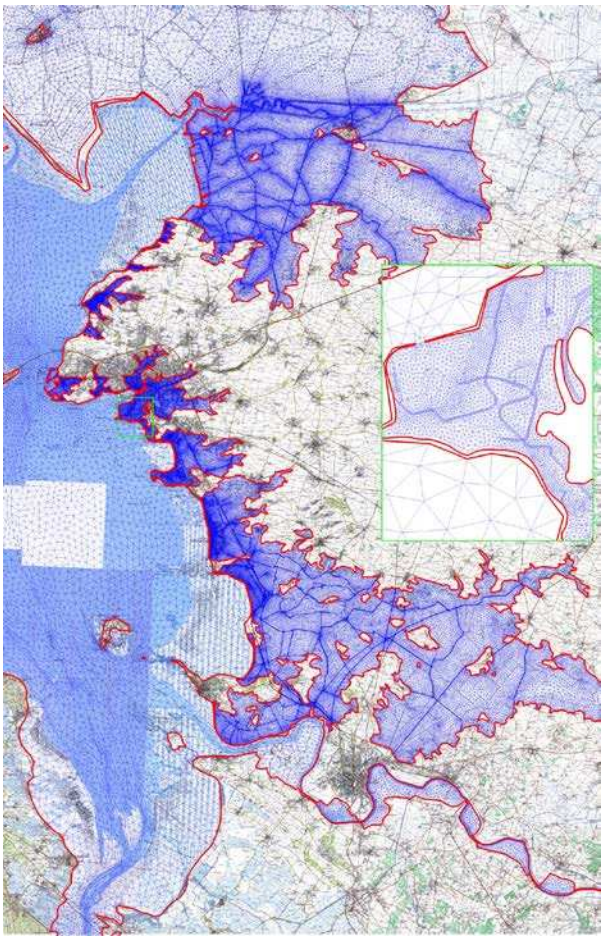

Figure 3. Mesh of the model.

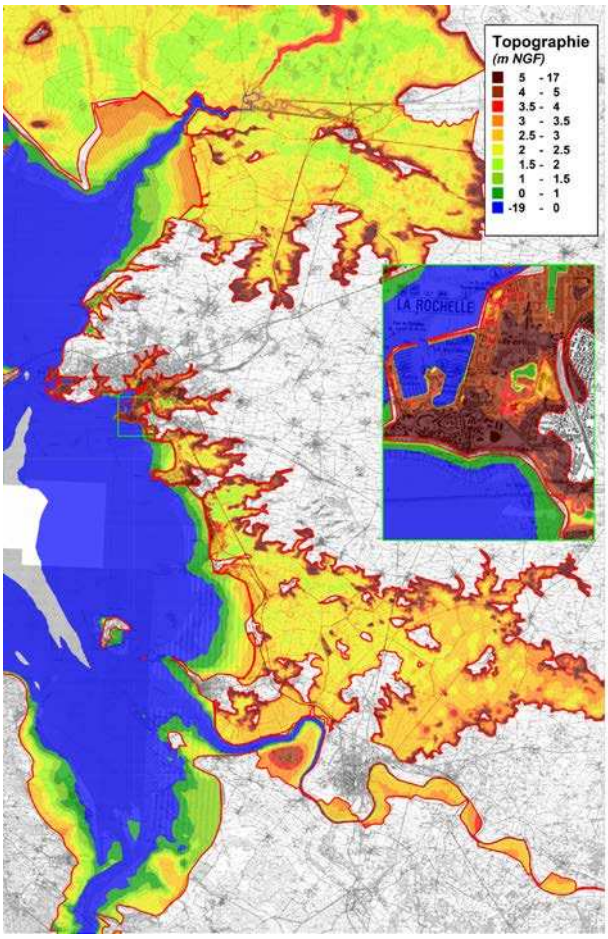

Figure 4. Bathymetry and topography of the model.

Fig. 4 shows the representation of the topography and bathymetry of the study.

III. IMPLEMENTATION OF THE COMPUTATION

Flooding taking into account swell but there is no interest to calculate it on the terrestrial part of the model, so we choice to separate TELEMAC 2D and TOMAWAC computations. We have therefore extracted the marine part of the model to calculate swell only on this area.

This quite light "submodel" in comparison with the global model allow us to calculate the swell conditions fairly quick. However, to take into account all of the phenomena a first hydrodynamic calculation taking into account the tide, the atmospheric set-up and the wind is made with TELEMAC-2D. The TOMAWAC computation uses this result to take into account the effects of currents. The results obtained (wave height, period, direction and the stress radiation) are projected on the global model. On the land area, the swell result is set to 0.

TELEMAC-2D "definitive" calculation can then be carried out. The result TOMAWAC (height, period and direction) is taken into account in the calculation of the overtopping of coastal protection dikes. Stress radiation allows taking in account the swell currents in the hydrodynamics.

IV. CALIBRATION OF THE MODEL

A. Calibration of the oceanic part for normal tide conditions

The hydrodynamic model is first calibrated using level and speed data on the maritime part for "normal" events, Fig. 5. That is to say with no specific hydro-meteorological conditions (storm surge, wind...).

This calibration is made by comparison between water level evolution provided by the hydrodynamic model for an astronomical tide cycle in the different gauges of the study area and predictions provided by SHOM for these same tide gauges.

This comparison is made on 19 days, from 20th February to 11th March 2010, in order to cover the whole tidal conditions that can be encountered within the study area.

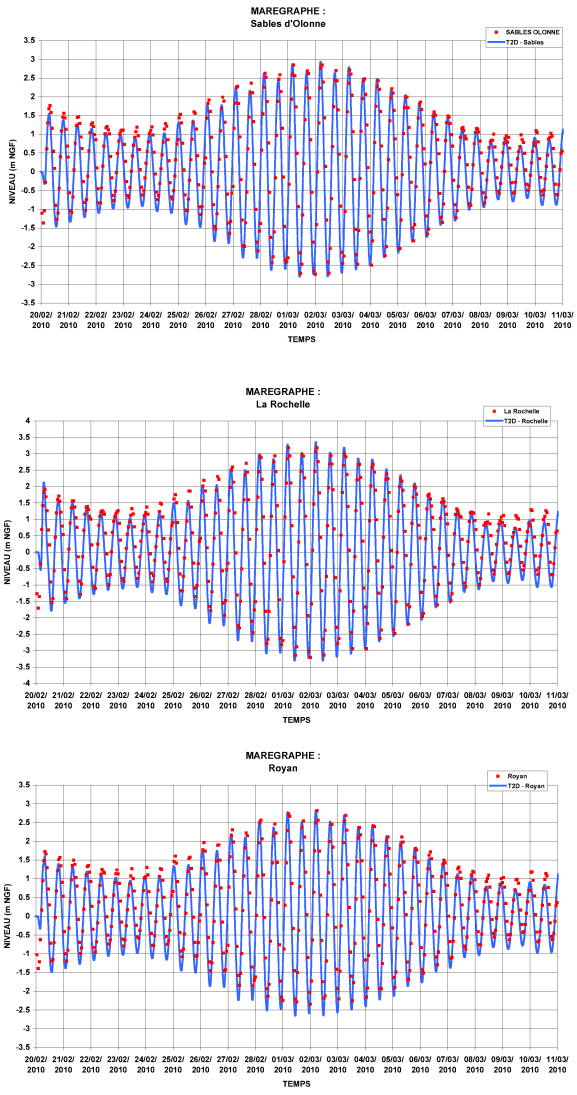

Figure 5. Comparison of the evolution of water levels given by the hydrodynamic model and those predicted by SHOM.

It is reminded here that simulated tides, as predictions of SHOM, correspond to the theoretical astronomical tides. The weather parameters that have an influence on observed actual tides (winds and atmospheric pressure which generate positive and negative surge at the large scale of the Bay of Biscay) are not represented by this simulation.

Indeed, the timing period incorporates the dates of occurrence of Storm Xynthia. Predicted level of tide on tide gauges and reproduced in the model are well below the levels found during the storm due to storm surge. However this does not change the validity of the model for the good representation of current in the area.

The evolution of the theoretical water level provided by the model is very close to that predicted by SHOM in amplitude and levels of high and low tide but also on the phasing of the tidal wave.

Velocities data (direction and intensity) for the characteristic tides (high and neap) which are available on SHOM maps on the area of study, Fig. 6, are also compared to the results provided by the model for the velocity of tidal currents.

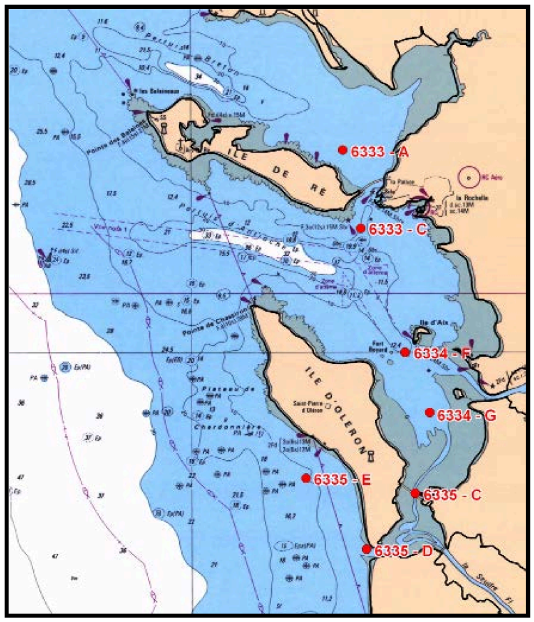

Figure 6. Location of SHOM points with velocities informations.

These comparisons are presented in Fig. 7. The lines correspond to the results of computation and points to the data provided by SHOM.

Note that SHOM provides velocities values in knots (integer values). These data correspond to velocities near the surface (problem of navigation). This generates some difficulties to compare that information with modelling (The velocities are integrated on the water column). Surface velocities are generally higher than the mean velocities.

This comparison shows that the model calculates tidal velocities similar to those provided by SHOM, in order of velocity magnitude as well as in direction.

The hydrodynamic model for its maritime part is able to reproduce the hydrodynamic phenomena associated with the tides for the "common" maritime events.

B. Calibration for events which generate significant levels of water

1) Storm Martin: It was firstly achieved a calibration of the model in comparison to the information available for Storm Martin (December 27[th] 1999). The collected data are only for the maritime part of the study area.

For this comparison, the influence of the chronicles of winds and also the positive surge due to atmospheric low pressure (37 cm maximum) was imposed in addition to the representation of the astronomical tide.

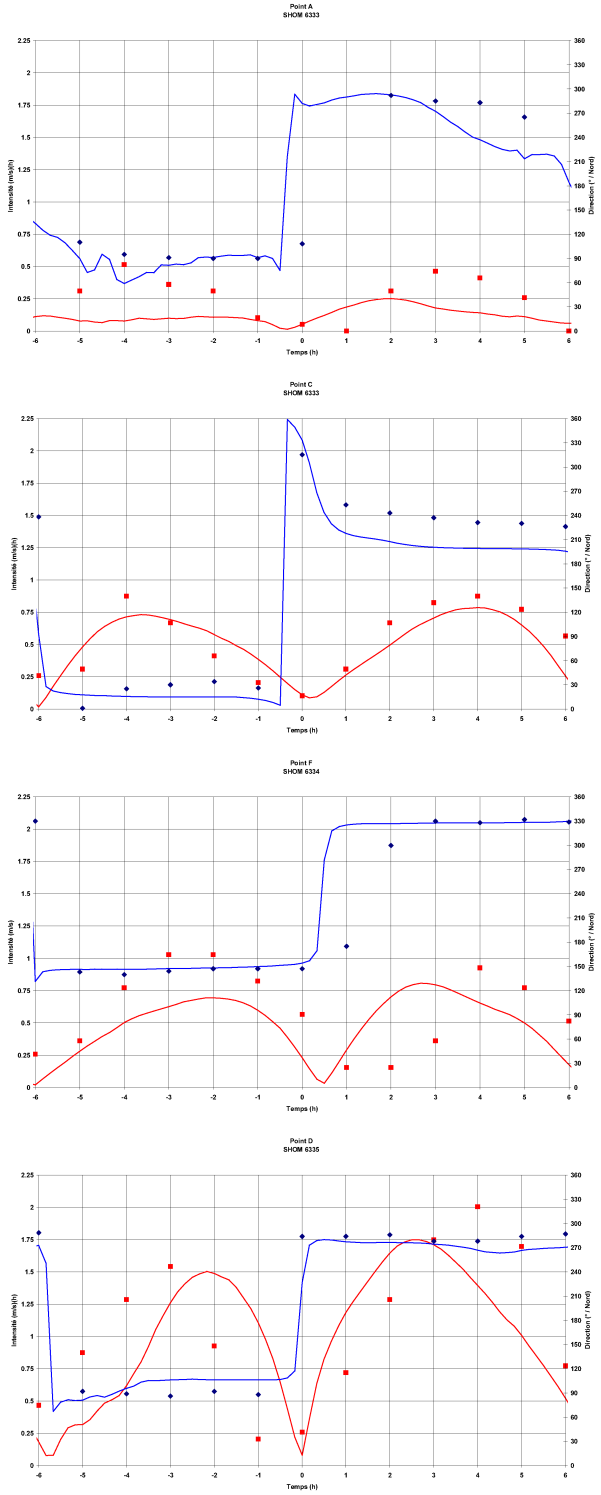

Figure 7. Comparison of calculated velocities and values provided by SHOM.

The swell was not considered for this computation due to the lack of information.

Fig. 8 shows the comparison of the observed and calculated water levels for Storm Martin. The maximum observed level was also drawn to counterbalance the lack of measurement at the peak of tide (December 27[th]).

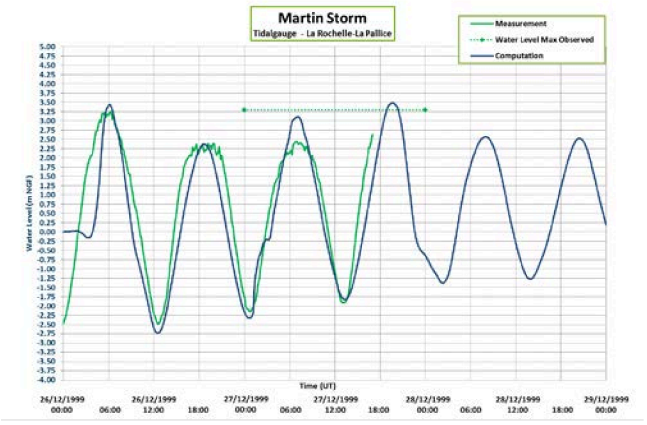

Figure 8. Storm Martin– Comparison at La Rochelle.

Without more information about this event, it is difficult to determine the representativeness of the model. Nevertheless, calculated water levels are consistent with estimation of maximum levels on the sector of La Rochelle.

2) Storm Xynthia:

a) Astronomical tide: February 2[nd] 2010 was a high spring tide. The theoretical high tide level at La Rochelle - La Pallice, was 2.99 m NGF (against about 4.50 m NGF reached during Storm Xynthia).

For this tide, hydrodynamic 2D model implemented in this study allows to represent the evolution of the theoretical tide, on magnitude and phase. This comparison between theoretical tide provided by SHOM and computed by the model is presented in Fig. 9:

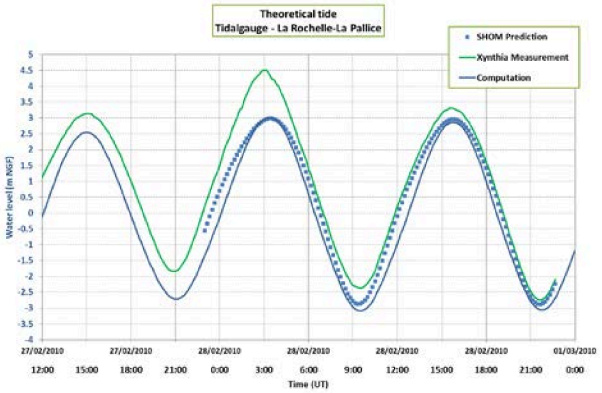

Figure 9. Storm Xynthia - Astronomical tide – Comparison at La Rochelle.

The following graph shows the comparison between the evolution of the theoretical tidal provided by SHOM and those calculated by the 2D model at Rochefort. The evolution of the water level recorded by the tide gauge for Storm Xynthia is also on this chart. The tide gauge is located in the Charente estuary, which explains the characteristic shape of the tidal wave which is observed. For this sector, the 2D

model is less accurate, particularly on the phasing of the tidal wave. High levels are however correctly approached.

This is explained by:

- Schematic representation of the channel of the Charente, which leads to an error on the representation of the oscillating volume at this level. This error generates a delay between the moments of high and low tide in comparison to the predictions.
- The imposition of a constant discharge of the Charente. This discharge is higher than the discharge considered for the calculation of the predictions of SHOM. This explains the low tide levels calculated higher than those predicted.

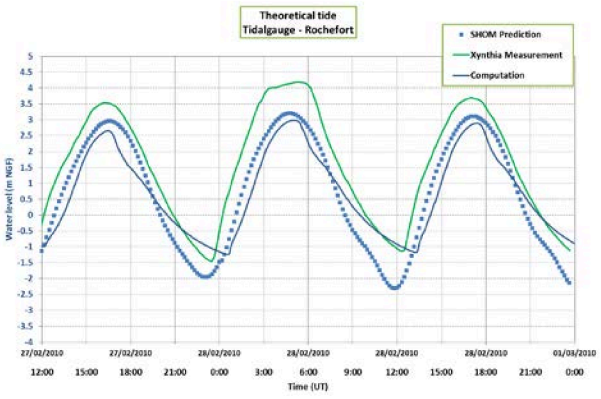

Figure 10. Storm Xynthia - Astronomical tide – Comparison at Rochefort.

The following graph shows the comparison of the evolution of water levels predicted by SHOM and calculated by the 2D model for the astronomical tide at the tide gauge of Le Verdon, at the mouth of the Gironde estuary. For this tide gauge, the model perfectly represents the evolution of the theoretical tide.

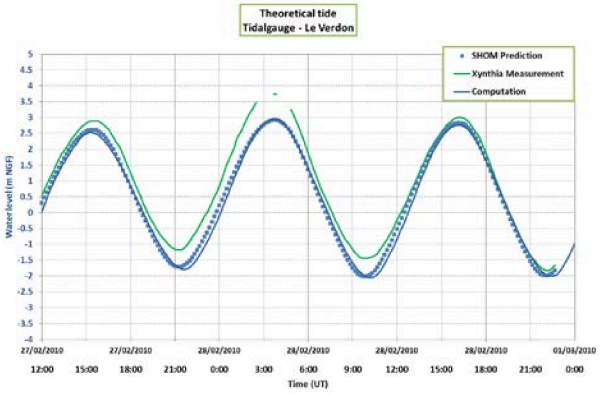

Figure 11. Storm Xynthia - Astronomical tide – Comparison at Le Verdon.

This analysis allows us to validate the representation by the model of astronomical tide on Charente-Maritime coast. We notice that the model represents less accurately the evolution of the tide in the estuary of the Charente, on an area which is outside of the main area of this study.

b) Atmospheric surge: To represent the real event as it has been observed, some hydro-meteorological parameters have been incorporated into the model. The first of them is the representation of the time evolution of the surge offshore. This positive (or negative according to the moments) surge, is characterized by the evolution in time of the mean sea level around which the astronomical tide oscillates. This variation of the mean level is mainly generated by the succession of low and high pressure area.

The chronicle of the imposed surge is determined by the method of inverse barometer: considering a rise in the average level of 1 cm for a decrease of 1hPa of the pressure at sea level. The evolution of the atmospheric pressure at La Rochelle during the passage Xynthia is used for this. A shift of 2 h is imposed to take in account the distance between the ocean limit of the model and La Rochelle (the propagation time of the storm). This method involves the imposition of a maximum surge around 50 cm offshore. This is illustrated in the following chart where the surge calculated at the level of the tide gauge of La Rochelle is also represented. There is no phenomenon of amplification of the surge offshore as a consequence of the bathymetry near the coast.

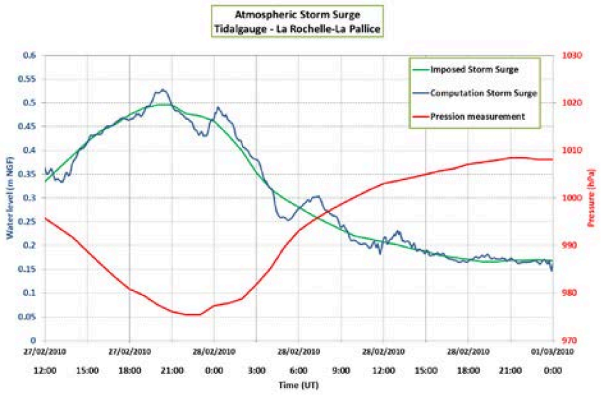

Figure 12. Storm Xynthia – Atmospheric surge.

c) Winds: The second parameter for the representation of the real event is the influence of wind on water. In this study, we impose a wind variable in time (intensity and direction) and uniform in space.

The influence of the wind is only considered on the maritime part of the model.

The chronicle of wind imposed has been defined by analysis of records available at the stations of Chassiron (Oléron Island).

The imposition of this wind chronicle on the maritime part gives a maximum positive surge around 1 m at La Rochelle - La Pallice.

d) Swells: The third parameter integrated in the model of Storm Xynthia is the influence of the swell on:

- The currents in the maritime part,

- The overtopping of the protections that flood the land areas.

The model built for this study takes into consideration in a couple ways, the influence of the swell on tidal currents that generate the set - up and the influence of tidal currents on the swell propagation.

The swell computed by TOMAWAC and imposed in the TELEMAC-2D (direction, period, and significant wave height) was calibrated to properly represent the data from SHOM swell buoy located offshore of Oléron island. This is illustrated in Fig. 13.

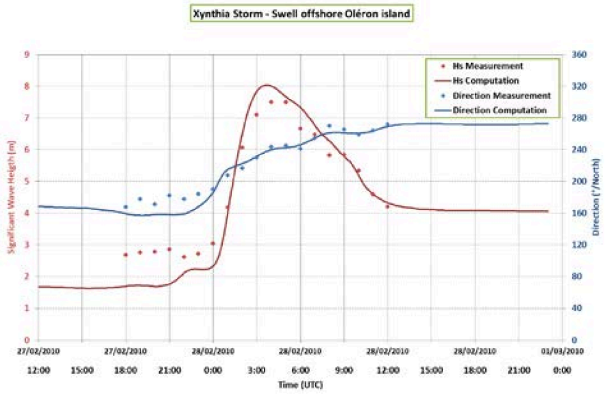

Figure 13. Storm Xynthia – Swell.

The maximum positive surge due to the consideration of the swell in hydrodynamic calculations is around 22 cm at La Rochelle - La Pallice. This maximum surge is observed 4 hours after the peak of the event, during the ebb. We could note that the swell then generates a negative surge of 15 cm up to 8 hours after the peak of Xynthia.

e) Maximum water levels at the tige gauges: The following figures present comparison at the tide gauges of La Rochelle - La Pallice, Rochefort, Le Verdon, La Cotinière and Royan, between the records during this storm and the results of model integrating the astronomical tide and the influences of the surge offshore, the wind and the swell. The theoretical tidal obtained with the 2D on the same period model is also draw to illustrate the importance of surges generated at the coast for the hydro meteorological parameters associated with this storm.

It appears from the analysis of these charts the following remarks:

- The evolution of water observed in tide of La Rochelle - La Pallice is very well represented by the model. There is a slight shift in the flow before the peak of the event,
- The model underestimated the level of the peak to the tide of Rochefort. The phase observed for the tide is similar to that observed for the astronomical tide.
- The tide gauge of Le Verdon is not exploitable for the peak of the Xynthia event. The exploitable period of the registration shows the good representation of the evolution of the water for the model
- For the tide of La Cotinière model underestimated about 25 cm the maximum water level observed in Storm Xynthia. A temporal shift is also observed for this tide,
- Data of Royan tide gauge is not consistent with data of Le Verdon, despite a near location on banks of the Gironde estuary.

Despite the low number of exploitable data, the model allows to precisely represent the maximum water level measured at the tide of La Rochelle - La Pallice. Outside the main study area, the model correctly represents the evolution of the water level, without offering such high level of precision.

On the study area, the model represents accurately the influence of the hydro meteorological parameters on the evolution of the water level (on maritime side).

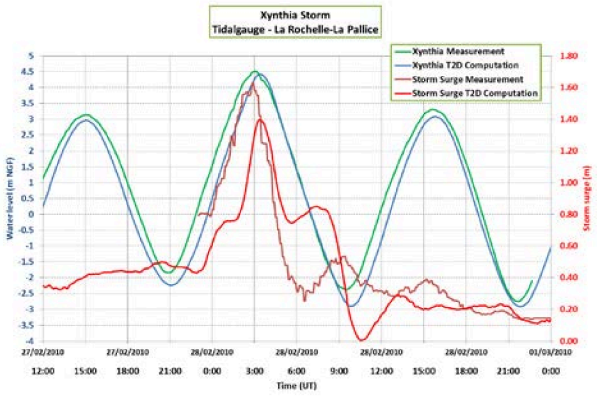

Figure 14. Storm Xynthia – Comparison at La Rochelle.

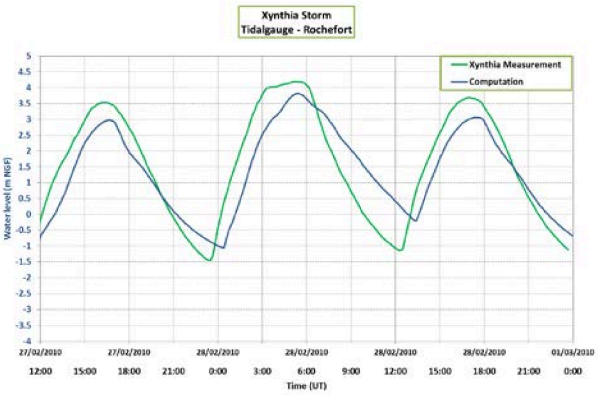

Figure 15. Storm Xynthia – Comparison at Rochefort.

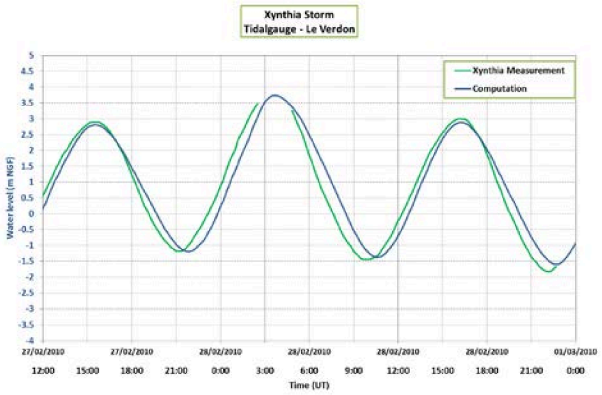

Figure 16. Storm Xynthia – Comparison at Le Verdon.

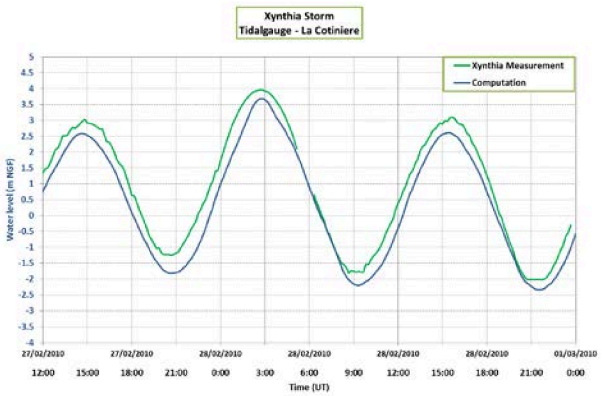

Figure 17. Storm Xynthia – Comparison at La Cotinière.

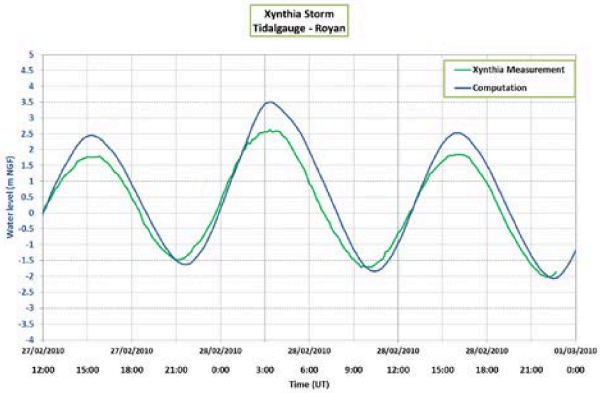

Figure 18. Storm Xynthia – Comparison at Royan.

f) Maximum water levels in the land: The calibration of the model in the land behind the dikes, for Storm Xynthia, is made by spatial comparison between the results of computation and:

- The limit of the area inundated or submerged determined in [3].
- The water marks identified in [3],

For this analysis of the representation, by the model, of flows on the land part, the configuration of protection has been modified from that currently observed. The level of protections has been puts at their level before Xynthia, on Charon and Yves sectors. Indeed, on these sectors, protections have been reconstructed with a higher level after the storm.

To properly represent the water volumes on the land part, ruptures and destruction of protection works have also been integrated in the model. These failures have been defined on the basis of the study [3]

The outline of the flooded areas is well represented by the model as it could be seen on Figs. 19 and 20.

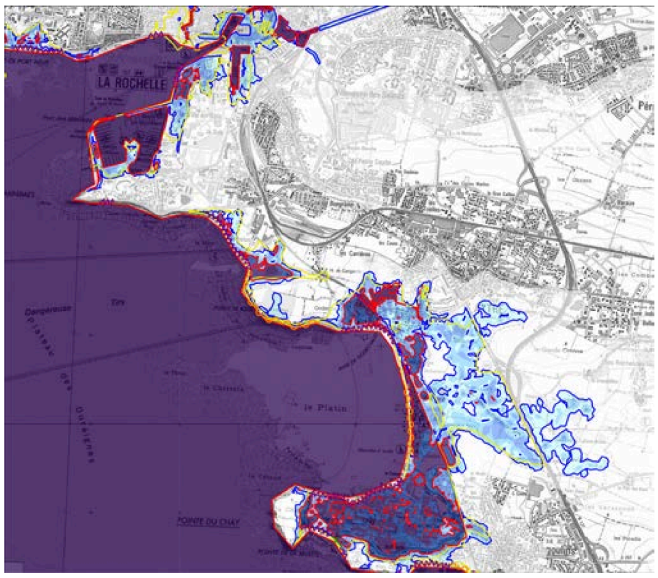

Figure 19. Storm Xynthia – Flooded area around La Rochelle.

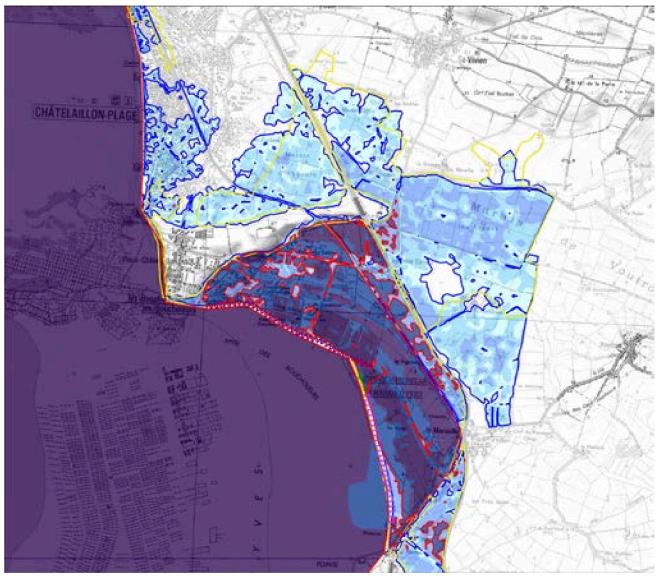

Figure 20. Storm Xynthia – Flooded area around Chatelaillon.

Table I presents, by communal territory, a summary of the differences between the observations and the results of the modelling.

At the end, more than 400 water marks were able to face the results of the model on the study area. Despite the great

disparity of information, the model provides a mean absolute deviation about 25 cm from the observations on this area.

The model correctly represents the maximum water levels on all the study area.

We could note that on the low areas behind the protections, the time of failure is an important control for the dynamic of filling and by consequence for the maximum water level observed.

TABLE I. SUMMARY OF DIFFERENCES BETWEEN OBSERVATIONS AND MODEL PREDICTIONS

Cities	**Water marks**				
	Total number	***Number used***	***%***	***Mean deviation***	***Absolute mean deviation***
Andilly	2	2	100	-0.03	0.24
Angoulins	33	32	97	0.09	0.13
Aytré	44	43	98	0.04	0.20
Charron	35	35	100	-0.01	0.22
Châtelaillon	64	54	84	-0.17	0.23
Esnandes	26	26	100	0.15	0.21
La Rochelle	111	86	77	-0.43	0.52
L'houmeau	18	17	94	-0.14	0.16
Marans	7	6	86	-0.02	0.17
Marsilly	18	17	94	-0.06	0.22
Nieul	37	35	95	0.03	0.16
Saint Ouen d'aunis	1	1	100	0.00	0.00
Villedoux	2	2	100	-0.04	0.04
Yves	53	53	100	-0.03	0.16
Total	**451**	**409**	**91**	**-0.11**	**0.26**

V. CONCLUSIONS

With the inaccuracies on the initial data which have a direct influence on overflow volumes entering on the land part of the model:

- Precise topography of the crest of the existing protections before the event,
- Chronology of the failures in the works of protection during the storm,
- And if we taking in account:
- The fact that the model cannot represent very local hydraulic effects in the disturbed areas (walls, water level in buildings ...).
- Inaccuracies (reliability) on some water marks,

All of the analyses conducted and detailed in the preceding paragraphs are sufficient to consider the model calibrate and valid for the representation of hydro meteorological events generating very high water levels in the Pertuis as well as the representation of the dynamic submersions on land side.

This model could be now used to test some reference events based on Storm Xynthia but also with a rise of sea level due to climate change.

REFERENCES

[1] J.M. Hervouet, Hydrodynaics of Free Surface Flows – modelling with the finite element method, John Wiley & Sons, Ltd, 2007.

[2] EurOtop Die Küste, Archive for Research and Technology on the North Sea and baltic Coast, Wave Overtopping of Sea Defences and Related Structures: Assessment Manual, Heft 73, Jahr 2007, Herausgeber: Kuratorium für forschung im Küsteningenieurwesen.

[3] Eléments de mémoire sur la tempête Xynthia du 27 et 28 Février 2010 en Charente Maritime, Rapport d'étude Artelia pour la Direction Départementale de Territoires et de la Mer de la Charente-Maritime, Aout 2010, unpublished

Study for the hydraulic framework of the lower course of Piave river (Italy)

Andrea GARZON
Hydraulic Engineering Research Department
CREA TECHNOLOGY Srl
Corso Milano, 9, 37138 – Verona (Italy)
aGarzon@creaurl.it

***Abstract*— The hydraulic study was designed to evaluate the hydrodynamic characteristics of Piave river (Venetian Region, Italy), studying deeply the hydraulic safety thematic of the lower course of the river, in order to define the existing conditions and eventually propose a new framework for the estuary configuration. To perform the study was used the particularly advanced two-dimensional finite element mathematical model TELEMAC-2D coupled with MEFH, developed by CREA, currently used by Consorzio Venezia Nuova for the regulation of mobile gates of MOSE. The lower course of Piave river has been accurately modeled in a adequate information system GIS inside Microstation CAD. At first the model has been tested to reproduce the analytic solution found in the case of a prismatic one dimensional channel, representing schematically the actual lower course of Piave river. Then the model has been applied, among other things, to simulate the effects of an important flooding of Piave river, which occurred during the period from 25th to 29th November 2002. Experimental measurements of the maximum levels and the same historic articles of the time fully confirm the results of this model, describing in a timely and precise curve the maximum levels obtained from the model results. Due to these results, the Venetian Region has requested a revision of the existing embankment altimetry for the safety of the territory. The results provided by the model, in fact, did not have agreement with those inferred from previous studies, which analyzed the same flooding event. In our opinion one of the most important problems to solve in order to obtain meaningful results from this kind of applications is to previously determine the flow pattern by the modeller, characterised by the equipotential and stream lines, then schematising the same by using the finite element mesh.**

I. INTRODUCTION

The Administration of Jesolo Municipality (VE) has entrusted the company Crea Srl a specialist professional task to realise a hydraulic study for the configuration of the estuary of Piave river in Jesolo Municipality.

To perform the study was used a 2D finite element mathematical model particularly advanced, able to solve the equations governing the water movement in 2D hydrodynamic systems using the most appropriate numerical methods in relation to the complexity of the actual hydrodynamic conditions.

In particular, the company CREA thanks to the experience gained through the development of its own 2D hydrodynamic finite element mathematical model MEFH, currently used by Consorzio Venezia Nuova's Information Service relating to the implementation and maintenance of CRUP system and by Consorzio Venezia Nuova for the assessment of hydrodynamic and dispersive effects produced by MOSE mobile barriers, has taken over and adapted to the purposes of the study the 2D finite element mathematical model TELEMAC-2D, in turn developed by a group of experts led by Jean Michel Hervouet of the French company Sogreah [16] [17] [18] [19], integrating and supplementing it with their own model [10] [11] [12] [13].

The developed software, which we called TelmH2D, is a mathematical model particularly advanced and devoted to study specifically the hydrodynamics of rivers, gathering all the bathymetric and hydraulic information of the finite elements of the mesh in a interactive development environment Microstation, in which the real physical system of Piave river, from the town of Zenson to the town of Cortellazzo, located at the river estuary, has been faithfully modeled with the necessary care to represent each particular discontinuity of the real physical system.

In the preliminary phase the model was tested in the case of a prismatic horizontal channel equivalent to the real Piave river, comparing the results provided by the model with those relating to a known analytical solution.

Subsequently, the attention has been devoted to investigate the critical flood wave propagation of the period since 25th to 29th November 2002, critically rebuilt by examining some of the studies previously realised.

II. THE MATHEMATICAL MODEL

TELEMAC-2D is an ideal modelling framework for the river environment due to its finite element grid which allows graded and refined mesh resolution. The model is based on the shallow water Saint-Venant equations of momentum and continuity, derived from the Navier-Stokes equations by taking the vertical average. A hydrostatic assumption is valid in this application where bed slopes are small and, hence, vertical accelerations caused by the pressure are balanced by gravity. The shallow water equations are solved either in a fully coupled mode or with the help of a wave equation, depending on the option chosen. Several advection schemes

are available depending on the type of flow. One of the most interesting and key features of TELEMAC-2D, characterising it from all the other finite element mathematical models, is the consideration of the characteristic method in order to solve the most difficult part of the Saint Venant equations, i.e. the non-linear advection terms. Other options include the streamline-upwind Petrov-Galerkin scheme (SUPG), in the conservative and non-conservative forms, and residual distributive schemes such as the N-scheme and PSI-scheme. TELEMAC-2D solves the turbulence model with four different methods, i.e. the classical $k-\varepsilon$ model, Elder, Smagorinski and constant isotropic diffusion. The matrix-storage in TELEMAC is edge-based and several linear solvers are available in the BIEF library, including conjugate gradient, conjugate residual, CGSTAB and GMRES solvers. TELEMAC-2D is fully parallelised using MPI.

CREA company has integrated this formidable software TELEMAC-2D with another finite element mathematical model, MEFH, developed by the same company to study the Venice lagoon hydrodynamic problems. Among the other, in MEFH is used a different method to assign the boundary condition to closed boundaries. MEFH routines, written in F90 like the main code TELEMAC-2D, have been added and linked, assembling the new model, called by the company TelmH2D.

This approach has given the possibility to use the interactive environment developed for the Venice lagoon inside Bentley Microstation CAD to create the input data GIS and the output for the model results. The preprocessor PreM2d to the data and the postprocessor PstM2d for the model results, also developed by Crea Company, were used to manage the interactivity with the user.

III. THE LOWER COURSE OF PIAVE RIVER

The lower course of Piave river, between Zenson del Piave (TV) and Cortellazzo (VE), has different characteristics along the river course.

The most meandering part is comprised between the towns of Zenson and San Donà along a reach equal to about 14 [Km], where the width of the watercourse is reduced to less than 100 [m] (Fig. 1). At the same time, the overall width of the hydraulic section varies between 250 and 1000 [m], due to large alluvial expansions following the main course of the river. Downstream San Donà till to Eraclea, for a reach equal to about 10 [Km], the Piave river follows a straight path and its cross section has a width practically constant, around 100 ÷ 130 [m] (Fig. 2). The river is enclosed between embankments rising about 4 to 5 [m] over the surrounding land while the river bed is, on average, about 10 [m] deep respect to the embankment plan, occupying the greater part of the liquid section. From the bridge of Eraclea to the estuary at Cortellazzo, for a distance approximately equal to 9 [Km], the river course again assumes a meandering path, characterised by enlargements of the section in the last meanders (Fig. 3).

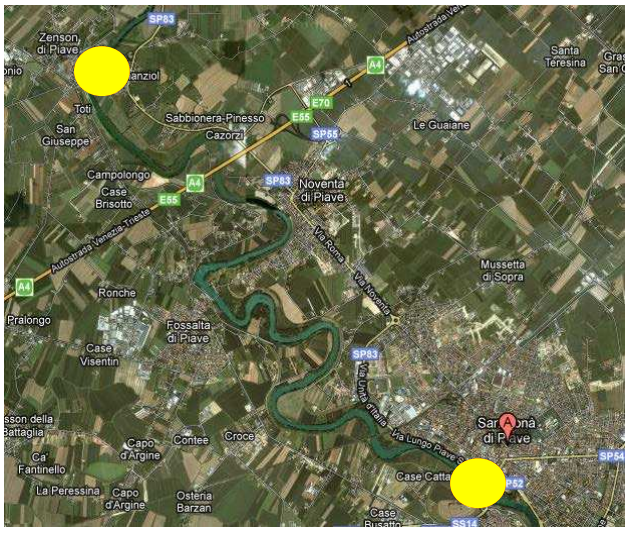

Figure 1. Piave river between Zenson and San Donà. It may be noted both the meandering path, both the large areas of floodplain between the embankments of the watercourse.

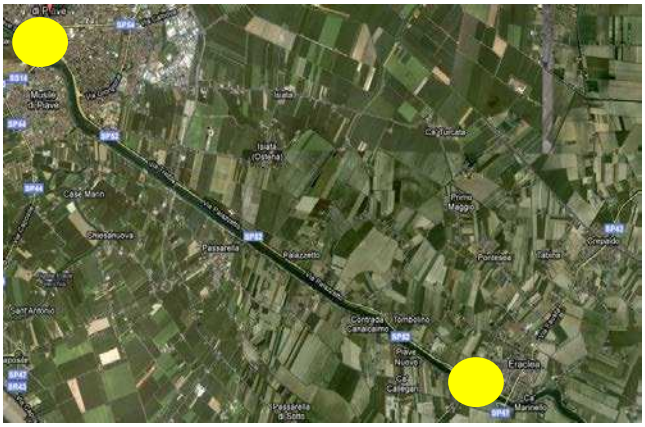

Figure 2. Piave river between San Donà and Eraclea. The river is straight without alluvial zones.

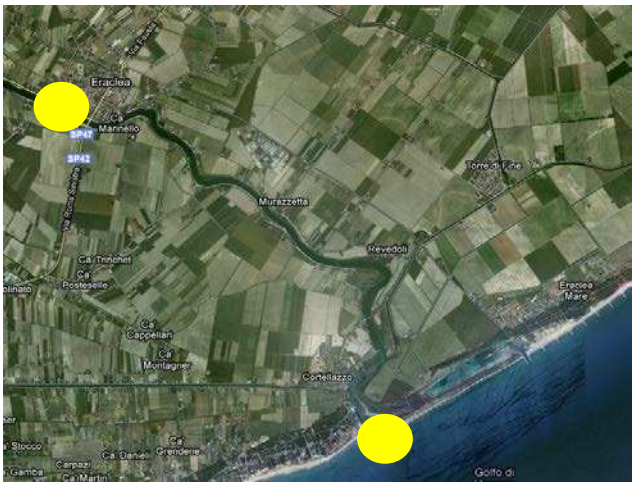

Figure 3. Piave river between Eraclea and the mouth of Cortellazzo.

Shortly before the mouth, at Cortellazzo (VE), Piave river is connected to the Venetian coastline waterway through two navigation locks currently disused and opened. The waters of Piave river can then penetrate freely in the watercourses of the channels Revedoli, on the left bank, and Cavetta, on the right one.

IV. CASE STUDY I: EQUIVALENT PIAVE RIVER

In order to assess the accuracy of the mathematical model, TelmH2D has been applied to the case of a schematic channel able to represent Piave watercourse.

To achieve this goal, the first step has been to evaluate either the volume with respect to the sea level, either the liquid surface and the length of Piave watercourse from Zenson and the mouth. The watercourse of Piave river has a total volume under the sea level approximately equal to 14104800 [m3], a liquid surface totalling 3235700 [m2] and a length of about 33600 [m], corresponding to an average width equal to 97.30 [m] and a mean depth equal to 4.539 [m]. To represent the watercourse has been assumed, then, a rectilinear schematic channel of length equal to 33000 [m], width 100 [m] and horizontal bottom. Since the liquid surface is, in this case, equal to 3300000 [m2], the equivalent depth has been evaluated equal to 4.274 [m].

The schematic channel has been, therefore, represented by a finite element mesh consisting of four flow tubes, each of width equal to 25 [m]. The length of the elements, in the direction of flow, has been assumed to be equal to 100 [m]. The Strickler roughness of the channel has been assumed to be 35 [$m^{1/3}/s$].

The initial part of the channel is represented in Fig. 4. The schematic outline of the channel needed 2640 finite elements corresponding to 1655 nodes.

The hydrograph imposed at the upstream section of the watercourse is represented in Fig. 5. The hydrograph reproduces, in its rising phase, the catastrophic flood event of 3-5 November 1966. After reaching the maximum value of 3740 [m^3/s], the flow was kept constant to determine conditions of permanent motion in the channel.

The level at the downstream section of the channel has been kept constant at a height of 1.00 [m] over the sea level.

In the schematic channel, then, some control points have been placed at a mutual distance of 5500 [m]. An upstream section PIAVE INP has been identified, together with five intermediate sections PIAVE 01, PIAVE 02, PIAVE 03, PIAVE 04, PIAVE 05 and, finally, the downstream section PIAVE OUT. A cross section, PIAVE MAIN, which runs throughout the axis of the channel, has also been introduced to derive the water level profiles in different moments of the simulation.

In Fig. 6, where the velocities at all control points are shown, one can observe the extremely high velocity (almost 7 [m/s]) that appears at the mouth of the channel, section PIAVE OUT.

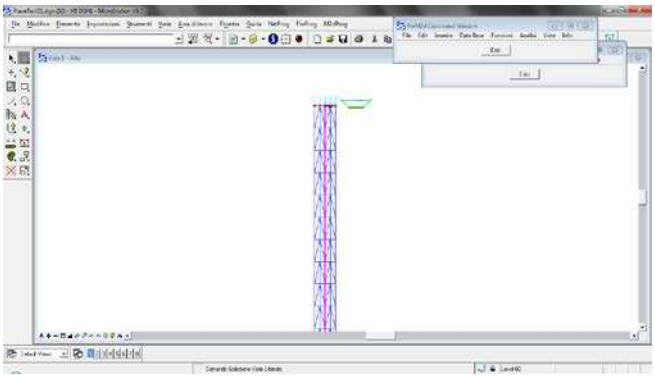

Figure 4. The lower course of Piave river has been schematised by an equivalent prismatic channel having length 33000 [m], width 100 [m] and depth 4.274 [m]. The channel mesh has been represented by four flow tubes of finite elements, each of width equal to 25 [m] and length 100 [m].

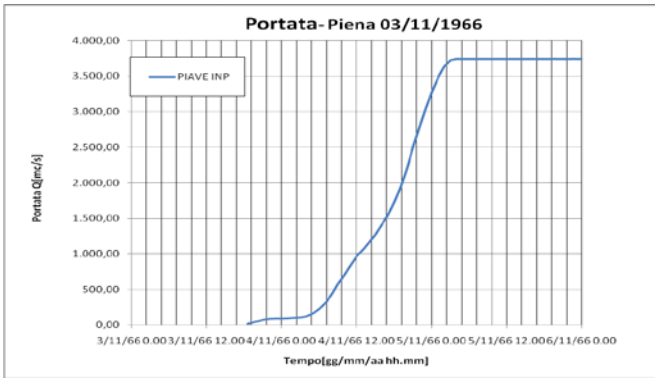

Figure 5. Hydrograph at the upstream section of the schematic channel, reproducing in its rising phase the flood event of 3-5 November 1966. After reaching the maximum capacity of 3740 [m^3/s], the flow has been kept constant to determine conditions of permanent motion in the channel.

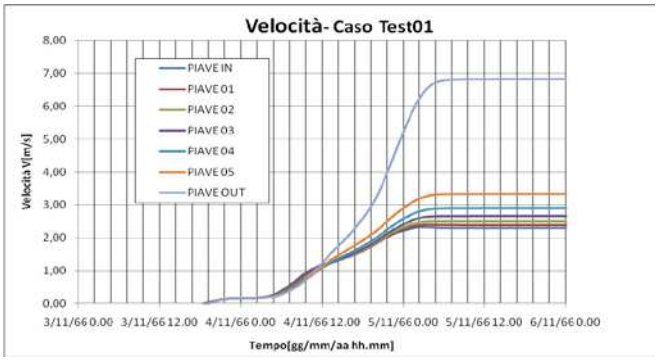

Figure 6. Velocities calculated by the model corresponding to the control sections arranged along the channel at a distance of 5500 [m]. One can observe the extremely high velocity (almost 7 [m/s]) appearing in the section at the mouth of the channel PIAVE OUT.

The shown test case of the schematic channel, with average characteristics similar to the lower course of Piave river from Zenson to the mouth, assumes a very special importance not only because it provides information relating to an extreme event for the river but, above all, because it is

possible, in the permanent motion conditions achieved during the terminal phase of the simulation, to compare the solution provided by the model with that one obtained analytically by solving, directly, the Saint Venant equations.

To calculate the analytical solution on considers, then, the specific energy E associated to a generic section of the channel, relating to the sum of kinetic and potential energies:

$$E = Z_f + h + \frac{v^2}{2g} \tag{1}$$

where Z_f is the bottom altitude [m], h the water depth [m], v the water velocity [m/s] and g the gravitational constant [m/s^2].

The momentum conservation equation allows writing, then, the following relation:

$$\frac{\partial E}{\partial x} = -J \tag{2}$$

being J the continuous energy loss according to Chézy formula:

$$J = \frac{v^2}{C^2 R_h} \tag{3}$$

in which C is the Chézy coefficient [m$^{1/2}$/s] and R_h the hydraulic radius [m].

In the case of a large rectangular section, in which the hydraulic radius R_h is almost equal to the water depth h, and considering the Strickler formula $C = k_s R_h^{1/6}$ on obtains:

$$J = \frac{Q^2}{B^2 k_s^2 h^{10/3}} \tag{4}$$

where Q is the flow [m^3/s], B the channel width [m] and k_s is the Strickler friction coefficient [m$^{1/3}$/s].

Since in the prismatic channel with horizontal bottom Z_f is constant, therefore its derivative along the x-axis of the channel is null. Then we have:

$$\frac{\partial E}{\partial x} = \frac{\partial h}{\partial x} + \frac{Q^2}{2gB^2}\frac{\partial}{\partial x}\left(\frac{1}{h^2}\right) = \frac{\partial h}{\partial x} - \frac{Q^2}{gB^2}\frac{1}{h^3}\frac{\partial h}{\partial x} = \left(1 - \frac{Q^2}{gB^2 h^3}\right)\frac{\partial h}{\partial x} \tag{5}$$

Substituting (5) and (4) in (2) one obtains:

$$\left(1 - \frac{Q^2}{gB^2 h^3}\right)\frac{\partial h}{\partial x} = -\frac{Q^2}{B^2 k_s^2 h^{10/3}} \tag{6}$$

directly integrable, by separating the variables, from $P_0(0, h_0)$, being $h_0 = 4.274 + 1.000 = 5.274$ [m], to $P(x, h)$:

$$\int_{h_0}^{h}\left(\frac{Q^2}{gB^2 h^3} - 1\right)\frac{B^2 k_s^2 h^{10/3}}{Q^2}dh = \int_0^x dx \tag{7}$$

Executing the integration of (7), after few simple analytical steps here omitted, on obtains the following expression, which provides the theoretical solution of the problem:

$$3k_s^2\left[\frac{1}{4g}\left(h^{4/3} - h_0^{4/3}\right) - \frac{1}{13}\frac{B^2}{Q^2}\left(h^{13/3} - h_0^{13/3}\right)\right] = x \tag{8}$$

In Fig. 7 is shown the comparison between the theoretical solution, expressed by (8), and the results provided by the model TelmH2D, relating to the depth h of the profile PIAVE MAIN. From this comparison between the theoretical solution and that provided by the model, one may observe the accuracy of the results obtainable by the application of TelmH2D to 2D hydrodynamic systems.

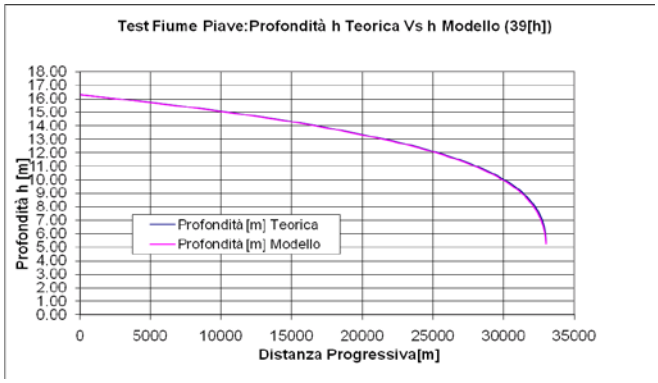

Figure 7. Comparison of the theoretical solution (8) and the results provided by the model TelmH2D relative to the water depth profile for a schematic channel equivalent to the Piave watercourse between Zenson and the mouth. For the design of the prismatic channel the liquid surface, the volume andthe total length of Piave between Zenson and the mouth have been conserved. The comparison shows the precision obtainable using the model in case of 2D hydrodynamic systems.

V. CASE STUDY II: LOWER COURSE OF PIAVE RIVER

A. Schematisation of topo-bathymetric plan

Relating to the topo-bathymetric data affected by the study, the High Adriatic Sea Authority (VE) has made available its DEM database, with its orthophotos, taken over in 2004.

The grid was then imported not only verifying the exact location of the spatial data, but assigning, at each point, a default colour connected to a specific locally graduated scale. Local reference for the colour allocation, where individual cells of the grid corresponding to a single ASCII file have referred, was related to the local average altitude computed in advance for the same ASCII file. Applying this methodology

it was possible not only to rebuild the entire topo-bathymetric plan, but also take advantage of specific colour references to determine barriers and embankments along the river, then essential information which was found at the time of designing the finite element mesh.

The detail of the reconstruction of the topo-bathymetric plan of Piave river basin from Zenson to San Donà is shown in Fig. 8.

B. Finite element schematisation

The most important problem to obtain meaningful results from the applications of mathematical models is to determine the mean size, and thus the number of finite elements, to be used in the schematisation of hydrodynamic system.

In particular, two conflicting requirements collide: the first is to increase, as far as possible, the size of finite elements and decrease the number of the nodes with which the solution is calculated, to not excessively burden the required computational effort; the second is to increase the number of finite elements and of the calculation points, to simulate with more detail and precision the situation of the watercourse, taking into account also that, at least from a theoretical point of view, there is no lower limit to the size of finite elements.

In the quest to simultaneously meet both the needs the Piave river, between the sections of Zenson del Piave and the mouth of Cortellazzo, aside from Cavetta and Revedoli channels, was schematised by about 3600 triangular finite elements, corresponding to a scatter of over 2200 nodes (Fig. 9).

In particular, the whole fluvial course was schematised by four flow tubes, corresponding to the mainstream, as well as other two partially submergible flow tubes, corresponding to the banks of the Piave river.

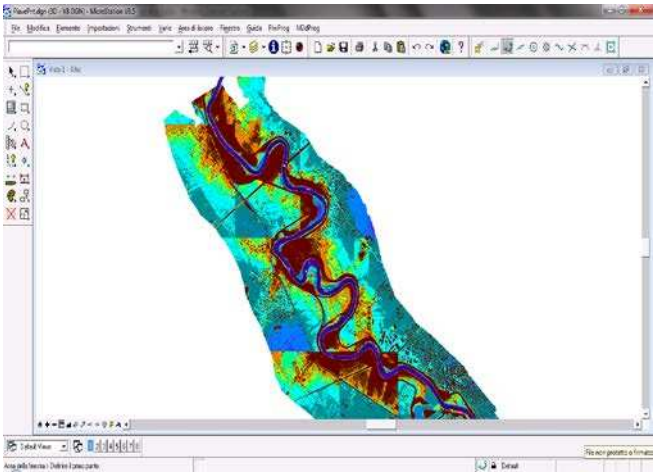

Figure 8. Detail of the reconstruction of the topo-bathymetric plan of Piave river basin from Zenson to San Donà derived from the ASCII files in ESRI GRID format. It can be seen both the meandering path of Piave river and the large alluvial areas comprised between the river embankments.

Particular attention has been paid to the schematisation of all alluvial areas existing along the river, either in the initial part of the river, between the towns of Zenson and San Donà and, especially, in the final part at Cortellazzo (Fig. 10), an area of particular interest to this study. In these areas has been sought, with careful examination, the alleged texture of the flow field that is established in critical condition of flow, dividing the same flow field in flow tubes through the preliminary identification of any current and equipotential lines.

C. Hydrological flood event of 2002

The event of 2002 did not result in a real flood, despite having constituted much more than just an emergency. In fact, in the period 25/11/2002-29/11/2002 the water level of

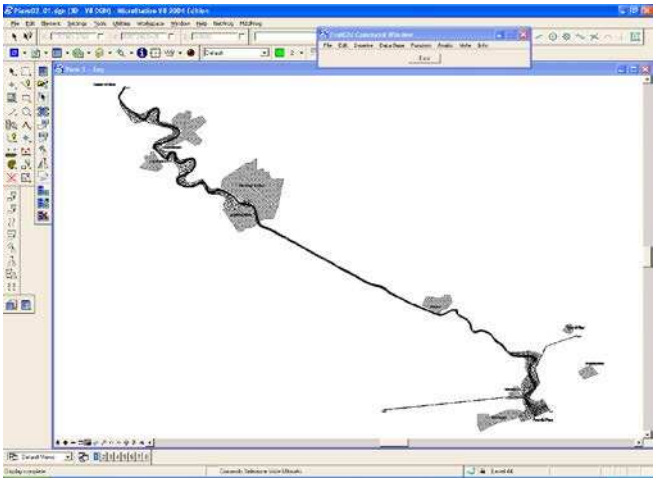

Figure 9. Schematisation of Piave river. The Piave river, between the sections of Zenson del Piave and the mouth of Cortellazzo, aside from Cavetta and Revedoli channels, was schematised by about 3600 triangular finite elements, corresponding to a scatter of over 2200 nodes

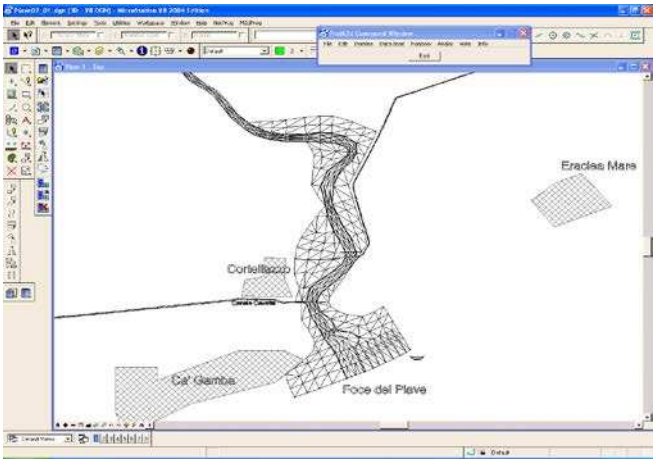

Figure 10. Schematisation of Piave river in the area of Cortellazzo. A particular attention has been devoted to the alluvial area schematisation, individuating the alleged texture of the flow field established in critical condition of flow and dividing the same field in flow tubes through the preliminary identification of any current and equipotential lines.

Piave river has raised to almost lick the summit portion of the banks of the river, causing great alarm for the whole population.

The flood of the period in question was preceded, inter alia, by another significant flood event, with the peak day 20/11/2002, which helped to soak and further weaken the banks of the river.

Since in relation to this flood event the hydrographical section of Busche (BL) has remained in complete efficiency, the flow of the watercourse has been adequately monitored and measured, constituting a reliable boundary condition for the mathematical model. A graph relative to the flow at Zenson del Piave, the upstream section of the model, is shown in Fig. 11.

In relation to the same event, the concomitant level tide in the Adriatic Sea has been applied as boundary condition at the mouth of Cortellazzo.

Strickler friction coefficients k_s have been assumed 35 [$m^{1/3}$/s] for the main channel finite elements, 25 [$m^{1/3}$/s] for bank elements and 20 [$m^{1/3}$/s] for alluvial elements.

To execute the simulation by means of TelmH2D, particular options regarding the algorithms allowed by the model have been applied. The most relevant are:

- the system of equations were coupled;
- the water depth h was solved using the SUPG in the conservative form, without unwinding operations;
- the velocities u and v were solved using the characteristics method with the modified SUPG method;
- the turbulence model was the Elder one;
- the flooding and dry process for alluvial areas was the level gradient method;
- the used solver was the generalised residual method.

The model has been run in Microstation CAD environment, using the pre-processor and the post-processor developed by CREA.

In Fig. 12, as an example, it is shown the velocity field and the contour lines for elevation in a particular instant, 58 [h] since the beginning of the simulation, at the mouth of Cortellazzo.

The application interest is not distributed evenly across the whole flood event simulated but is concentrated in the period between the days 25/11/2002 and 29/11/2002, in which Piave river has actually risked to overflow and to flood the surrounding land.

To assess the flood propagation effects along the course of Piave river between Zenson and the mouth on considers, with a single image, all levels connected together in a unitary overall profile in the different instants of flood phenomenon.

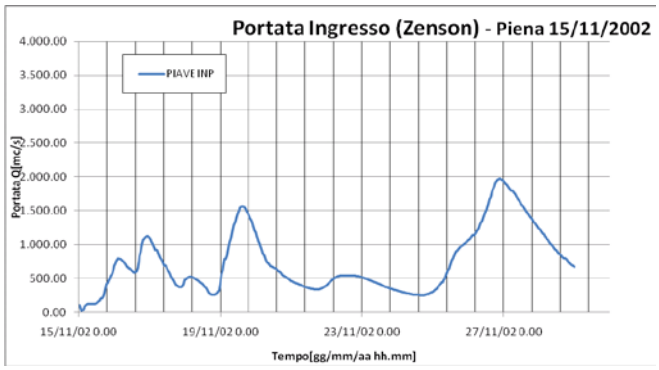

Figure 11. Graph relative to the flow at Zenson del Piave, the upstream section of the model, in the period 15/11/2002-29/11/2002.

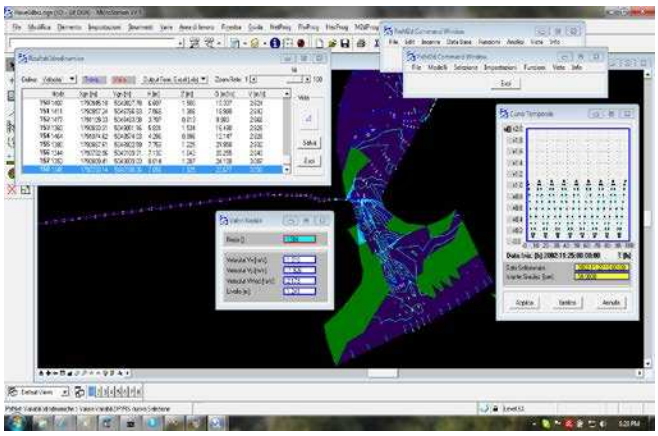

Figure 12. Microstation CAD environment to show model's results. As an example, it is shown the velocity field and the contour lines for elevation in a particular instant 58 [h] of the simulation at the mouth of Cortellazzo.

In Fig. 13 these profiles are detected with an interval of 4 [h] since the beginning of the simulation November 24th, 2002 at 24 [h].

It may be noted that, according to the realised hydrodynamic finite element model, the maximum level of the flood wave is approximately equal to 10.68 [m] at Zenson after 48 [h] from the beginning of the simulation.

The most interesting phenomenon appears near the mouth, where the water level shows a sudden decrease in proximity of the mouth itself, at the point where Piave river connects, on the right bank, the Cavetta channel. This result could be foreseen by observing the graph of Fig. 7 relative to the profile of the depth in the case of a schematic channel.

In Fig. 14 it is shown the plot of the maximum level envelope provided by the model during the flood event of 25-29 November 2002 along the Piave River between Zenson and Cortellazzo.

By analysing the profile of the maximum level envelope shown in Fig. 14, resulting from the application of the 2D finite element hydrodynamic model, it appears near the mouth, where it detaches, on the orographic right, the Cavetta channel, a sharp decrease of the level. The results obtained

Figure 13. Profiles of the levels along Piave River between Zenson and Cortellazzo, detected, with an interval of 4 [h], since the beginning of the simulation November 24th, 2002 at 24 [h]. It may be noted that, according to the realised hydrodynamic finite element model, the maximum level of the flood is equal to 10.68 [m] at Zenson 48 [h] from the beginning of the simulation. It can be seen that the levels decrease sharply only near the mouth, even downstream of Cavetta channel placed at only 1300 [m] from the sea mouth of Piave river.

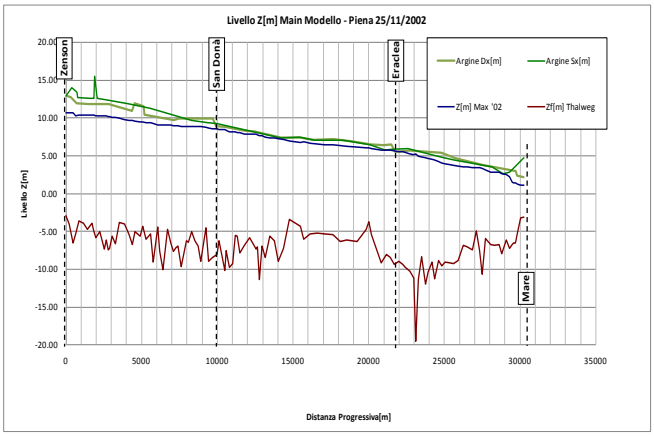

Figure 14. Plot of the maximum levels' envelope during the flood event of 25-29 November 2002 along the Piave River between Zenson and Cortellazzo, provided by the finite element hydrodynamic model. The results obtained by means of the model TelmH2D show a rapid decrease in the free surface at the point where it detaches, on the right bank, the Cavetta channel. The narrowing of the section in that point of the river supports an increase in the hydrometric levels throughout the course of the river, until to Zenson. The profile obtained from the application of this model shows both the attainment of the top of the bank at Eraclea, both the need to raise the embankment in this tract of embankment with sandbags to protect the town, both the situation of great alarm and emergency throughout the whole Sandonatese and, in general, for all the lower course of Piave river, including Jesolo, as confirmed by the chronicles of the time.

by the application of TelmH2D model confirm that the narrowing of the section at that point of the watercourse supports an increase in the hydrometric level throughout the course of the river, until to Zenson.

As there were no precise measurements on water levels reached along the river embankments, we report, as factual evidence, two articles appeared in the Gazzettino of Venice the 28/11/2002, one of which written by G. Bedin. At least the macroscopic effects on the territory, the attainment of the top embankment at Eraclea, the intervention of the Civil


Data: giovedì 28.11.2002
IL GAZZETTINO
Estratto da Pagina: 4
Il Piave è straripato ad Eraclea, tra Fossalta e Noventa è un lago di fango

Figure 15. 'Il Piave è straripato a Eraclea' ('The Piave river burst its banks at Eraclea'). Article published on Gazzettino of Venice, 28.11.2002 p. 4 which shows the flooding of the Piave River at Eraclea without causing serious damage.


Data: giovedì 28.11.2002
IL GAZZETTINO Venezia
Estratto da Pagina: 6
Allarme nella notte, il Piave esonda a Eraclea
Il parco fluviale si trasforma in un lago di fango, chiusi i sottopassi, tre famiglie evacuate a Fossalta e Noventa

Figure 16. ''Il Piave esonda a Eraclea' ('The Piave river overflows at Eraclea'). Article published on Gazzettino of Venice, 28.11.2002 p. 6 by Gianfranco Bedin. The article describes the profile of the maximum levels provided by the model TelmH2D of Fig. 14 as better it couldn't. The profile obtained from the application of this model, in fact, shows both the attainment of the top of the bank at Eraclea, both the need to raise the embankment in this tract of embankment with sand bags, both the situation of great alarm and emergency for all the Sandonatese and, in general, for all the lower course of Piave.

Protection and the sensations caused by that event on the population appear clarified.

VI. CONCLUSIONS

The model TelmH2D has been used to study the hydraulic framework of the lower course of Piave river (Italy). This model consists by coupling two 2D finite element models, the first TELEMAC-2D, extremely powerful, versatile to solve hydrodynamic and dispersive problems in the case of rivers, the other MEFH developed by CREA in the case of the Venice lagoon.

This coupling has given the possibility to use the interactive environment developed by CREA for the Venice lagoon inside Bentley Microstation CAD to create the input data GIS and the output for the model results. The pre-processor PreM2d to the data and the postprocessor PstM2d for the model results, also developed by Crea Company, were used to manage the interactivity with the user.

At first the model TelmH2D has been tested in the case of a prismatic channel having characteristics equivalent to the real lower watercourse of Piave river. After having found an analytical solution for this simple case in permanent motion conditions, the model results have been compared obtaining a perfect approximation of the same solution.

Subsequently the model has been applied to simulate the hydrological flood event of the period 25/11/2002-29/11/2002. During this event the water levels of Piave river have raised to almost lick the summit portion of the banks of the river, causing great alarm for the whole population.

This study has achieved an important result. Before this study it was believed that Piave river could transport a discharge near to or more than 3000 [m^3/s]. These, in fact, were the conclusions obtained by the previous researches realised to analyze the hydraulic behaviour of Piave river.

On the other side we have to remember, also, that this river was responsible, in November 1966, of a very catastrophic flooding event for its entire basin, with great damages and many deaths.

On the contrary, this study demonstrates, unequivocally, that the maximum value of the flow that can be transported by the lower course of Piave river is 2000 [m^3/s], diminishing a lot the return time for the river flooding and, at the same time, increasing the need for action to prevent further catastrophic events.

As a result of our experience we believe that, in order to obtain good results from the application of mathematical models, two components are necessary, both extremely important.

The first one is naturally constituted by the need to use a mathematical model of an undoubted quality as TELEMAC-2D, which, for example, is able to solve the nonlinear terms of the hydrodynamic two-dimensional shallow water equations with the most appropriate method of the characteristic curves.

The second, fairly important in our experience, is tied to the design of the finite element mesh, which must be able to follow the cross linked flow constituted by the orthogonal curves of the current and equipotential lines, a priori identified by the skilful designer engineer.

ACKNOWLEDGEMENT

This work was founded through the Jesolo Municipality (VE), to which manager Dr. Gianni Favaretto go in particular our thanks. We are pleased to thank also Dr. Francesco Maicu for his support. Secondly, we thank the High Adriatic Sea Authority (VE) which has made available its DEM database, with its orthophotos, taken over in 2004, and has given its kind readiness in the different phases of the work.

REFERENCES

[1] Autorità di Bacino dei fiumi Isonzo, Tagliamento, Livenza, Piave, Brenta-Bacchiglione, “Bacino del Fiume Piave – Piano Stralcio per la Sicurezza Idraulica del Medio e Basso Corso”, Comitato Tecnico, 2000.

[2] Autorità di Bacino dei fiumi Isonzo, Tagliamento, Livenza, Piave, Brenta-Bacchiglione, “Bacino del Fiume Piave – Progetto del Piano Stralcio per la Sicurezza Idraulica del Medio e Basso Corso”, Comitato Tecnico, 2000.

[3] Bates P.D., Stewart M.D., Siggers G.B., Smith C.N., Hervouet J.M. e Selin R.H.J., ”Internal and external validation of a two-dimensional finite element code for river flood simulations“, Proceedings of the Institutions of Civil Engineers, Water, Maritime and Energy, vol. 130, pg. 127-241,1998.

[4] Bates P.D., Anderson M.G., Hervouet J.M., ”Computation of a flood event using a two-dimensional finite element model and its comparison to field data“, Modelling of Flood Propagation Over Initially Dry Areas, American Society of Civil Engineers, New York, pg. 238-248, 1994.

[5] Brooks A.N., Hugues T.J.R., ”Streamline Upwind Petrov Galerkin Formulations for Convection Dominated Flows with Particular Emphasis on the Navier-Stokes Equations“, Computer Methods in Applied Mechanics and Engineering. pg. 199-259, 32, 1982.

[6] D’Alpaos L., Defina A., “Modellazione matematica del comportamento idrodinamico di una zona di barene solcate da una serie di canali minori”. Istituto Veneto di SS.LL.AA., volume XII, Venezia 1995.

[7] D’Alpaos, Ipros S.r.l., “Studio finalizzato al riconoscimento delle aree di pertinenza idraulica e di sicurezza idraulica lungo il Piave a valle di Nervesa della Battaglia, mediante modello matematico bidimensionale”, Autorità di Bacino dei fiumi Isonzo, Tagliamento, Livenza, Piave, Brenta-Bacchiglione, 1997.

[8] Defina A., D’Alpaos L., Matticchio B., “A new set of equation for very shallow water and partially dry areas suitable to 2D numerical models”. Proceedings of Modelling of Flood Propagation Over Initially Dry Areas, ASCE Eds., Milano 1994.

[9] D’Alpaos, Dipartimento IMAGE Università di Padova, “Modello matematico bidimensionale per lo studio della propagazione delle piene nel fiume Piave tra Macchietto e la foce”, Autorità di Bacino dei fiumi Isonzo, Tagliamento, Livenza, Piave, Brenta-Bacchiglione, 2008.

[10] Garzon A., ”Taratura e calibrazione del modello idrodinamico 2-D agli elementi finiti“, Consorzio Venezia Nuova, Crea s.r.l., Gennaio 1995.

[11] Garzon A., Cecconi G., ”A Two Dimensional Semi-Implicit Finite Element Model for Tidal Propagation in the Venice Lagoon”, Proceedings of the Ninth International Conference on ”FINITE ELEMENTS in FLUIDS, New Trends and Applications”, Venezia, 15-21 Ottobre 1995.

[12] Garzon A., “Deformazione dell’onda di marea astronomica nella laguna di Venezia con l’utilizzo del modello matematico bidimensionale agli elementi finiti”, Consorzio Venezia Nuova, Crea srl , 1997.

[13] Garzon A., Tommasi E., “Fornitura di supporto tecnico alle attività di aggiornamento della schematizzazione del modello agli elementi finiti con le ultime rilevazioni batimetriche del 2000”, Consorzio Venezia Nuova, Crea srl, Aprile 2004.

[14] Ghetti A., Berti L., Scardellato E., “Studio per la sistemazione del Piave a difesa dalle piene”, Provincia di Treviso, 1970.

[15] Goutal N. , “Résolution des équations de Saint Venant en Régime transcritique par une methode d’élément finis. Application aux bancs decouvrants”, Thèse de doctoract de l’Université Paris VI.

[16] Hervouet J.M., ”Vectorisation et simplification des algorithmes en elements finis“, E.D.F. Bulletin del la Direction des Etudes et Recherches. Serie C, Mathematiques, Informatique, pg. 1-37, 1991.

[17] Hervouet J.M., ”Characteristiques and mass-conservation. New developments in Telemac-2D“, Rapport E.D.F. HE-43, 1992.

[18] Hervouet J.M.,”Telemac-2D. Version 3.0: Principle Note“, Sogreah, 2000.

[19] Hervouet J.M.,”Telemac-2D. Version 5.0: Validation Document“, Sogreah, 2000.

[20] Ministero dei Lavori Pubblici - Magistrato Alle Acque - Nucleo Operativo di Treviso - “Progetto di interventi straordinari di regimazione idraulica in alcuni tratti d’alveo riguardanti il fiume Piave”, Treviso, 1994.

[21] Rastogi A.K., Rodi W., ”Predictions of Heat and Mass Transfer in Open Channels“, Journal of the Hydraulics Division, ASCE, n. HY3, pg. 397-420, 1978.

[22] Tonini D., “Le piene nel Veneto, Friuli-Venezia Giulia nel novembre 1966”, Accademia Naz. dei Lincei - Quad. N.112: Atti del conv.: “Le scienze della natura di fronte agli eventi idrogeologici”, Roma, 1967.

[23] Ufficio Idrografico del Magistrato alle Acque di Venezia, “Piano di bacino del Piave - Fase conoscitiva 1° lotto - 3.1 Idrologia e climatologia - Relazione”, CBP Consorzio Bacino Piave, 1986.

[24] Zollet Ingegneria S.p.A., Studio Sicem S.r.l., “Indagine sulle portate massime convogliabili dall’asta principale del fiume Piave ai fini della difesa idraulica e valutazione dell’efficacia di interventi di moderazione delle piene - Prima fase”, Autorità di Bacino dei fiumi Isonzo, Tagliamento, Livenza, Piave, Brenta-Bacchiglione, 1993.

Testing TELEMAC-2D suitability for tsunami propagation from source to near shore

Alan COOPER, Giovanni CUOMO, Sébastien BOURBAN,
Michael TURNBULL, David ROSCOE
HR Wallingford Ltd
Wallingford OX10 8BA, UK
a.cooper@hrwallingford.com

***Abstract*—When a tsunami has a large source area it may be the case that important wavelengths of the resulting tsunami wave are in the shallow water domain (i.e. wavelength is greater than 20 times the water depth). In this case TELEMAC-2D should be suitable. If shorter wavelengths are important then the best approach could be to use TELEMAC-3D non-hydrostatic.**

TELEMAC-2D should be tested for ability to model wave propagation correctly as well as diffraction and refraction phenomena. In this case, it is not expected that the inundation behaviour will be represented in the same model as the propagation to near shore is modelled using the wave equation formulation in TELEMAC-2D and the inundation phase (if required) will use the finite volume (kinetic scheme) in TELEMAC-2D.

So it is important to find analytical or laboratory test cases that are within the shallow water equations' limit of validity. Some such test cases have been identified and the performance of TELEMAC-2D in comparison is presented in this paper.

I. INTRODUCTION

To be used for tsunami propagation modelling it is important that a flow model be able to propagate waves a long way across oceans with small energy dissipation, especially where the wave is of small amplitude in great water depth. It should also be able to refract waves under conditions of varying water depth and diffract around structures and islands. It should evolve the wave shape correctly in going into shallower water.

TELEMAC has many possible options for the modelling of tsunami propagation. For example, TELEMAC-2D wave equation formulation or primitive equations or Roe scheme or Kinetic scheme first or second order or Boussinesq equations or TELEMAC-3D hydrostatic or non-hydrostatic.

When a tsunami has a large source area it may be the case that important wavelengths of the resulting tsunami wave are in the shallow water domain (i.e. wavelength is greater than 20 times the water depth). In this case TELEMAC-2D should be suitable. If shorter wavelengths are important then the best approach could be to use TELEMAC-3D non-hydrostatic.

TELEMAC-2D should be tested for ability to model wave propagation correctly as well as diffraction and refraction phenomena. In this case, it is not expected in general that the inundation of dry land will be represented in the same model. This is because the propagation to near shore is modelled using the wave equation formulation in TELEMAC-2D and the inundation phase (if required) will use the finite volume (kinetic scheme) in TELEMAC-2D.

So it is important to find analytical or laboratory test cases that are within the shallow water equations' limit of validity. Some such test cases have been identified and the performance of TELEMAC-2D in comparison is presented.

II. TESTING TELEMAC-2D SUITABILITY FOR TSUNAMI PROPAGATION

The test cases considered here are cases where the waves are long and so can be simulated using the shallow water equations. The first two cases are of wave diffraction occurring at the point of a semi-infinite breakwater [1] and refraction around a circular island [2]. Both of these processes are extremely important as tsunami waves travel a long way and are subject to diffraction around islands, headlands etc., and are subject to refraction wherever there are significant variations of water depth. A third test case is the Monai tsunami physical model test case [3].

A. Diffraction by semi-infinite breakwater [1]

This case is the analytical solution for a sinusoidal train of waves travelling north and diffracting around the tip of a semi-infinite breakwater along the positive x-axis as depicted in Fig. 1.

The TELEMAC-2D flow model was run using the wave equation formulation and no friction or viscosity. The implicitation coefficients were taken as 0.501 (the model is second order accurate if implicitation = 0.5, but on the edge of instability as the scheme is unstable if implicitation < 0.5) and the free surface gradient compatibility was taken as 0.9 (recommended value). The water depth was taken uniform so that the wave celerity is constant everywhere. The water depth was also taken sufficiently low that the wave length was greater than 20 times the water depth and so the shallow

water wave equations were valid. The wave amplitude was also taken very small so as to minimise nonlinear effects.

The incident wave boundary condition (from the south) was taken as an absorbing wave paddle and the open exit boundaries (east, west and north) were all taken as absorbing boundaries using the Thompson boundary condition. The model extends south of the breakwater so that the tip of the breakwater is an internal point of the model grid and the boundary condition on the front and back face of the breakwater is a solid wall (100% reflection condition).

In Fig. 1 the y axis shows distance from the breakwater line non-dimensionalised by the wave length. Fig. 2 shows a comparison between the wave amplitude from the model and the analytical solution along two lines parallel to and behind the breakwater at two and eight wavelengths.

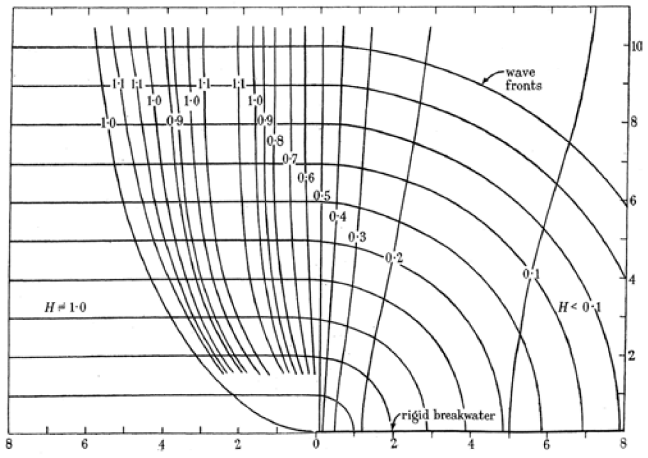

Figure 1. Wave fronts and contour lines of maximum wave heights in the lee of a breakwater. Waves are coming from the south.

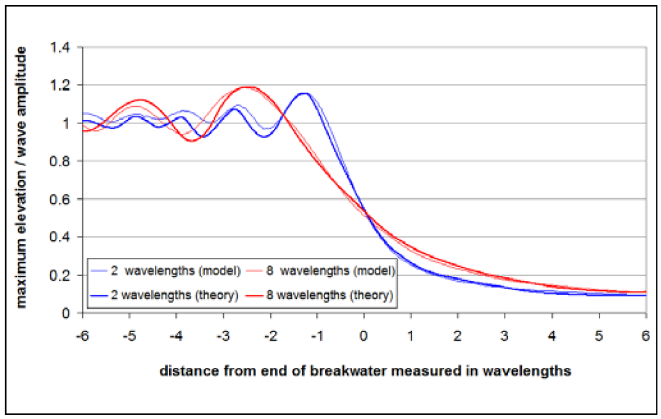

Figure 2. Wave amplitude along two lines parallel to and behind the breakwater at 2 and 8 wavelengths.
Model (thin lines) and analytical (thick lines) solutions.

The model gives a good representation of the reduction of the wave amplitude in the lee of the breakwater at two and eight wavelengths from the structure showing the diffraction process. The variation of the wave amplitude not in the lee is reasonable but rather less accurate.

B. Wave refraction and diffraction around a circular island [2]

This case is the analytical solution for a wave train travelling over a circular island, which vertical cross-section is shown in Fig. 3.

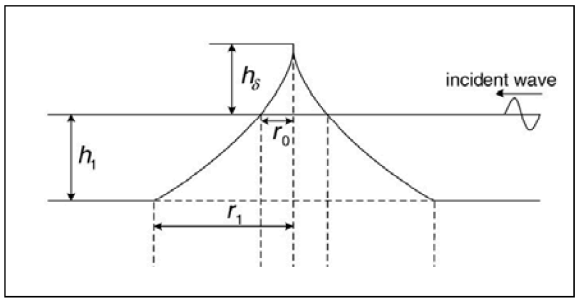

Figure 3. Vertical cross-section through circular island.

This is a case where refraction and diffraction of a wave both occur. TELEMAC-2D was again run using the wave equation formulation. The bed friction and viscosity were again set to zero and Thompson boundary condition was used so waves could pass out from the modelled domain. Free surface gradient compatibility was 0.9 and implicitation coefficients were 0.501 again.

The model is compared with the analytical solution by contouring the wave amplitude (Fig. 5) to compare with the analytical solution (Fig. 4). These figures are for a profile in which the depth varies as the 2/3 power of the radius as shown in Fig. 3.

It can be seen that the wave height pattern is well reproduced for this situation.

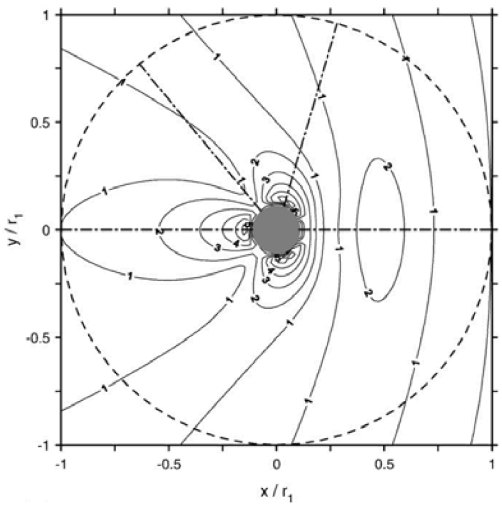

Figure 4. Wave amplitude contours for a circular island with $r_1=9r_0$, $r_0=10$ km, $h_1=4$ km. Analytical solution.

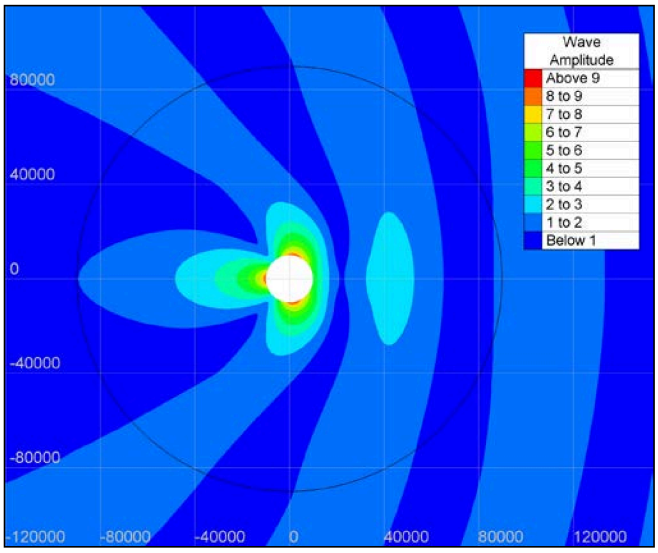

Figure 5. Wave amplitude contours for a circular island with $r_1=9r_0$, $r_0=10$ km, $h_1=4$ km.. Model solution.

C. *Monai tsunami physical model test case [3]*

In the Monai tsunami physical model test case [3], a tsunami wave propagates in to an inlet and transforms as the water becomes shallow. The physical model is depicted in Fig. 6.

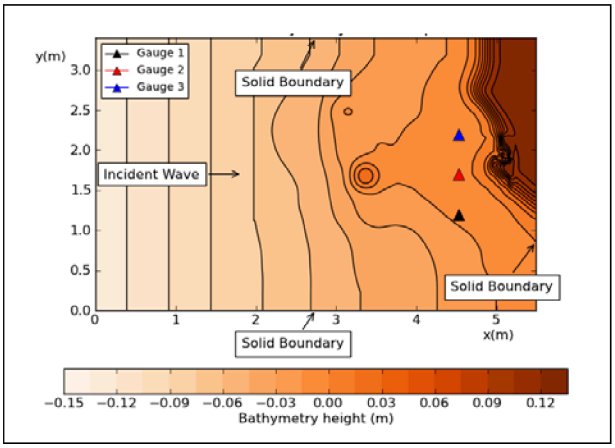

Figure 6. Monai tsunami physical model test. Bathymetry and setup.

Because this is a case where there is some inundation (see incident wave in Fig. 7) it was modelled first using the second order Kinetic finite volume scheme. Good results for all three gauges were found (Fig. 8, 9 and 10).

In view of this success the simulation was repeated using the finite element method (with free surface gradient compatibility taken as 0.9, and implicitation coefficients as 0.55). The results using the FE method are depicted in Figs 11-13. Comparing them with the finite volume method solution it seems that the results are a bit less good. In particular the solution readily creates oscillations as the wave steepens. However it could also be considered that the finite volume model produces fewer oscillations than the observed data. It seems that the FE method is giving good results in the initially wet parts of the domain but the finite volume method becomes better in the areas which are initially dry.

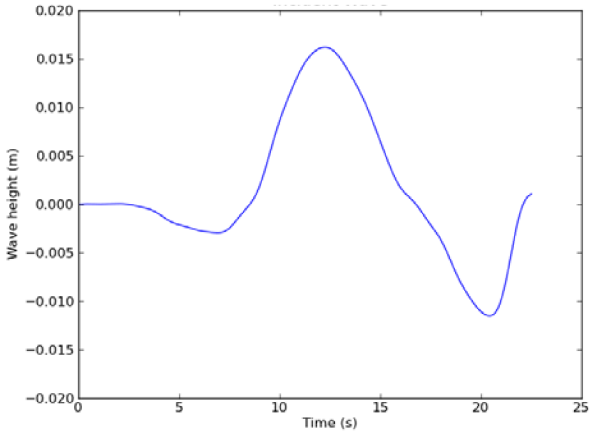

Figure 7. Monai tsunami physical model test. Incident wave.

III. CONCLUSIONS

Tests carried out have shown good reproduction in TELEMAC-2D, using the finite element wave equation formulation with free surface gradient compatibility of 0.9, of diffraction and refraction processes provided cases are in the domain of validity of the shallow water equations (wave length at least 20 times the water depth). For the case of wave transformation in an inlet with inundation of initially dry zones it is found that the results using the wave equation approach reproduce the height of the wave, but a closer match to the water level gauges is found by using the finite volume method.

ACKNOWLEDGEMENTS

The authors would like to thank Damien Violeau and Jean-Michel Hervouet at EDF-LNHE for their support in this project.

REFERENCES

[1] W. G. Penney and A. T. Price, Mar. 4, 1952. “Part I. The Diffraction Theory of Sea Waves and the Shelter Afforded by Breakwaters”, Philosophical Transactions of the Royal Society of London. Series A, Mathematical and Physical Sciences, Vol. 244, No. 882, pp. 236-253.

[2] Tae-Hwa Jung, Changhoon Lee, Yong-Sik Cho, 2010. “Analytical solutions for long waves over a circular island”, Coastal Engineering 57, pp. 440–446.

[3] Costas E Synolakis, Eddie N. Bernard, Vasily V. Titov, Utku Kanoglu, Frank I. Gonzalez, 2007. Standards, Criteria, and Procedures for NOAA Evaluation of tsunami numerical models. p45, 3.4.

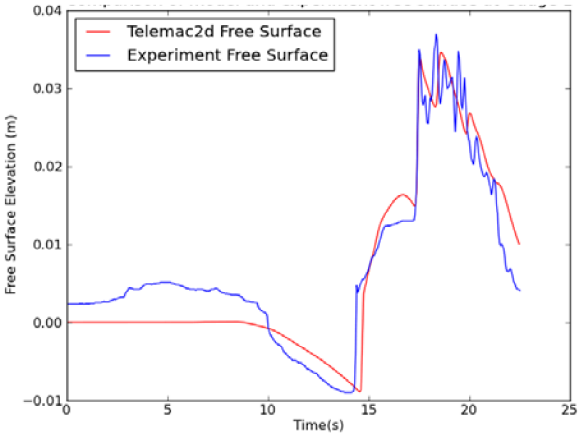

Figure 8. Comparison of model (second order Kinetic finite volume scheme) and experiment free surface at Gauge 1.

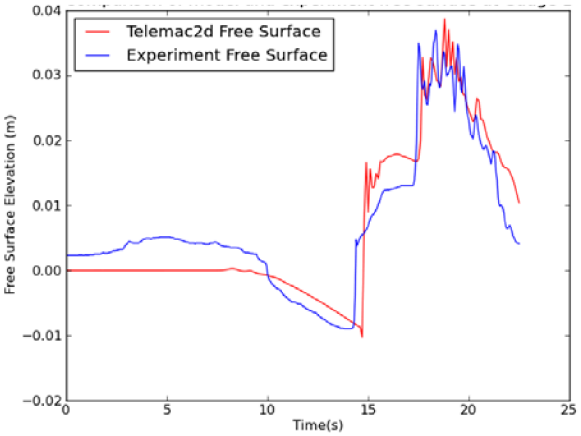

Figure 11. Comparison of model (finite element) and experiment free surface at Gauge 1.

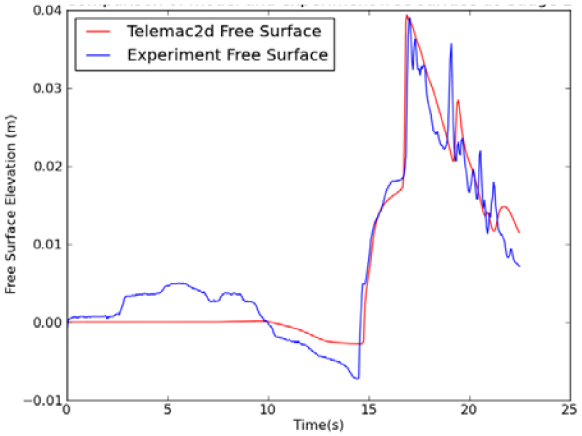

Figure 9. Comparison of model (second order Kinetic finite volume scheme) and experiment free surface at Gauge 2.

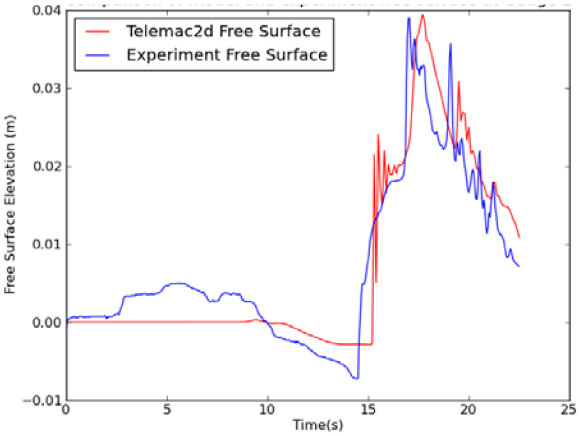

Figure 12. Comparison of model (finite element) and experiment free surface at Gauge 2.

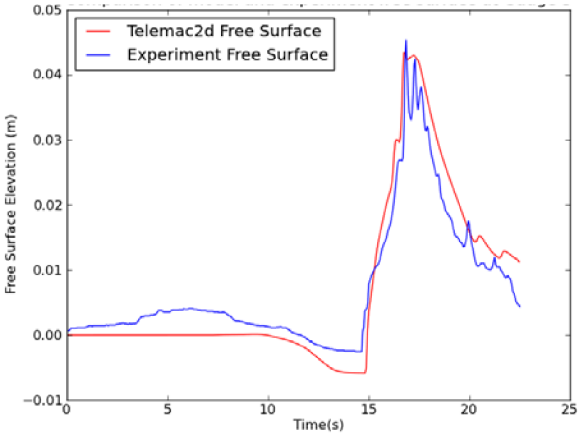

Figure 10. Comparison of model (second order Kinetic finite volume scheme) and experiment free surface at Gauge 3.

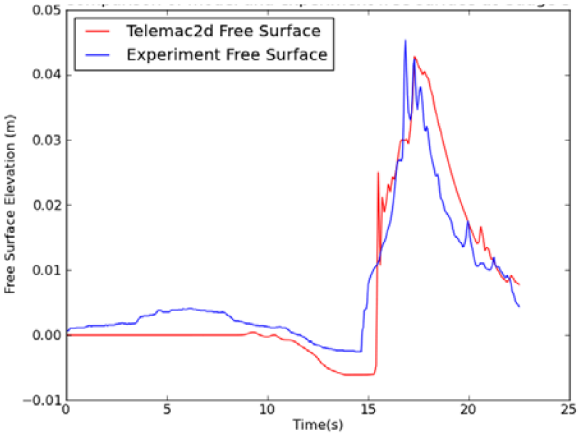

Figure 13. Comparison of model (finite element) and experiment free surface at Gauge 3.

TELEMAC-2D new finite volume schemes for shallow water equations with source terms on 2D unstructured grids

Riadh Ata
EDF-R&D- LNHE
Saint-Venant Laboratory for Hydraulics
6 Quai Watier, Bat. I, Chatou, 78400, France.
riadh.ata@edf.fr

***Abstract*—We present the newly added (in TELEMAC-2D) finite volume schemes (Zokagoa, Tchamen, HLLC and WAF), which give the possibility for users to choose the scheme suited for each kind of application. Depending on the chosen scheme, several interesting numerical properties are obtained. Indeed, the mass conservation, the positivity of water depth, wetting and drying, shock capturing and small numerical diffusion are proved and/or observed. The treatment of a tracer transport in a coupled/split way is not implemented yet and will be the subject of future developments.**

I. INTRODUCTION

We try in this paper to present briefly the new finite volumes (FV) schemes added to TELEMAC-2D in version V6P1 and V6P2. We aim to give a theoretical base for users to understand the algorithmic and the implementation aspects in order to help them toward an optimal use.

We do not claim a complete originality through this work. Indeed, the HLLC, for instance, is a well-known and a widely used scheme. Nevertheless, the remaining schemes are introduced on a vertex-centered 2D unstructured meshes for the first time (as far as we know). Moreover, some major numerical novelties dealing with the WAF scheme are introduced for the first time and are an exclusivity of TELEMAC-2D.

II. TELEMAC-2D FINITE VOLUMES FRAMEWORK

A. The Saint Venant equations

We recall the Saint-Venant equations written in a conservative form:

$$\frac{\partial \boldsymbol{U}}{\partial x}+\frac{\partial \boldsymbol{G}(\boldsymbol{U})}{\partial x}+\frac{\partial \boldsymbol{H}(\boldsymbol{U})}{\partial x}=\boldsymbol{S}(\boldsymbol{U})\ on\ \Omega\times[0,\mathrm{T_s}]$$

where $\boldsymbol{U}=\begin{bmatrix}h\\hu\\hv\end{bmatrix}, \boldsymbol{G}(\boldsymbol{U})=\begin{bmatrix}hu\\hu^2+\frac{1}{2}gh^2\\huv\end{bmatrix}$,

$$\boldsymbol{H}(\boldsymbol{U})=\begin{bmatrix}hu\\huv\\hv^2+\frac{1}{2}gh^2\end{bmatrix}, \boldsymbol{S}(\boldsymbol{U})=\begin{bmatrix}0\\gh(S_{0x}-S_{fx})\\gh(S_{0y}-S_{fy})\end{bmatrix},$$

$$\boldsymbol{S_0}=\begin{bmatrix}\boldsymbol{S_{0x}}=\frac{\partial z}{\partial x}\\\boldsymbol{S_{0y}}=\frac{\partial z}{\partial y}\end{bmatrix}, \boldsymbol{S_f}=\begin{bmatrix}\boldsymbol{S_{fx}}=\frac{n^2u\sqrt{u^2+v^2}}{h^{\frac{4}{3}}}\\\boldsymbol{S_{fy}}=\frac{n^2v\sqrt{u^2+v^2}}{h^{\frac{4}{3}}}\end{bmatrix}$$

where h=η-z is the water depth, η is the free surface, z is the bathymetry, (u,v) are the x and y components of the velocity, g is the gravity acceleration, n is the Manning roughness coefficient and T_s is the simulation time.

This system is widely studied in the literature, we recall here some of its main properties:

- It is strictly hyperbolic for h>0 and loses its hyperbolicity for h=0. This means that water depth could vanish and dry areas may appear in the domain.
- It has an entropy inequality ($\tilde{\alpha}$) related to physical energy (α):

$$\frac{\partial \tilde{\alpha}(U)}{\partial t}+\frac{\partial \tilde{G}(U)}{\partial x}\leq 0$$

where $\alpha(U)=\frac{hu^2}{2}+\frac{gh^2}{2}, G(U)=\left(\frac{hu^2}{2}+gh^2\right)u,$

$\tilde{\alpha}(U,z)=\alpha(U)+hgz, \tilde{G}(U,z)=G(U)+hgzu$

- It admits non trivial steady states, such as the lake at rest (i.e. h+z=cst for u=0).

B. The finite volume framework

We present here the general framework of the finite volume approach used for all the schemes of TELEMAC-2D. The entire domain Ω is subdivided into N sub-domains called control volumes K_i associated to a vertex i. In TELEMAC-2D, we use a vertex-centred approach based on "dual mesh". Specifically, the dual cell is obtained by joining the centres

of mass of the triangles T_i surrounding the vertex i, see Fig. 1.

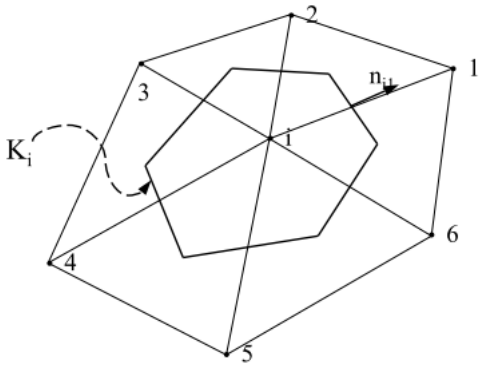

Figure 1. Finite volume framework in TELEMAC-2D

After integration over the control volume defined by Fig. 1 and using the Gauss theorem, last equation gives:

$$U^{n+1} = U^n - \sum_{j=1}^{m_i} \sigma_{ij} F\left(U_i^n, U_j^n, n_{ij}\right) - \sigma_{ij} F(U_i^n, U_e^n, n_i) + \Delta t\, S_i^n$$

where $F\left(U_i^n, U_j^n, n_{ij}\right)$ is an estimation of the normal component of the flux $F(U).n$ along the edge Γ_{ij} separating the nodes i and j.

To have a finite volume method, it is enough to prescribe a numerical flux *F* and a numerical source term S_i.

III. PRESENTATION OF THE NEW SCHEMES

In TELEMAC-2D, there exists already Roe and (first and second order in space) kinetic schemes. We will not present these two schemes in this paper. We will focus only on the newly added schemes, i.e. Zokagoa, Tchamen, HLLC and WAF.

A. Zokagoa and Tchamen schemes

We present these two schemes together since they make similar assumptions and have similar formulations of their numerical fluxes. The peculiarity of these schemes is that the numerical flux is calculated assuming a new set of unknowns where the first component is the free surface elevation η and no more the water depth h. They are recommended for problems with important wetting and drying sequences. See [4] for more details.

These two schemes are based on the discretisation of the geometrical source term $g\int_{K_i} h\nabla z\, d\Omega$. Substituting z by η − h gives:

$$\int_{K_i} h\nabla z\, d\Omega = \int_{K_i} h\nabla\eta\, d\Omega - \int_{K_i} \frac{1}{2} h\nabla \mathrm{h}^2\, d\Omega$$

Since $\int_{K_i} \frac{1}{2} h\nabla \mathrm{h}^2\, d\Omega$ exists in the advection part, the geometrical source term becomes:

$$\mathbf{S}_{\mathrm{b_i}} = \int_{K_i} gh\nabla\eta\, d\Omega$$

Several strategies could be used for the discretisation of this integral. We give hereafter the ideas of Tchamen and Zokagoa:

- Tchamen proposed a local linearisation of Sbi: $S_{b_i} = \bar{h}\int_{K_i} g\nabla\eta\, d\Omega$, where $\bar{h}$ is a mean value of the water depth in the cell, defined with respect to conservation properties and interface states (wet/dry).
- Zokagoa proposed a nonlinear model derived in order to compute more accurately the propagation of discontinuities. The water depth is substituted by the difference between the free surface and the bottom levels: h=η−z, but with the constraint h=η−z> 0, which gives:

$$S_{b_i} = \int_{K_i} gh\nabla\eta\, d\Omega = \int_{K_i} gh\nabla\frac{\eta^2}{2} d\Omega - \int_{K_i} gz\nabla\eta d\Omega .$$

In a similar way, by assuming $z = \bar{z}$ on the control volume, the source term is approximated as: $S_{b_i} \approx g\int_{K_i} \nabla\left(\frac{\eta^2}{2} - \overline{z\eta}\right) d\Omega$

The final fluxes are given by:

$$\mathcal{F}_{\mathbf{ij}}(\mathbf{V_i}, \mathbf{V_j}, \mathbf{n_{ij}}) = \frac{1}{2}\begin{bmatrix} h_i u_{i,n} + h_j u_{j,n} \\ h_i u_{j,n}^2 + g h_i(\eta_i + \eta_j) \\ h_i u_{i,n} v_{i,n} + h_j u_{j,n} v_{j,n} \end{bmatrix}$$

$$- \frac{1}{2} D_{ij} \begin{bmatrix} \eta_j - \eta_i \\ h_j u_{j,n} - h_i u_{i,n} \\ h_j v_{j,n} - h_i v_{i,n}, \end{bmatrix}$$

where $u_{k,n} = u_k n_{ij}^x + v_k n_{ij}^y$ and $v_{k,n} = v_k n_{ij}^x + u_k n_{ij}^y$. In TELEMAC-2D, two choices are possible for the updwinding D_{ij}:

- Toro's choice (default): $D_{ij} = max\{|u_{i,n}| + \sqrt{gh_i}\,, |u_{j,n}| + \sqrt{gh_j}\}$
- Zokagoa's choice: $D_{ij} = \lambda_{ij} = \alpha\, max\{|\tilde{u}_{i,n} - \tilde{c}_{i,n}|, |u_{j,n}|, |\tilde{u}_{i,n} + \tilde{c}_{i,n}|\}$, where $0 \le \alpha \le 1$, $\tilde{u}_{i,n} = \frac{u_{i,n} + u_{j,n}}{2}$ and $\tilde{c}_{i,n} = \sqrt{\frac{h_i + h_j}{2}}$

B. HLLC scheme

The HLLC (C standing for Contact, the missing intermediate wave) is an amelioration proposed by Toro et al.[1] of the basic HLL (Harten, Lax, van Leer) scheme. Indeed, the HLL scheme requires estimates of the wave speeds S_L and S_R of the left and right waves present in the

solution of the Riemann problem defined with data $U_L = U_i^n$, $U_R = U_{i+1}^n$ and corresponding fluxes $F_L = F(U_L)$, $F_R = F(U_R)$ (see Fig. 2). To consider the effect of the intermediate waves, such as shear waves and contact discontinuities, another intermediate speed, called S_*, has to be considered.

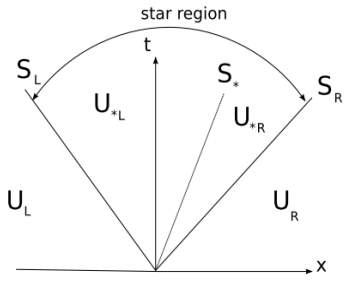

Figure 2. Structure of the solution of the Riemann problem described above.

The general solution of the Riemann problem defined above is:

$$\tilde{\mathbf{U}}(x,t) = \begin{cases} \mathbf{U_L}, & \text{if} \quad \frac{x}{t} \le S_L \\ \mathbf{U_{*L}}, & \text{if} \quad S_L \le \frac{x}{t} \le S_* \\ \mathbf{U_{*R}}, & \text{if} \quad S_* \le \frac{x}{t} \le S_R \\ \mathbf{U_R}, & \text{if} \quad \frac{x}{t} \ge S_R \end{cases}$$

The three star states are:

$$\boldsymbol{U}_{*K} = h_K \left(\frac{S_K - U_K}{S_K - S_*}\right) \begin{bmatrix} 1 \\ S_* \\ v_K \end{bmatrix}$$

with k = L,R.

The corresponding HLLC flux is:

$$\mathcal{F}_{i+\frac{1}{2}}^{hllc} = \begin{cases} \mathbf{F_L}, & \text{if} \quad 0 \le S_L \\ \mathbf{F_{*L}}, & \text{if} \quad S_L \le 0 \le S_* \\ \mathbf{F_{*R}}, & \text{if} \quad S_* \le 0 \le S_R \\ \mathbf{F_R}, & \text{if} \quad 0 \ge S_R \end{cases}$$

The star components of the flux can be obtained, for instance by applying the Rankine-Hugoniot condition for each of the waves; which gives:

$$\mathbf{F}_{*L} = \mathbf{F}_L + S_L(\mathbf{U_{*L}} - \mathbf{U}_L)$$
$$\mathbf{F}_{*R} = \mathbf{F}_{*L} + S_L(\mathbf{U_{*R}} - \mathbf{U}_{*L})$$
$$\mathbf{F}_{*R} = \mathbf{F}_R + S_R(\mathbf{U_{*R}} - \mathbf{U}_R)$$

where the water depth and normal component of the velocity in the star region are given by:

$$h_{*L} = h_{*R} = h_*$$
$$u_{*L} = u_{*R} = u_*$$

and the tangential velocity component:

$$v_{*L} = v_L$$
$$v_{*R} = v_R$$

where

$$h_* = \frac{(h_L + h_R)}{2} - \frac{1}{4}\frac{(u_R - u_L)(h_L + h_R)}{c_R + c_L}$$
$$u_* = \frac{(u_L + u_R)}{2} - \frac{1}{4}\frac{(h_R - h_L)(c_L + c_R)}{h_R + h_L}$$

The detection of a shock or a rarefaction wave is achieved by a comparison between $h_{L,R}$ and h_*

C. Weighted Averaged Flux (WAF) scheme

The WAF method was first introduced by Toro (1989) in [5]. It is assumed to guarantee second order accuracy in time and space. Second order accuracy in space is obtained with no need for data reconstruction.

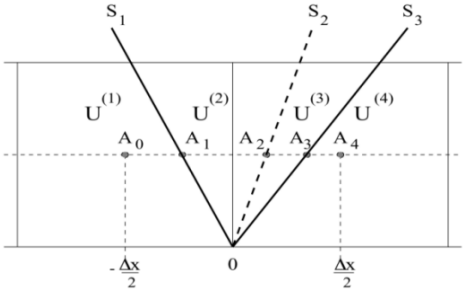

Figure 3. space time (x-t) diagram for the WAF approach.

The original version of the WAF scheme is a weighted sum of the fluxes in all regions of the solution of the piecewise constant data Riemann problem [5], namely:

$$F_{i+\frac{1}{2}} = \frac{1}{\Delta x}\int_{-\frac{\Delta x}{2}}^{\frac{\Delta x}{2}} F\left(U_{i+\frac{1}{2}}\left(x, \frac{\Delta t}{2}\right)\right) dx$$

where $U_{i+\frac{1}{2}}(x,t)$ is the solution of the Riemann problem defined in the previous section. The second order in space and time is obtained since we use one Gauss point to compute this integral (in time and space, i.e. $\frac{\Delta t}{2}$ and $\frac{\Delta x}{2}$).

The integral is therefore easily computed, based on the diagram of Fig. 3, which gives:

$$F_{i+\frac{1}{2}} = \sum_{k=1}^{N+1} \beta_k F_{i+\frac{1}{2}}^{(k)}$$

where $F_{i+\frac{1}{2}}^{(k)} = F\left(U^{(k)}\right)$, $U^{(1)} = U_i^n$, $U^{(2)} = U_L^*$, $U^{(3)} = U_R^*$ and $U^{(4)} = U_{i+1}^n$, N is the number of waves in the solution of the Riemann problem, $\beta_k (k = 0, \dots, N)$ are the normalised lengths of segments A_kA_{k+1}, which correspond to the difference between the local Courant numbers c_k for successive wave speeds S_k:

$$\beta_k = \frac{|A_k A_{k+1}|}{\Delta x} = \frac{1}{2}(c_k - c_{k-1})$$

$$c_k = \frac{\Delta t S_k}{\Delta x},\ c_0 = -1\ and\ c_{N+1} = 1$$

The generalisation of the WAF description to 2D unstructured meshes in a proper way was achieved by Ata et al.[2]. The procedure cannot be explained in details within this paper, however, it can be summarised as the following: it consists on the writing, in a 2D finite volume framework, the final expression of the discretised SWE combined with a TVD extension to prevent any spurious oscillations in the vicinity of steep gradient.

IV. BOUNDARY CONDITIONS AND TIME DISCRETISATION

We need to define the status U_e, which represents the state in a fictitious cell adjacent to the boundary. In the case of a solid wall, we impose a perfect slipping condition in order to obtain the continuity of the tangential component. In the case of a liquid boundary, we need to distinguish two sub-cases: the subcritical and super-critical cases. It is necessary to specify for every point along the boundary, a number of conditions which depends on the regime: For a subcritical input or output, only one boundary condition (h or Q) is necessary, since there is one characteristic starting within the domain and directed to the entry. For a super-critical input, two conditions (h and Q) are required, while for a supercritical outlet, there is no need for any condition.

For time discretisation, a Newmark scheme is implemented which offers the possibility to retrieve, depending on user choice, a first or a second order accurate scheme.

V. SOURCE TERM TREATMENT

The geometric source term is discretised, as for kinetic schemes, using the hydrostatic reconstruction of Audusse et al. This fundamental aspect ensures the positivity of water depth, the conservation of mass, the well-balanceness (or C-property). More details can be found in [2].

For the discretisation of the friction term, a semi-implicit algorithm is implemented. The friction term is written as:

$$S_f \approx \frac{|q_i^n| q_i^{n+1}}{K^2 h_i^n (h_i^{n+1})^{\frac{4}{3}}}$$

This discretisation is very robust and handles well probable instabilities caused by possible abrupt changes in water depths and velocities.

VI. ASSESSMENT AND VALIDATION

Even though we have achieved a large set of validation cases, we will present here only three of them showing the major good numerical properties of these schemes.

A. C-property

The well-balanceness or C-property is an essential criterion that every numerical scheme should satisfy. In our case, we chose the benchmark proposed by Goutal et al.[2]. It represents a 2D channel with a severe variation of the bathymetry in the longitudinal direction. The schemes have to maintain a lake at rest for a long simulation time. In our case, we fixed a t_{max}= 1000s. The results (water elevation and velocity) are presented in Fig. 4.

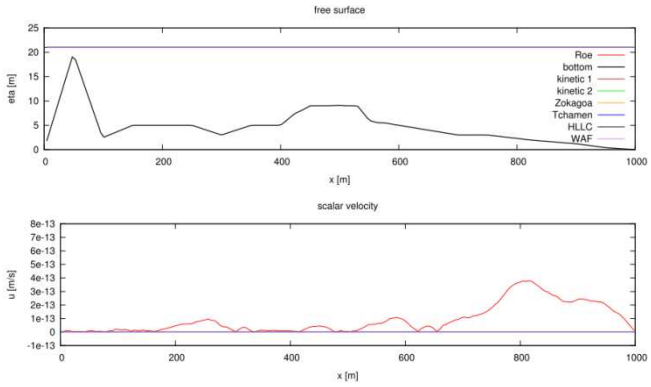

Figure 4. Lake at rest test case - comparison between all the schemes of TELEMAC-2D.

We can conclude, from Fig. 4, that the C-property is well satisfied for all the schemes.

B. Wet and dry dambreak

The second test case is the theoretical dam break with wet (Stoker problem) and dry (Ritter) downstream. These tests permit to ass the shock-capturing capabilities of the schemes and to quantify the numerical diffusion which is located mostly in the shock areas. Initial conditions are defined by water depths of 4m and 1m (or 0m for Ritter case) respectively upstream and downstream of the dam. This latter is located at x=1000m. Figs. 5 and 6 show the obtained results which prove that WAF scheme gives excellent results comparing to the analytical solution and to other schemes.

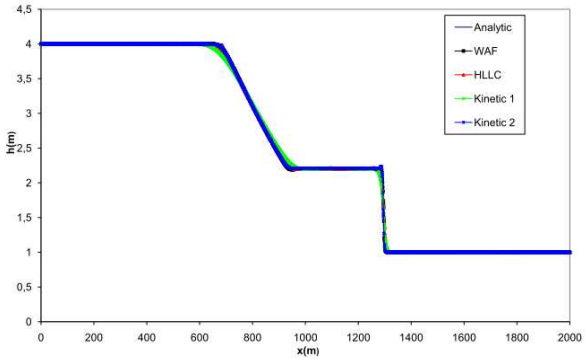

Figure 5. Stoker problem: comparison of water depth and obtained by each scheme.

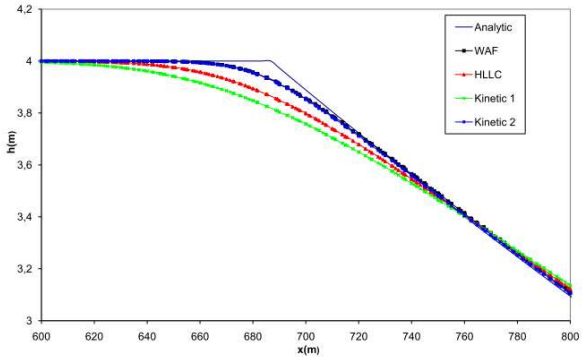

Figure 6. Stoker problem: comparison of water depth zoom on the rarefaction wave that shows the numerical diffusion of each scheme.

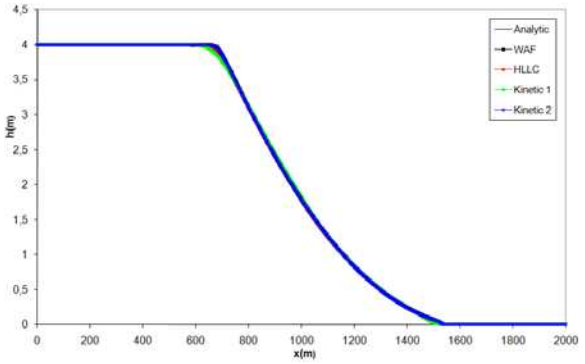

Figure 7. Ritter problem: Comparison between all the FV schemes.

C. *Malpasset dam break*

The last validation case is the real case of Malpasset dam break. All the details about this problem as well as the reference solution are given in [2]. This problem is interesting since it allows to see how the schemes behaves in case of real case which include almost all the numerical challenges (shock-capturing, wetting and drying, steep bathymetry etc.).

The used mesh contains 5435 nodes and 10049 elements. The CFL number is fixed to 0.8 and the Strickler number is assumed to be 30 everywhere in the domain. The simulation time is 4000s. The water depth at several times is shown in Figs. 8, 9 and 10.

The CPU time for some of the schemes is given in the following table (we used a 8-Core HP Z600, Linux, with 4Go of RAM):

TABLE I. CPU TIME RELATIVE TO THE MALPASSET PROBLEM

	HLLC	**Kinetic 1st order**	**Kinetic 2nd order**	**WAF**
CPU time	46 s	55s	1mn56s	1mn08s

The results were compared with those obtained by real measurements and by a physical reduced order model. A L1-type error was used to quantify the error between obtained results (elevation and arrival times) and reference ones. The results are encouraging especially if we consider the fact that we used a single value of the Strickler coefficient and that we have not proceeded by any calibration step before simulating the case.

VII. CONCLUSIONS AND FUTURE WORKS

We presented in this paper a comparative study of the newly added finite volume schemes of TELEMAC-2D. We showed the specific aspects of each scheme and its recommended application. Moreover, we presented a numerical assessment of these schemes through some theoretical and real test cases. The obtained results are very encouraging since we obtained very interesting numerical properties such as positivity of water depth, mass conservation, very nice shock-capturing, low numerical diffusion and very robust wetting and drying treatment. These encouraging results open wide perspectives to apply such formulation in specific applications that need strong and robust numerical properties such as the transport of passive tracer and sediments.

ACKNOWLEDGEMENT

A part of the validation cases showed in this paper were achieved during the training of S. Pavan. The author would like to acknowledge her contribution to this work.

REFERENCES

[1] E.F. Toro, M. Spuce and W. Speares, “Restoration of the contact surface to the Harten-Lax-van der Leer solver”. Journal of Shock Waves,(4) 25-34, 1994.

[2] R. Ata, S. Pavan, S. Khelladi and E.F. Toro, “WAF approximation for shallow water equations with friction and real topography”. Submitted.

[3] S.J. Billett and E.F. Toro, “WAF-Type Schemes for Multidimensional Hyperbolic Conservation Laws” .J. Comput. Physics, Vol.130, pp.1-24.

[4] J.M. Zokagoa., A. Soulaimani. “Modeling of wetting-drying transition in free surface flows over complex topographies.” Computer Methods in Applied Mechanics and Engineering, Vol.199, pp.2281-2304, 2010.

[5] E.F. Toro. A Weighted Average Flux Method for Hyperbolic Conservation Laws (1989). Proc. Roy.Soc.London, (423) 401-418

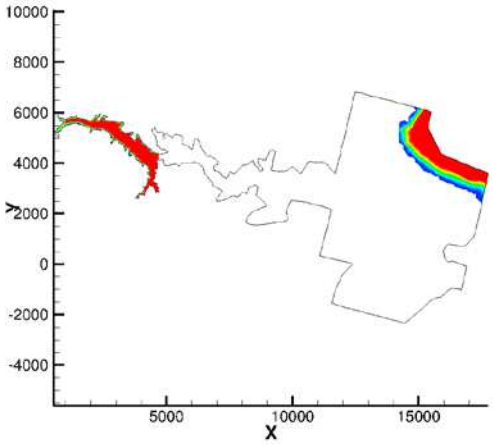

Figure 8. Malpasset dam break initial conditions t=0s.

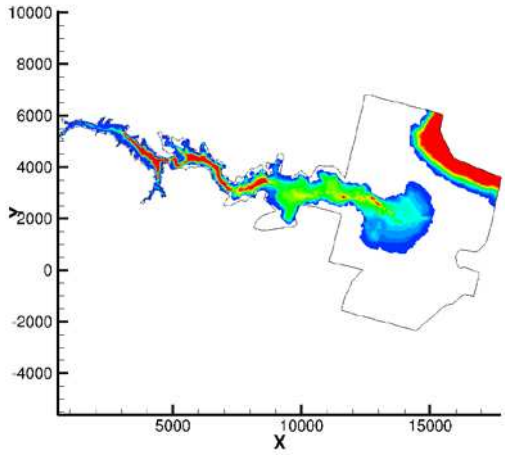

Figure 9. Malpasset dam break: elevation at t=2450s.

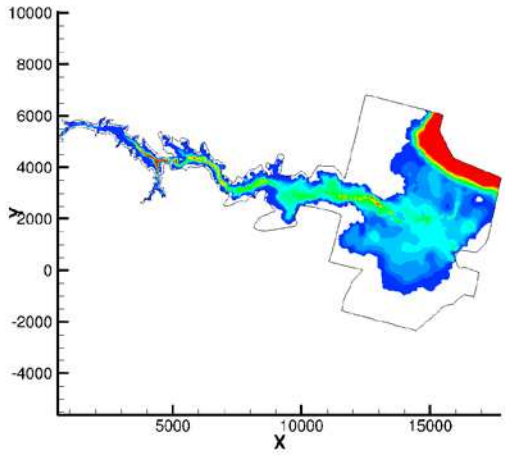

Figure 10. Malpasset dam break: elevation at t=4000s

Numerical Modelling of PCB transport in a segment of the Rhone River

Anne Levasseur, Mathieu Delinares, Florence Gandilhon
ARTELIA eau et environnement
6 rue de Lorraine, 38130, Echirolles, France
anne.levasseur@arteliagroup.com

***Abstract*—As part of the PCB-AXELERA research program, a simple model of PCBs (polychlorinated biphenyl) contamination in the Rhone river has been developed. The main objective is to assess the distribution of PCBs under various hydraulic regimes. This model uses TELEMAC-3D to simulate the water flow, and is coupled to DELFT3D-WAQ to simulate the transport of sediment and PCBs. The vertical resolution of the grid is 10 layers. The transport of sediments is modelled using the Krone and Partheniades formulation. The PCBs distribution between organic matter and water is treated as an equilibrium portioning, which accounts for the processes of adsorption and desorption of PCBs on the sediment. The model is run on an idealised channel. A sensitivity analysis is made to assess the impact of the numerical scheme and the vertical diffusion on the distribution of sediment in the water column using DELFT3D-WAQ. The modelled PCBs concentrations are in the same order of magnitude that the observations, which validates the set of parameters and the processes selected**

I. INTRODUCTION

PCBs are a class of micropollutant widely used in industry since the late 1930s, due to their specific properties of high stability and low reactivity. They are released in the environment through the processes of evaporation in the atmosphere by incineration of PCB-contaminated wastes, discharge of industrial wastewater effluents in rivers, and accidental spillage of PCB-contaminated hydraulic fluid. They have been identified as presenting public health and ecosystem risk due to their toxicity even at low level. For this reason, PCBs have been banned in France since 1987. Some commercial mixtures of PCBs are highly persistent, which explained why they are still found at high level in rivers and fishes. Water quality standards for PCB have been established and the PCB contamination in fish, river water, and sediment is regularly monitored. Processes affecting PCBs in the environment are [1]:

- bioaccumulation,
- volatilisation,
- adsorption and desorption to organic matter, and
- biodegradation and transformation.

Through this various processes, they contaminated the compartments of the aquatic system: water, soil, air and fishes. PCBs are characterized by a low solubility, and bind strongly to organic particles in sediments and soils. Therefore most PCBs are found adsorbed on the sediments.

The main objective of this study was to develop a model of PCB transport at the scale of a river segment to understand the mechanisms of transport and fate of PCBs. The study area is located approximately 50km downstream of Lyon, in southern-east of France, near Condrieu (Fig. 1). This site is formed by two side-arms of the main stream of the Rhone river, called 'lône', which are favourable to sediment deposition (Fig. 2).

At first, an inventory of datasets available to determine the concentration of dissolved PCB and adsorbed PCB is presented. Then the model is run on an idealised channel, based on the geometry of a part of the side-arm. A sensitivity analysis is made to assess the impact of the numerical scheme and vertical diffusion on the distribution of sediment in the water column. Finally the results of the model are compared against dataset to validate the set of parameters determining the transport of sediments and PCBs.

Figure 1. Study site.

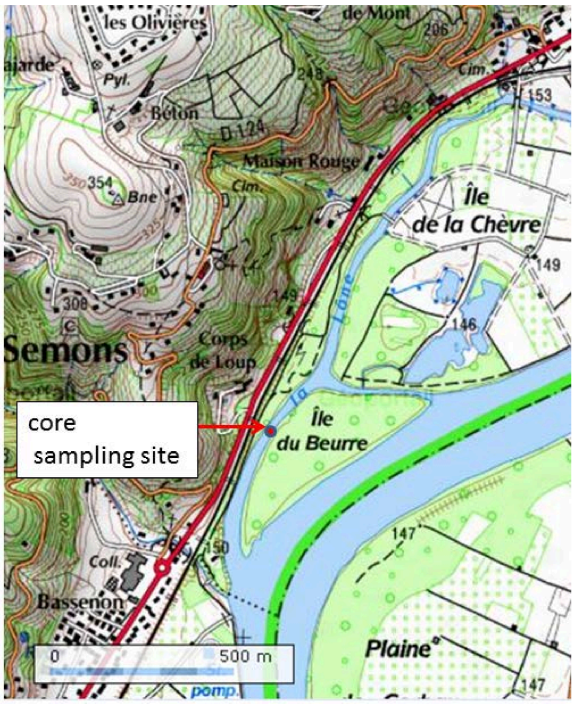

Figure 2. Location of the core sampling site.

II. AVAILABLE DATA

Datasets of adsorbed PCB on SPM (suspended particulate matter) are available through the Regional Water Agency (Table I) at the station of Chasse-sur-Rhône (Fig. 1), upstream Condrieu. Datasets of dissolved PCB were only available at the station of Arles (Fig. 1), another study site of the research project. In addition, a sediment core from the side-arm (location on Fig. 2) was collected in 2008 and gives PCB concentration and organic matter content of the river bed sediment (Table II) [2, 3]. The core gives a record of the PCB concentration adsorbed on sediment deposited from 1965 to 2008. This dataset gives the level of PCB contamination of the sediment at the study site.

III. MODEL DESCRIPTION

A. *Model grid and topography*

The model is formed from the side-arm delineating the island of Beurre (Fig. 3). It includes 527 nodes on the horizontal plan. The vertical resolution is 10 layers. Triangles are of 15 meters size approximately. Topography is lowered to 144.4 m NGF along the river bank to always get a minimum water depth over the whole domain and avoid spurious effects due to uncovered nodes.

B. *Modelling hydrodynamic and sediment using TELEMAC-3D*

Simulation with the model TELEMAC-3D using a constant flow rate upstream and imposing a constant water level downstream is made during 6 hours. Sediment transport is modelled using the Krone and Partheniades formula for sedimentation and re-suspension. Sediment bed is not erodible, but sediment deposited during the previous time-step can be re-suspended. Friction at the bottom is modelled by the law of Nikuradse with the Nikuradse length set at 0.15 m after validation against data [4].

The parameters of the law of Krone and Partheniades are the Partheniades constant, settling velocity, the critical shear stress for sedimentation, the critical shear stress for erosion. These values are set after calibration against datasets [4, 5]. They are given in Table III. The model is forced upstream with a constant flow of 5 m^3s^{-1}, a constant value for inorganic matter of 10 mg/L and a PCB total concentration of 10^{-7} mg/L. The water level imposed downstream is 144.7m NGH.

C. *Modelling sediment and PCB distribution using DELFT3D-WAQ*

PCB distribution is modelled using the results of the hydrodynamics modelled by TELEMAC-3D coupled to the

TABLE I. DATASETS FROM THE FRENCH WATER AGENCY

Type of measurement	Sampling frequency	year	average	Standard Deviation	Total number of measurements
Dissolved PCB at Arles	3 measurements (march, april and december)	2010	0.0039 µg/L	0.0028 µg/L	3
PCB in SPM at Chasse sur Rhone	Every 3 months	1991-2009	0.014 mg/kg DM	0.015 mg/kg DM	33
PCB in sediment of the river bed at Chasse sur Rhône	Once a year	1994-2009	75.11 µg/kg DM	183.16 µg/kg DM	7

TABLE II. DATASETS FROM THE SEDIMENT CORE

Type of measurement	Age of sediment collected	average	Standard Deviation	Total number of sub samples after sectioning of the core
PCB in sediment of the river bed	1965-2008	0.0605 mg/kg DM	0.065 mg/kg DM	20
Total Organic Carbon of sediment	1965-2008	11598.63 mg/kg DM	3696 mg/kg DM	20

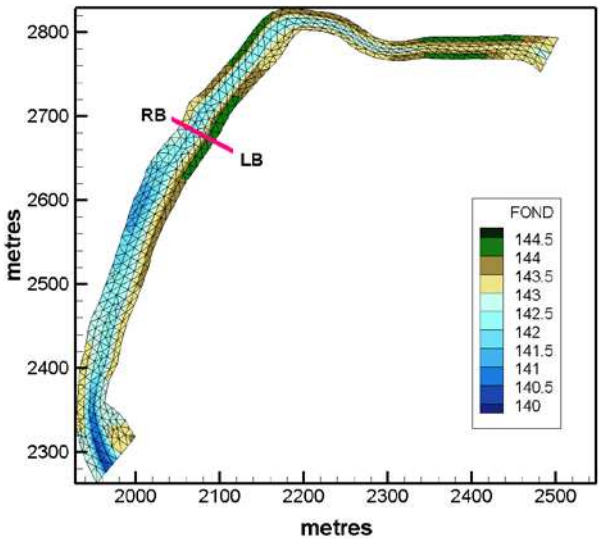

Figure 3. Model grid, bathymetry and position of the vertical slice.

TABLE III. PARAMETERS FOR SEDIMENTATION AND RE-SUSPENSION IN TELEMAC-3D

Parameter	Value	Unit
Partheniades constant	$6.50\ 10^{6}$	kg m^{-2} s^{-1}
Critical shear stress for sedimentation	10000	N m^{-2}
Critical shear stress for erosion	$5.33\ 10^{-2}$	N m^{-2}
Settling velocity	0.0001	m s^{-1}
Porosity	0.45	%
Nikuradse length	0.15	m

DELFT3D-WAQ module. The following variables are modelled in DELFT3D-WAQ: IM1 (inorganic matter), POM (particulate organic matter), PCB-par (PCB adsorbed on sediment particle), PCB-dis (PCB dissolved in water). The model accounts for the PCB and sediment deposited at the bed layer. The variables representing the content of the bed layer are the following: IM1S1, POMS1, PCB-disS1, PCB-parS1. The processes accounted for the transport of sediment, organic matter and adsorbed PCB are sedimentation and re-suspension following the law of Krone and Partheniades. Adsorption and desorption of PCB on the SPM (suspended particulate matter) is modelled by partition coefficients, following the Langmuir law. The fraction of PCB adsorbed (fpoc) and the fraction of PCB dissolved (fdf) is therefore calculated at each time step. We assume that the chemical reaction is at equilibrium, therefore Koc is a constant. The following equations (1) (2) (3) (4) determine the distribution between the PCB adsorbed (PCB-par) and the PCB dissolved (PCB-dis), as fraction of the total PCB concentration (PCB-tot):

$$\text{PCB-par}=\text{fpoc PCB-tot} \quad (1)$$

$$\text{PCB-dis} =\text{fdf 153-tot} = (1-\text{fpoc})\ \text{PCB-tot} \quad (2)$$

$$\text{PCB-tot} = \text{PCB-par}+\text{PCB-dis} \quad (3)$$

$$\text{fdf} = (1/\text{Kp SS})=1/(1+\text{Koc POC}) \quad (4)$$

We also assume that adsorption occurs only on the organic matter content of the sediment. The content of Particulate Organic Matter (POM) in the sediment is expressed as a fraction of inorganic matter (5):

$$\text{POM} = \%\text{OM\_IM1} \times \text{IM1} \quad (5)$$

The suspended solid (SS) is the sum of inorganic matter and particulate organic matter (POM) (6):

$$\text{SS=suspended solid} = \text{IM1}+\text{POM} \quad (6)$$

The particulate organic matter is expressed as a ratio of the particulate organic carbon using the coefficient fdm (7):

$$\text{POM} = \text{fdm POC} \quad (7)$$

The equation of Karickhoff (8) links Koc, the octanol/water partition coefficient, with Kow, the octanol/water partition coefficient [6]:

$$\log(\text{Koc})=\log(\text{Kow}) \quad (8)$$

The values of the parameters are given in Table IV.

The variables IM1, IM1S1, POM, POMS1 are subject to the processes of re-suspension and sedimentation, with the same parameter values than in TELEMAC-3D (Table III). A representation of model structure (processes and variables) is given Fig. 4.

TABLE IV. PARAMETERS FOR SORPTION AND DESORPTION OF PCB IN DELFT3D-WAQ

Parameter	Value	Unit	Reference
Kow	$10^{6.11}$	L/kg	[6]
%OM_IM1	0.01	-	Data from Table II
fdm	2.6	gDM/gC	[7]

IV. SENSITIVITY ANALYSIS

A. *Influence of vertical diffusion*

Simulation with DELFT3D-WAQ was made over 8 hours. The spin up time, which is the time to reach an

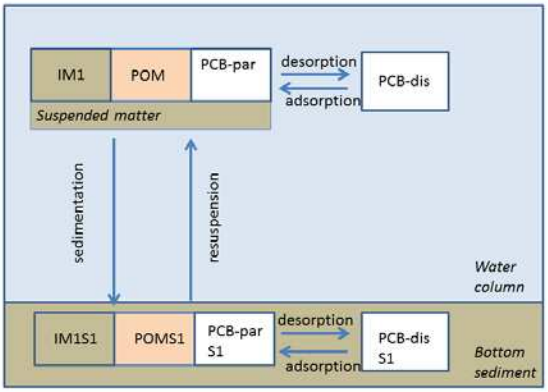

Figure 4. Variables and processes activated in DELFT3D-WAQ to simulate PCB transport and reactions.

equilibrium state under a permanent regime on this small domain, is 3 hours. Several values of the vertical diffusion were tested. Sediment distribution modelled with DELFT3D-WAQ varies depending on the vertical diffusion. The objective was to calibrate the coefficient of vertical diffusion in DELFT3D-WAQ to approach the results of the sediment distribution over the vertical obtained with TELEMAC-3D, as previous work has been made to calibrate and validate a numerical model of sediment transport using TELEMAC-3D on this area [4, 5]. Results were compared for a vertical slice B going from the left bank (LB) to the right bank (RB) (Fig. 3). Sediment distribution modelled with TELEMAC-3D is presented Fig. 5. It shows a vertical gradient in sediment distribution, with higher concentration near the bed (around 2 mg/L). DELFT3D-WAQ can account for the vertical diffusion calculated by TELEMAC-3D. In this case the results produce non-homogeneous distribution of sediment with spikes of concentration. Therefore a constant vertical diffusion coefficient was selected. Results for various values of the coefficient of vertical diffusion are shown on Fig. 6. The raising of the vertical diffusion results in the smoothing of the vertical gradient of sediment concentration. A value of vertical diffusion of $10^{-4}m^2s^{-1}$ in DELFT3D-WAQ was then selected as it avoids spikes on the vertical distribution compared to lower values, and gives results similar qualitatively to the vertical distribution obtained with TELEMAC-3D.

B. Comparison between numerical schemes

In a second stage, a comparison between two numerical schemes (n°16 and n°21) was made (Fig. 7). The numerical scheme n°16 is an implicit upwind scheme in horizontal, centrally discretised vertically, with an iterative solver [8]. The numerical scheme n°21 is a local-theta flux-corrected transport scheme [8]. The highest differences are shown on the left bank (X=2090m), with concentration reaching 35mg/L when using numerical scheme 21 instead of 30mg/L with numerical scheme n°16. The numerical scheme n°21 seems to reduce the effect of smoothing of the vertical

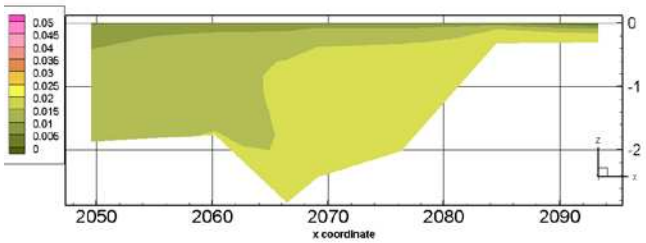

Figure 5. Vertical distribution of suspended sediment using TELEMAC-3D in g/L.

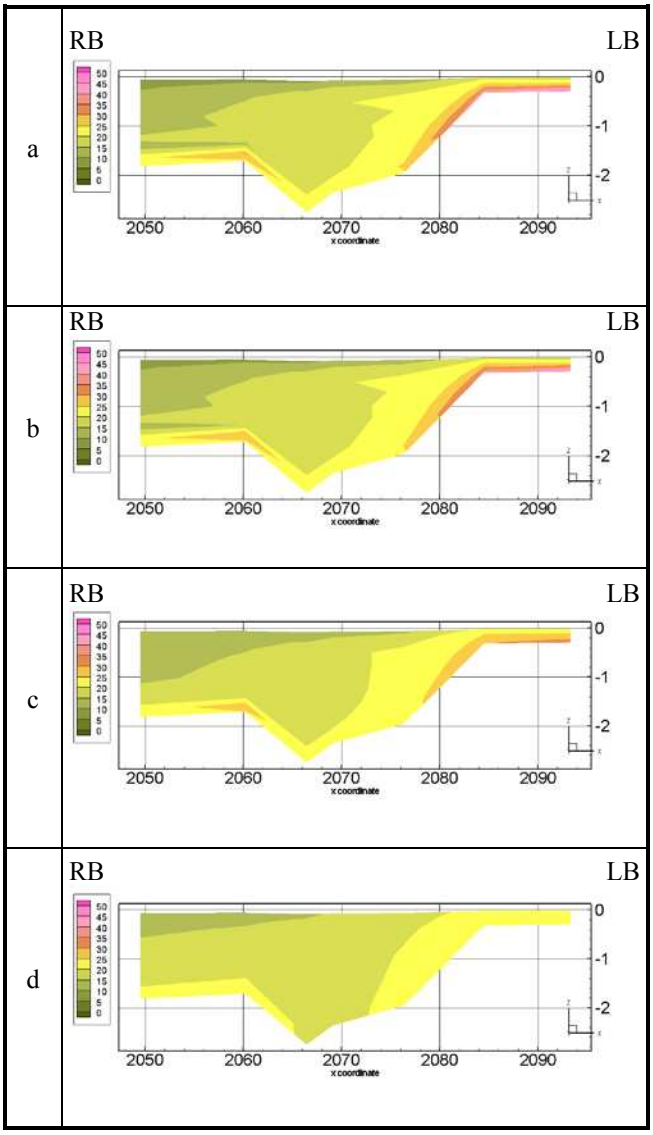

Figure 6. Vertical distribution of suspended sediment in mg/L using TELEMAC-3D a) 10^{-7} m^2s^{-1}, b) 10^{-6} m^2s^{-1},c) 10^{-5} m^2s^{-1},d) 10^{-4} m^2s^{-1}.

gradient induced by the use of the vertical dispersion of $10^{-4}m^2s^{-1}$.

V. VALIDATION OF THE NUMERICAL MODEL OF PCB TRANSPORT

In the second stage, DELFT3D-WAQ was run over 2 months under permanent flow. We use the numerical scheme 21 and a time-step of 10s. Fig. 8 shows the result of the vertical distribution of PCB-par, PCB-dis and PCB-tot in the water column. The model shows that PCB-dis varies from 5.10^{-6} to 7.10^{-6} mg/L (Fig. 8a). This order of magnitude is in agreement with the dataset (Table I). PCB-par varies from $1.3\ 10^{-6}$ to $5\ 10^{-7}$ mg/L (Fig. 8b). PCB-dis is therefore the main contributor of PCB-tot, compared to the other component PCB-par. PCB-tot varies from $7\ 10^{-6}$ to $6.2\ 10^{-6}$mg/L and shows vertical variations (Fig. 8c).

The modelled POC concentration varies from 0.2 to 0.4 mgC/L (Fig. 9a), which is lower than the order of magnitude generally found in rivers (from 1 mgC/L to 2 mgC/L) [9, 10]. The comparison between Figs. 9a and 9b shows that the vertical distribution of POC is correlated to IM1, the inorganic fraction, in agreement with the model equation (5). The highest concentration in IM1 and POC are found at the bottom of the left bank side and the right bank side. The PCB content of the sediment Q153SS is defined as the ratio of PCB adsorbed divided by the suspended solid, equation (9):

$$Q153SS = 10^6\ PCB\text{-}par\ /\ SS = 10^6\ PCB\text{-}par/(IM1+POM) \quad (9)$$

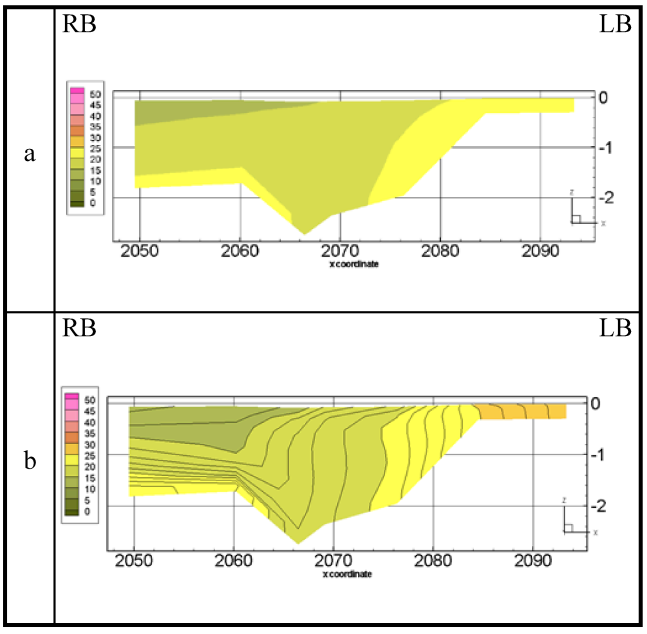

Figure 7. Comparison between 2 numerical scheme : a) scheme 16, b) scheme 21. The vertical diffusion is 10^{-4} m^2s^{-1} in both case.

The modelled PCB content in the sediment varies from 0.042 to 0.048 mg/kgDM (Fig. 9c). This value is also in the order of magnitude of the core data (Table I). Modelled vertical distribution indicates that higher PCB content in the sediment is found near the water surface of the right bank.

VI. CONCLUSION AND OUTLOOK

A numerical model of PCB transport has been developed using DELFT3D-WAQ. The model simulates the transport of sediment and PCB in a small channel, representative of a portion of a side-arm of the Rhone River. Comparison between sediment modelled with TELEMAC-3D and DELFT3D-WAQ has shown that a constant vertical diffusion of 10^{-4} $m^2s^{-1}$and the choice of the numerical scheme 21 was giving results similar to the sediment distribution modelled with TELEMAC-3D.

In a second stage, simulation over 2 months to simulate sediment transport and PCB transport was made. Results of the dissolved PCB and PCB adsorbed on sediment were compared against data available. It shows that modelled results are in the same order of magnitude than the datasets, which validates the PCB transport model processes and the parameters selected.

Future work will consist in running realistic simulation on a wider grid covering the main Rhone and both side-arms. The main objective is to assess the preferential area of deposition of PCB during high hydraulic flow.

ACKNOWLEDGEMENT

We are grateful to IRSTEA for providing the core data. This research was supported by the urban community Grenoble Alpes Metropole.

REFERENCES

[1] A. Beyer, M. Biziuk, “Environmental Fate and Global Distribution of Polychlorinated Biphenyls” in Reviews of Environmental Contamination and Toxicology”, DM Whitacre(ed.), vol. 201, pp. 137–157, .

[2] M. Babut, C. Miège, A. Roy, C. Lopes, G. Roux, M. Desmet, H. Persat. “Transfert de contaminants hydrophobes du sédiment au biote, construction de modèle dans un perspective de gestion.” Rapport Final, CEMAGREF

[3] E. Leclerc, ‘Caractérisation sédimentologique et géochimique des sédiments du Rhône’,2008, Master’s thesis.

[4] L. Vincent, “Modélisation tridimensionnelle des écoulements et du transport de sédiment fins sur un tronçon du Rhône”, 2011 Master’s thesis .

[5] ARTELIA « Etude du Transport de PCB dans le système Rhone , Modélisation fine sur un site pilote », technical report, juillet 2012, N°1741264R2

[6] J. L. Schnoor, “Environmental Modelling : Fate and Transport of pollutant in water, air and soil” , Wiley-Interscience Publication,1996, p682 .

[7] M. Babin, A. Morel, V. Fournier-Sicre, D. Fell-Stramsky, Light scattering properties of marine particles in coastal and open ocean waters relatied to the particles mass concentration.Limnology and Oceanography, 48(2), 2003, p843-859.

[8] DELFT-WAQ user manual,version 4.03, DELTARES, 18 may 2011

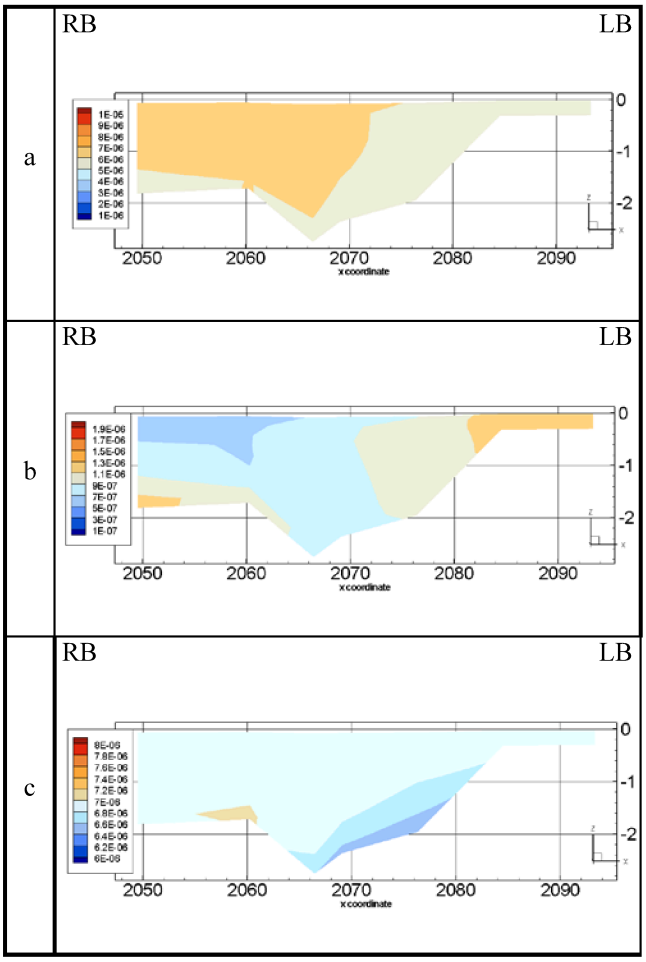

Figure 8. Vertical distribution of : a) PCB-dis (mg/L) b) PCB-par (mg/L), c) PCBtot=PCB-par+PCB-dis (mg/L).

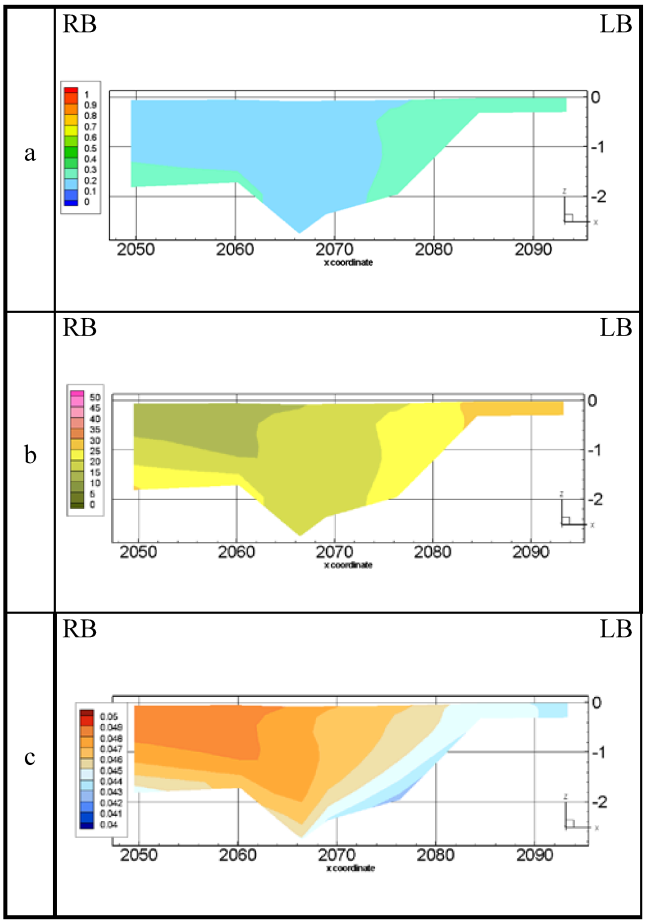

Figure 9. Vertical distribution of: a) POC (mgC/L), b) IM1 (mg/L), c) Q153SS (mg/kg DM).

[9] E. M.Thurman,1984. Organic geochemistry of natural waters, Wileys and Sons, New-York.p507.

[10] M. Meybeck, 1982. Carbon, nitrogen and phosphorus transport by world rivers. American Journal of Science 282, 401-450.

A one dimensional (1-D) numerical modelling of pesticide transfer through the wetland drainage channels of Breton-Vendéen marsh (west coast of France)

Gille J.[1], El Kadi Abderrezzak K.[2,3], Zaoui, F.[2], Robin M.[1], Gaillard S.[1]
[1] Université de Nantes, LETG Littoral, Environnement, Télédétection, Géomatique (GEOLITTOMER), UMR CNRS 6554, chemin la Censive du Tertre, B.P. 81227, 44312 Nantes Cedex 3, France
[2] EDF R&D, Laboratoire National d'Hydraulique et Environnement (LNHE), 6 Quai Watier, 78401 Chatou Cedex, France
[3] Laboratoire Hydraulique de Saint Venant (EDF-R&D-LNHE, ENPC, Paris-Est), 6 Quai Watier, 78401 Chatou Cedex, France
julian.gille@univ-nantes.fr

***Abstract*—Predicting pollutant transport in coastal ecosystems has become an important topic in many industrial and environmental projects, because of the degradation of water quality and conflicts related to multiple use of coastal resources. Most numerical studies on coastal catchment do not consider flow and pollutant fluxes through wetlands, or simulates theses transfers using "black box" based on linear regressions that greatly simplifies the complexity of the underlying processes.**

This paper presents a numerical study on the simulation of pesticide transport and degradation in the artificial wetland drainage channels of the Breton-Vendéen marsh (west coast of France). The one-dimensional (1-D), open source MASCARET modelling tool is used. The 1-D unsteady water flow through a network of open channels is represented by the shallow water equations. The water quality module of MASCARET simulates solute transport processes, consisting of advection, dispersion and mass reduction/generation by physical, chemical and biological mechanisms. Results show that the 1-D model is a reliable tool for simulating pollutant transfer through the coastal wetlands drainage channels. Moreover, it is possible to link landward and seaward models to MASCARET, which allows simulating water and pollutant propagation from watershed to coastal sea through wetland drainage channels with a high level of confidence

I. INTRODUCTION

The maritime marshes are wetlands where there is an interface between the watersheds and the coastal area. The particular conditions of these environments favour the development of specific flora and fauna with rare or threatened species. In accordance with their nature, they are used in diverse human activities, pasturing of prairies, reduce reeds, fishing, fish husbandry in fresh or salt water, shellfish farming and salt production on the coast, hunting, activities of discovering nature [10]. Since their international recognition in 1971, the preservation and the management of these sustainable humid zones have been placed in the framework of sustainable management of the natural resources and the preservation of the biodiversity [8]. On the European scale, these actions are notably promoted by the Water Framework Directive with the objective to attain a good ecological potential and a good chemical state of all bodies of water [1]. Developing a agro-hydrologic model for watersheds, coupled with a hydrodynamic model for the coastal area constructs a tool for the development of an integrated coastal zone management. This study goes further in developing a model for the pesticide transfer through the wetland drainage channels. The calculation and validation of the models is not finished but this article will present the modification of the source code, the method, discussion and perspective.

II. MODIFICATION OF THE SOURCE CODE

Among the six water quality models which are contained in the model *Tracer*, there was no model in which the degradation of pesticide is possible. The choice was to modify the transport of the tracers model *Transport_Pur* and to throw a degradation kinetic of the first order (1) and following open a source of the MASCARET code.

$$C_t = C_0 \times e^{(-k.t)} \quad (1)$$

with

$$k = -\frac{\ln(0.5)}{DT_{50}} \quad (2)$$

where C_t: concentration of pesticide over time t ($\mu g.s^{-1}$), C_0: initial concentration of pesticide ($\mu g.s^{-1}$), k: rate of degradation or constant dissipation (T^{-1}), DT_{50}: time of half-life (days).

The pesticide chosen is the glyposate. It is the most found in the studied zone. Its time of half-life is 69 days for a PH of 7 [Agritox]. The coefficient k is equal at 1.162686×10^{-7} s^{-1} (Fig. 1).

```
SUBROUTINE CALCS_RIEN( RNU , S , &
                       Nbsect , NBTRA , Nbsing , &
                       Q , A , H , RH , ST , C , &
                       SA , T , DT )

   use M_PRECISION
   use M_CONSTANTES_TRACER_T
   use M_PARAMETRES_QUALITE_EAU_T

   Implicit none

   real(DOUBLE) , Dimension(:,:) , intent(inout) :: RNU , S , SA
   real(DOUBLE) , Dimension(:)   , intent(in   ) :: Q , A , H , ST, RH
   real(DOUBLE) , Dimension(:,:) , intent(inout) :: C
   INTEGER      :: Nbsect , NBTRA , nbsing
   REAL(DOUBLE) :: T, DT

   REAL(DOUBLE), Dimension (Nbsect,nbtra) :: RNUS , SS , SSA , SV
   INTEGER I, K

   DO K = 1 , Nbtra
      DO I = 1 , nbsect
         S(I,K)   = SA(I,K) - C(I,K)*1.162686D-7
         RNU(I,K) = 0
      ENDDO
   ENDDO

   RETURN
END SUBROUTINE CALCS_RIEN
```

Figure 1. Modification of model.

III. METHOD

The place of study is the marsh of Breton-Vendéen, the fifth largest French metropolitan coastal wetland, situated in south of the estuary of the Loire. It is the receptacle of the water fluxes of the catchment where they continue to the Bourgneuf bay (Fig. 2).

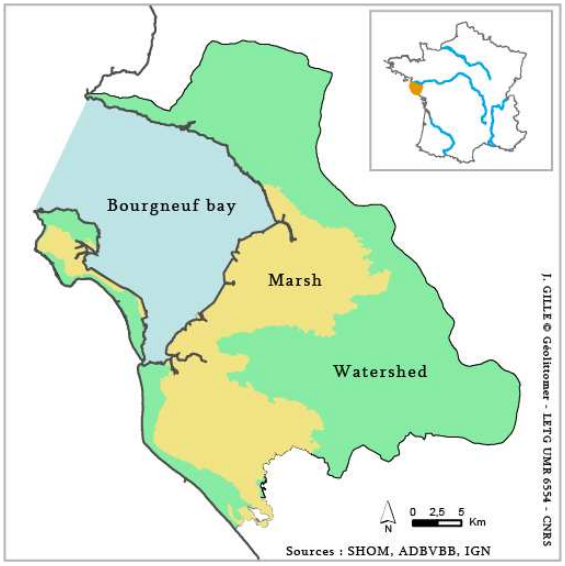

Figure 2. The geographic map off the section of study.

The marsh is fed by the river draining into the small watershed of an area of 10 km², except the one of the Falleron river of an area of 137 km². The flow of the Falleron river is known at the inlet to the marsh. For the other rivers, the distribution of the flow was realized according to the function of the under watershed area.

The period of study is May 26, 2007 to December 6, 2007 the discharge was less to 3 $m^3.s^{-1}$. This discharge threshold marks the overflow of river. It generally goes over between 30-50 days per year during the years. The mean annual discharge is equal to 1.2 $m^3.s^{-1}$ (Fig. 3).

The objective is to follow the transfer of the water flow in the Bourgneuf bay catchment. The model is carried out in the pilot area situated in north of Breton-Vendéen marsh (Fig. 5). The one dimensional (1-D) numerical modelling MASCARET is used [2]. The main drainage channels are defined by 20 reaches and 153 channel sections (Fig. 6). The channel section are created by measures of the ground. The length (AB) and depth (AL) of the channel are known (Fig.4). Finally to reconstruct the entire channel section, it was chosen to take an angle a equal to 30 degrees when it's possible, otherwise equal to 70 degrees for the maximum the points M and N are similar.

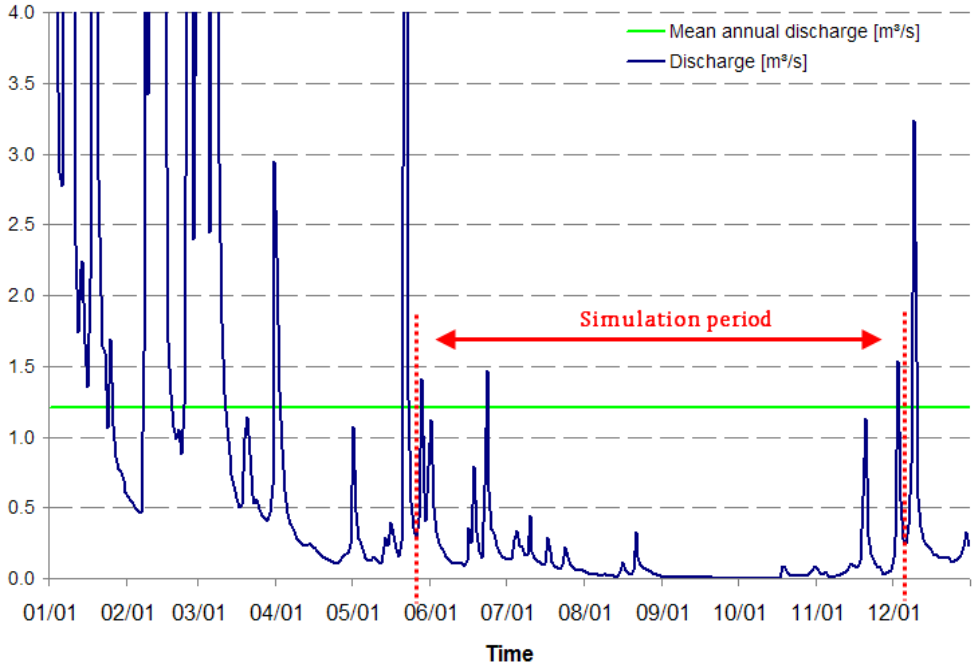

Figure 3. Discharge at the entrance of the marsh in 2007.

The bottom slope is 0.03 ‰, the mesh of 1 m, the planimetry of 0.01 m and the downstream side is constantly equal to 1.8 m. The calculation time is 60 s.

The concentrations of the glyphostate measured in the main river vary between 0.2 and 1.6 µg.L^{-1}. The inlets are forced to a average concentration of 1 µg.L^{-1}.

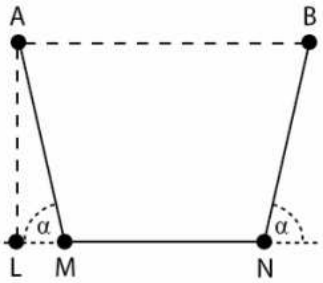

Figure 4. Drawing of the channel section.

IV. Discussion and Perspectives

In these hydro-geomorphologic and hydrodynamics conditions, the longitudinal dispersion coefficient is less influent. The finite-difference method 2 (FD2) is less dispersive to those of finite-difference 1 (FD1). Only the roughness seems to have an important impact of the discharge superior to 1 m^3.s^{-1} (Fig. 7). In the hypothesis where the hydraulic management are not modified the flow circulation, the time of pesticide transfer in the marsh is estimated at about 1.5 day for a discharge of 2 m^3.s^{-1} and about 8 days for a discharge of 0.5 m^3.s^{-1}.

From the 43rd day, the concentration of glyphosate evolved in a manner similar to the outlet of the marsh, like the dispersion coefficient and the Strickler coefficient. The discharge is too weak for these coefficients to impact sufficiently the concentration of glyphosate.

Where the marsh does not carry glyphosate, the reduction can get to 50% when it goes out of the marsh during the study period. This model can equally permit the differences between the dilution loss and the degradation loss. In this case, the difference comes up to a maximum of 0.2 µg.L^{-1}.

Finally if these first estimations remain to refine and to validate, they are already particularly interesting for economic activities as the shellfish farming, for which the quality of the water is essential. These last years, strong mortalities are observed on the French coast. Pesticides are suspected by the shellfish farmers to be there partially originally. The chaining of the agro-hydrologic model SWAT [7] with the hydrodynamic model MARS 2D [6] was already able to allow to bring some elements of answer for shellfish ponds of Croisic and Pen-Bé [5], of the Payré channels [4] and of the Thau lagoon [9].

By adding it the modelling marsh (Fig. 8), this kind of study can allow to follow the quality of the water from the watershed to the bay (Fig. 9), to test scenarios aiming at the improvement of the quality of coastal waters and conservation of the activities bound to the marine cultures and so to contribute to the implementation of an integrated coastal zone management [3].

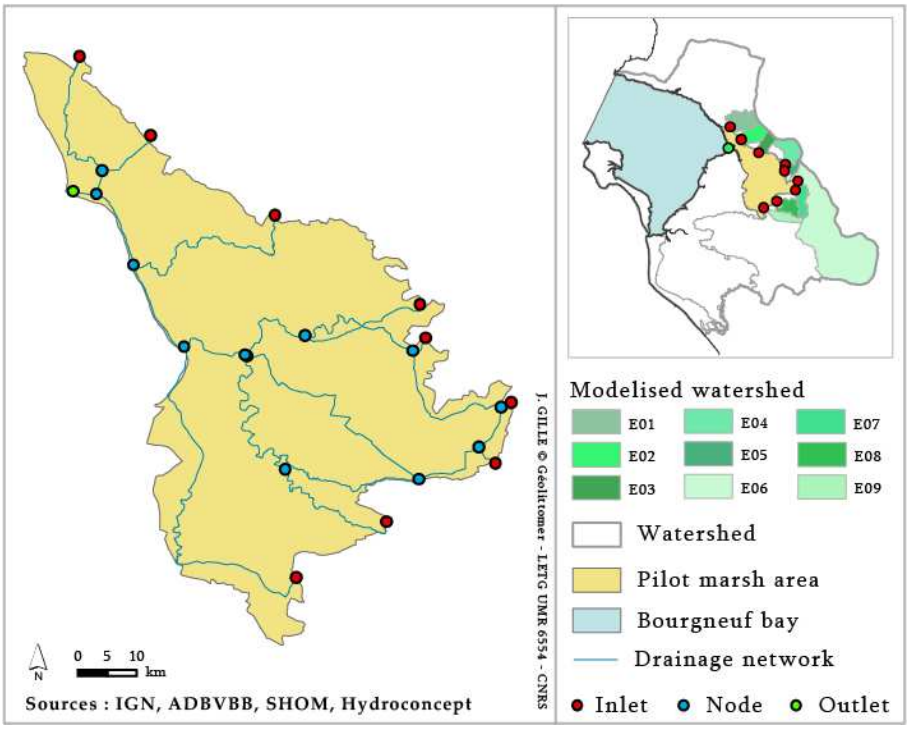

Figure 5. Drainage channel in the pilot area.

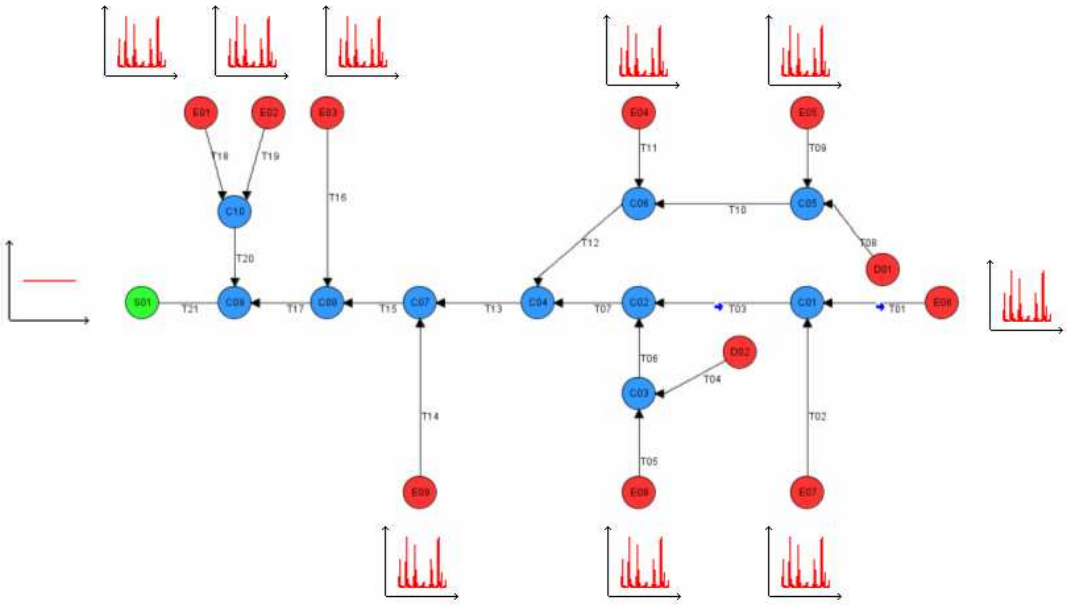

Figure 6. Architecture of the modelling channel in MASCARET with the hydraulic laws in extremities.

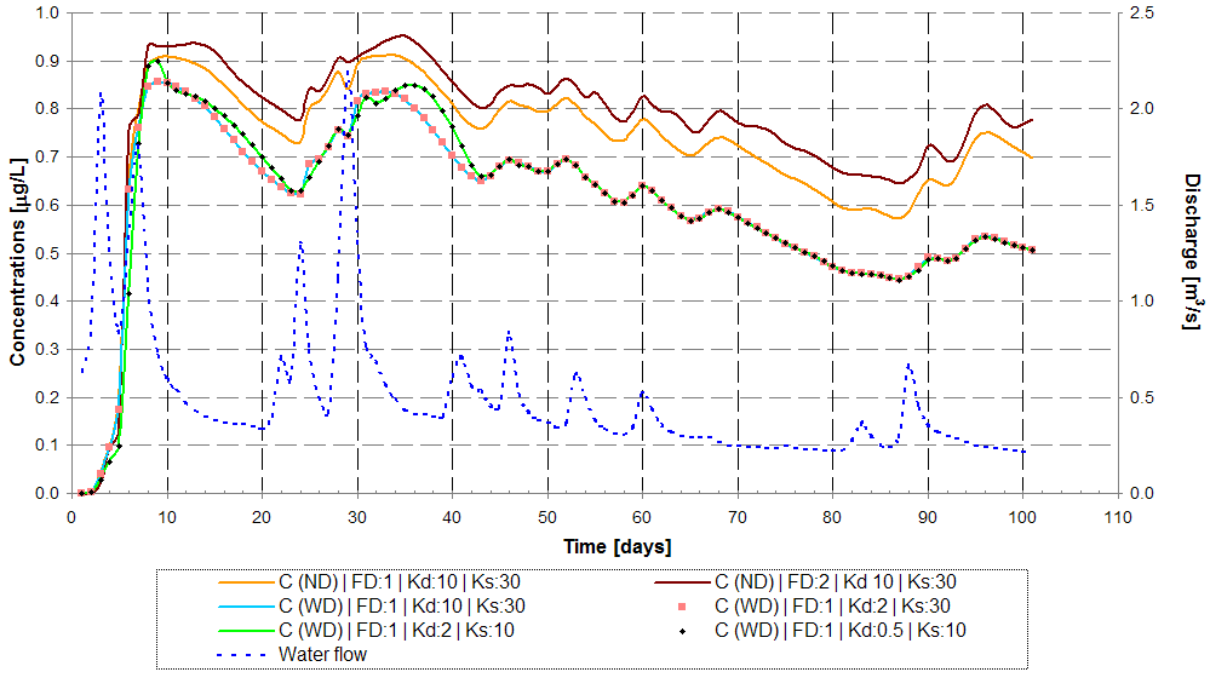

Figure 7. Evolution of discharge and concentration of glyphosate at the port of Collet
(C: concentration, ND: no degradation, WD: with degradation, FD: finite-difference method, Kd: dispersion coefficient, Ks: Strickler coefficient).

Figure 8. Chaining of models.

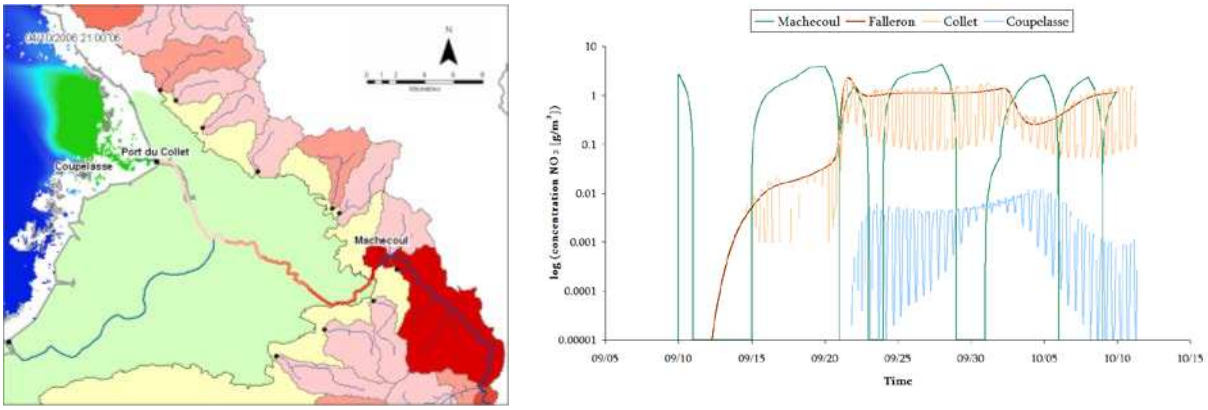

Figure 9. Pollutant evolution in the environment
(left: red for the highest concentrations, blue for the weakest;
right: concentration in the inlet marsh (Machecoul) and the outlet marsh (Falleron and Collet), in the oyster park (Coupelasse)).

ACKNOWLEDGEMENTS

This study was financed by the Pays de la Loire region and piloted jointly by Ifremer and the University of Nantes. It joins in the third axis of the research program GERRICO (*GEstion globale des Ressources marines et des RIsques dans les espaces COtiers*), aiming at the development of decision-making tools for the integrated coastal zone management. Several establishments or institutions were contacted for input data. The authors are anxious to thank particularly Météo France, the CEP / SAH Sud Loire, Hydroconcept, the ADBVBB and the DREAL of Pays de la Loire for having given it the access. Finally, one thank you to the team of the MASCARET model developers without whom the modifications of code and the handling would not have been able to be possible.

REFERENCES

[1] CE (2000): "Directive 2000/60/CE du Parlement Européen et du Conseil du 23 octobre 2000 établissant un cadre pour une politique communautaire dans le domaine de l'eau", Journal Officiel des Communautés Européennes, L 327, 22 décembre 2000, 72p.

[2] CETMEF (2008): "Guide de prise en main de Fudaa-Mascaret 3.0", Notice n°GT 08.01, Avril 2008, 137p.

[3] Gille J., Gaillard S., Hitier B., Robin M., Oger-Jeanneret H., Lecomte P. (2010): "Modélisation des apports des bassins versants en baie de Bourgneuf" in, Actes des XIèmes Journées Nationales Génie Côtier – Génie Civil, 22-25 juin 2010, © Editions Paralia CFL, Les Sables d'Olonne, pp.275-282

[4] IFREMER (2007): "Mesure des flux hydrauliques dans les chenaux du Payré : lien avec la contamination microbiologique des zones ostréicoles - Approche hydrodynamique", Appel à proposition 2007 du Comité Scientifique et Technique et du SMIDAP pour la Région des Pays de la Loire, 15p.

[5] Jeanneret H., Gendronneau M., Haure J., Le Merrer Y., Lequette C., Lomakine C., Martin J.-L., Papin M., Ponthoreau C., Robin M. (2006): "Étude des secteurs du Croisic et de Pen-Bé : estimation des apports continentaux et évaluation des stocks conchylicoles", Fiche documentaire, Ifremer, Mars 2006, 118p. + annexes

[6] Lazure P., Dumas F. (2008): "An external-internal mode coupling for a 3D hydrodynamical model for applications at regional scale (MARS)", Advances in Water Resources, 31(2), pp.233-250

[7] Neitsch S.L., Arnold J.G., Kiniry J.R., Williams J.R., King K.W. (2002): "Soil and Water Assessment Tool", Theoretical documentation, 506p.

[8] ONU (1971): "Convention relative aux zones humides d'importance internationale, particulièrement comme habitats des oiseaux d'eau", 2 février 1971, Ramsar (Iran), 6p.

[9] Plus M., Maurer D., Stanisière J.-Y., Dumas F. (2006): "Caractérisation des composantes hydrodynamiques d'une lagune mésotidale, le Bassin d'Arcachon", Ifremer - Laboratoire Environnement littoral - Ressources aquacoles d'ARcachon, 01 novembre 2006, 54p.

[10] Verger F. (2005): "Marais et estuaires du littoral français", Belin, Paris, 335p.

An oil spill model for inland waters applied to the "Happy Bride" accident

Cédric Goeury[1], Jean-Michel Hervouet[1,2], Olivier Bertrand[3], Régis Walther[3], François Thouvenel[4], Isabelle Baudin-Bizien[4], Johann Mazzella[4]

[1] Saint-Venant Laboratory for Hydraulics (joint research unit between EDF R&D, CETMEF and Ecole des Ponts) Chatou, France

[2]EDF R&D, Laboratoire National d'Hydraulique et Environnement (LNHE), Chatou, France

[3]ARTELIA, Echirolles, France

[4]VEOLIA Recherche et Innovation (VERI), Rueil-Malmaison, France

isabelle.baudin-bizien@veolia.com and francois.thouvenel@veolia.com

***Abstract*—The application of the European Water Framework Directive and the monitoring obligation on water quality for human consumption and industrial activities create a need for water quality assessment and monitoring systems. The Migr'Hycar research project (see: http://www.migrhycar.com), partly funded by the French National Research Agency (ANR) as part of the PRECODD programme for Ecotechnology and Sustainable Development, was initiated to provide decisional tools, and to fulfil operational needs, for risks connected to oil spill drifts in continental waters (rivers, lakes, estuaries).**

Within the framework of the Migr'Hycar project, a new numerical oil spill model has been developed by combining Lagrangian and Eulerian methods within the TELEMAC modelling system. The Lagrangian model describes the transport of an oil spill near the free surface. The oil slick is represented by a large set of small hydrocarbon particles. This model simulates the main processes that act on the spilled oil: advection, diffusion, evaporation, dissolution, spreading and volatilization. Though generally considered a minor process, dissolution is important from the point of view of toxicity. Dissolved oil in water is modelled by an Eulerian advection-diffusion method. The fraction of dissolved oil is represented by a passive Eulerian scalar and its quantity directly depends on the dissolved mass of Lagrangian particles. This model is able to follow dissolved hydrocarbons in the water column (naphthalene, anthracene, phenanthrene, chrysene).

Numerical oil spill simulation is controlled using a Graphical User Interface (GUI). This modelling interface will make the program easy to use in a crisis context, and will gather all relevant information so that the stakeholders can make the right decision.

The oil spill system and the GUI are validated by simulating an actual accidental spill incident in the Loire estuary (France). In January 2006, the tanker "Sigmagas", after a rudder problem, collided with the "Happy Bride". 60 tons of heavy fuel were spilled into the estuary.

I. INTRODUCTION

Although in almost half of all instances of contamination the exact cause is never determined, oil spills can be due to human error, accidental or deliberate discharge of cargo residues, domestic or industrial tank overflow, leakage from fuel stations, traffic accidents or fire, amongst other causes.

When faced with hydrocarbon contamination of inland waterways, authorities and other organizations can seldom rely on dedicated decision-making tools to intervene in an effective way.

Whereas considerable management and monitoring resources are rapidly deployed for off- or inshore oil incidents, the more frequent occurrence of continental water pollution is dealt with using relatively modest means. A limited grasp of the nature and magnitude of such events often renders both industry and government powerless in controlling their impact.

The Migr'Hycar research project (www.migrhycar.com) was initiated to provide decisional tools, and fulfil operational needs, for risks connected with oil spill drift in continental waters (rivers, lakes, estuaries). These tools are meant to be used in the decision-making process after an oil spill and/or as reference tools to study potential impact scenarios of pollution on a given site. The Migr'Hycar consortium has been organized to closely match project objectives and comprises modelling technology developers (EDF, Saint-Venant Laboratory for Hydraulics, ARTELIA, VEOLIA), researchers with long-standing experience of hydrocarbon physicochemical behaviour (Agribusiness laboratory LCA, CEDRE), engineering consultants liaising closely with local and regional authorities (ARTELIA), two water intake operators directly concerned with project-related issues and well experienced in applying protective warning systems (EDF, VEOLIA), and a major player in the oil industry (TOTAL). The consortium has therefore the expertise required to develop a surface-water risk monitoring and prevention system against oil spillage contamination.

The proposed application of the deterministic model developed for this project is the modelling of the collision that took place between two butane carriers in the Loire estuary on 4 January 2006. On this date the Happy Bride's heavy fuel oil tank was struck by the Sigmagas and subsequently spilt its 60 m3 reservoir of IFO 380. This event is presented below alongside a discussion of the results obtained and the areas for improvement to be considered.

II. THE 3D OIL SPILL MODEL

Within the framework of the Migr'Hycar project, a 3-D oil spill model has been developed, inside the TELEMAC system [1], by combining Lagrangian and Eulerian methods. This model can be used to simulate the main processes acting on the spilled oil: advection, diffusion, evaporation, dissolution, spreading and volatilization (Fig. 1). Though generally considered as a minor process, dissolution is important from the point of view of toxicity. The Lagrangian model describes the transport of an oil spill near the free surface.

To model dissolved oil in water, an Eulerian advection-diffusion model is used. The fraction of dissolved oil is represented by a passive Eulerian scalar. This model can monitor dissolved hydrocarbons in the water column (PAH: Polycyclic Aromatic Hydrocarbons). The Eulerian model is coupled with the Lagrangian model [2], [3].

III. THE GRAPHICAL USER INTERFACE

The graphical user interface has been designed to control the numerical oil spill model developed in the Migr'Hycar project. With this decision-aid tool it should be easy to simulate an accidental event occurring in a river or estuary and quickly provide clear information to make the right decisions in a crisis situation.

A. Development environment

Migr'Hycar interface is developed in VB.Net on Visual Studio 2010 Professional, with the .NET Framework 4. It uses the Windows Forms application technology.

Input files are used to run TELEMAC. Based on the information entered by the user, Migr'Hycar will create a directory containing all the files needed for a TELEMAC calculation.

Specifically for the configuration file, it is based on a system of frames files, in which the expert user can define parameters he wants static, and those whose value will be evaluated dynamically each time.

The application will then launch the calculation TELEMAC, and get the output listings for several treatments (curves, logs...).

B. GUI features and functions

The interface is designed to be accessible and intuitive, and there is no need to have any knowledge of modelling. In fact, the tool is dedicated to operators of drinking water plants and environmental authorities so they can take action as soon as possible. The functionalities of this interface have been developed around two pilot sites, the river Garonne and the Loire estuary. This paper presents the interface for the estuary model.

The first window allows the user to choose between three options, "new pollution", "calculate hydraulic archive" and "archive pollution." The interface is composed of a 2D map view of the model in a central position and a side panel to provide certain information and to change window.

The pollution definition begins with location of the accident ("Generalities" tab). The location can be defined directly by clicking on the 2D map or by providing 2D coordinates. The model boundary conditions must then be specified, for example the flow of the Loire and the water height at the ocean edge. A tide file can also be provided if this condition is not included in the code. The operator can give a value of wind intensity and direction (if constant), or provide a suitable file. Other parameters such as water temperature, salinity and suspended matter can also be changed in this tab. Fig. 2 presents the interface first window, called "Generalities".

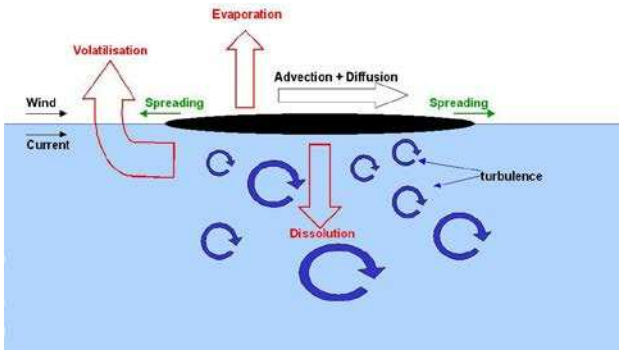

Figure 1. Fate and transport oil surface slick processes.

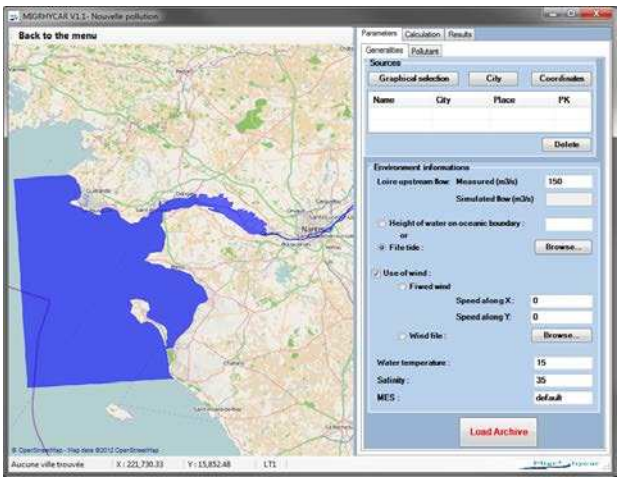

Figure 2. "Generalities" tab.

In the "pollution" tab the volume and surface contaminant discharged must be specified and the operator can also enter more specific pollutant characteristics, such as density and kinematic viscosity (default values are proposed). It is also possible to change the name, the recording date and time of the pollution. Once all these steps are validated, the TELEMAC calculation can be started (tab "Calculation").

During the calculation step, a graph shows the fluctuations in certain parameters such as the amount of dissolved pollutant mass, etc. The calculation ends when either of two conditions is satisfied: when the oil spill is exhausted, or when the set computation time is reached.

Results are displayed through two windows, the first being a graphical visualisation of the results and the second presenting pollutographs. In the "visualisation" window, the model is displayed on the 2D map with a side panel providing options for displaying results. The parameter to be display and the desired depth / water layer can be chosen. The bottom of the window is dedicated to animation management, speed display, time selection, reading and pause etc.

Parameters can also be visualised more precisely on a point or along a segment. For this purpose, the options "point" or "line" on top of the 2D base map are used.

Two graphs in the side panel allow the operator to observe the results of the "point" or "line" options, the first presents the selected parameter variations and the second is the parameter variation depending on depth (this will be a section with the "segment" option). The time can be varied while watching the two graphs Fig. 3.

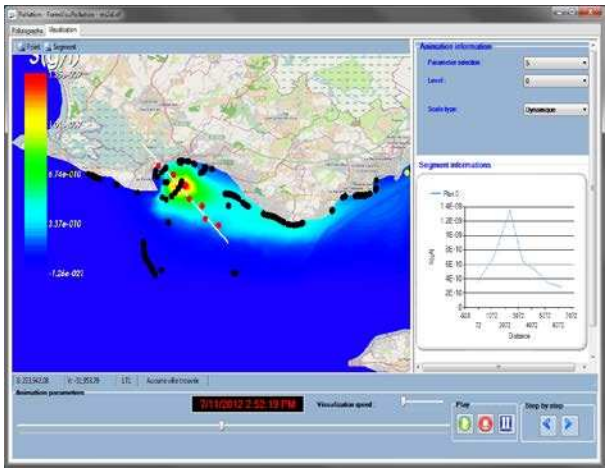

Figure 3. 2D visualization with "Segment" mode.

The pollutographs can be displayed from the "visualisation" window. These show the concentration fluctuations at previously defined "points of interest" (water intakes, protected areas, beaches), but also give a reminder of the event conditions. The "Alert" box becomes active if threshold pollution is exceeded on one of the intakes. Critical information is shown, such as arrival time, duration of the alert and end of the event. A comprehensive report can be generated giving information that can be used by the authorities.

Simulations are automatically archived and a simulation can be loaded using the "pollution archives" available on opening the GUI.

For a river model, a hydraulic archive can be recalculated if the data in the database are not suitable. This "new hydraulic archive" method is also available on opening the tool.

IV. THE LOIRE ESTUARY

The Loire estuary is one of the three major French estuaries. It opens out into the Atlantic Ocean at Saint-Nazaire. It is a macro-tidal estuary with a mean spring tidal range of about 5 m allowing the tide to propagate up to Ancenis, 90 km upstream of Saint-Nazaire. The main city, Nantes, is located 55 km upstream. The long-term mean discharge of the Loire river is 825 m^3/s with considerable variations ranging from 60 to 6,000m^3/s.

Given its physical configuration and demographics, the Loire estuary is subject to considerable constraints and constitutes an area in which different human activities overlap. For the most part, the various industrial and commercial centres are concentrated around the major urban areas. The activity of the Nantes Saint-Nazaire port (now known as the Grand Port Maritime), in particular, has allowed several industries to flourish in the industrial port area of Montoir-Donges.

At the same time, the organisation and distribution of the drinking water production network reflects the specific features of the physical environment, and as such consists of relatively few production units in relation to the population served and is supplied predominantly from surface water sources.

Together, all of these factors make the estuary a sensitive environment where hydrocarbon pollution could have a serious impact on both the water and, by extension, its use for agriculture, drinking water supply and industrial use at the EDF power plant at Cordemais.

The GIP Loire Estuaire (GIPLE) appointed Artelia to carry out a study to develop and operate a three-dimensional hydro-sedimentary model of the Loire estuary in the context of its "Programme to restore the Loire estuary downstream of Nantes". This hydrodynamic model [4] was reused in the context of the Migr'Hycar project and was checked with regard to tide propagation in the estuary and upriver as far as Nantes. A description of the model is given below.

A. The 3D hydraulic model

The Loire estuary forms the meeting point between the river and the ocean and, as a result, has complex dynamics. For example, salt water intrusion generates density currents

and stratification effects. 3D modelling would therefore seem to be the most appropriate way of studying this area where the hydrodynamics is determined by the tidal range, the river flow rate, water salinity and weather conditions.

The developed model covers an area extending from Ancenis upstream to Grande Baie downstream, including the Bourgneuf Bay to the south and the headland of Le Croisic to the north, totalling around 90 km of river and 40 km of coastal waters out to sea.

The daily flow rate measured at Montjean was imposed at the upstream limit of the model (Ancenis) and, at times of flood, includes the flow rates from the Sèvre and the Erdre rivers (confluences located at Nantes). The astronomical tide is imposed at the maritime limit of the model, with the average level calculated using tidal measurements from Saint-Nazaire for the period simulated.

For the calibration of the model, the value of wind intensity at sea (as extracted from point CROISIC1 in the Prévimer database) is applied equally across the maritime part of the model, and is then interpolated from the downstream limit of the Saint-Nazaire port access channel to downstream of Donges where its value is considered negligible. The aim of taking wind into account in the model is to avoid having to simulate tidal surges in the estuary, as this would require a more elaborate hydro-meteorological model. In any case, surge is taken into account by the time-dependent change in the average level in the boundary conditions. The aim of including wind factors in the 3D model is to generate the three-dimensional water circulation in the external estuary that is likely to lead to significant changes in the residual circulation of the astronomic tide. Such effects are in contrast negligible in the internal estuary, where the dominant effects are turbid and saline stratification together with the tide and the flow rate of the Loire. Later, to study the oil spill event, a spatially interpolated wind from the CFSR model has been used (Climate Forecast System Reanalysis (ftp://nomads.ncdc.noaa.gov/CFSR)).

B. Calibration of the model

The main purpose of the hydrodynamic calibration of the model was to adjust the friction coefficients per zone in order to represent tidal propagation correctly in the estuary. The friction laws chosen are the Nikuradse law downstream of Sainte-Luce-sur-Loire and the Strickler law upstream of this point. The Nikuradse formulation depends on the grain size of sediment and on the velocity profile over the bottom, whereas the Strickler formulation, only deals with the vertically averaged velocity. The Strickler formulation is preferable for including, in the friction term, other head losses such as vegetation on the banks, groynes, weirs, bridge piers.

Taking liquid mud into account in the calibration stage required the use of a lower friction coefficient (in relation to the standard friction coefficient for a sandy riverbed) in the area in which liquid mud is assumed to be present. This coefficient varies with the flow rate (Fig. 5).

Figure 4. Horizontal mesh of the Loire mouth.

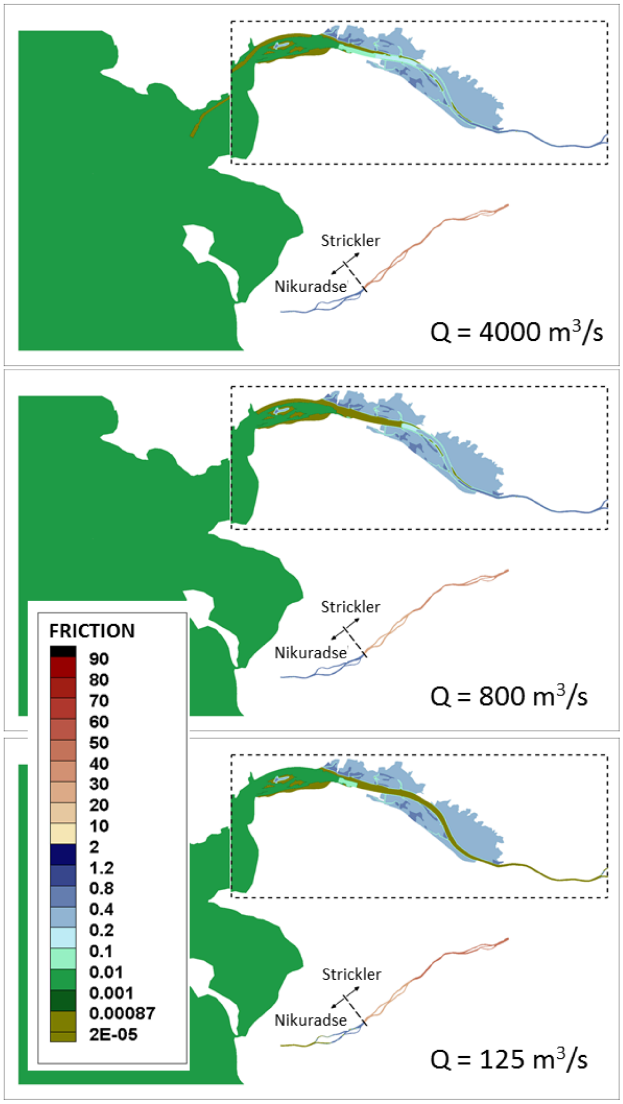

Figure 5. Friction maps for various flow rates.

The results obtained for tidal propagation in the estuary are presented in Figs. 6 and 7 for flood and low water periods respectively.

V. THE HAPPY BRIDE AND SIGMAGAS EVENT

A. *Description of the collision*

The Donges refinery produces liquid butane gas, part of which is transported by sea. Consequently, LPG tankers regularly transit through the Loire estuary. On 4 January 2006, the LPG tanker "Sigmagas" left the refinery after having loaded its cargo of butane while the LPG tanker "Happy Bride" entered the channel on its way to the refinery. A few minutes before they passed each other, the Sigmagas experienced a rudder problem which caused the vessel to veer to port on a collision course with the Happy Bride. At 8.20 pm, the Sigmagas hit the middle port side of the Happy Bride, rupturing a bunker oil tank. All the fuel oil contained in this tank (60 m^3 of IFO 380) subsequently spilled into the estuary. Further details on the circumstances of this accident are available in the BEAmer enquiry report (2006).

On 5 January, an aircraft operated by the French Customs authorities reported a 17 km long, 300 m wide oil slick (with an estimated quantity of 13 m^3) running from Saint-Nazaire bridge in a west/south-westerly direction. In addition to the observations, the MOTHY model operated by Météo France (http://www.meteorologie.eu.org/mothy/) was used to obtain a weather forecast for the area and oil slick drift maps as quickly as possible.

The mathematical model of oil slick drift developed in the Migr'Hycar project and the 3D hydrodynamic model of the estuary were used to simulate the drift of the polluting slick caused by the collision between the two liquid butane carriers.

B. *Modelling of the oil slick*

Figs. 9 to 11 show the change in the surface oil slick as recorded by monitoring teams during the first three days compared with the simulation results.

1) Situation on Thursday 5 January 2006 (Fig. 9): At the time of the collision, the current was directed downstream towards the Loire estuary outlet (high tide at 7.50 pm) and the slick was therefore carried towards the estuary outlet. This phenomenon was no doubt amplified by the saline stratification of the water. In the first few hours following the spill, the oil slick remained located in the northern part of the estuary, as shown on the maps produced by the accident crisis management teams (CEDRE, 2006a). This result was mirrored by the simulations, specially under the effect of a south-westerly wind.

2) Situation on Friday 6 January 2006 (Fig. 10): On 6 January, a helicopter survey was arranged in order to assess

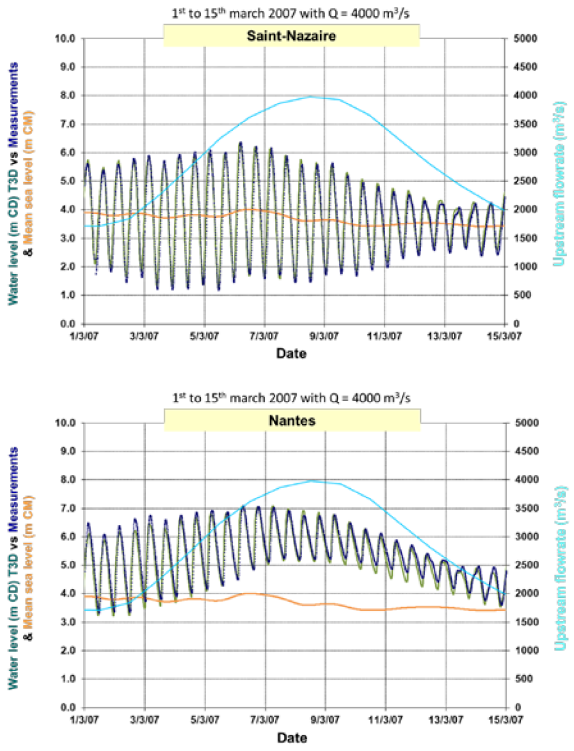

Figure 6. Comparison of the water level between model and measurements at Saint-Nazaire (top) and Nantes (bottom) for a flood period.

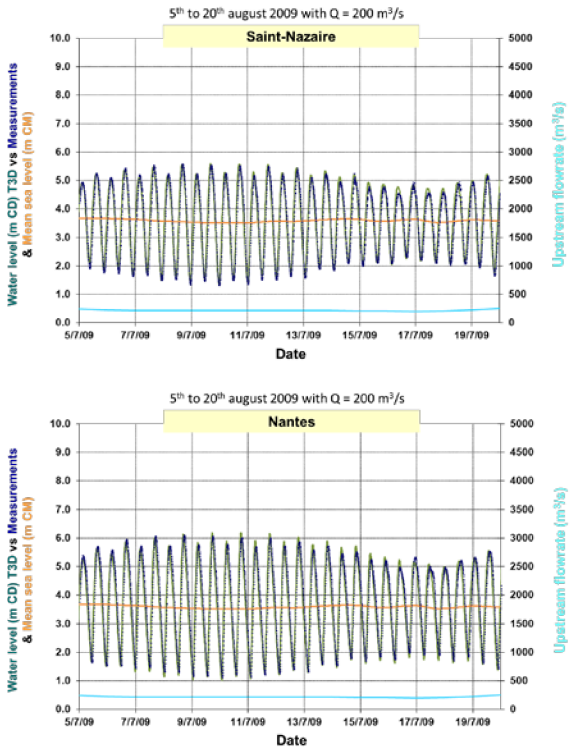

Figure 7. Comparison of the water level between model and measurements at Saint-Nazaire (top) and Nantes (bottom) for a low water period.

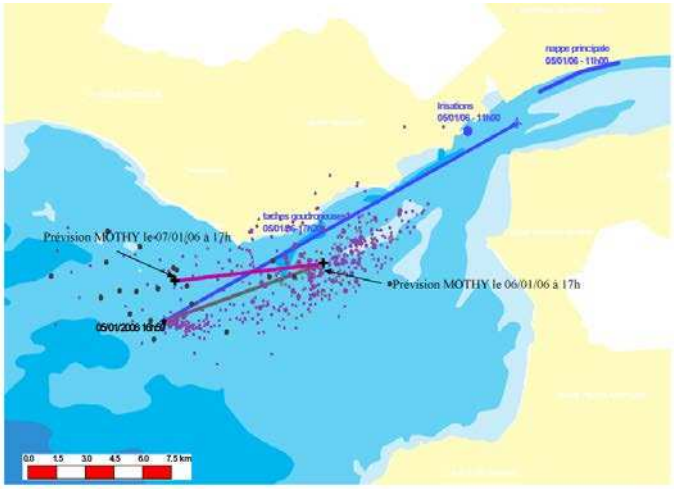

Figure 8. Summary of sea observations on 05/01/06 and probable drift forecast by MOTHY over a 48-hour period.

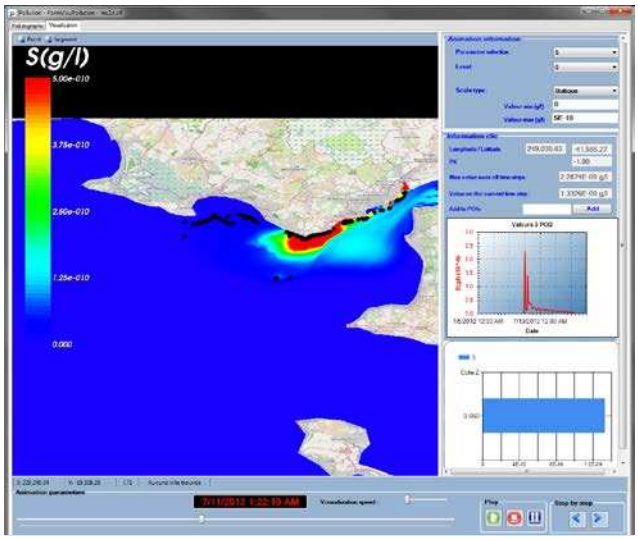

Figure 9. Oil slick location on 01/05/2006, 5 PM.

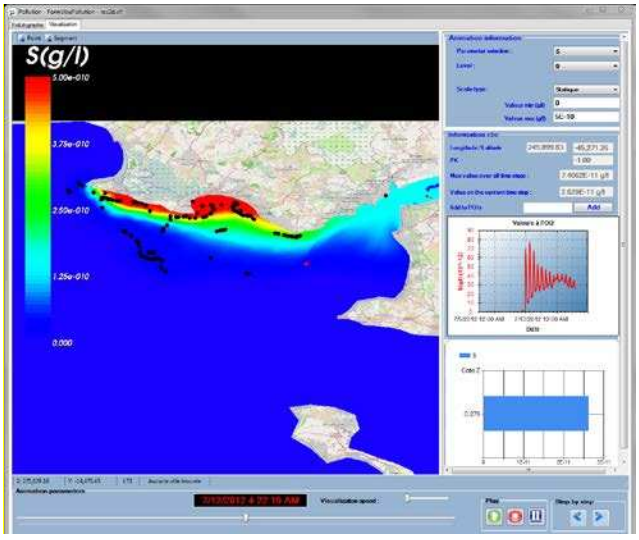

Figure 10. Oil slick location on 01/06/2006, 5 PM.

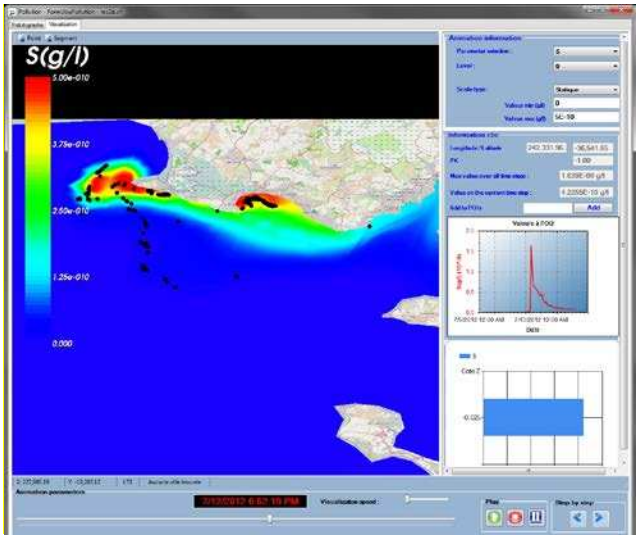

Figure 11. Oil slick location on 01/07/2006, 5 PM.

the extent of the pollution in a polygonal area. In this fly-over zone, the digital results at the different times recorded are consistent with the observations. However, the model predicts the presence of a major part of the slick outside the aerial survey zone. Observations taken on land also indicate residual deposits on the south-west shore of Paimboeuf, and on the Bilho sand bank. These pollution points are not detected by the model. The results show that improvements can be made by refining data on the adherence of the oil slick to the estuary banks. However, this parameter is very delicate because it depends not just on the location (distinguishing between different types of bank) but also on the date on which the simulated spill took place (different vegetation depending on the season).

3) Situation on Saturday 7 January 2006 (Fig. 11): Observations taken on land indicate the presence of small lumps of solidified oil in La Baule bay and residues at the mouth of the estuary. The results obtained by the model match these observations.

Residual deposits are observed in the upstream and downstream vicinity of Donges refinery and on the right bank of the estuary. These deposits are probably due to lumps of oil previously deposited on the shore being picked up again as a result of tidal level variations.

The results obtained from this oil slick modelling procedure are encouraging and demonstrate the forecasting feasibility of the model with a view to preventing pollution of installations that might be affected in continental waters. In this same area dominated by tidal currents and the Loire river flow, oil slick drift is affected to a large extent by wind conditions. By making better allowance for wind, by processing more detailed data in time and in space, it should be possible to represent oil slick drift more accurately. The results can also be improved by a more detailed analysis of the adherence of the oil slick to the estuary banks.

C. *Variation in PAH content in the water*

When pollutants affect continental waters, compounds containing Polycyclic Aromatic Hydrocarbons (PAH) are likely to interact with the marine environment under the water surface as a result of their solubility. Moreover, these compounds are carcinogenic and, as a result, are most toxic to man. Consequently, they are considered to be "priority hazardous substances" by the water framework directive (Article 16-2).

At the time of the oil slick, the *Direction Départementale des Affaires Sanitaires et Sociales* (local health and social affairs department) and Ifremer collected shellfish samples in order to assess the level of PAH contamination in sensitive areas in the Loire estuary. Marine organisms like shellfish are used as quantitative indicators of chemical contamination as they have the faculty of accumulating the contaminants present in this environment until equilibrium is reached. Determination of the pollutant amounts in the organisms is facilitated by the high concentrations found in them.

The results of the sampling survey of 11 January 2006 reflect a substantial increase in shellfish contamination by PAH compared to the values measured on 5 January 2006, especially in the northern part of the estuary (Fig. 12).

Without any other sampling survey, it is difficult to compare the concentrations obtained by the computation code with the results of analyses carried out during the pollution event because the bioaccumulation phenomenon taking place in living organisms requires detailed knowledge of PAH exposure time of the shellfish, as well as a concentration factor between the environment and the living organism. The comparison between the numerical model and the observations will require a more detailed survey to finalise this study.

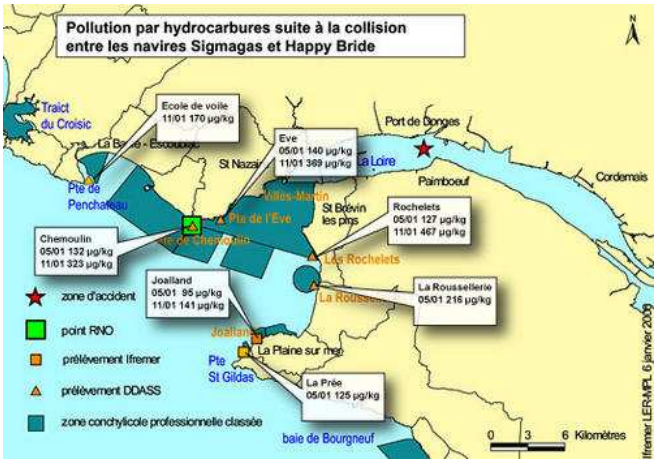

Figure 12. Summary of PAH determinations following the spill (source: IFREMER http://envlit.ifremer.fr)

VI. CONCLUSION

While major oil spill catastrophes, occurring mainly in an oceanic or coastal environment, result in the rapid deployment of large-scale crisis monitoring and management tools, accidents of lesser importance, despite occurring much more frequently, are more often than not managed with only limited facilities, especially with regard to pollutant spills affecting continental waters. Given the limited knowledge of the nature and importance of such events, local authorities charged with taking the necessary health or economic protection measures are generally powerless when confronted with the environmental consequences. Accidents involving the oil pollution of continental waters are increasing at an alarming rate, with an average of one spill every 40 hours over the 2008-2010 period [5].

Application of the Water Framework Directive and the obligation to monitor the quality of water used for human consumption and for recreational or industrial activities, has led to a massive rise in demand for water quality assessment and monitoring systems.

The Migr'Hycar project was set up in this context and has been used to develop a modelling tool to simulate the migration of oil slicks in continental and estuary waters. Linked to a database for hydrocarbon physical-chemical characterisation, this tool is destined for operational use.

A mathematical model of oil slick drift, comprising a Lagrangian model coupled with an Eulerian model, was therefore developed within the TELEMAC hydro-informatic platform.

At the same time, a user-friendly interface for controlling the simulations and simplifying model operation in a crisis situation was programmed. This interface must collect all useful information so that the user can take appropriate measures. Once a pollution event has been identified, the interface will therefore provide the operators with a clear summary of the anticipated risks involved, to allow them to communicate informatively with the local authorities and all stakeholders concerned.

The Loire estuary test site, following the Happy Bride accident, was chosen in order to evaluate the relevance of the tools developed. This application illustrates the hydrodynamic complexity of the environment in these stratified areas where sea water mixes with fresh water from the river. A further difficulty is the need to properly reproduce the transport of oil pollution which is governed by currents and weather conditions. Given the complex dynamics of estuaries, 3D modelling seemed to be the only valid means of adequately predicting hydrocarbon drift and of assessing the impacts of dissolved compounds contained in the water from the surface to the bed.

The results obtained are encouraging and demonstrate the feasibility of pollution prevention for installations that could be affected by this type of pollution.

In the future, and in order to validate the concentrations of dissolved species found by the model, it will be essential

to undertake a more accurate study of the bioaccumulation process of living organisms in order to be capable of converting the dissolved PAH concentrations obtained with the model into the measured concentration contained in shellfish samples collected.

ACKNOWLEDGEMENT

The Migr'Hycar project (Artelia, CEDRE, EDF, LCA, LHSV, Total, Veolia) is a collaborative project forming part of the PRECODD 2008 programme financed by the French National Agency for Research (ANR). GIP Loire estuary funded the development of the hydrodynamic model of the Loire.

REFERENCES

[1] J.-M. Hervouet, "Hydrodynamics of Free Surface Flow: modeling with the finite element method", Edition Wiley, 2007.

[2] C. Goeury, "Modélisation du transport des nappes d'hydrocarbures en zones continentales et estuariennes", thèse de doctoracten mécanique des fluides de l'université de Paris Est, in press.

[3] C. Goeury, J.-M. Hervouet, I. Baudin-Bizien, F. Thouvenel, "A lagrangian/Eulerian oil spill model for continental waters", Journal of Hydraulic Research, in press.

[4] Artelia, "Développement et exploitation d'un modèle hydrosédimentaire en trois dimensions sur l'estuaire de la Loire, technical report, unpublished.

[5] J. Bonnemains, C. Bossard, E. Crépeau, and E. Fenn, "Atlas des marées noires dans les eaux intérieures du 1er janvier 2008 au 31 décembre 2010", Technical report, Association des Robins des Bois, 2011.

Using Reliability Analysis in Morphodynamic Simulation with TELEMAC-2D / SISYPHE

Rebekka Kopmann
Department of Hydraulic Engineering
Waterways Engineering and Research Institute (BAW)
Karlsruhe, Germany
rebekka.kopmann@baw.de

Uwe Merkel
Consulting Engineer
Karlsruhe, Germany
uwe.merkel@uwe-merkel.com

Jan Riehme
LuFG Informatik 12: Software and Tools for Computational Engineering (STCE),
RWTH Aachen University,
Aachen, Germany
riehme@stce.rwth-aachen.de

***Abstract* — Using reliability analysis in morphodynamic simulation should be seen as a standard proceeding in project work. Due to deficient description of the physical processes, natural variability or imprecision of model parameters morphodynamic simulation becomes uncertain through highly sensitive model parameters. The sensitivity of these model parameters should be determined and their contributions to the variance of the model results should be quantified.**

Reliability analyses are compared by using three methods: a simple Scatter Analysis, a Monte Carlo method specialised to confidence limits and a first order method based on tangent-linear algorithmic differentiation (AD) of TELEMAC / SISYPHE. Showing the advantages of each method, different applications were used either from flume experiments or from project work. The influence of either wide spread or high sensitive input parameters could be estimated as well as areas of higher and lower uncertainty. Unfortunately all methods have relevant drawbacks applying in project work. Some new ideas are presented to overcome these limitations.

Moreover, a first example of automatic calibration of model parameters is shown. For that, an adjoint model of TELEMAC / SISYPHE was generated by the AD-enabled NAG Fortran compiler.

I. Introduction

In the last few years bed load management for the purpose of creating a dynamic bottom balance in federal waterways has increased significantly in importance. Numerical simulations of morphodynamic processes become an essential tool for bed load management. But these tools incorporate a lot of uncertainties due to unknown initial and boundary conditions, the natural variability or the imprecision of model parameters and the deficient description of the complex physical processes. Morphodynamic tasks are mostly connected to large scales and long term periods. Therefore the demand for calibration and validation increases as well as the uncertainty of model predictions. Evaluation and careful interpretation of numerical results are needed. Reliability analysis can be helpful with that, as it quantifies the uncertainties in time and space as well as according to its source.

Several sources determine the overall uncertainty of a numerical model. Most of them cannot be influenced by the user of a numerical program, except for the input parameters. It is well known that the range of model parameters accepted in literature can be quite huge. Therefore the influence of uncertain input parameters to morphodynamic model results is considered in this article. The advantage of using even a quite simple reliability method shall be shown. The effect of uncertain input parameters to the bottom evolution as the main result of the morphodynamic simulation is investigated. Instead of just one value for the bottom evolution in space and time a most probable value and a certain range, equivalent to the confidence interval can be given.

Many parameters of simulations processes must be estimated in advance. Calibrating the model parameters based on observations taken from measurements can be done by solving a least squares problem, where the sum of squared errors between observations and simulated values is minimised. Gradient based methods might be used to solve these problems, if gradients of the residual with respect to the parameters can be computed efficiently. Reverse mode AD can be used to create an adjoint model of the simulation, which can compute a gradient by just one adjoint model evaluation independent of the number of parameters to calibrate. A first adjoint model of TELEMAC / SISYPHE generated by the AD-enabled NAG Fortran compiler was used successfully to calibrate a set of parameters for a first example.

II. Reliability Methods

Three reliability methods and a method for automatic calibration based on algorithmic differentiation were applied for a project or two different flume experiments.

A. Scatter Analysis

The Scatter Analysis is a first order method. Therefore it is only adequate for linear or slightly non-linear problems. From the root mean square (RMS) the deviations are assumed. The RMS can be calculated from the first derivative multiplied by the standard deviation. When calculating the confidence limits only the first order terms are taken into account. The confidence interval of the evolution for a 68 % probability is two times the RMS and for a 95 % probability 4 times the RMS. For a detailed description please refer to [1].

The RMS of the state variable evolution E, which describes the bed level changes e.g. in a river, influenced by the friction coefficient ks with a Gaussian distribution, can be calculated as:

$$rms(E) = \frac{1}{2}\left[E(ks_0 + \sigma) - E(ks_0 - \sigma)\right] \quad (1)$$

$E(ks_0+/-\sigma)$ are results from two simulation runs with $ks_0+\sigma$ and $ks_0-\sigma$, while σ is the standard deviation of ks and ks_0 the mean value. The calculations of the deviations or the confidence intervals of the bed level changes E for n uncertain parameters need only n*2 + 1 simulation runs [2].

Deciding whether a linear method is valid, the distortion for the evolution E can be used:

$$\delta E = \frac{1}{2} E''(ks_0)\sigma^2 << rms \quad (2)$$

The distortion can be calculated with the second derivative of E (E'') concerning an uncertain parameter (in this case ks) and the standard deviation of this parameter. In case of a linear function of E, the second derivative would be zero. The distortion can be used as an indicator for linearity. It should be much smaller than the RMS, otherwise the function is not slightly non-linear and the method is not adequate for this special problem. However, the distortion can only be used as an indicator for slight non-linearity in case of symmetric distributions.

B. Monte Carlo CL and Metamodel

The MC-CL method is a specialized Monte Carlo method which focuses on the confidence limits. It is not limited to linear problems and determines the confidence limits approximately while using as few as possible simulations. In case of strong non-linearities the confidence limits cannot be deduced from the root mean square (RMS) any more. Moreover it is not possible to calculate the RMS from the deviations. A connection between the confidence limits and the root mean square only exists in case of non-distorted Gaussian distribution as in linear functions. For strong non-linear functions the root mean square and the confidence limits are not equivalent, not proportional and furthermore there is no functional connection between them. A more detailed description of this method can be found in [1], [3].

All Monte Carlo methods require a large sample number for precise determination of the confidence limits and need even more samples for the probability density function. In order to reduce the number of required samples and / or increase the precision, a computationally efficient interpolation (metamodel) can be used. Such a model can be constructed using a moderate number of simulations. Afterwards a huge number of model results can be created by the metamodel. With these results the confidence limits and the probability density functions (PDF) can be found with a higher precision. The metamodel is using radial basis functions. For details refer to [4] and [5]. The used simulations for constructing the metamodel should be chosen in such a way, that the whole parameter space is covered as even as possible. As for the MC-CL method a generator is used to create the parameter set. In order to guarantee an optimal construction of the metamodel a uniform distribution of each parameter must be assumed.

C. First Order Reliability Method with Algorithmic differentiation

First-Order Reliability Method (FORM) is a linear method, successfully used in structure analysis (see for example [6] or [7]. As for the Scatter Analysis the wanted deviations of the results are calculated from the first derivative (more precisely these first order derivatives forms the so called Jacobian) multiplied by the vector of standard deviations of the uncertain parameters. These Jacobian – vector – products can be computed efficiently by a so called Tangent-Linear Model (TLM) of the original simulation. A TLM can be generated by Algorithmic Differentiation (AD) [8, 9]: AD tools transform the original simulation into a TLM by instrumenting the model with additional code, that allows to compute the desired Jacobian projection almost automatically.

For TELEMAC-2D and SISYPHE a TLM was created by the AD-enabled NAG Fortran compiler [10], a joint effort of the Software and Tools for Computational Engineering Institute (STCE), RWTH Aachen University, the University of Hertfordshire, and the Numerical Algorithm Group Ltd., Oxford, UK.

D. Automatic calibration based on Algorithmic Differentiation

Model calibration tries to improve the quality of the simulation by modifying parameters in such a way, that results known from experiments are reproduced by the simulation. These data, called "observation" or "truth", can be generated by real world measurements, or by using results of other simulations, or even by the simulation system itself. Using the simulation itself can of course not verify that the simulation will match what happens in the real word. But it will give interesting insights in the behaviour of the simulation and can be used to test the chosen optimisation algorithm.

Starting from an initial set of parameter values (not necessarily valid), an optimisation problem can be formulated (twin experiment): Minimise the sum over the squares of all errors between the simulation results of the current parameter set and the observations plus an optional regularisation term (not required in our experiment). Note that there is no guarantee that the original parameter set can be found again: Other valid parameter sets can exist with results matching the observations closely. However the chosen optimisation method and the initial parameter set have strong influence on the result of the calibration.

With the adjoint model of TELEMAC / SISYPHE generated by the AD-enabled NAG Fortran compiler gradient based methods can be used to calibrate parameters of experiments. An adjoint model can compute a gradient of a scalar valued function (like the sum of error squares above) in one sweep at a fixed multiple of the runtime of the original problem (relative costs). The gradient is a vector whose elements are the sensitivities of the output value with respect to the individual input parameters. Increasing the number of parameters does not increase the relative costs required to get the gradient. In contrast, the computational effort of approximating the gradient with finite differences or computing the gradient with a tangent linear model depend directly on the number of parameters.

Note that the adjoint model is in development state, thus only small examples can be handled at the moment. Ongoing work on the adjoint model (checkpointing, parallelism, special handling of linear solvers etc.) will increase the possible problem size dramatically.

III. APPLICATIONS

Since about 10 years BAW deals with reliability analysis for morphodynamic models mainly within a research and development project. In the following some applications are shown from flume experiments and from project work. The advantages of each method are presented as well as the drawbacks.

A. Reliability analysis in project work – River Rhine model

For a 60 km long stretch of river Rhine from Iffezheim to Speyer TELEMAC-2D coupled with the morphodynamic module SISYPHE and the dredging module DredgeSim was applied. A historical hydrograph of 10 years was simulated to calibrate the model including artificial bed load supply and dredging activities. Such long term simulations incorporate a large scope of natural and numerical uncertainties. From the experiences gained during the calibration 9 parameters were assumed to be uncertain: The active layer thickness, the pre-factor of the Meyer-Peter Mueller formula, the parameter of the slope effect of Koch & Flokstra, the parameter for the secondary current approach, the sieve line including the mean grain size of the transported material and of the artificial bed load supply and the Nikuradse roughness coefficient of three different zones (river channel, bank area, groynes). The corresponding formulas for all parameters can be found in [11]. The three most sensitive parameters are the active layer thickness, the friction coefficient of the river channel and the parameter for the slope effect. For the reliability analysis the Scatter Analysis, the MC-CL and the metamodelling (not presented here) were chosen. Unfortunately the FORM method with algorithmic differentiation could not be compared. The incorporated module DredgeSim is not in the AD version yet. A detailed description of this reliability analysis can be found in [12].

Fig. 1 shows the 68% deviation of the bottom evolution according to the river channel friction coefficient.

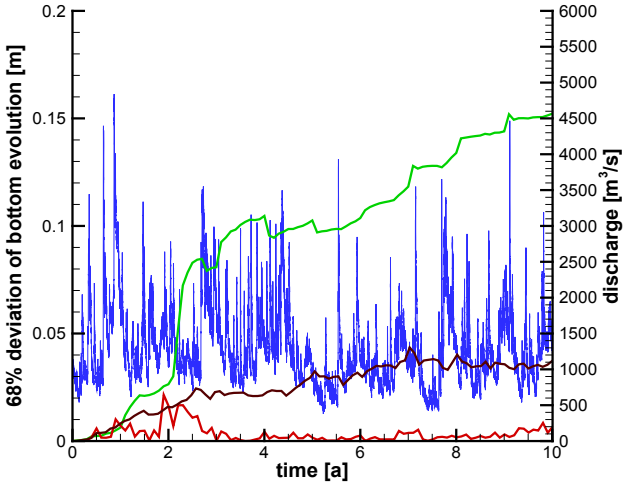

Figure 1. 68% deviation of the bottom evolution according to the river channel friction coefficient calculated with the Scatter Analysis for 10 years (green: mean value for the whole model area, red: representative point in the river channel, brown: averaged value for the fairway without disposal areas, blue: discharge).

A Gaussian distribution for this friction coefficient is assumed with a mean value of 2 cm and a standard deviation of 1.33 mm. With the Scatter Analysis a period of 10 years could be analysed. The green line represents the mean value for the whole model area. The red line is the product of just one node, a representative one, in the river channel. And the brown line contains an averaged value for the fairway excluding some disposal areas, which have enormous uncertainties. Generally the mean value for the whole model area increases over the time (Fig. 1 green line). Only in some rare occasions it decreases. The increase of uncertainty is higher during smaller discharges (e.g. low water conditions during the 3rd year). It seems that declines mostly occur during high water conditions. Contrarily to the assumption that the uncertainty is proportional to the amount of sediment transport (at least in this example), high water conditions lead to a state of the system which is more independent of the parameters. This has to be verified further. Unfortunately the averaged 68% deviation didn't reach a maximum level even over such a long period, but follows a trend. On the other hand the local deviation at some point in the river channel as well as the averaged value over the fairway excluding the disposal areas has indeed a maximum level and no trend. As expected, the overall uncertainty increases with time and

long term simulation should be analysed very carefully. Nevertheless for some parts the local deviations reach a maximum and afterwards level around a mean value (e.g. in the river channel, Fig. 1 brown line). This means, that the presented model can be used for long term prediction without losing a certain confidence interval.

The assumption of linear system behaviour is probably not valid for such long time periods. So far all methods for non-linear system behaviour used at BAW are based on Monte Carlo simulations. All these methods need enormous amount of computing time. For this reason a comparison between the SA and the MC-CL is made for a shorter period. Fig. 2 shows the 95% deviation of the bottom evolution for the first 17 months. For the first 5 months both methods come to the same results. Afterwards only a qualitatively agreement exists. The SA overestimates the values clearly with increasing tendency. Nevertheless due to the qualitative compliance it can be assumed, that also with the MC-CL the deviations will not increase infinitely but reach a certain level.

For the project both methods are not completely satisfying. The Scatter Analysis loses comparably fast the validity due to strong non-linear system behaviour. For a Monte Carlo CL method at least 150 simulation runs were needed (better twice as much or more, see section B). For that 64 cores for approx. 130 days on a parallel compute server at BAW were used to simulate only 17 months. But for morphodynamic tasks simulations for much longer time periods like decades are of interest. The needed computing time is still not available for project work.

B. Comparison MC-CL and FORM with AD – Sisyphe validation test case "BOSSE"

The validation test case of SISYPHE called "BOSSE" is used to show the differences between FORM with AD and MC-CL. In this experiment a sinusoidal dune is moved 4 hours due to a constant flow. The simulation is done with SISYPHE stand-alone. Further details can be found in the SISYPHE validation document [13]. The influence of the roughness coefficient (Strickler) and the slope effect (parameter beta in Koch & Flokstra formulation) is investigated. A Gaussian distribution is assumed for both input parameters.

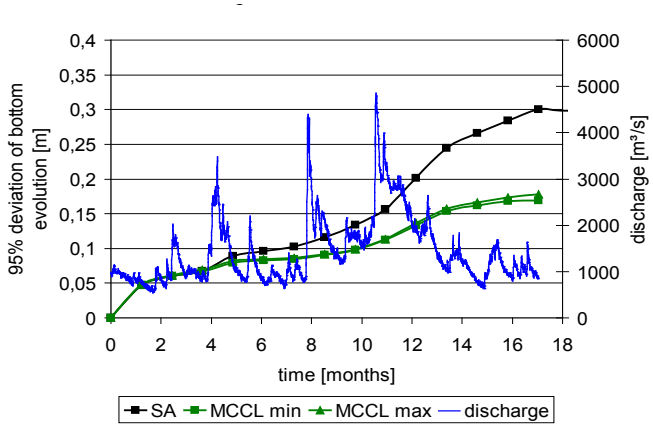

Figure 2. Comparison of the 95 % deviation of bottom evolution calculated with the Scatter Analysis and MC-CL.

The Strickler value had a mean value of 40 $m^{1/3}/s$ with a standard deviation of 0.5 $m^{1/3}/s$, the dimensionless parameter beta had a mean value of 1.3 with a standard deviation of 0.3. With these distributions the effect to the bottom evolution is about the same for both parameters. The standard deviations were set to small values in order to stay into a range with slightly linear system behaviour.

Fig. 3 shows the 95 % deviation of bottom evolution in respect to the Strickler and the slope effect parameter calculated with FORM and MC-CL with 100 and 1000 simulation runs. Assuming, that the MC-CL with 1000 simulation calculates the best results, the linear method matches the results quite well. Interestingly the FORM results match even better than the MC-CL with only 100 simulation runs. The differences are strongest at the stoss-side of the dune, where the maximum slope is located.

For the MC-CL the CDF (cumulative distribution function) is approximated with an EDF (Empirical Distribution Function). The corresponding error err_{CDF} is dependent on the number of experiments N_{exp} and the confidence level α. It can be calculated with

$$e\ r_C\ r_D = \sqrt{\frac{(1-\alpha^2)}{4N_{exp}}} \tag{3}$$

if the number of experiments is much higher than $2/(1-\alpha)$.

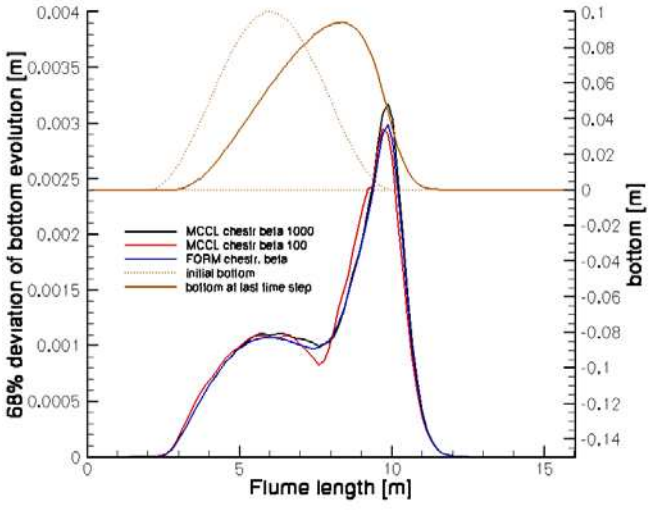

Figure 3. Comparison of the 68 % deviation of bottom evolution calculated with MC-CL using 100 (red line) and 1000 (black line) simulation runs and with FORM (blue line).

A confidence level of 68 % needs much more simulation runs than 40. For the shown 68% deviation and 100 experiments an error of 0.037 is gained. With 1000 simulations the error reduces to 0.012. From this example it must be derived that either the number of 100 simulation runs is not sufficiently higher than 40, or that an error of approx. 4 % is not satisfying. This leads to even higher numbers for the MC-CL method, which is often not possible for project work.

C. Comparison MC-CL and FORM with AD - Laboratory experiment with 180° bend

Another validation case which tests the effect of secondary currents is the experiment of Yen and Lee [14] in a flume with a 180° bend. In this experiment an unsteady flow discharge modifies the initial flat bottom to a typically cross section with an outer and inner bank. Starting from an initial flow rate of 0.02 m^3/s (corresponding to incipient motion), the flow discharge is linearly increased during 5 h up to 0.053 m^3/s and then progressively decreased back to its initial value. The results of the coupled hydrodynamic / morphodynamic model are reasonably satisfying for a depth averaged model (see [15]). For a further calibration the sensitivities of the bed level changes concerning the input parameters were conducted. Exemplarily the effect of a Gaussian distributed roughness coefficient to the bed evolution is chosen. The mean value of the roughness coefficient of Nikuradse was set to 3 mm with a standard deviation of 0.1 mm. The sensitivities were calculated with the AD version of SISYPHE and TELEMAC-2D v6p0 and the MC-CL method with 1000 simulation runs. The AD-model needed approx. only 0.7 % of the computing time of 1000 MC-CL simulation runs. This illustrates very clearly the big advantage of the AD based FORM method. Fig. 4 shows the comparison of the 68% deviation of bottom evolution according to the roughness coefficient for both methods after 5 hours.

The results of both methods match qualitatively and quantitatively well. Nevertheless there are some higher local differences at the side walls (see Fig. 5). These originate from locally high deviations that were calculated with both methods, but not exactly at the same position. The assumed variation of the roughness coefficient from 2.7 to 3.3 mm is comparably small. As expected the resulting deviations after 5 hours simulation are small too. For most points the 68% deviation is less than 1/100 of the maximum bottom evolution. The locally high deviations suggest some strong non-linear system behaviour or some simulation instability, which intensify for the deviations. Both methods predict them at slightly different places and they occur immediately and not after some time. Again it seems that both methods are not optimal to give reliable values for the deviations respectively the confidence intervals.

Nevertheless some important assumptions can be drawn from the calculated deviations: The influence due to such a small roughness change is small compared to the bed level

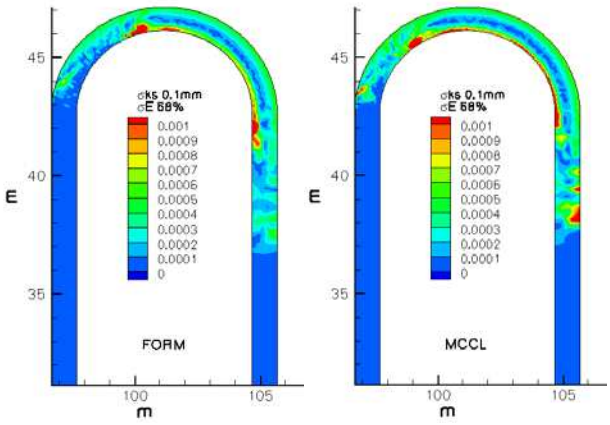

Figure 4. Comparison of the 68 % deviation of bottom evolution according to the friction coefficient calculated with FORM and AD (left) and MCCL (right).

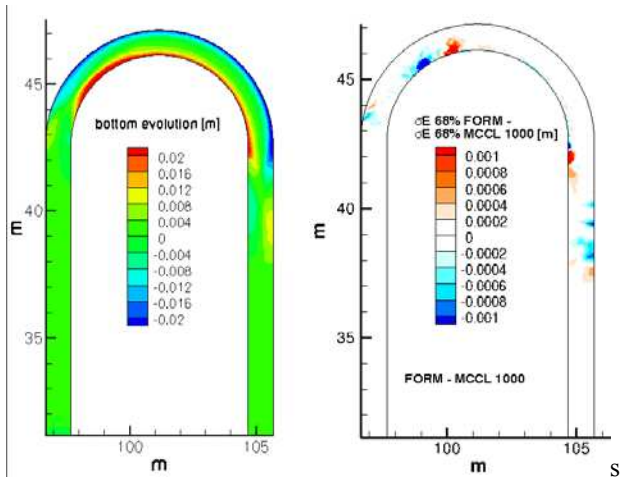

Figure 5. Bottom evolution calculated with the mean value of the roughness coefficient (left) and differences of the 68 % deviation of bottom evolution according to the friction coefficient between the MCCL and FORM based on AD (right).

changes. At the inner part of the channel the simulation is far less uncertain than at the boundaries. This means that the mean bed level change can be predicted much better, than the cross slope.

D. Automatic calibration based on AD – Sisyphe validation test case "BOSSE"

For a first calibration test at STCE the SISYPHE validation test case "BOSSE" was modified to support a zonal model for the Strickler roughness coefficient *kst*. Instead of one scalar value for all grid nodes, the roughness coefficient was set for all grid nodes by a special designed function *kst(p)* taking an input vector $p \in R^{92}$ of 92 input parameters.

Looking at SISYPHE as a function $E_{kst}(p)$: $R^{92} \rightarrow R^{891}$ that maps first an input vector p according to $kst(p)$ into roughness coefficients of all grid points, and then computes the bottom evolution $E_{kst}(p) \in R^{891}$, SISYPHE was used to compute the observations $E^{obs} = E_{kst}(p^{obs})$. The parameters p^{obs} were chosen in such a way, that 48 roughness zones were created by $kst(p^{obs})$ as shown in Fig. 6.

A least squares residual functional was defined for arbitrary input vectors $p \in R^{92}$ as

$$g(p) = \sum_{i=1}^{891} \left(E_{kst,i}(p) - E_i^{obs} \right)^2 \cdot w_i \qquad (4)$$

with weights $w_i = 10^5$, that measures the error in the bottom evolution for an input vector p. The optimisation method BFGS (Broyden-Fletcher-Goldfarb-Shanno) from the Python - package SciPy (www.scipy.org) was used to solve the minimisation problem

$$\min_{p \in R^{92}} g(p) \qquad (5)$$

The algorithm requires two functions: One to evaluate the value of $E_{kst}(p)$, and another to compute the gradient of $E_{kst}(p)$ with respect to the input parameter p. The gradient is used to determine a search direction; the evaluation of E_{kst} is used to decide on the step length along the direction given by the gradient. The evaluation of E_{kst} is done by just calling SISYPHE, whereas the gradient is computed via the adjoint model of SISYPHE generated by the AD- enabled NAG Fortran compiler.

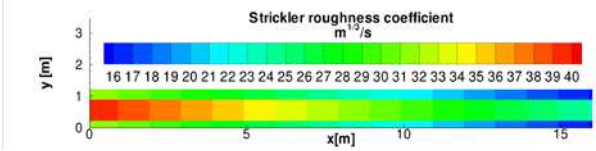

Figure 6. 48 roughness coefficient zones for optimisation problem.

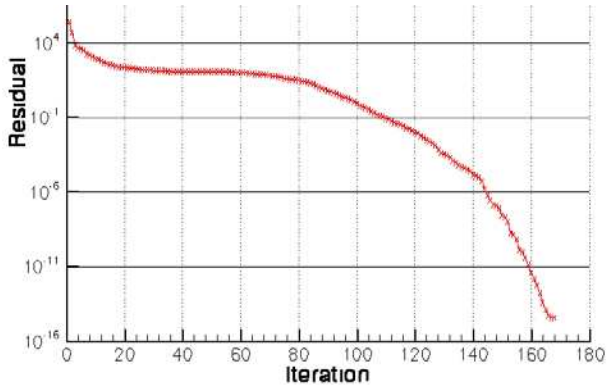

Figure 7. Development of the residual.

Fig. 7 shows (in log scale) the development of the residual $g(p)$ starting from an initial guess p^0 for the parameter vector p such that $kst(p^0)$ gave a value of 80 for the roughness of all grid points. Thus the initial residual $g(p^0)$ was around 260,000. After 131 Iterations the norm of the gradient was reduced from roughly 2,300 to less than 0.1 (residual around 0.002), after 167 iterations the algorithm terminates with gradient norm below10^{-7}. The minimiser found matched the true parameter vector p^{obs} up to at least 8 decimal digits, the residual value was within the numerical noise (less than 10^{-14}). For a first try on automatic calibration these results are very promising.

To investigate more realistic calibration problems the adjoint model needs to (and will) be improved (checkpointing, parallelism, special handling of linear solvers etc.). Moreover problem specific optimisation routines need to be selected, implemented or even created. (For instance, the optimisation given above should not be unconstrained, since a Strickler roughness coefficient below zero or above 100 does not make sense).

IV. DISCUSSION OF APPLIED RELIABILITY METHODS

The applied reliability methods are not satisfying, while they have all relevant drawbacks if it comes to project work. The possibility to get reliable quantitative statements from linear approaches like FORM or Scatter Analysis decreases very fast with simulation time.

On the other hand all applied non-linear methods are based on Monte Carlo simulations. The big disadvantage is the needed huge number of simulation runs. The required computing time is simply not available. Model extents as well as simulated time periods are usually too high in project work. With new and faster computers model dimensions and time periods always increased in the past. For that reason it cannot be hoped to overcome this limitation of the Monte Carlo method only by increasing computer power. Hence non-linear methods based on algorithmic differentiation seem the more promising way. Some ideas are already scheduled for testing. AD can also provide second derivatives. This gives the possibility to apply a second order reliability method (SORM). Furthermore in AD a vector mode exists. With that multiple Jacobian projections can be calculated simultaneously. Furthermore with a newly implemented very precise restart option derivates can be calculated faster for different parameter sets. Each derivative would be still linear, but the analysis space can be enhanced.

V. CONCLUSIONS AND OUTLOOK

In this paper three reliability methods have been applied to flume experiments and project work. Two linear methods, the Scatter Analysis and the first order reliability method (FORM) using algorithmic differentiation (AD) were compared to a specialised Monte Carlo method (MC-CL). For linear or slightly non-linear model behaviour the linear methods are very useful. However, most morphodynamic tasks are of long term and large scale. Both imply an increasing non-linear behaviour. With that model class only

qualitative statements can be made. On the other hand Monte Carlo methods require such amount of computing time that it is simply not possible to conduct in project work. Further investigations for non-linear methods based on algorithmic differentiation seem most promising.

First results of automatic calibration using an optimisation due to algorithmic differentiation in adjoint mode have been shown. The quality of the calibrated parameter set was determined within the optimisation algorithm. This increases the prediction ability of the model respectively the model reliability.

ACKNOWLEDGEMENT

The authors thank Judith Riemann and Thomas Brudy-Zippelius for providing us with the calibrated model of Iffezheim-Speyer.

REFERENCES

[1] Kopmann, R., Schmidt, A., "Comparison of different reliability analysis methods for a 2D morphodynamic numerical model of River Danube," River Flow 2010 – International Conference on Fluvial Hydraulics, Braunschweig, 8.-10.9.2010 pp.1615-1620.

[2] Nikitina, L., Nikitin, I., Clees, T., „Studie Zuverlässigkeitsanalyse morphodynamischer Modelle. Abschlussbericht zum Arbeitspaket 1", Fraunhofer Institut Algorithmen und Wissenschaftliches Rechnen, 2008.

[3] Nikitina, L., Nikitin, I., Clees, T., „Studie Zuverlässigkeitsanalyse morphodynamischer Modelle," Abschlussbericht zum Arbeitspaket 2, Fraunhofer Institut Algorithmen und Wissenschaftliches Rechnen, 2009.

[4] Buhmann, N.D., "Radial basis functions: theory and implementations," Cambridge University Press, 2003.

[5] Nikitina, L., Nikitin, I. Stefes-lai, D., Clees, T., "Studie Zuverlässigkeitsanalyse morphodynamischer Modelle. Abschlussbericht der Zuverlässigkeitsanalyse für stark nichtlineare Funktionen y(x) mittels einer speziellen, durch RBF-Metamodellierung beschleunigten Monte-Carlo-basierten Methode zur CL-Berechnung," Fraunhofer Institut Algorithmen und Wissenschaftliches Rechnen, 2010.

[6] Melching, C.S., "An improved first-order reliabil-ity approach for assessing uncertainties in hydrologic modeling," Journal of Hydrology, 132, pp157-177, 1992.

[7] Yen, B.C., Cheng S. and Melching, C.S., "First order reliability analysis, Stochastic and risk Analysis in hydraulic Engineering," International Symposium on Stochastic Hydraulics 4, Littleton, Colorado 1984, Water Resources Publication, 1986.

[8] Griewank, A., Walther, A., "Evaluating Derivatives: Principles and Techniques of Algorithmic Differentiation," Second Edition, SIAM, 2008.

[9] Naumann, U., "The Art of Differentiating Computer Programs – An Introduction to Algorithmic Differentiation, SIAM, Philadelphia, 2012.

[10] Naumann, U., Riehme, J., "A differentiation-enabled Fortran 95 compiler," ACM Transactions on Mathematical Software, 31(4):458–474, 2005.

[11] Villaret, C., "Sisyphe 6.0 User Manual," H-P73-2010-01219-FR, Laboratoire National D'Hydraulique et Environnement, Electricité de France, Chatou, 2010.

[12] Kopmann, R., Brudy-Zippelius, T., „Using Reliability Methods for Quantifying Uncertainties in a 2D-Morphodynamic Numercial Model of River Rhine," 2nd European IAHR conference, Munich, 27.-29.06.2012.

[13] Villaret, C. , Gonzales de Linares, M., "Sisyphe Release 5.5 Validation Manual," HP-76/05/014/A, Laboratoire National D'Hydraulique et Environnement, Electricité de France, Chatou, 2005.

[14] Yen, C., Lee, K.T., "Bed topography and sediment sorting in channel bend with unsteady flow," Journal of Hydraulic Engineering 121 (8), 591–599, 1995.

[15] Villaret, C., Hervouet, J.-M., Kopmann, R., and Merkel, U.," Morphodynamic modelling using the Telemac finite-element system," Computer & Geosciences, 2011.

Estimation of lateral inflows using data assimilation in the context of real-time flood forecasting for the Marne catchment in France

Johan Habert
DREAL Champagne-Ardenne,
Chalons-en-Champagne, France
johan.habert@developpement-durable.gouv.fr

Etienne Le Pape
SCHAPI, Toulouse, France
Etienne.lepape@developpement-durable.gouv.fr

Olivier Thual
URA1875/CERFACS and INPT, CNRS, IMFT, Toulouse
thual@imft.fr

Sophie Ricci, Andrea Piacentini, Gabriel Jonville,
Thierry Morel, Florent Duchaine, Anthony Thevenin
URA 1875/CERFACS, Toulouse, France
ricci@cerfacs.fr , piacentini@cerfacs.fr ,
jonville@cerfacs.fr , morel@cerfacs.fr ,
duchaine@cerfacs.fr , thevenin@cerfacs.fr

Nicole Goutal, Fabrice Zaoui, Riadh Ata
LNHE EDF-R&D, Chatou, France
nicole.goutal@edf.fr , fabrice.zaoui@edf.fr ,
riadh.ata@edf.fr

***Abstract*— The present study describes the assimilation of discharge in-situ data for operational flood forecasting. The study was carried out on the Marne river (France) catchment where lateral inflows's uncertainty are important due to karstic areas. This source of error was partly accounted for using an Extended Kalman Filter algorithm built on top on a monodimensional hydraulic model. The Data Assimilation algorithm is achieved using the OpenPALM dynamic coupling software that allows for a computationally efficient implementation.**

I. INTRODUCTION

In 2006, 9% of the French population was exposed to flood risk, one of the greatest natural risks causing damage and human loss [21]. The French flood forecasting service (SCHAPI - Service Central d'Hydrométéorologie et d'Appui à la Prévision des Inondations), in collaboration with the 22 local flood forecasting centers (SPC- Service de Prévision des Crues) produces a twice-daily broadcast vigilance map available to governemental authorities and general public (http://www.vigicrues.gouv.fr).

In order to effectively support emergency management and decision making it is essential to properly characterize the different sources of uncertainty in hydrologic forecasts [3][25]. The reliability of flood forecasting strongly depends on the quality of the hydraulics model, its boundary conditions (upstream and lateral inflow), hydrological initial conditions and numerical parameters. Much effort has been directed towards the estimation of hydrologic and hydraulic model parameters especially for the statistical analysis of parameters uncertainties usually using a historical batch of data, assuming time-invariant parameters [6][24]. In practice, in addition to model simulation and batch calibration, the reliable operation of a watershed system requires a continuous correction of the forecast as observational data become available [18]. The application of data assimilation (DA) [1], which optimally merges information from model simulations and independent observations with appropriate uncertainty modelling, has proved promising in improving prediction accuracy and quantifying uncertainty [11][13][14][16]. Still, the use of such methods by operational agencies is rare and the need for implementing effective DA in the flood forecast process is increasing when flood frequency is likely to increase as a result of altered precipitation patterns triggered by climate change [5].

DA offers a convenient framework to overcome some of the limits of the calibration processes: observations and simulation outputs are combined to estimate an optimal set of model parameters and consequently reduce uncertainties in the simulation. With the increasing abundance of new in-situ and remote sensing observations, DA was applied in several studies formulated in an operational framework. A great number of implementations were made on top of hydrological models in order to improve soil moisture initial conditions. Thirel et al. (2010a,b) [22][23] assimilated past discharges to obtain a better initial soil moisture state and improve ensemble streamflow simulations. Dechant and Moradkhani (2011a) [4] used SNOTEL data to improve the estimation of snow water storage and consequently improve the ensemble streamflow prediction from the National Weather Service River Forecast System (USA). Seo et al. (2003, 2009) [19][20] explored variational assimilation of hydrologic and hydro-meteorologic data into operational hydrologic forecast. The Kalman Filter (KF) [8] algorithm is the most commonly used sequential DA algorithm which

results in the optimal estimation for linear dynamic models with Gaussian uncertainties. It was extended to nonlinear problems using a first order approximation of Taylor series, namely Extended Kalman Filter (EKF), or an ensemble approach for the Ensemble Kalman Filter (EnKF) [7]. These algorithms are also now widely being used in hydrology and hydraulics for the estimation of model states [10][12] as well as model parameters [15].

In the context of hydrodynamics modelling, Ricci et al. (2011) [17] showed that the EKF assimilation of water level observations on the Adour catchment with the 1D hydraulic model MASCARET [9] developed by LNHE (Laboratoire National d'Hydraulique et d'environnement) from EDF-R&D (Electricité De France Recherche et Développement) enabled to improve flood forecasting of 60% at a one hour lead time and of 25% at a twelve-hour lead time. In the present study, a similar approach is applied to flood forecasting in the Marne catchment where the presence of karstic areas makes it hard to correctly specify upstream and lateral inflows to the model. In the framework of operational flood forecasting, the SAMA (Seine Amont Marne Amont) SPC has developed two different models on two limited areas of the Marne catchment described in Fig. 1. On these limited areas, the batch calibration of the model was possible and the uncertainties due to lateral inflow were accounted for by artificially adjusting the Strickler coefficients. Still, in order to increase the forecast time on the Marne catchment, both models were recently merged into a global model far more difficult to calibrate. The need for a coherent estimation of the so far neglected inflows, which represent the dynamics of the karstic areas, and the non-modelled tributaries, which represent the dynamics of catchment areas, motivates the use of a DA procedure using in situ measurements. A realistic and time varying estimation of the lateral inflows is then achieved using a sequential data assimilation approach on 10 flood events over 2001-2010. It is shown that, in spite of certain limitations described further on, this approach provides a reliable estimate of the lateral inflows and leads to the improvement of the flood forecast at meaningful lead times for operational use.

The structure of the paper is as follows. Section II provides a description of the Marne catchment. The DA method is described in Section III along with the choices made for the implementation of the algorithm. Section IV gives an overview of the results, highlighting the merits of the approach for flood forecasting along with its limitations on a representative flood event. Conclusions are given in Section V.

II. MODELLING THE MARNE CATCHMENT

The Marne catchment is a karstic basin located East of the Paris basin. The Marne river is a 525 km long tributary of the Seine river, its source is located in the Langres Plateau in the Haute-Marne department (Fig. 1). The study is carried out on the upstream part of the river that is strongly sensitive to local precipitation and where flash floods (5 to 120 $m^3.s^{-1}$ within a 24h period in October 2006 at Condes) occur.

The landscape of the catchment is defined by forested plateaus, incised valleys and presents numerous limestone outcrops. Therefore the catchment area includes karstic areas and tributaries whose behaviour is highly nonlinear and thus difficult to forecast. As of today, the operational forecast relies on the integration of two sub-models on the Marne Amont and Marne Vallage areas (Fig. 1). These models are based on the mono-dimensional numerical code MASCARET for hydraulics describing the Saint-Venant (Shallow Water) equations and developed by EDF and CETMEF (Centre d'Etudes Techniques Maritimes Et Fluviales). They provide a satisfying water level signal, still discharges are usually underestimated and the maximum lead time for the forecast is 15 hours.

In order to extend the maximum lead time and benefit from measurements at Saucourt, the sub-models were merged into a global model extending from Villiers to Chamouilley and including the karstic areas of the Rognon. The upstream flows are specified at five upstream stations (Marnay, Louvières, Villiers, La Crête and Humberville). This global model underestimates the discharges of 50% on average over ten significant events for a representative event for Condes and Mussey observing stations. Indeed, the global model area is about 2250 km^2 when the area controlled by the five upstream stations is only about 755 km^2. Thus it appears that the modelling of lateral inflows, despite the lack of hydrologic rainfall-runoff model on the area, represents a key step towards the use of the global model for the Marne catchment. Five lateral inflows were then added to the model to represent the exsurgences of the Suize (Q_1), the Seurre on the Rognon catchment (Q_2 and Q_3), and tributaries upstream Musey (Q_4) and Chamouilley (Q_5). Given the homogeneous response of the catchment to an oceanic rainfall event, a water budget approach enables to describe a coherent, yet perfectible, behaviour of the catchment. Characteristic hydrographs of the catchment are used to represent the additional inflows with a multiplicative coefficient. The multiplicative coefficients A_i, with i in [1, 5] and their statistics were identified over a batch calibration of 10 flood events and are presented in Table I. This estimation can be greatly improved with a sequential method that allows for temporal variability of the coefficients, essential for instance for summer and early autumn events when the karst behaviour is complex and the Villiers station may not be representative of the entire catchment's dynamics.

TABLE I. MULTIPLICATIVE CORRECTIVE COEFFICIENTS A_i FOR LATERAL INFLOWS AND STANDARD DEVIATIONS WITH i IN [1, 5]

Q_i	Elementary hydrograph	A_i	Std
Q_1	Villiers	3	0.8
Q_2	Villiers	4	1.3
Q_3	Humberville	3	1.8
Q_4	Villiers	2.5	1.4
Q_5	Villiers	5.5	2

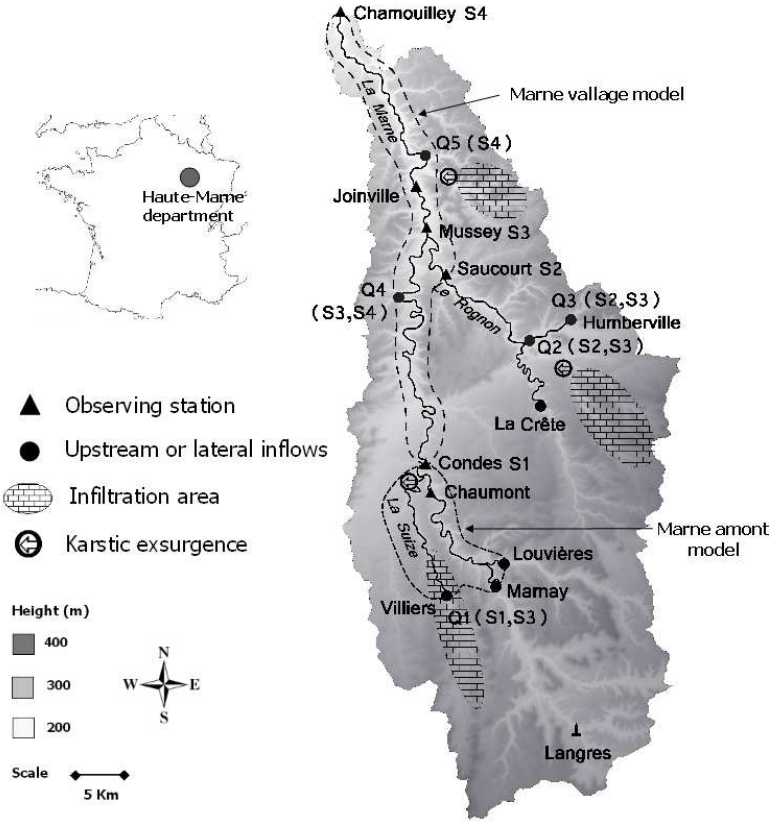

Figure 1. The Marne catchment, the sub-models are circled with dashed lines. The hydrological observing stations S1, S2, S3 and S4 are represented by black triangles. Lateral inflows Q1, Q2, Q3, Q4 and Q5 are represented by black dots and the observing stations on which they depend are in parentheses.

III. SEQUENTIAL DATA ASSIMILATION METHOD

A. Extended Kalman Filter

Data assimilation approaches aims at identifying the optimal estimate of the true value of an unknown variable $\mathbf{x}$ that includes, in this work, the set of corrective coefficients A_i with i in [1, 5]. The a priori knowledge on these coefficients given in Table 1 describes the background vector $\mathbf{x}^b$. The observation vector $\mathbf{y}^o$ is composed of hourly discharge measurements, a conservative variable, at Condes, Saucourt, Mussey and Chamouilley (respectively denoted by S_1, S_2, S_3 and S_4 in Fig. 1). The analysis is performed on a sliding time window, over which the A_i coefficients are assumed to be constant. Assuming that the background, the observation and the analysis are unbiased, the analysis vector $\mathbf{x}^a$ for cycle k can be formulated as a correction to the background parameters:

$$\mathbf{x}_k^a = \mathbf{x}_k^b + \mathbf{K}_k\left(\mathbf{y}_k^o - H(\mathbf{x}_k^b)\right)$$

where $\mathbf{K}_k = \mathbf{B}_k\mathbf{H}_{k,b}^T(\mathbf{H}_k\mathbf{B}_k\mathbf{H}_k^T + \mathbf{R}_k^{-1})$ is the gain matrix, $\mathbf{B}_k, \mathbf{R}_k$ are the background and observation errors covariance matrices and $\mathbf{y}_k$ $H_k(\mathbf{x}_k)$ is the model equivalent of the observations, generated by the observation operator H_k.

The observation operator consists of two operations, the costliest of which is the non-linear integration of the hydraulics model given the upstream and lateral flow conditions over the assimilation window. The second operation is the selection of the calculated discharges at the observation points and at the observation times. $H_k(\mathbf{x}_k^b)$ represents the discharges at the observation points and times computed by MASCARET using the background parameters $A_i = 1$.

The analysis is cycled over the period covering the entire flood event, thus allowing A_i to vary between the cycles. For cycle k, the observations over the first 8 hours (the re-analysis period) are used to estimate the optimal coefficients and a 24-hour forecast is carried out. Each of the five lateral inflows Q_1, Q_2 , Q_3, Q_4, Q_5 is controlled using downstream measurements from the hydrological observing station as described in Fig. 1; Q_1 is controlled by Condes and Mussey, Q_2 and Q_3 are controlled by Saucourt and Mussey, Q_4 is controlled by Mussey and Chamouilley and Q_5 is controlled by Chamouilley only. A 5 $m^3.s^{-1}$ standard deviation error is assumed on the discharge measurements to account for errors in misadjustment of pressure tube and extrapolation of water level-discharge rating curves. The background error

covariance is described by a diagonal matrix with the same standard deviation error on every A_i estimated as the mean of those described in Table I.

B. Local estimation of the observation operator

The Jacobian matrix $\mathbf{H}_{k,0}$ is the tangent linear of the hydraulics model computed in the vicinity of $\mathbf{x}_k^0$ as follows:

$$H_k(\mathbf{x}_k^0 + \Delta\mathbf{x}) \quad H_k(\mathbf{x}_k^0) + \mathbf{H}_{k,b}\Delta\mathbf{x}$$

and $\mathbf{H}_{k,b}$ $\mathbf{H}_{k,b}^0$ can be approximated using a finite differences scheme written as:

$$\mathbf{H}_{k,b} \quad \frac{\partial y}{\partial x} \quad \frac{\partial H_k(\mathbf{x}_k^b)}{\partial x} \approx \frac{H_k(\mathbf{x}_k^b + \Delta\mathbf{x}) \quad H_k(\mathbf{x}_k^0)}{\Delta x} \quad \frac{\Delta y}{\Delta x}$$

The local estimation of the tangent linear dynamics of the model with respect to the boundary conditions of the domain is a strong hypothesis. This method can be seen as an EKF algorithm without model errors (the model is considered as perfect). Since there is no propagation model for the parameters, the usual propagation steps of the KF algorithm are irrelevant here: the background error covariance matrix is invariant between the cycles.

The data assimilation algorithm was implemented using the OpenPALM dynamic coupler developed at CERFACS. This software was originally developed for the implementation of data assimilation in oceanography for use with the MERCATOR project. OpenPALM allows for the coupling of independent code components with a high level of modularity in the data exchanges and treatment while providing a straightforward parallelization environment [2]. The Parasol functionality in OpenPALM allows to automatically launch several executables of the same numerical code, in parallel. In this study, the Parasol functionality is used to launch the different integrations of MASCARET required for the finite difference scheme previously described. This allows for an efficient implementation of the DA algorithm with a reduced computational cost. For instance, when 5 inflows are corrected, at least 5 additional integrations of MASCARET are required to compute $H_{k,b}$. Provided a large enough number of processors are available, these integrations can be achieved simultaneously.

IV. RESULTS

The benefits from the application of the sequential analysis over the 10 floods events for the Marne catchment are summarized in Table II presenting the Nash-Sutcliffe criteria computed with data assimilation (DA) and without (Free Run) at the maximum lead time for the forecast at each observing station. It was shown that the assimilation of discharge measurements allows for a significant improvement of the simulated discharges in re-analysis (not shown) and forecast mode; with an the average improvement of 0.91 at the maximum lead time.

TABLE II. NASH-SUTCLIFFE CRITERIA FOR FREE RUN AND DA SIMULATIONS AVERAGED OVER 10 FLOOD EVENTS OVER 2001-2010 AT MAXIMUM LEAD TIME FOR EACH OBSERVING STATION

Observing station	**S1**	**S2**	**Joinville**	**S3**	**S4**
Forecast lead time	+6h	+10h	+13h	+12h	+21h
Free Run	0.61	-0.2	0.14	0.01	-1.38
DA	0.87	0.8	0.55	0.78	0.47

For the major flood event in December 2010, the use of the DA procedure for real-time forecast would have improved both discharge peak forecasts of 15 % as illustrated in Fig. 2 (only the first peak is shown). The discharges are presented on the left vertical axis and water levels are on the right vertical axis with solid thin and thick lines, respectively. Observations are represented by blue crossed curves, the Free Run 12 hour forecast by black solid curves and the analysis 12 hour forecast by red dashed curves. For the discharge and water level, the area between observation and Free Run is shaded in red when the model underestimates the signal and in blue when it overestimates the signal. The corrective coefficients for Q_1, Q_2, Q_3, Q_4 and Q_5 represented in Fig. 3 are globally smaller than 1 when the Free Run overestimates the observed discharge and bigger than 1 where the Free Run underestimates the observed discharge. These values also depend on the sensitivity of the discharge at the observing station with respect to each A_i; this information is accounted for within the linearized observation operator H.

Still, the assumption of a constant correction of the lateral inflows over a DA analysis cycle can lead to an inappropriate correction as displayed in Fig. 2 for Day 3. The 12-hour forecasted discharge at Day 3, resulting from the DA procedure (175 $m^3.s^{-1}$ where the solid vertical line intersects the thick red dotted curve) is computed using the corrected inflows resulting from the assimilation of the difference between the Free Run and the observation during the 8-hour period in Fig. 2 represented in grey between the two thin vertical lines at Day 2 + 2h and Day 2 + 10h. Over this period, the average discharge (thick curves) difference is bigger than that at Day 3, thus the DA procedure leads to an over correction of the discharge (an over decrease in this case): the solid red line at Day 3 is below the blue crossed line. To sum it up, if the model-observation error is not monotonous over the re-analysis and forecast period, the DA procedure can lead to an under or over correction. A possible leverage for this problem is to shorten the re-analysis period and thus allow for more temporal variability of the corrective coefficient.

Globally in Fig. 2, the water level is also significantly improved (thin curves), still the correction of the lateral inflows with assimilation of the discharge measurements

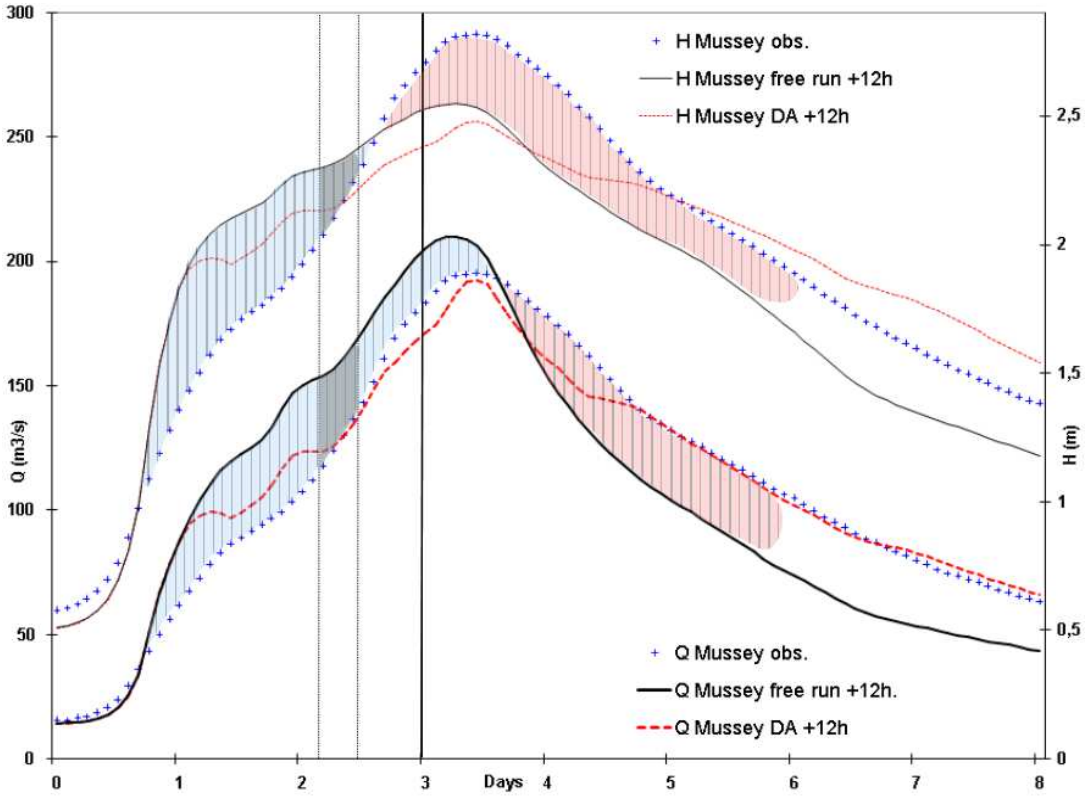

Figure 2. Discharge (thick curves) and water level (thin curves) at +12h, December 2010 (Mussey): Observations (blue crossed curves), Free Run (black solid curves), DA analysis (red dashed curves).

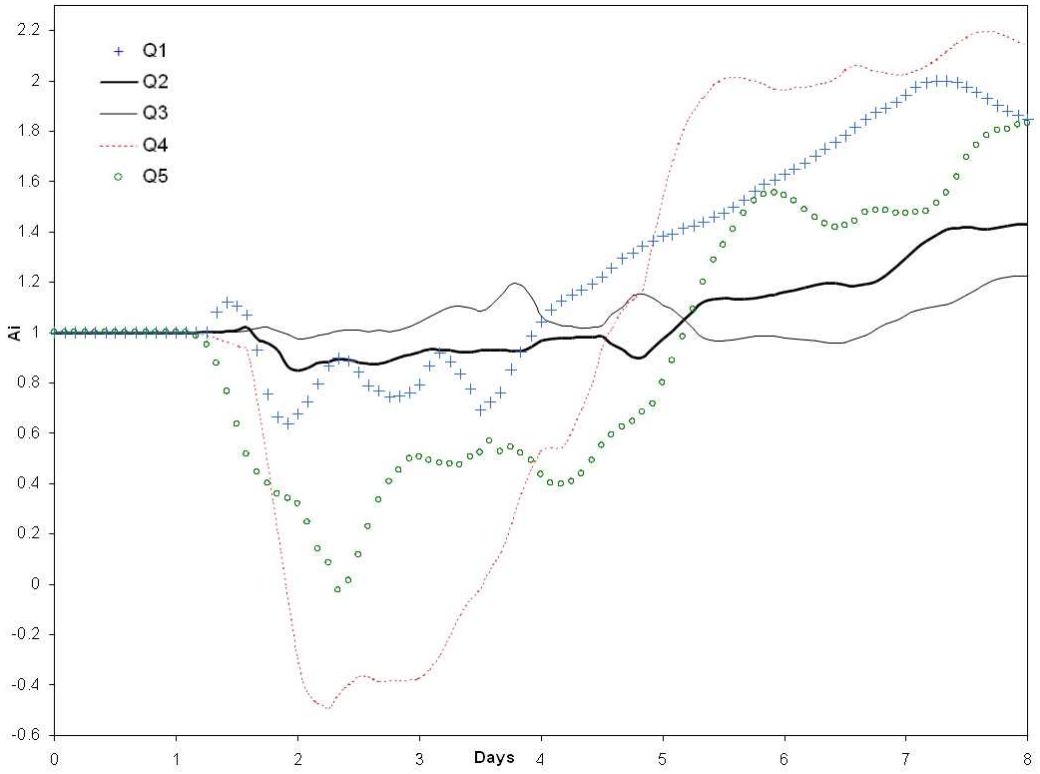

Figure 3. Ai coefficients for Q1, Q2, Q3, Q4 and Q5 during December 2010 event.

does not improve the water level peak simulation, it even degrades the first peak at Day 3 + 12h. Indeed, when the relation between water level and discharge in the model is not coherent with the relation between water level and discharge in the observation, the sign of model-observation error on discharge is different from the sign of the model-observation error on water level. This is the case from Day 2.5 to Day 3.5; the Free Run simulation overestimates the discharge (blue area in Fig. 2) but underestimates the water level (red area in Fig. 2). Here, the DA correction tends to decrease the lateral inflow in order to decrease the simulated discharge, thus leading to the decrease of the simulated water level when the latter was already too small.

The friction coefficients (Ks) of the hydraulic model are mean values obtained from the calibration procedure using discharge data, over 10 flood events. The resulting values for the hydraulic section containing Mussey are 20 for the river channel and 13 for the flood plain. These values are potentially not well suited for high discharge events and might be responsible for a non-physical local relation between discharge and water level. To account for uncertainty in the topography and bathymetry, a local correction of the Ks coefficient at Mussey is applied (over a 200m section downstream of the observing station). As illustrated in Fig. 3, a change in Ks allows to improve the simulated water level while the discharge is left unchanged by this local modification. Once the lateral inflows were corrected through the DA procedure, the simulated discharge is improved over the whole flood event, still the water level is overestimated (red areas in Fig. 3) from day 1 to 2.5 and 5 to 9 and underestimated at the flood peak (blue area in Fig. 3). An approximate calibration of the Ks coefficients is achieved to obtain the green curves in Fig. 3; the river channel and the flood plain coefficients are increased to 27 and 15 respectively over the overestimation periods and decreased to 16 and 9 over the underestimation period. The local correction of the Ks coefficients improves water level forecasts without changing discharges. Based on these results, ongoing work aims at including the Ks coefficients within the DA control vector of the previously described procedure.

As the correction of lateral inflows, Ks coefficients must be corrected sequentially as observations become available. The linear approximation of the relation between the Ks coefficients and the simulated hydraulic state should be investigated. Fig. 4 illustrates the nonlinear impact of the perturbation of the river channel Ks at the flood peak, at Mussey, around the reference value Ks = 20. For instance, a perturbation of 4 leads to a maximum discrepancy in water level of 2cm with respect to the linear approximation computed for dKs = 2 (pink dashed line in Fig. 4). For a positive perturbation in Ks, the non-linearity is significantly smaller than for negative perturbations with a water level difference of 6 cm when the Ks is increased from 20 to 32 and up to 33 cm when the Ks is decreased from 20 to 8. In order to keep the non-linearity impact small on the EKF analysis, the correction to the Ks coefficient should remain in a limited interval such as [-5, 5].

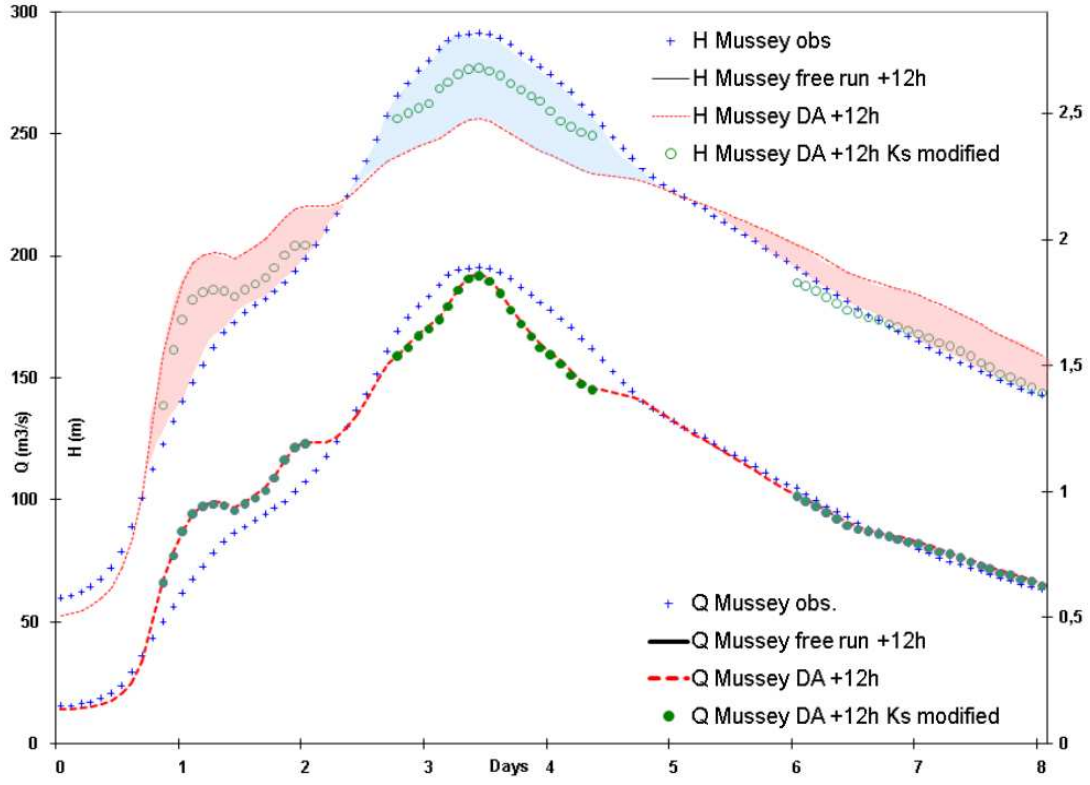

Figure 4. Discharge (thick curves) and water level (thin curves) at +12h, December 2010 (Mussey): observations (blue crossed curves), DA analysis (red dasched curves) and DA analysis with modified Strickler coefficient (green dotted curves).

V. CONCLUSION

The sequential assimilation of discharge measurements in real time mode was presented in this paper. The study focuses on the application of an Extended Kalman Filter (EKF) algorithm for the Marne catchment under the assumption that the relation between the lateral boundary conditions of the domain and the simulated discharge is fairly linear. It was shown that the estimation of the time varying contributions of the karstic areas and the neglected tributaries can be achieved. This leads to the improvement of the hydraulic state forecast at meaningful lead time for operational use. Since the method developed here is not catchment dependent, it was applied for other French catchments and it is currently being integrated in the real-time forecasting platform for operational use at SCHAPI. The reduced computational cost of the procedure is also a strong advantage. The extension of the control vector to model parameters such as the Strickler coefficients is one of the perspectives for further works as it will allow to correct the relation between water level and discharge within the model.

REFERENCES

[1] F. Bouttier and P. Courtier: Data assimilation concepts and methods, ECMWF Lecture Note, 1999.

[2] S. Buis, A. Piacentini, and D. Déclat: PALM: A computational framework for assembling high performance computing applications, Concurrency Computat.: Pract. Exper., 18(2), 247-262, 2006.

[3] G. Coccia and E. Todini: Recent developments in predictive uncertainty assessment based on the model conditional processor approach, Hydrol. Earth Syst. Sci., 7, 9219-9270; 2008b.

[4] C.M. Dechant and H. Moradkhani: Radiance data assimilation for operationnal snow and streamflow forecasting, Adv. Water Resour. Res., 34, 351-364, 2011a.

[5] G. Drogue, L. Pfister, T. Leviandier, A. El Idrissi, J.F. Iffly, P. Matgen, J. Humbert, and L. Hoffmann: Simulating the spatio-temporal variability of streamflow response to climatechange scenarios in a mesoscale basin, J. Hydrol., 293,255–269, 2004.

[6] Q. Duan, V. Gupta, S. Sorooshian, A.N. Rousseau and R. Turcotte: Preface in calibration of watershed Models, Water Sci. Appli. Ser., vol. 6; edited by Q. Duan et al., p. v, AGU, Washington, D. C, 2003.

[7] G. Evensen: Sequential data assimilation with a non linear quasi-geostrophic model using Monte Carlo methods to forecast error statistics. J. Geophys. Res., 99:10143-62, 1994.

[8] A. Gelb: Applied optimal estimation, Cambridge Mass.: MIT Press, 1974.

[9] N. Goutal and F. Maurel: A finite volume solver for 1D shallow water equations applied in an actual river, Int. J. Numer. Meth. Fluids, 38(2), 1-19, 2002.

[10] N. Jean-Baptiste, P.O. Malaterre, C. Dorée and J. Sau: Data assimilation for real-time estimation of hydraulics states and unmeasured perturbations in a 1d hydrodynamic model. Math. and Computers in Simulation, 81, 2201-2214, 2009.

[11] Y. Liu and H.V. Gupta: Uncertainty in hydrologic modeling: Toward an integrated data assimilation framework, Water Res. Ser., 43, W07401, 2007.

[12] P.O. Malaterre, J.P. Baume and N. Jean-Baptiste: Calibration of open channel flow models: a system analysis and control engineering approach, SimHydro 2010.

[13] D. Maclaughlin and L. Townley: A reassessment of the groundwater inverse problem, Water Resour. Res., 32, 1131-1161, 1996.

[14] D. Maclaughlin: An integrated approach to hydrologic data assimilation: interpolation, smoothing, and filtering, Adv. Water Res., 25, 1275-1286, 2002.

[15] H. Moradkhani, S. Sorooshian, H. Gupta and P. Houser: Dual-state parameters estimation of hydrolocal models using ensemble Kalman filter. Adv. Water Res., 28, 135-147, 2005.

[16] R.H. Reichle: Data assimilation methods in the Earth sciences, Adv. Water Resour. 31; 1411-1418, 2008.

[17] S. Ricci, A. Piacentini, O. Thual, E. Le Pape and G. Jonville: Correction of upstream flow and hydraulics state with data assimilation in the context of flood forecasting, Hydrol. Earth Syst. Sci, 15, 1-21, 2011.

[18] G. Schumann, P.D. Bates, M.S. Horritt, P. Matgen and F. Pappenberger: Progress in integration of remote sensing derived flood extend and stage data and hydraulic models, Rev. Geophys., 47, 2009.

[19] D.J. Seo, L. Cajina, R. Corby and T. Howieson: Automatic state updating for operational streamflow forecasting via variational data assimilation, J. Hydrol., 367, 255-275, 2009.

[20] D.J. Seo, V. Koren and N. Cajina: Real-time variational assimilation of hydrologic and hydrometeorological data into operational hydrologic forecasting, J. Hydrometeorol., 4, 627-641, 2003.

[21] SOeS - CGDD (Service de l'Observation et des Statistiques - Commissariat Général au Développement Durable): Croissance du nombre de logements en zones inondables, Le point sur, 6, Février 2009.

[22] G. Thirel, E. Martin, J.F. Mahfouf, S. Massart, S. Ricci and F. Habets: A past discharges assimilation system for ensemble streamflow forecasts over France, Part 1: Description and validation of the assimilation system, Hydrol. Earth Syst. Sci., 14, 1623-1637, 2010a.

[23] G. Thirel, E. Martin, J.F. Mahfouf, S. Massart, S. Ricci, F. Regimbeau and F. Habets: A past discharges assimilation system for ensemble streamflow forecasts over France, Part 2: Impact on the streamflow forecasts, Hydrol. Earth Syst. Sci., 14, 1639-1653, 2010b.

[24] J.A. Vrugt, H.V. Gupta, W. Bouten and S. Sorooshian: A shuffled complex evolution metropolis algorithm for optimization and uncertainty assessment of hydrological parameters. Water Resour. Res., 39(8), 1-14, 2003.

[25] A.H. Weerts and Y. Liu: Advances in data assimilation for operational hydrologic forecasting, Eos Trans. AGU, 92, 2011.

A numerical study of wave and current fields around Ramsey Island - tidal energy resource assessment

M. Reza Hashemi
Centre for applied marine sciences
School of Ocean Sciences, Bangor University
Bangor, UK;
Dept. of Water Engineering, Shiraz University
r.hashemi@bangor.ac.uk

Simon P. Neill, G. Davies
Centre for applied marine sciences
School of Ocean Sciences, Bangor University
Bangor, UK

***Abstract*—In the Irish Sea, the best marine renewable energy sites are subjected to strong currents and exposed to relatively large waves (e.g. around Ramsey island and in the Bristol Channel). The objective of this research is to present the potential of the TELEMAC modelling system in various aspects of marine renewable energy studies such as multi-scale modelling, and wave-tide interaction. Firstly, an idealised triangular domain was modelled to study the impact of tides on quantifying the wave power resource. The overall dimensions of this case study resemble those of the Bristol Channel. The results of the idealised case study demonstrate that ignoring the tides when estimating wave power generates considerable errors, since wave power is related to significant wave height squared. Next, a multi-scale unstructured mesh model of the Irish Sea was developed using TELEMAC. Spatial and temporal variations of the currents around Ramsey Sound were captured using a relatively fine mesh (~40m). Despite the strong current field and complex bathymetry of this region, the multi-scale tidal model led to convincing results. Some recommendations for research and priorities for data collection have been identified.**

I. INTRODUCTION

A key step towards the successful deployment of marine energy devices is site selection. Assessment of the physical, environmental and socioeconomic constraints at a specific site is highly dependent on a proper understanding of the current (e.g. resource assessment for tidal energy devices) and wave (e.g. cost due to wave loads on tidal energy devices, or wave power estimation) fields. Due to consistently high current speeds, Ramsey Sound in the southern Irish Sea has attracted both academic and business interest as a suitable site for tidal energy extraction. Hence, companies are planning to install tidal energy devices here as pilot studies. Further, the Bristol Channel is one of the most energetic sites in the Irish Sea for tidal and wave energy devices. Numerical simulations of the hydrodynamics of these areas is a challenging task, as a result of the highly irregular bathymetry, strong tides and relatively energetic wave climate. Additionally, in most studies relating to marine renewable energy, waves and currents have been treated separately.

In the most recent version of TELEMAC (i.e. 6.1), it has been possible to develop current and wave models of a region based on the same mesh and boundary conditions, including one-way or two-way coupling of those models.

In the present research, the TELEMAC modelling system has been used to study tides, waves, and their interactions, in terms of estimating renewable energy resources. An idealised triangular case along with a multi-scale Irish Sea model has been developed and discussed to address this aim.

II. STUDY AREA

The UK is located in a highly energetic environment in terms of marine renewable energy resources. In some areas like the Bristol Channel and around Ramsey Island, many studies have assessed the wave and tidal energy resources. The Bristol Channel is exposed to long fetch lengths from the Atlantic Ocean, potentially exceeding 1000 km. Hence, it is considered as one of the potential places for wave energy extraction in the UK. Further, with a mean spring tidal range of 12.2 m, and a mean neap range of 6.0 m at Avonmouth, the Bristol Channel has one of the highest tidal energy resources in the world. Depths in the approaches to the Bristol Channel are around 50 m. Ramsey Island is about 1 km off the coast of the St David's peninsula in Pembrokeshire in southwest Wales. Tidal currents are very strong particularly in the channel located at the east side of the island (i.e., Ramsey Sound).

III. TELEMAC-2D - TOMAWAC MODELLING APPROACH

TELEMAC-2D and TOMAWAC were used to model tides, waves and their interaction [1]. TELEMAC-2D is a well-known and popular model which solves the 2-D shallow water equations using FEM. One of the attractive features of this model is its unstructured discretization. This makes it suitable for multi-scale problems without resort to nesting. As an example, to model the flow and waves around Ramsey Island a multi-scale Irish Sea model was developed in the present work. A mesh size of 7000 m was used around the southern boundary (Celtic Sea), while a much finer 40 m mesh was used to resolve the bathymetry and capture the flow field inside Ramsey Sound.

A. TOMAWAC

TOMAWAC is a third generation wave model which solves the evolution of the directional spectrum of wave action in Cartesian or spherical coordinates. It includes deep and shallow water physics such as refraction, white capping, bottom friction and wave breaking, as well as nonlinear wave-wave quadruplet and triad interactions. TOMAWAC can be applied to oceanic scales, to continental shelf seas, and to the coastal zone [1].

B. Wave-current interaction in TOMAWAC

Tides modulate the water depth and generate currents, both of which then affect the wave field. An extensive effort in the previous literature has been made to assess the interaction of waves and tides, and that is beyond the scope of the present research (e.g. [2,3]). Here, the mechanism of wave-current interaction in TELEMAC is briefly mentioned.

The dispersion equation can be expressed as,

$$\sigma^2 = gk \tanh kh \tag{1}$$

where σ is the relative wave angular frequency, which can be observed in a coordinate system moving with the same velocity as currents, k is the wave number, and h is the water depth. The relative wave frequency is dependent on the ambient current velocity and absolute wave frequency as follows,

$$\sigma = \omega - \vec{k}.\vec{U} \tag{2}$$

in which ω is the absolute wave angular frequency, which can be observed in a stationary coordinate system, and $\vec{U}$ is the vertically-integrated current velocity.

Referring to the dispersion equation, the refraction of waves in intermediate and shallow water is related to the water depth, and hence the wave field in the presence of a tide is modulated, even in the case of stationary steady wind. Further, the tidal currents modify the refractive wave propagation direction as well as the wave period through the Doppler Effect (Eq. (2)).

When waves encounter an opposing current, part of the wave energy is dissipated, because the group velocity of the highest frequencies might be lower than the opposite current velocity. Therefore, the wave height may also change depending on the current direction in relation to the wave field.

In TOMAWAC, it is possible to include variation of water level due to tide and/or currents (e.g. by reading the TELEMAC-2D results file). This is considered as one-way coupling.

From another perspective, waves possess momentum and generate radiation stresses. The radiation stresses can be expressed in terms of the wave energy as follows [4],

$$\begin{cases} S_{xx} = \sum \frac{E}{2} [2n(\cos\theta)^2 + (2n-1)]\Delta\sigma\Delta\theta \\ S_{xy} = S_{yx} = \sum En \sin\theta \cos\theta \Delta\sigma\Delta\theta \\ S_{yy} = \sum \frac{E}{2} [2n(\sin\theta)^2 + (2n-1)]\Delta\sigma\Delta\theta \end{cases} \tag{3}$$

where E is the wave energy, S is the radiation stress, θ is the angle of the wave propagation and,

$$n = \frac{c_g}{c} = \frac{1}{2}\left(1 + \frac{2kh}{\sinh 2kh}\right) \tag{4}$$

Obviously, n is 1 in shallow water and ½ in deep water, which can lead to more simplified forms of Eq. (1). The wave induced forces are generated by the gradient of the radiation stresses,

$$\begin{cases} F_x = -\left(\frac{\partial S_{xx}}{\partial x} + \frac{\partial S_{xy}}{\partial y}\right) \\ F_y = -\left(\frac{\partial S_{yy}}{\partial y} + \frac{\partial S_{yx}}{\partial x}\right) \end{cases} \tag{5}$$

If these forces are significant, the current field, which is computed based on the momentum equation, is affected by wave radiation forces. Wave induced currents can be simulated in TELEMAC-2D. In a recent version of TELEMAC, it is possible to implement a two-way interaction of the wave and tidal models [3].

IV. Results and Discussion

To avoid complexities, particularly those related to bathymetry, a simplified idealised case was studied initially and is presented in subsection A. In this idealised case, different wave and current scenarios were modelled, and the results analysed in terms of estimating the wave power resource. The model of the Irish Sea, including Ramsey Sound and the Bristol Channel, is presented in subsection B.

A. Idealised triangular case

Fig. 1 shows a triangular channel, representing either an estuary, or a channel with a closed end. The dimensions and the bathymetry of this idealised case are parameterised on the Bristol Channel, with a length of 200 km and a width of 100km along the open boundary. The maximum water depth is 50 m at the centre of the open boundary, and the depth of channel gradually approaches zero toward the closed boundaries by a quadratic function.

The open boundary was forced with a harmonic semi-diurnal tide of amplitude 2 m and period of 12 h (for comparison, the M2 amplitude at the mouth of the Bristol Channel is about 2 m).

The waves were generated by a uniform steady westerly wind of 20 m/s. Further, it was assumed that the waves at the open boundary have a fetch length of 300 km. This can be approximately implemented in TOMAWAC by assuming a peak frequency of 0.091 and Phillips constant of 0.0107,

using empirical JONSWAP formulae [5]. Alternatively, the open boundary can be forced with a specified significant wave height. A simplified wave estimation for the fetch limited seas can be written as [5],

$$H_{mo} = \frac{4.13\times10^{-2} C_D U_{10}^2}{g}\left(\frac{gX}{C_D U_{10}^2}\right)^{\frac{1}{2}} \quad (6)$$

$$C_D = 0.001(1.1 + 0.035U_{10})$$

where H_{mo} is the significant wave height, X is fetch length, and U_{10} is the wind velocity 10 m above MSL, all variables expressed in SI units. The estimated wave height at the boundary for the given wind speed is about 6.2 m based on this formulation.

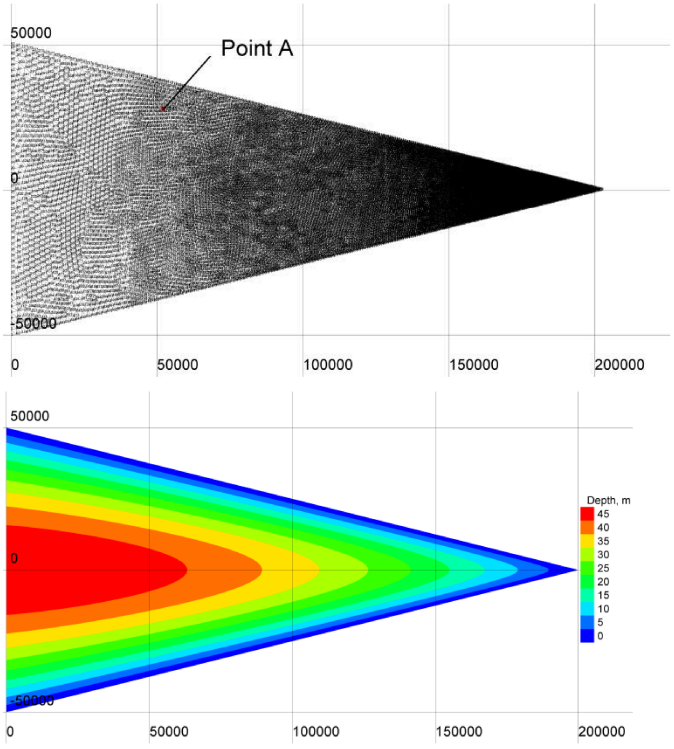

Figure 1. Geometry, mesh, and the bathymetry of the triangular idealised case. The only open boundary is on the west boundary.

Several scenarios for wave modelling were examined as follows:

- Ignoring tidal effects
- Considering only tidal water depth variations
- Inclusion of tidal water depth variations and currents
- Fully interactive wave-tidal model

Fig. 2 shows the wave field simulated by the wave model with no tidal effects. The wave height is about 6.3 m near the open boundary, and gradually approaches zero towards the closed boundary. The inclusion of tides leads to a modulation of the wave field according to the stage as the tide. Fig. 3 and Fig. 4 show the wave field at different times during the tidal cycle. Generally the wave heights are higher during flood but the times mentioned in these figures do not exactly correspond to the ebb and flood tide. As can be seen, the wave field is significantly affected by the tide.

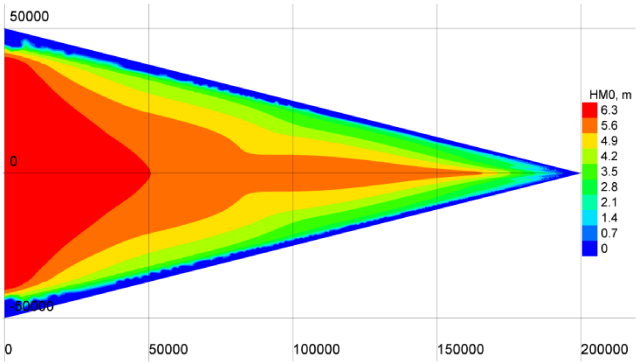

Figure 2. Modelled significant wave height for 20 m/s westerly wind when tidal effects are not included. H_{mo}=6.33 at x=50,000, y=0.

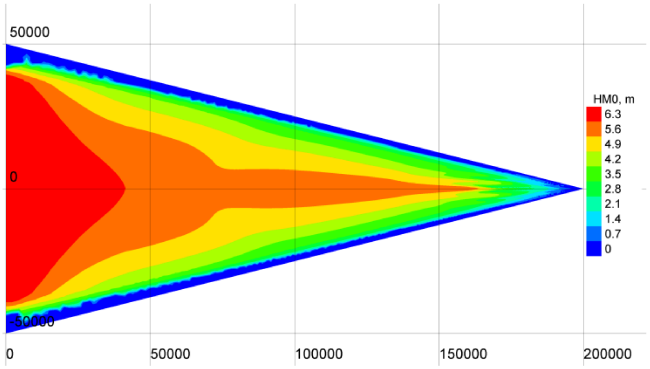

Figure 3. Modelled significant wave height for 20 m/s westerly wind when tidal effects are included. H_{mo}=6.08 at x=50,000, y=0 and, t=13h40.

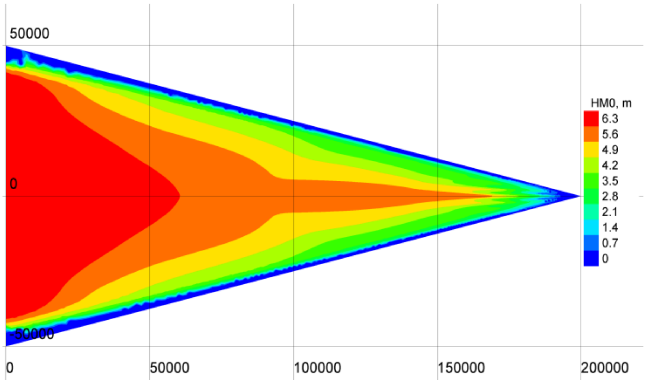

Figure 4. Modelled significant wave height for 20 m/s westerly wind when tidal effects are included. H_{mo}=6.54 at x=50,000, y=0 and, t=7h20.

Referring to Fig. 1, the hydrodynamic variables at a typical point A (x=52191 m, y=27993 m and d =19.9 m) were extracted for more detailed analysis. Point A is

relatively near the coast and will be affected by the refraction and shallow water wave physics. Fig. 5 shows the variation of the water depth along with computed significant height for various modelling scenarios. The estimated H_{mo} based on a pure wave model is 4.77 m. If the tidal variations in water depth are included, H_{mo} fluctuates in the range 4.56 - 4.95 m. For the case of fully interactive wave tide model, H_{mo} can reach 5.08 m. Therefore, ignoring the tide could lead to a maximum 12% error in estimating the wave height. Further analysis showed that as the amplitude of the tide increases, this error grows. Hence, tidal effects are more important towards the end of the channel which has a higher tidal range.

Similar results were observed for the other wave parameters such as the mean wave direction and mean wave period. As Fig. 6 demonstrates, water depth fluctuation and tidal currents both have a distinct effect on modulating wave direction and period.

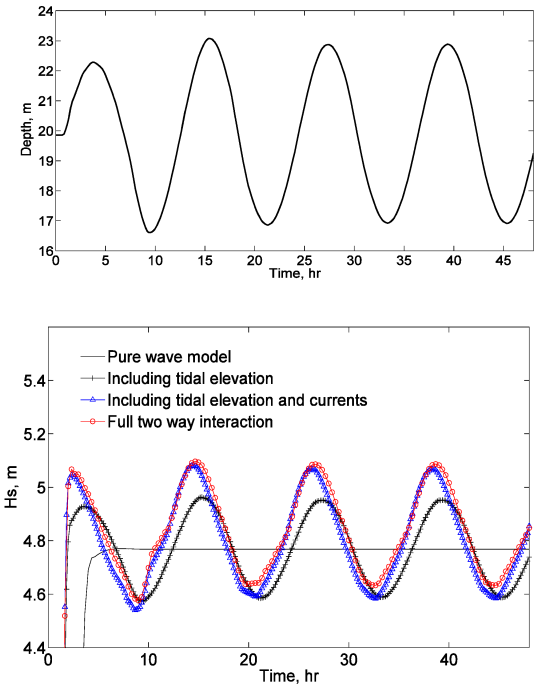

Figure 5. The variation of water depth and significant wave height at Point A (Fig. 1), assuming various wave modelling scenarios.

Both significant wave height and wave period contribute to the estimation of the wave power.

1) Effect of tide on wave power estimation: It is possible to extract wave power from the results of TOMAWAC directly (*POW* output variable).

There are several formulations for the estimation of the wave power. For instance [6],

$$P = \frac{1}{64}\frac{\rho g^2}{\pi}\left(H_{mo}{}^2 T^2\right) \qquad (7)$$

where, T is the wave period. According to the above equation, any error in estimating wave height and wave period could be magnified when estimating wave power. Fig. 7 shows the time series of the estimated wave power at Point A (Fig. 1).

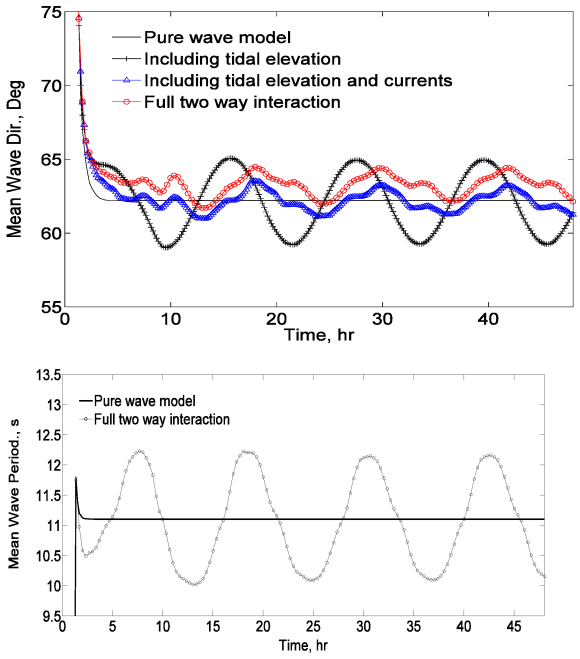

Figure 6. Time series of wave parameters at Point A (Fig. 1), assuming various scenarios for wave modelling.

As this figure shows, not only the estimated wave power varies with the tide, but there is an error associated with net power estimated over a tidal period. In Table I, the estimated errors at this typical point have been summarised. The results show that the estimated error in the predicted power (6%) is about twice that in the significant wave height (3%). Further, the error increases as tidal amplitude increases. For instance, if the west boundary is forced by a tidal amplitude of 3 m, the error in estimating the mean wave power increases from 6.0% to 9.2%.

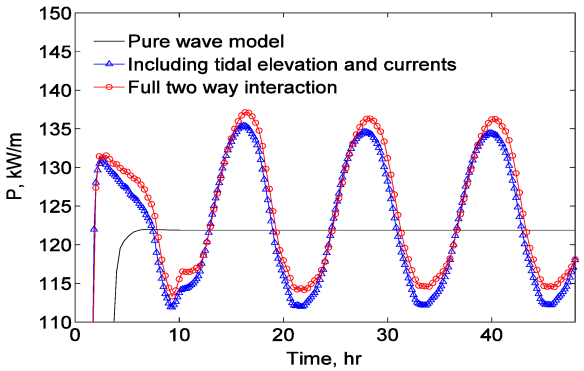

Figure 7. The fluctuation of the wave power as a result of the tide at point A (Fig. 1).

TABLE I. ESTIMATED ERROR IN THE WAVE POWER ESTIMATION DUE TO THE TIDE AT POINT A FOR FULLY COUPLED MODELS (FIG. 1)

	Percentage error			
	a*=2		a=3	
	H_{mo}	*Wave Power*	H_{mo}	*Wave Power*
Average	3.0	6.0	4.7	9.2
Max.	6.7	11.9	9.8	16.2

* The tidal amplitude at the left open boundary

2) Other considerations: Apart from estimating wave power, other parameters which have a primary role in the design of marine renewable energy schemes can be affected by wave-tidal interactions. Accordingly, the extreme wave loads have traditionally been used for the structural design of nearshore or offshore structures. Hence, underestimating wave height due to ignoring wave-tidal effects can increase the risk of damage to a tidal energy device.

As a final discussion point for this idealised case, the effect of waves on tidal currents is briefly demonstrated. The predicted current fields with and without inclusion of the wave forces have been subtracted and plotted in Fig. 8 to represent a typical time snapshot. Also, the corresponding wave forces are presented in Fig. 9. As expected, the wave-generated currents are more noticeable in the nearshore zone. This can lead to 0.40 m/s error, which is about 20% in the prediction of tidal currents. There is a clear association between this difference and wave generated forces.

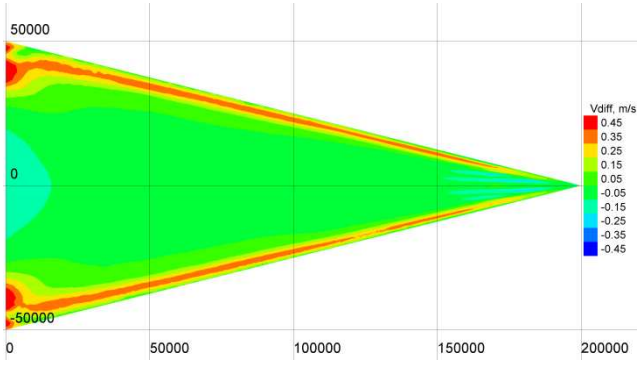

Figure 8. The difference of current speed with and without the inclusion of wave forces at t=14h00.

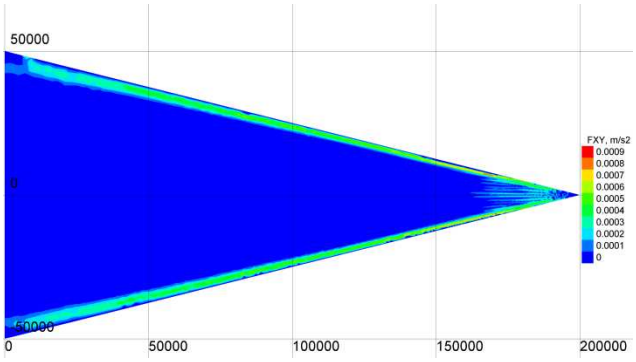

Figure 9. Wave forces at t=14h00.

B. *Irish Sea/Ramsey Sound Model*

The FEM mesh of the Irish Sea model is presented in Fig. 10. The mesh size is about 7 km near the southern boundary in the Celtic Sea, and gradually approaches 40 m around Ramsey Sound (Figs. 11 and 12).

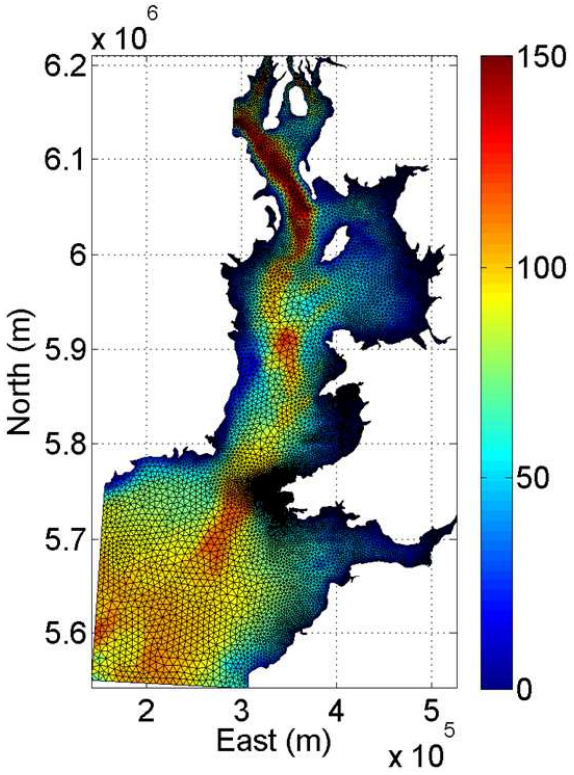

Figure 10. Bathymetry and FEM mesh of the Irish sea TELEMAC model.

The model was forced by tidal water elevations at the open boundaries. The tidal constituents at the open boundaries were interpolated from an analysis of POLCOMS shelf scale model output. Model results at different tidal gauge locations in the Bristol Channel and Liverpool bay compared well with observed data (not presented here). ADCP data collected during the spring tide of May-2011 (14-20 May 2011) were used to evaluate the simulated currents around Ramsey Island. As an example, Fig. 12 and Fig. 13 demonstrate the flow pattern on 15-May-2011 at 11:30, along with measured ADCP data. As can be seen, the spatial variations of the currents in this region are extensive, and the model and observations have a convincing agreement. The current speed approaches 3.5 m/s inside Ramsey sound during this period.

A TOMAWAC wave model of the same area was developed. Since the majority of waves in the Irish Sea are generated by winds emanating from the southwest [7], the

distribution of the significant wave height for a typical southwesterly wind speed of 20 m/s is plotted in Fig. 14.

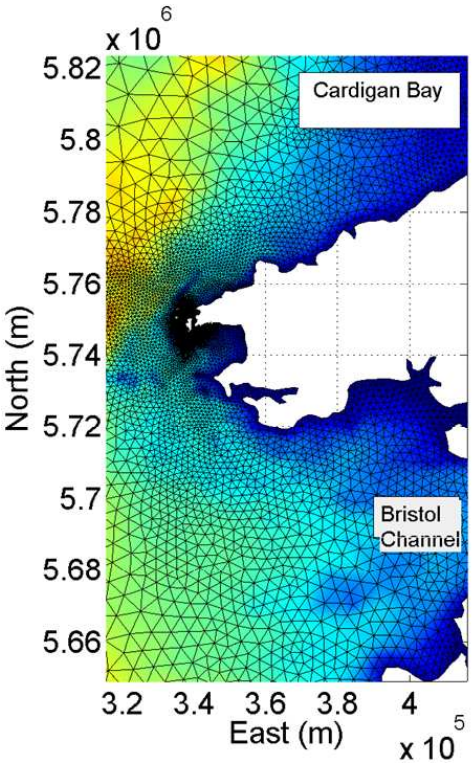

Figure 11. A closer view of the variable mesh density with very fine mesh around Ramsey Island.

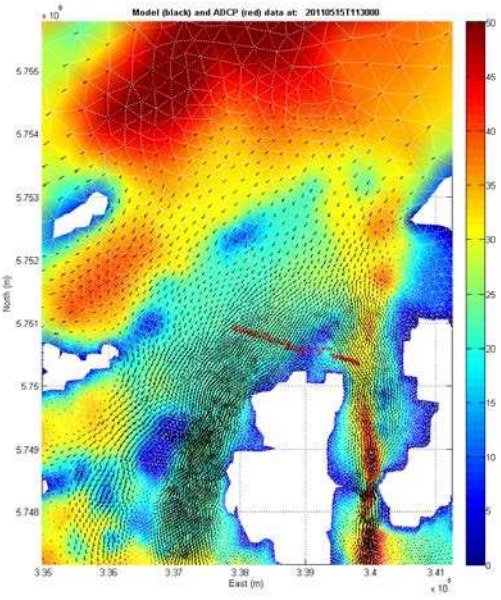

Figure 12. A typical flow pattern in the vicinity of Ramsey Island at 15-May-2011 11:30 PM compared with ADCP data (measured data were collected by Cardiff University).

It is clear that Ramsey Sound is sheltered from this typical southwesterly wind event. However, the wave heights to the west of Ramsey Island reach up to 7 m for this event. This suggests that running a coupled wave current model is more essential to the west of the island, while the wave energy inside Ramsey sound is not that significant. Further, the model results could be improved, particularly by improving the bathymetry near the coastline and intertidal zone.

To the best of our knowledge, no wave buoy data are available around Ramsey Island. However, wave data exist for Scarweather WaveNet Site, which is located at the middle of the Bristol Channel. The effect of the inclusion of tides on estimated wave heights during an event in October-2005 is depicted in Fig. 15. Fluctuations of the wave height due to the tide are present in both the measurement and the coupled wave current model. However, a pure wave model cannot capture these fluctuations. Further work is underway to improve the wave-current model and assessment of wave energy resources using this coupled model.

V. CONCLUSIONS AND RECOMMENDATIONS

Our study of wave-tidal interactions in an idealised triangular domain suggest that assessment of the wave energy resource, without considering the effect of tides, could lead to errors of up to 10% in high tidal range areas like the Bristol Channel. Further research is underway to investigate this for the actual bathymetry of the Irish Sea. The errors associated with estimating wave power are almost twice those errors in simulating the significant wave height. Additionally, for the safe design of offshore or nearshore tidal energy devices, the effect of tides on modulating the wave heights should be considered.

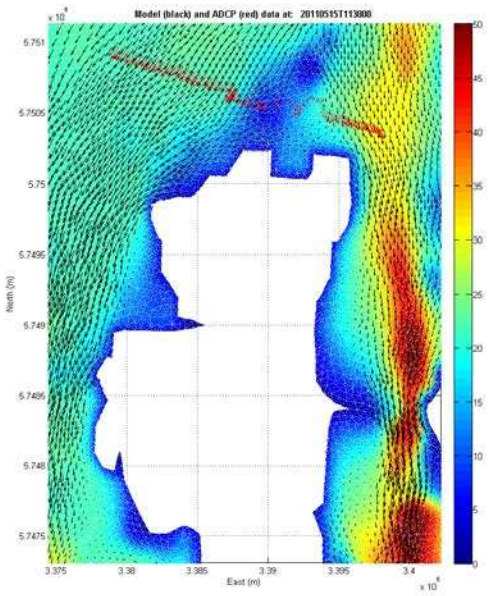

Figure 13. A closer view of flow around Ramsey Island (see also Fig. 12).

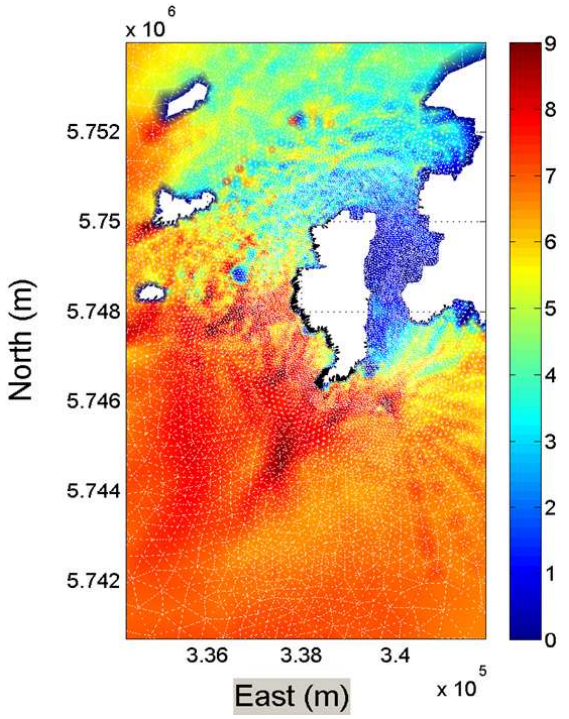

Figure 14. The distribution of the significant wave height around Ramsey Island for a typical southwesterly wind of 20 m/s simulated by TOMAWAC.

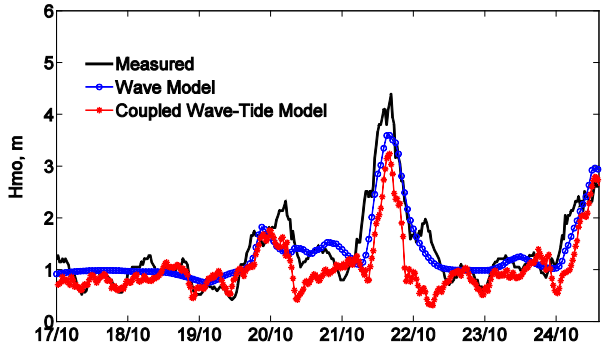

Figure 15. Effect of including the tide on wave prediction at a Scarweather WaveNet Site, Bristol Channel (51°26'.00N and 003°55'.99W), 17-24 October 2005.

The primary hydrodynamic model of Ramsey Sound demonstrated the suitability of TELEMAC for multi-scale modelling of waves and currents in highly energetic environments with complex bathymetry. The resolution of the bathymetry, especially near coasts and in the intertidal zone, is the key factor for improving the model results.

Ramsey Sound is sheltered from southwesterly wind waves, while the interaction of waves and tides to the west and southwest of Ramsey Island is important, and can be simulated by models like TELEMAC.

ACKNOWLEDGEMENT

Thanks to Marine Digimap for supplying the bathymetry data, and LCRI-Marine (Cardiff) for ADCP data. Wave data were supplied by the British Oceanographic Data Centre (BODC). This work was undertaken as part of the SEACAMS project, which is part-funded by the EU's Convergence European Regional Development Fund through the Welsh Government.

REFERENCES

[1] The TELEMAC Modelling System, www.opentelemac.org

[2] J.M. Brown and A.G. Davies, "Methods for medium-term prediction of the net sediment transport by waves and currents in complex coastal regions", CONT. SHELF RES., vol. 29, pp 1502-1514, 2009.

[3] N. Guillou and G. Chapalain, "Modeling the tide-induced modulation of wave height in the outer Seine estuary", J COASTAL RES, vol. 28, pp. 213-223, 2012

[4] C C Mei, The Applied Dynamics Of Ocean Surface Waves, Advanced series on Ocean Engineering, vol 1, World Scientific, 2003.

[5] US Army Corps of Engineers, Coastal Engineering Manual - Part II, 2008.

[6] A.S. Bahaj, "Generating electricity from the oceans". RENEW. SUST. ENERG. REV., vol. 15, pp. 3399-3416, 2011.

[7] S.P. Neill, J.D. Scourse, G.R. Bigg and K. Uehara " Changes in wave climate over the northwest European shelf seas during the last 12,000 years", J. GEOPHYS. RES., vol. 114, C06015, 2009.

Coastal Shelf Model of Northern European waters to inform tidal power industry decisions

Sébastien BOURBAN, Noémie DURAND, Michael TURNBULL
HR Wallingford Ltd
Wallingford OX10 8BA, UK
s.bourban@hrwallingford.com

Sian WILSON
Black & Veatch Ltd
Redhill RH1 1LQ, UK

Simon CHEESEMAN
The Energy Technologies Institute
Loughborough LE11 3UZ, UK

***Abstract*—The Energy Technologies Institute has commissioned a Continental Shelf Model of Northern European waters. Its principal aims are to assess the tidal energy potential around the UK, to inform the design of energy harnessing schemes, to understand the interaction between different tidal range and tidal stream energy schemes, and to evaluate their impact on Northern European coasts. To that effect, coarse and detailed resolution versions of the model were developed.**

Considerable effort was invested in identifying, obtaining and analysing suitable data for the model calibration and validation exercise. Good agreement was achieved overall, and in particular against discrete observed velocity data at two high energy sites in the Irish Sea/North Channel.

Computing time for a 15-day period is under 15 minutes on a 12-core desktop computer, and under 3 hours on a standard multi-core desktop computer for the coarser model. That for the detailed model is under 1.5 hours on an 8 x 12-core blade cluster. This allows simulations to be run efficiently and could open the way for parameter estimation and optimisation and ultimately for uncertainty analysis.

This makes the Continental Shelf Model a suitable tool for the tidal power industry to predict future tidal energy scheme scenarios, and the interaction between different energy schemes.

I. INTRODUCTION

Renewable energy extraction from tidal range and/or tidal current technologies in a particular area will affect the hydrodynamics of the local tidal system, impacting the tidal resource itself. There may also be a regional effect on the hydrodynamics, impacting other tidal energy extraction schemes' resource and potential energy yield. The impact of large scale and/or widespread tidal energy extraction on the tidal system is therefore important to understand in order to inform optimisation and management of the tidal resource.

This paper describes the development of coarse and detailed resolution versions of a Continental Shelf Model of Northern European waters (CCSM and DCSM respectively, CSM generically), and its anticipated use by the tidal power industry. [15] summarises the conclusions drawn from the CSM in terms of inter scheme interactions. The work was commissioned by the Energy Technologies Institute (The ETI) in 2011 with the aim of improving understanding of the possible interactions between proposed tidal energy extraction schemes. It was undertaken by Black & Veatch Ltd in partnership with HR Wallingford and the University of Edinburgh.

II. THE CONTINENTAL SHELF MODEL SETUP

The open source, industry driven, TELEMAC system, and more specifically its two dimensional flow module, TELEMAC-2D, forms the underlying modelling tool for the development of the CSM.

A. Extent

Recent publications [1, 4] have indicated that relatively small tidal power projects can affect very distant locations. In order to cater for long-range impacts and interactions between energy schemes, the CSM not only covers UK waters, but extends offshore slightly beyond the Northern European continental shelf (defined principally by the 300 m depth contour), and includes the coastlines of the United Kingdom, Ireland, the Channel Islands, France, Belgium, the Netherlands, Germany, Denmark, Sweden and Norway. It includes, amongst others, the Malin Sea, Irish Sea, Celtic Sea, English Channel and the North Sea. The Baltic Sea is not included in the model because of its very limited tidal range and minimal mean spring tidal current velocities [2]. An annual mean discharge is instead imposed as an inflow in the model. The extent of the CSM is shown in Figs. 3 and 4.

B. Resolution and exclusions

Two versions of the CSM were developed as follows:

- The Coarse resolution of the CCSM starts from c. 1 km at the coastline, on islands and locations of selected tidal range and tidal current energy schemes, with a growth rate of 8%, to reach a maximum of c. 35 km in open water. The total number of nodes is c. 161,500; the number of elements is c. 301,000.
- The Detailed resolution of the DCSM starts from c. 200 m at the coastline, on islands and energy scheme sites, with a growth rate of 8%, to reach a maximum of c. 35 km. The total number of nodes is c. 1,625,000; the number of elements is c. 3,055,000.

While the resolution of the DCSM provides more detailed predictions than that of the CCSM, its purpose, like the CCSM, is primarily to provide preliminary impact assessment results for the entire Northern European continental shelf. It is not to be used in place of a refined local model when considering resources / impacts in specific areas.

In both versions of the CSM, the unstructured mesh used by TELEMAC-2D was fitted to predefined internal lines and refined locally to facilitate the inclusion of coastal sites of interest, or the geographical locations of anticipated tidal range and tidal current energy schemes at a later date. Particular attention was paid to coastal features such as small inlets, passages and islands, to ensure they were adequately represented in the models.

The level of detail with which sites of interest, the coastline and islands are represented in a model depends largely on the local resolution. For illustrative purposes, Fig. 1 shows representations of an hypothetical island, in a detailed- (top image) or coarse- (bottom image) resolution model. In Fig. 1, the colour contours show arbitrary elevations in the vicinity of the island. The unstructured mesh defined by the model resolution is shown in grey and a see-through surface is shown in blue that represents the still water level.

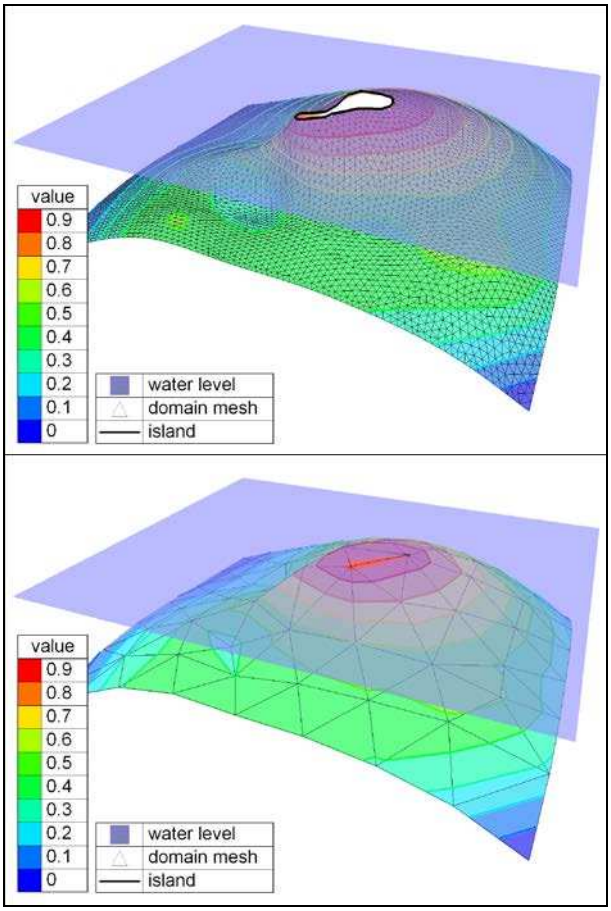

Figure 1. Representation of an island in different resolution models.

In the coarser model, the island is represented as a bathymetric feature; that is, all the elements are part of the unstructured mesh. As the water level goes down with the tide, dry cells will be introduced at the tip of the (under water) island (marked as a thin red patch). The cells will become wet again when the water level goes up.

In addition, significant effort was invested in this project to identify and group together clusters of small islands into larger land masses, in order to represent the hydrodynamics as closely as possible. Examples include the Isles of Scilly, the islands between Ile d'Ouessant and Ile de Molène off the coast of Brittany, or islands along the rugged coastline of Norway to name a few.

In the example illustrated in Fig. 2, the Isles of Scilly were individually contoured in the DCSM (purple contours) but clustered, to some extent, in the CCSM (orange contours). This was made necessary by the model resolution.

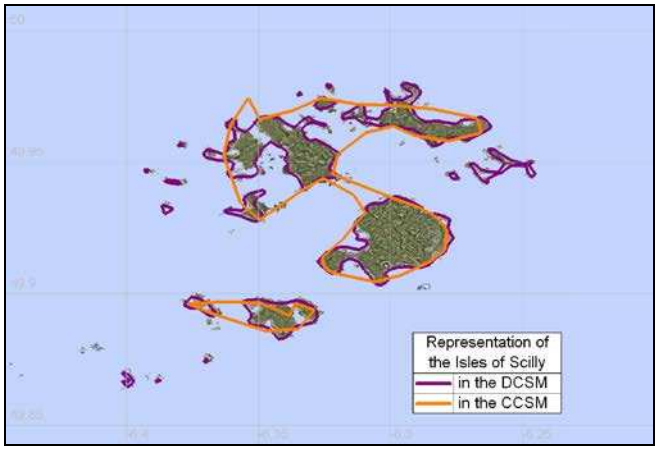

Figure 2. Representation of the Isles of Scilly in the CSM.

C. *Seabed map*

The bathymetry in the CSM was developed from Admiralty Chart data processed and provided by SeaZone of HR Wallingford. Significant effort was invested in the pre-processing of the digitised bathymetric charts to ensure consistency across all regions as many of the charts overlapped. The level of detail included in the charts was deemed sufficient for the purpose of the CSM, given its resolution.

The CSM was developed in a bespoke spherical coordinate system due to its large extent, true to distances in m. The vertical reference datum was Mean Sea Level (MSL).

D. *Tidal forcing*

The CSM is driven by spatially varying time histories of water levels along the model offshore boundaries, combined with a radiative algorithm (Thompson boundary [8, 13]) that allows internal waves to leave the domain with little or no reflection. The time histories were synthesised at every computational point directly from TELEMAC [12], based on the 13 constituents available from the Northern European

TPXO dataset (8 primary, 2 long-period and 3 non-linear constituents).

The TPXO dataset is one of the most accurate global models of ocean tides [11]. It is based on a best-fit of tidal levels measured along remote sensing tracks from the TOPEX/POSEIDON satellite project in operation since 2002. The Northern European dataset was deemed adequate to define tidal levels in deep water, at the model boundary.

III. THE CSM CALIBRATION, VALIDATION AND VERIFICATION

The CSM was first calibrated (against coastal observed tidal data), then validated (against offshore observed tidal data) and verified (against velocity data and atlases). Considerable effort was invested in identifying, obtaining and analysing suitable data from various organisations, metocean and hydrographic offices to that effect.

A. Calibration

Calibration was carried out over a complete 15-day tidal cycle featuring above average spring conditions and below average neap conditions, to ensure that the CSM performs well for the entire range of expected tidal conditions. Calibration was achieved by tuning the CSM bed friction parameter, at a global level first and within 4 regions of the domain eventually, until good overall agreement was reached at 24 coastal tidal gauges [6, 9, 14].

These locations were selected such that (a) they cover the entire model area (this is particularly relevant since one of the principal aims of the CSM is to inform the impact of the implementation of tidal energy schemes upon other interests); (b) they represent the possible range of expected spatial variations in tidal amplitude throughout the model area; and (c) they are located close to key areas of interest (e.g. Hinkley Point – Avonmouth in the Bristol Channel, Portrush in the North Channel).

Agreement of the CSM results with observed data was primarily illustrated by comparison of the predicted and observed water level traces over the full 15-day tidal cycle, at all calibration locations. Examples for a subset of locations (marked in Fig. 4 and representative of the model area) are given in Fig. 5 for the DCSM. In these plots, the horizontal axis is time; the vertical axis is free surface elevation in m. To aid visualisation of the results, the vertical axis was coloured according to range (dark green for ±4 m, bright blue for ±8 m, and red for ±12 m).

While the time histories give an immediate visual impression of the agreement, the quality of the CSM calibration was assessed by computing the difference in tidal levels between the model predictions and the re-synthesised data at each time step throughout the 15-day tidal cycle. The result of this assessment was presented in terms of normalised Root Mean Square Error (RMSE) and Mean Absolute Error (MAE) values for all the calibration locations. A target normalised RMSE value of 10% is often deemed to reflect a good calibration. This metrics was used for the CSM.

The analysis confirmed the suitability of both versions of the CSM. In the St George's Channel, Bristol Channel, Irish Sea and North Channel area, normalised RMSE values were generally well below the target value of 10%. The agreement was also strong around the Orkney and Shetland Islands although the calibration locations were not directly located in areas of significant tidal energy potential (due to lack of data at the time of the study).

In Fig. 3 and Fig. 4, the spots mark all the calibration locations considered in this project; the colour identifies the normalised RMSE value obtained from the calibrated CSM. For example, dark and light green spots indicate locations where the normalised RMSE value was below 5% and 10% respectively, that is, where the calibration target for the CSM was met or exceeded.

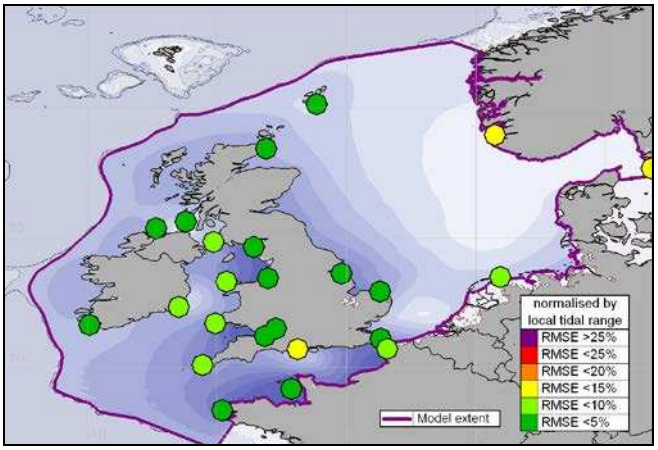

Figure 3. Quality of the CCSM calibration exercise measured in terms of normalised RMSE. The model extent is also shown.

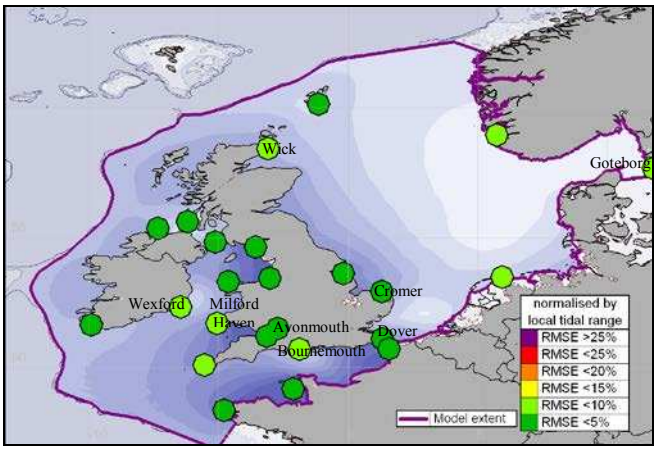

Figure 4. Quality of the DCSM calibration exercise.

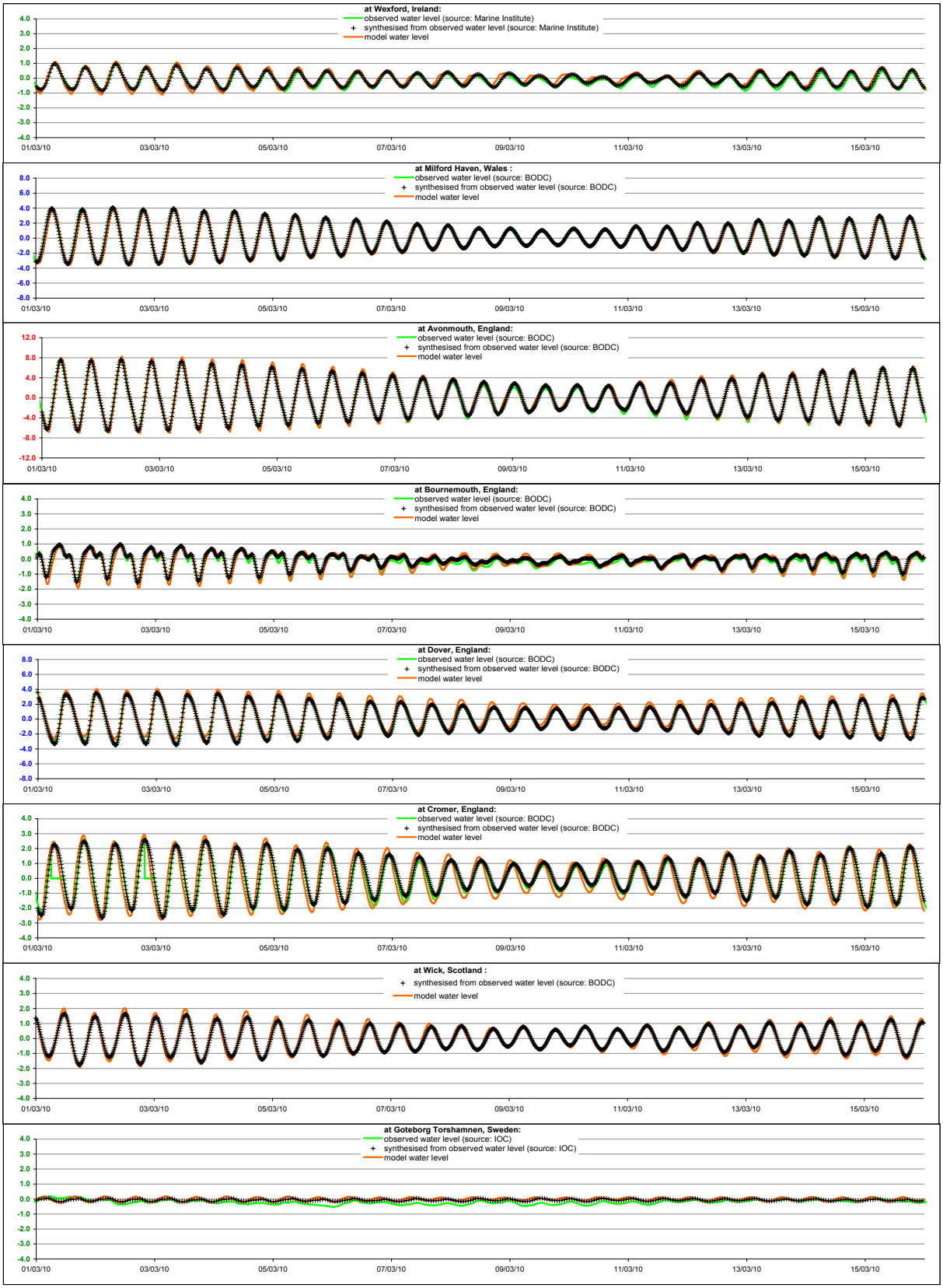

Figure 5. Tidal range time histories. The tidal levels predicted by the DCSM are indicated as a thick orange line, the levels obtained by tidal re-synthesis are shown as black crosses. When available concurrently to the calibration period, the observations [6, 9, 14] are represented by a thick light green line.

B. Validation

Validation of the CSM was performed against independent sets of observed offshore tidal gauge and bottom pressure data (at 11 stations). Comparison against these data sets confirmed the suitability of the CSM in high energy key areas.

C. Verification

The data used to verify the CSM comprised velocity data and atlases of tidal range and peak current speed. Although the agreement of the CCSM with velocity data was mixed (principally because of its coarse resolution), the DCSM velocity predictions compared very favourably with measurements available at the time of the study. The results of this analysis cannot be shown in this paper to protect the copyright attached to the measured velocity data.

Verification against the MAFF Atlas [10] was successful with the amphidromic points (e.g. off Wexford) and the areas of high tidal range (e.g. Morecambe Bay) qualitatively very well reproduced in both versions of the CSM.

Verification against the UK Marine Renewable Energy Resources Atlas [5] was also positive for known energetic areas. It is noted that the finer resolution of the CSM (compared to that used in the UK Atlas [5]) allows a far better discretisation of the velocity field in key areas. As such, the DCSM (and to a lesser extent the CCSM) identified strong current areas (e.g. at the Falls of Warness, or in the North Channel off Larne) that had been previously misrepresented in the UK Atlas.

These comparisons against atlases, as opposed to the spot checks performed in the calibration/validation exercise, enhance the overall CSM credibility.

D. Discussion

It is noted that the CCSM and the DCSM have similar tidal level behaviour. Overall, the predicted tidal ranges are higher with the DCSM than with the CCSM. Differences are not unexpected. The DCSM understandably provides far superior resolution everywhere. This is most apparent on current velocity maps.

The CCSM and the DCSM also have similar levels of performance, with the DCSM, generally, only marginally more accurate than the CCSM in terms of normalised RMSE (the principal measure chosen to evaluate performance).

This gives confidence in the CSM predictions, and in the model robustness.

Verification against existing models was successful and enhances the CSM credibility. It is noted that the DCSM is two orders of magnitude finer (at sites of interest) than the existing UK Marine Renewable Energy Resources Atlas.

E. Sensitivity

A sensitivity analysis was subsequently performed in an effort to assess the response of the CSM to tuneable parameters such as bed friction, turbulence and numerical schemes. Sensitivity to freshwater discharges was also considered.

The main conclusions are:

- Based on experience with hydrodynamic models, the parameter with the most impact on model results is the bathymetry.
- The good level of agreement between the CCSM and the DCSM (obtained with very different model resolutions) demonstrates grid insensitivity, although the DCSM results will be more resolved.
- It has been shown that the formulation employed to represent bed friction is not of particular importance.
- However, the selection of the bed friction parameter has a significant effect on the CSM predictions (water levels and current speeds), hence on the performance against observations. In general terms, the highest impact in terms of levels is observed in the English Channel, in the Severn Estuary, and in the Irish Sea east of the Isle of Man.
- Turbulence has a noticeable effect on the predicted current speeds in some specific areas. However, in the absence of observed velocity data available globally around the UK to calibrate against, it is difficult to discard (or favour) one turbulence formulation over the other. While the constant viscosity and Smagorinski models were tested, the Elder model was eventually retained based on HR Wallingford experience.
- The other parameters tested - “free surface gradient compatibility criteria”, discharge rate applied in the Thames and/or the Baltic Sea, and tidal force (calculating the astronomical terms required in the tidal forcing terms) - all have a limited impact on the CSM water level and velocity predictions.

IV. THE CSM AS A TOOL TO INVESTIGATE TIDAL POWER PROJECTS AROUND THE UK

From the outset, it was the intention that the CSM would become publicly available for the tidal power industry to understand the possible interactions between proposed tidal energy schemes across Northern European waters. With that in mind, the CSM was designed to be versatile. Each tidal scheme, in the CSM, is defined by:

- a geographical extent and location. The geographic extent and location are stored within binary geospatial files, commonly called shape files. The format of these files is the standard ESRI format, produced by many geographic information systems (GIS) and by analysis and visualisation software such as Blue Kenue.
- parameters informing how the CSM should respond to the presence of the tidal range and/or tidal current

schemes. Implementation of various energy schemes by the end-user is done through generic parameterised formulations representing schemes at the scale and resolution of the CSM, and catering for all types of technology, current and future. These formulations rely on the existing functionalities of the TELEMAC system.

A. TELEMAC-2D

TELEMAC-2D solves the 2D depth-averaged shallow water equations, also called the St Venant equations ([7]). These comprise three equations: one equation for the conservation of the volume of water and two equations representing the conservation of the water momentum, as follows:

continuity equation:

$$\frac{\partial h}{\partial t} + \frac{\partial hu}{\partial x} + \frac{\partial hv}{\partial y} = Srce \tag{1}$$

where *Srce* is a variation of the volume of water within the water column (including rain, evaporation and other intakes and outlets such as those found around hydraulic structures). This makes the continuity equation well suited to represent flows through tidal range schemes.

x-momentum equation:

$$\rho h\frac{\partial u}{\partial t} + \rho hu\frac{\partial u}{\partial x} + \rho hv\frac{\partial u}{\partial y} = -\rho gh\frac{\partial (h+b)}{\partial x} + \frac{\partial}{\partial x}\left[\rho h \nu_e \frac{\partial u}{\partial x}\right] + \frac{\partial}{\partial y}\left[\rho h \nu_e \frac{\partial u}{\partial y}\right] + hF_x \tag{2}$$

y-momentum equation:

$$\rho h\frac{\partial v}{\partial t} + \rho hu\frac{\partial v}{\partial x} + \rho hv\frac{\partial v}{\partial y} = -\rho gh\frac{\partial (h+b)}{\partial y} + \frac{\partial}{\partial x}\left[\rho h \nu_e \frac{\partial v}{\partial x}\right] + \frac{\partial}{\partial y}\left[\rho h \nu_e \frac{\partial v}{\partial y}\right] + hF_y \tag{3}$$

where F_x and F_y are source terms and body forces acting on the water momentum (including seabed friction, Coriolis, drag, and possible energy extraction devices). This makes the momentum equations well suited to represent drag and energy extraction at tidal current schemes.

B. Tidal range scheme implementation in the CSM

1) Identification

The location of a tidal range scheme is defined by a polyline representing the barrage or lagoon alignment along which embankment, turbines and sluices lie. The mesh elements which this polyline crosses are automatically identified and masked to represent the blockage; the corresponding nodes are listed for source and sink terms to be applied.

To facilitate the process, a convention on the orientation of the polyline determines which nodes are upstream and which are downstream of the structure. This is particularly relevant to schemes operating only during ebb tides or flood tides. This methodology also allows barrages to be defined between islands for example, where the coastline cannot be used to identify the upstream and downstream of the works.

The turbines and sluices are then sited along the line of the structure using their specified width, starting from the deepest regions.

2) Parameterisation

As introduced earlier, a tidal range scheme is represented in the continuity equation (1) through the source/sink term *Srce* (subroutine PROSOU). The discharge (by extension the power generated) is a function of the head and energy difference across the control structure as follows:

$$Q = D_1 + D_2\,\Delta h + D_3\,\Delta h^2 + D_4\,\Delta h^3 + D_5\,h\sqrt{\Delta h} + D_6\sqrt{\Delta h} + D_7\,\Delta u^2 \tag{4}$$

where Q is the discharge in m^3/s, Δh is the head difference in m, h is the average water depth in m, Δu^2 relates to the energy difference and can be used to represent other energy losses, and where D_1 to D_7 are constants defined by the technology type, the operational procedures, the turbine capacity, the size, submergence and types of the openings and other key turbine parameters.

In addition to the parameters representing head-discharge-power characteristics, a tidal range scheme is characterised by a mode (Ebb, Flood, Dual or Wall) and an extensive list of numerical parameters. They include various turbine characteristics and operating rules for three different types of turbines. Thus, while the number of parameters (79 in total) is significant, not all the parameters are required to define a particular scheme.

C. Tidal current scheme implementation in the CSM

1) Identification

The extent of a tidal current scheme is defined by a closed polygon representing the area within which the turbines are to be sited. The additional momentum forces are applied to all the nodes automatically listed with the closed polygon.

It is noted that a methodology was developed as part of this project to delineate the regions of most interest for tidal current device deployment. These regions are constrained by a number of pre-defined criteria, such as geographic constraints (e.g. distance from shore, political boundaries), technology constraints (e.g. turbine operational depth, minimum operational resource), environmental constraints (e.g. reduction in mean velocity) or targeted installed capacity. The regions respecting the search criteria and with the highest kinetic power density are delineated first.

This methodology is illustrated in Fig. 6 for the incremental development, with different decades, of the available resource at a proposed tidal current scheme site[1].

In Fig. 6, the x and y axes are easting and northing, and the colour of the polygons identifies different decades. For example, light blue identifies the region developed during the 1st period because of the proximity to shore. The other deployments (dark blue to deep pink) were delineated incrementally from the 1st time period, and therefore a given decade deployment has fed into the next decade. It is clear from Fig. 6 that the deployments follow the (extent and shape of the) resource.

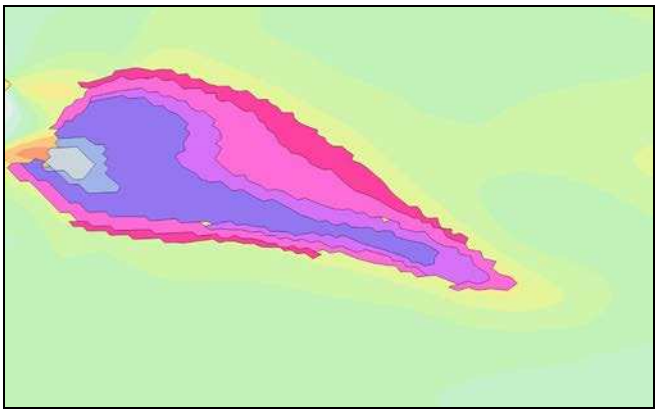

Figure 6. Identification of the "best" available resource corresponding to different decades (search criteria). Underlying map shows maximum current speed as predicted by the DCSM.

2) Parameterisation

When tidal current devices are introduced in the hydrodynamic system, the system loses energy, whether the energy is extracted or whether drag forces are introduced. The various contributions for the loss of energy are represented as additional terms (subroutine DRAGFO), the sum of which will be F_x and F_y in the momentum equations (2) and (3).

These additional momentum terms are a means of parameterising physical processes that occur at higher resolution than is used within the model. The parameterised terms replace small-scale physical processes (from the point of view of model resolution) with a continuous property applied across computational cell.

A tidal current scheme is, therefore, characterised by: (a) a number of devices per km^2 (or a device footprint in m^2, whichever is readily known); (b) a structural drag coefficient and associated support structure area, which both depend on the technology; and (c) a power/thrust curve for extracted energy, which also depends on the technology. It is noted that the power/thrust curve relates to mechanical power (that which is removed from the system in the CSM), as opposed to electrical power delivered to the grid. An efficiency factor of 0.8 was assumed to that effect since the electrical power curve is that typically known.

Should the user not know the power/thrust curve for a particular device, it is possible to estimate it based on the device characteristics (e.g. turbine diameter, cut-in and rated velocity). In that case, the estimate would be based on a 5th order polynomial function of the rated velocity.

D. Example applications

Not detailed in this paper, but the subject of [15], the CSM was employed in this project to investigate a number of viable options, introduced in [3] and corresponding to a real interest in terms of tidal power resource.

Fig. 7 and Fig. 8 present examples of such tidal range and tidal current scheme implementations in the DCSM. In these figures, the schemes are identified as black dashed lines; the impact is expressed in terms of tidal range difference in % for tidal range schemes, and in terms of kinetic power density changes in % for tidal current schemes, relative to the no-scheme scenario. Unfortunately the scales cannot be shown to protect the value of the CSM results, prior to its official release, but the effect of the schemes is clear.

For example, in Fig. 7, a significant reduction in maximum tidal range (pink areas) was observed upstream of the longest barrage following its construction. The smaller barrage yielded a lesser, yet noticeable, reduction (deep blue areas). This configuration did not conform to the expressed requirement to maintain at least 80% of the natural tidal range in the basin, and alternative options were considered.

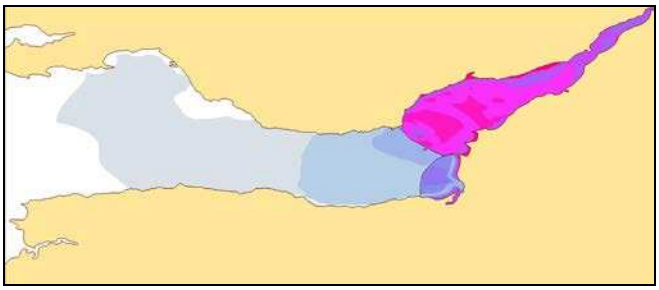

Figure 7. Example impact of two tidal range schemes implemented in the DCSM. Expressed in terms of maximum range difference (%).

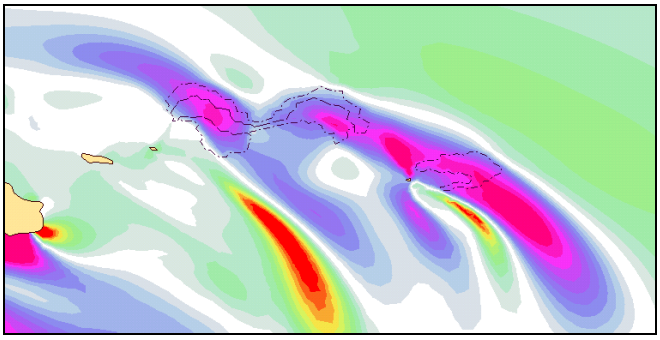

Figure 8. Example impact of a tidal current scheme implemented in the DCSM. Expressed in terms of mean kinetic power density change (%).

[1] Its location has been purposefully disguised in this figure, to protect the ETI, prior to the official release of the CSM.

In Fig. 8, it is apparent that the resource is redistributed as a result of the tidal scheme implementation with a deficit in mean kinetic power density in the lee of the devices, and a pocket of higher energy further south. This case highlighted problematic intra-scheme interactions with some of the devices in the wake of others.

V. WHAT NEXT?

The CSM has proven, as expected, to be an extremely useful modelling tool for the analysis of tidal characteristics on the Northern European continental shelf and, most importantly for this project, of the interactions resulting from the development of schemes to harness these tidal characteristics, be they tidal range or tidal current schemes. A paper is being presented at the ICOE 2012 conference [15] summarising the conclusions drawn from this work in terms of inter scheme interactions.

From the outset, the ETI had decided to make the CSM publicly available, through a fee-for-service arrangement[2]. A Web User Interface has, therefore, been put in place, which principal goal is to provide users with a simple functional tool to operate the CSM irrespective of the chosen resolution. Users will be able to upload tidal energy schemes, automatically triggering submission on the appropriate high performance computers.

The CCSM computes a 15-day period within 3 hours on a standard multi-core desktop computer. If used in parallel on one 12-core workstation, the CCSM only takes 15 minutes for the same predicted period. The DCSM computes a 15-day period within 15 hours on one 12-core workstation and in less than 2 hours on one 8-blade 12-core high performance computer. These times do not include pre- and post-processing of data and transfer of files to and from the targeted computers.

The CSM will provide the industry with a UK scale tool for assessing likely interactions between schemes. It is generally recommended that the CCSM be used for high level tidal range and broad tidal current investigations. However, the DCSM should generally be used in preference to the CCSM for investigation of tidal current schemes, as the greater resolution predicts tidal currents (and spatial variability thereof) more accurately. For detailed site specific investigations, more detailed analysis is required.

Building on the experience gained with the CCSM and the DCSM, it could now be envisaged to further refine the CSM, within a couple of years, to include more resolved bathymetry data (e.g. TruDepth from SeaZone). This Refined CSM (RCSM) would aim at solving different problems and would require a minimum resolution of c. 50m at the sites of interest and at the coastline if not smaller to match up with bathymetry resolution.

REFERENCES

[1] R. Burrows et al, 2009. Tapping the Tidal Power Potential of the Eastern Irish Sea, Joule Project JIRP106/03, University of Liverpool and Proudman Oceanographic Laboratory, NERC.

[2] M. Carlsson, 1997. Sea Level and Salinity Variations in the Baltic Sea - an Oceanographic Study using Historical Data. Department of Oceanography, Göteborg University. ISSN 1400-3813.

[3] Carbon Trust, 2011. UK Tidal Current Resource & Economics

[4] A. Cornett, J. Cousineau, and I. Nistor, 2011. Hydrodynamic Impacts due to Tidal Power Lagoons in the Upper Bay of Fundy, Canada.

[5] Department for Business Enterprise and Regulatory Reform, 2008. Atlas of UK Marine Renewable Energy Resources. Produced by ABPMer.

[6] Global and regional networks of real time sea level stations. Data available from the Sea Level Station Monitoring Facility, part of the Intergovernmental Oceanographic Commission, IOC.

[7] J.M. Hervouet, 2007. Hydrodynamics of Free Surface Flows: Modelling with the Finite Element Method. Wiley Blackwell. 360p. ISBN-13: 978-0470035580.

[8] J.M. Hervouet, C. Denis and E. David, 2011. Revisiting the Thompson boundary conditions. XVIIIth TELEMAC & MASCARET User Club Conference, Proceedings. 153p. October 2011.

[9] Irish National Tide Gauge Network. Data available from the Marine Institute.

[10] Ministry of Agriculture, Fisheries and Food, 1981. Atlas of the Seas around the British Isles. ISBN 0 907545 00 9.

[11] OSU, 2008. OSU Tidal Data Inversion Software and Atlas, Oregon State University, European Shelf.

[12] C-T. Pham and F. Lyard._ Boundary conditions for tide in TELEMAC. XIXth TELEMAC-MASCARET User Club Conference Proceedings, in press.

[13] K.W. Thompson, 1987. Time dependent boundary conditions for hyperbolic systems. Journal of Computational Physics 68, 1-24.

[14] UK National Tide Gauge Network, part of the National Tidal & Sea Level Facility (NTSLF). Data available from the British Oceanographic Data Centre.

[15] S. Wilson, S. Bourban and S. Couch. Understanding the interactions of tidal power projects across the UK Continental Shelf. ICOE 2012 Proceedings, in press.

[2] Fees will be re-invested to maintain and develop the CSM.

Experiments and numerical modelling of the performance and wake of a tidal converter

Bozonnet Pauline, Andreewsky Marc, Buvat Clément,
Menon Jean-Michel, Martin Vanessa
LNHE (National Laboratory for Hydraulics and Environment), SINETICS[2] (SImulation NEutronique, Technologies de l'Information et Calcul Scientifique)

Denis Christophe,
EDF R&D
6, quai Watier, 78400 Chatou, France
marc.andreewsky@edf.fr

***Abstract*—In the framework of the project called PerAWaT (Performance Assessment of Wave and Tidal Array Systems) which has been commissioned and funded by the Energy Technologies Institute (ETI) and which aims at developing a software to help developers of marine energy converters (tidal and wave) farm arrays, the LNHE conducted both experiments in their facilities and numerical modelling with Telemac2D.**

The flow around a 1/30th scale turbine in a flume has been investigated. Torque and thrust sensors on the rotor of the turbine, together with the measurement of the rotational speed, yield the power and thrust coefficients of the rotor for different Tip Speed Ratios (TSR). An Acoustic Doppler Velocity meter (ADV) is used to record local 3D velocity and turbulence intensity and lead to a detail mapping of the wake.

A numerical model of a turbine has been developed within Telemac2D and calibrated against these experimental measurements. First, the model was adjusted and validated for the simple case of an island in a channel, extensively described in the literature. An extensive convergence study as well as a test for several numerical options of Telemac2D were carried out. Numerical errors propagation was also evaluated with the CADNA library. Second, and based on the first simulation conclusions, the LNHE turbine experiment was reproduced. With an appropriate set of parameters, the velocity comparisons between measurements and simulations are satisfying. Extension to other rotational speeds is not as straightforward as expected because of the complexity of phenomena at stake in the wake of a tidal converter.

I. INTRODUCTION

In the framework of the project called PerAWaT (**Per**formance **A**ssessment of **Wa**ve and **T**idal Array Systems) which has been commissioned and funded by the **E**nergy **T**echnologies **I**nstitute (ETI) and which aims at improving understanding of array interactions and at developing modelling tools, the LNHE (Laboratoire National d'Hydraulique et Environnement) conducted experiments in their facilities and numerical modelling with Telemac2D [1]. Performance and wake are the key parameters in developing farms of tidal converters. The energy extracted by the converters can be strongly affected by flow conditions such as the current velocity, the turbulence of the flow, the distance between the rotor and the free surface or the presence of waves.

Coastal basin scale simulations are extremely complex and are computationally expensive. Representing a 3D converter in a 3D mesh would add to this complexity, and therefore a 2D approach has been preferred so far. In order to predict the wake and the performance of a full array, the following methodology is applied: First, the quality of simulations obtained with Telemac2D and the validity of the numerical model will be checked for the flow around a simple cylinder. The best set of numerical options will also be investigated. Second, based on those first step conclusions, the model is applied to the flow around one converter in a flume and compared to the LNHE experimental data in order to validate it.

II. FIRST STEP: MODELLING THE CYLINDER WAKE

The free surface flow in a flume around a cylinder is well documented and can be considered close to the flow around a tidal turbine if the two obstacles and the inflow velocity are of the same order of magnitude. Consequently, this simple case is selected to investigate the different numerical options, as well as the time and mesh convergences in Telemac2D. Simulations are run and validated by comparing the experimental data to the simulated velocity fields.

A. Experimental data for the cylinder[2]

A turbulent flow in a flume around a vertical cylinder is experimentally investigated in [2] and is chosen to validate Telemac2D simulations because of its proximity with the LNHE experiments (Reynolds numbers and size of obstacles are of the same order of magnitude). The experimental setup and the important flow information are provided in Fig. 1. The flow is permanent because the Reynolds number corresponds to a critical and transitional regime, thus there is no vortex-shedding. This PhD report provides the depth-averaged velocity at approximately 50 locations all around the cylinder, up to a distance which is equal to twice the diameter of the cylinder.

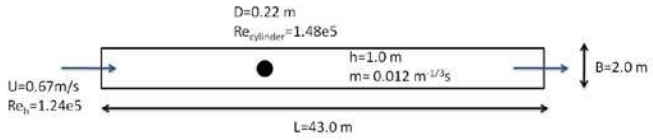

Figure 1. Sketch of the experimental setup and main flow characteristics for the cylinder case

B. Simulations

The flow described previously is simulated in Telemac2D. The mesh reproduces the whole flume, the cylinder being simply represented by a hole. The following numerical options, summarised in Fig. 2, are investigated:

- Two advection schemes are used: the method of characteristics, which is unconditionally stable but does not conserve the mass and the PSI scheme, which verifies mass conservation but also implies a stability criterion on the time step (Courant–Friedrichs–Lewy condition).
- Two turbulence models are selected: the constant viscosity model and the k-ε model. More details will be given afterward.
- Two types of mesh are tested: structured ones, which are regular and made of equilateral triangles and the unstructured ones (cf. Fig. 3). The first ones are supposed to give better results but in real applications, with complex coast, the mesh is always unstructured.
- The simulations are run for different mesh sizes and time steps to study the convergence.

Regarding the turbulence models, the constant viscosity ν_t has to be set by the user for this model. Note that this value is then given for the whole study domain which could be problematic when a converter array will be studied.

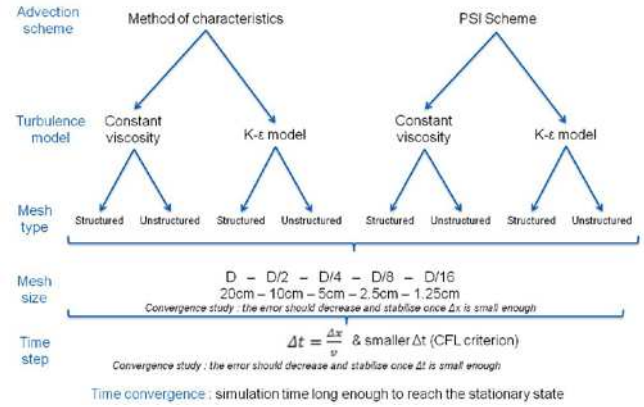

Figure 2. Summary of all numerical options tested for the simulations (advection schemes, turbulence models, mesh and time steps)

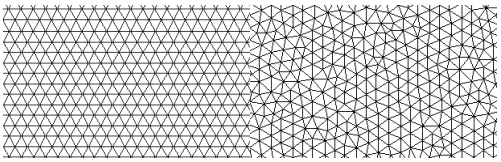

Figure 3. Two different mesh types: structured (left) and unstructured (right)

C. Preliminary simulation results: case with vortex sheddding

To have a better understanding of this model, the simulations are run for different values of ν_t, corresponding to different equivalent Reynolds numbers, defined as follows:

$$Re_{eq} = UL / \nu_t. \quad (1)$$

When νt is large enough, the equivalent Reynolds is in the laminar range of Reynolds. The constant viscosity decreasing beyond a certain value, the equivalent Reynolds increases and vortex shedding occurs. The apparition of such oscillations in Telemac2D corresponds to the conventional Reynolds range for which vortex shedding usually occurs (Re>50 [3]). For the different values of constant viscosity with vortex shedding phenomena, the Strouhal number can be calculated from the simulated velocity field:

$$St = fD / U. \quad (2)$$

It has been checked that the calculated Strouhal numbers for different Reynolds numbers correspond quite well to well-known and tabulated values [4]. It provides a general validation of the flow around a cylinder.

It also gives further understanding for the results obtained with the k-ε model, for which the turbulent viscosity is derived from k and ε values in each nodes. When using this particular model, the derived turbulent viscosity is always large, thus the equivalent Reynolds number is always small and will never lead to vortex shedding. The velocity is completely averaged.

D. Simulation results: case without vortex shedding [2]

To evaluate the quality of simulations, the relative error between the experimental (U_{exp}) and the simulated (U_{simu}) depth averaged velocity is calculated as follows:

$$\frac{1}{N}\sum_{i=1}^{N}\frac{|U_{exp} - U_{simu}|}{|U_{\exp}|}, \quad (3)$$

the sum being made on the different points for which measurements are available.

The points for which the velocity is too small (approximately U<0.1 m/s) are not taken into account because even a small absolute error can lead to a very large relative one. This mainly eliminates few points in the axis

downstream the cylinder. To compensate, the far wake will be further validated in this paper with self similarity.

For the constant viscosity model, the constant is set so that the error is minimised.

For the method of characteristics, the relative error versus the mesh size is presented in Fig. 4 for both turbulence models and both mesh types. For each point in Fig. 4, the time step convergence has been ensured beforehand. On the first part of the graph (the left part), as expected, the error decreases with the mesh size. For Δx=2.5 cm, or one eighth of the cylinder diameter, the four simulations correspond nearly to the same error, convergence is probably established. On the last part of the graph (the right part), a noticeable trend appears: the error increases.

For the PSI scheme, the same graph is plotted on Fig. 5. The same observations can be made: convergence is reached for Δx=2.5 cm. However the same problem occurs, the error increases back with very small mesh size and, which is specific to this advection scheme, with very small time step as well.

This trend could be explained by the large number of calculations needed when very small time step and mesh size are selected. The numerical error becomes so large that it exceeds the numerical solution in itself. This hypothesis is being validated as explained in the next paragraph.

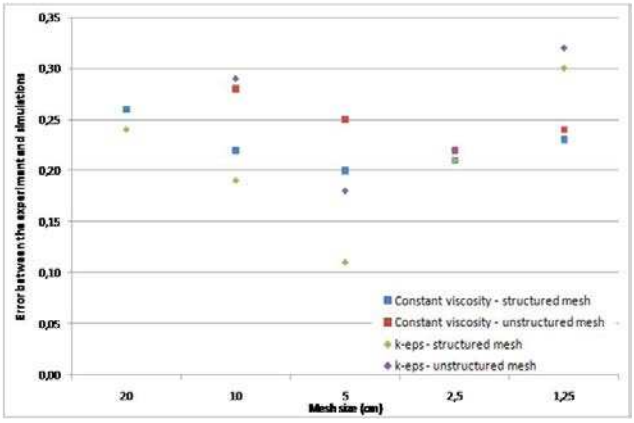

Figure 4. Method of characteristics: relative error between experiment and simulations on the x-component of the velocity, for different mesh sizes (cm), for two turbulence models and two mesh types

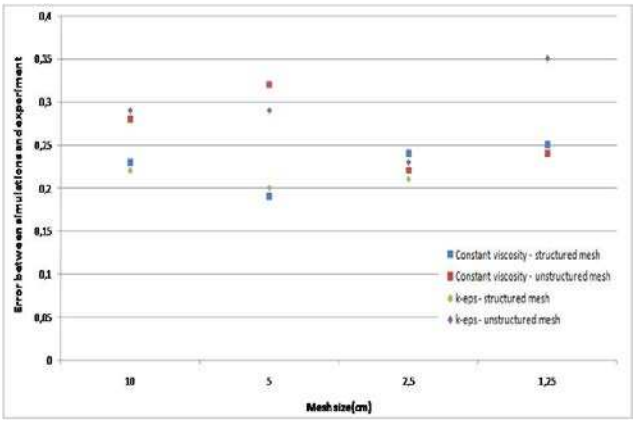

Figure 5. PSI scheme: relative error between experiment and simulations on the x-componenet of the velocity, for different mesh sizes (cm), for two turbulence models and two mesh types

E. Numerical verification by using the xD+P approach

The use of finite-precision arithmetic generates round-off errors at each arithmetical expression so some mathematical properties are lost during the computing of a numerical code. The fields of a numerical simulation using a finite element method are most often represented simply by their values in xD (1-D, 2-D, or 3-D). A new approach called xD+P was introduced in order to measure the numerical quality of the computed values [5]. More precisely, P represents the number of decimal significant digits which are not affected by round-off errors. The number of significant digits is computed by using the CADNA library [6]. The CADNA (Control of Accuracy and Debugging for Numerical Applications) library, developed by the Laboratoire d'Informatique de Paris 6 (http://www.lip6.fr/), uses an implementation of discrete stochastic arithmetic (DSA) based on the CESTAC method. The discrete stochastic arithmetic replaces the computer's deterministic arithmetic by performing each floating point operation 3 times, randomly rounding each time. The computing time of a program using CADNA increases as:

- the number of floating point operations is multiplied by three in contrast of the original code;
- frequent systems calls are performed to change the rounding mode;
- the number of cache defaults increases.

The use of the xD+P approach has permitted to verify for example that the water elevation computed in this study case is accurate from 10 to 15 significant digits for the first 2000 time steps as presented in Fig. 6.

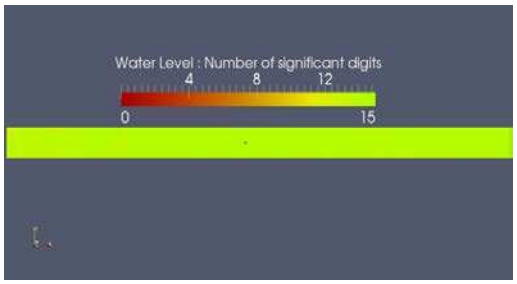

Figure 6. Number of significant digits on the water level field

Unfortunately, it was not possible to perform the numerical verification for all the time steps of the study case as the computing was performed only on eight processors on a local cluster. Séthy Montan, PhD student at EDF R&D, is currently working to implement efficiently CADNA in the TELEMAC system on supercomputers like IBM BG/P to perform large scale simulations.

F. Validation of the far wake

To validate the far wake, since the experimental data are only available for a maximum distance of 2 equivalent diameters from the cylinder, it has been checked that self-similarity of transversal velocity profile is verified along the flume. This is done for a specific set of options summarised in the paragraph G.

[7] derives the following formula, at the given longitudinal coordinate, x, of the flume:

$$\varphi(\zeta) = \exp(-\tfrac{1}{2}\,\zeta^2), \tag{4}$$

$$\text{where } \zeta = y / l(x). \tag{5}$$

This function φ defines the velocity deficit:

$$u_{def} = u_{\infty} - u(x,y) = u_{def\text{-}max}\,\varphi(\zeta). \tag{6}$$

The function φ, calculated with the analytical formula and with the velocity field from the simulations, is plotted versus ζ on the Fig. 7, for different distances from the cylinder. Those curves correspond to the constant viscosity model. Since the curves from the analytical formula and from the simulations are well matched, it validates the far wake. The same result is obtained with the k-ε model.

G. Conclusions

Time step and mesh size convergences have been checked. There are always optimal values for those both options, which additionally lead to nearly the same results whatever the advection scheme and the turbulent model chosen. However, the user has to be careful when using very small time step or mesh size because the error could increase.

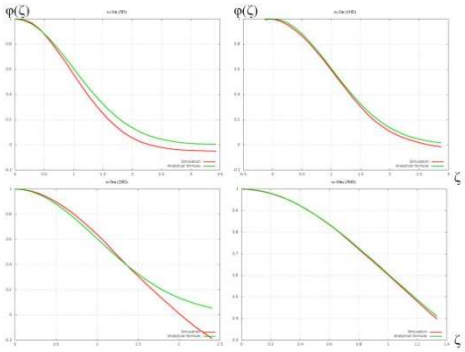

Figure 7. Selfsimilarity function φ(ζ) calculated with the simulations (red curve) and with the analytical formula (4) (green curve) at different distances from the turbine (from left to right, from top to bottom: x= 5D, x=10D, x=25D, x=50D), for the constant viscosity model

Regarding the other numerical options, the following conclusions are drawn:

- Regarding the advection scheme, both of them lead to quite the same velocity field once convergence is reached. Thus, the PSI scheme is considered as the best one since it conserves the mass.
- Regarding turbulence models, no definitive conclusion can be drawn. Both will be used for the converter application.
- Regarding mesh type, the structured mesh enables convergence to be reached with larger mesh size and time step. However an error as small as the previous one can be reached with unstructured mesh thanks to smaller mesh size. For the application to a real array on the open sea, the mesh has to be unstructured, thus this type of mesh is selected for the next step of methodology.

Finally, those conclusions display a recommended set of numerical options, relevant for the rest of the study.

III. THE DRAGFO ROUTINE: TRANSITION FROM THE CYLINDER TO THE TIDAL CONVERTER

A. Presentation of the DRAGFO routine

The model used to simulate the tidal converter is based on the Fortran DRAGFO routine, available in Telemac2D to simulate bridge piles. The obstacle is not represented in the mesh but is modelled by the application of a drag force on the fluid, on an area A which has to be defined by the user. The drag force can be expressed with:

$$F_d = -\tfrac{1}{2}\,\rho\, C_d\, S\, V^2, \tag{7}$$

where Cd is the drag coefficient, S the surface of the obstacle perpendicular to the flow and V is usually the value of the velocity if the obstacle were not there.

For stability reason, in our model, V is simply the local velocity (which exists since the obstacle is not meshed). This

leads to a new definition of the drag coefficient. Cd becomes a parameter of the model, adjusted to a value which could be different from the one coming from the experiment.

Another improvement has been brought to the obstacle model for the k-ε turbulence model. Since the cylinder or the converter is not meshed anymore, there is no self production of turbulence downstream the obstacle. A production term is added in the equation of k and ε, so that turbulent kinetic energy is generated by the model, on the area A where the drag force is applied. This term is equal to:

$$\eta \cdot \tfrac{1}{2} C_d S V^3 \cdot 1/Ah, \quad (8)$$

where Cd, S, V and A are defined as previously explained, h is the water height and η is a coefficient between 0 and 1. η can be understood as the part of the energy lost by the flow, which is converted to kinetic turbulent energy and then dissipated into heat.

B. Validation of DRAGFO for the cylinder case

The model has to be validated on the previous cylinder case before it is applied to the study of a tidal device. Simulations with the optimal set of options (found in the first step) and the DRAGFO routine are run for a mesh where the cylinder is not represented anymore. The drag coefficient is set so that the mechanical energy loss due to the cylinder is the same as the one obtained with the meshed cylinder.

Fig. 8 displays the velocity in m/s and the mechanical power for one slice of fluid in kW, for the constant viscosity model. The black points correspond to the experimental data, the red curve to the previous simulations with the cylinder and the green one to the simulation with the DRAGFO routine and Cd=6. Note that Cd=1.15 (green curve) for a cylinder at this Reynolds number [8]. But as explained in the previous paragraph, this tabulated value has to be tuned because the local velocity, instead of a reference velocity, is used to calculate the drag force. The velocity and the mechanical power along the flume are both well reproduced with DRAGFO, except for the field very close to the cylinder. Thus, the model is validated in a simple case and can be used to reproduce the tidal converter effects on the flow. This approach is justified because the perturbation on the flow for the converter should be similar to the cylinder one (at least, far from the obstacle), if the dimension of the two obstacles and the velocity of the flow are of the same order of magnitude.

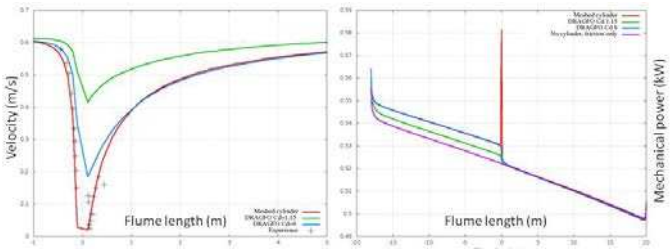

Figure 8. Velocity in m/s (left) and mechanical power in kW (right) along the flume for the experimental data (black dots), for the simulation with the meshed cylinder (red curve) and with the DRAGFO routine (Cd=1.5 green curve and Cd=6 blue curve), for the constant viscosity model

C. DRAGFO routine particularities for the converter case

The DRAGFO routine can be used to model a tidal converter with some particularities. The area S becomes a disc with an area equal to πR^2, where R is the radius of the turbine. A is defined as a rectangle, as schematised on Fig. 9.

In the present study, the drag coefficient is derived from the thrust measured on the device rotor and from a reference velocity. It has already been mentioned that Cd becomes a parameter since the velocity considered for the drag force calculation is a local one. This parameter should also take into account a large variety of phenomena, so that the model reproduces properly all the energy losses:

- The stress applied by the whole converter - including the rotor, the mast and the hub - on the flow, which consists of the reciprocal drag force (including form drag and friction drag) and of the reciprocal lift force
- The energy dissipated by the turbulence generated by the obstacle and the rotation of the rotor
- The energy dissipated in the sheared flow downstream

IV. MODELLING THE TIDAL TURBINE WAKE

A. Experimental data for the turbine in the flume

To quantify the effects of the current velocity, the turbulence of the flow, the distance between the rotor and the free surface or the presence of waves on the performance and wake , a 1/30th scale turbine with a 0.60 meter diameter rotor (D), has been manufactured (Fig. 10). Experiments take place in an 80-meter-long, 1.5-meter-wide flume equipped with a reversible current circuit (maximum flow rate of 1000 l/s) and a wave paddle (Fig.11).

Combined with a measurement of the speed of rotation, sensors of torque and thrust on the rotor of the turbine allow calculating the power and thrust coefficients of the rotor for different speeds of rotation. An Acoustic Doppler Velocity meter (ADV) is used to record local 3D velocity and turbulence intensity. Moving the ADV along the flume, upstream and downstream of the turbine, allows the mapping of the wake.

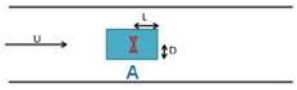

Figure 9. Sketch of the flow around the turbine and of the area A where the drag force is applied

Figure 10. Photo of the 1/30th scale turbine used in the LNHE experiments

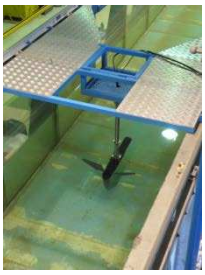

Figure 11. Photo of the turbine and of the flume used in the LNHE experiments

The flow velocity, U, is the measurement of the flow at about 5 diameters upstream the turbine at the height of the rotor. The turbulence intensity (TI) is called "low" (measured between 5 and 10% in a cross section) for the flume in its usual state or "high" (measured between 15 and 20%) when breezeblocks are placed on the flume floor increasing its roughness.

Fig. 12 shows an example of measured power and thrust curves obtained for U=0.55 m/s, 0.8 m of water height and low turbulence intensity.

$$C_p = Power / ½\ \rho S U^3 \text{ and} \quad (8)$$

$$C_T = Thrust / ½\ \rho S U^2, \quad (9)$$

are respectively the power and thrust coefficients with ρ the density and

$$S = \pi\ (D/2)^2, \quad (10)$$

the surface of the rotor. The Tip Speed Ratio (TSR) is defined as:

$$(D/2)\cdot\omega / U, \quad (11)$$

with ω the rotor's speed of rotation. Fig. 13 shows the velocity and turbulence intensity measurements in the wake of the turbine (Arrows represent the 3D velocity and spheres represent the turbulence intensity).

The reference test used for the simulations described in this article corresponds to the low velocity (U=0.27 m/s), low turbulence intensity (TI between 5 and 10%), small water height (H=0.8 m).

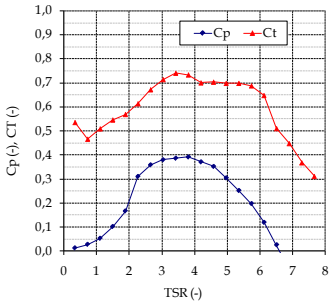

Figure 12. Example of measured power and thrust curves obtained for U=0.55 m/s, 0.8 m of water height and low turbulence intensity

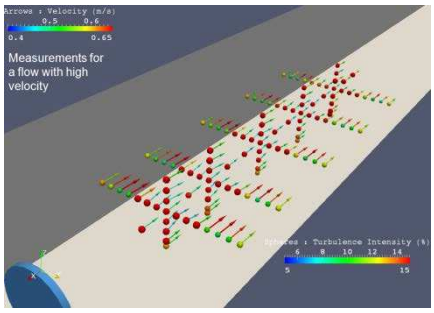

Figure 13. The velocity and turbulence intensity measurements in the wake of the turbine (arrows represent the 3D velocity and spheres represent the turbulence intensity)

B. *Simulation options*

The mesh represents the whole flume. The options chosen for the simulations are the ones described in the cylinder case, namely the PSI scheme, an unstructured mesh, the constant viscosity and k-ε models. The mesh size and the optimal time step are also based on the cylinder flow but a convergence study is still necessary to ensure the latter.

The inlet flow, respectively the friction coefficient, is set so that the upstream velocity, respectively the kinetic turbulent energy, matches the experimental one. A parametric study is carried out on the following parameters:

- Cd
- The rectangular area A defined by its transversal half-length D and its longitudinal half-length L (cf. Fig. 9)
- the turbine location which corresponds to the centre of the A rectangle
- the turbulent viscosity when the constant viscosity model is selected
- η when the k-ε model is used

C. *Simulation results for one TSR*

An extensive parametric study is carried out for one TSR equal to 3.5. The axial wake is investigated as well as one transversal velocity profile, two diameters downstream of the turbine. The axial wake is characterised by the velocity deficit (the minimum velocity in the wake), the location of this deficit and the slope of the speed recovery.

The initial Cd corresponds to the one measured for the rotor, it has to be increased in order to take into account all the energy losses. Increasing the Cd leads to a rise of the velocity deficit downstream without modifying the far wake. On the contrary, increasing D leads to a decrease of the velocity deficit. It also results in a wider and flatter transversal wake.

Increasing L slightly increases the velocity deficit and switches it more downstream. The precise location of velocity deficit can also be displaced by moving the location of A i.e. of the turbine.

For the turbulence model based on constant viscosity, increasing the turbulent viscosity has the effect of slowing down the speed recovery.

For the k-ε turbulence model, adding a production term in k and ε equations enables to change the trend of turbulence downstream: without any modification, k diminishes behind the turbine, whereas it rises with the new production term, which is conform to experimental observations. Tuning η allows to match the k values in the wake to the experimental ones. The speed is not modified much by this term (much less than 1 cm/s), the deficit is slightly decreased and the recovery slope slightly increased. This confirms experimental data: more turbulence leads to more mixing and a faster speed recovery.

Taking into account the result of the parametric study, an optimal set of parameters summarised in Table I. can be found to reproduce the wake properly for this specific case. The axial wake and the transversal profile simulated with the two turbulence models are presented in Fig. 14 and Fig. 15. The maximum error relatively to the experimental data is observed for the transversal flow and is equal to 2 cm/s, the velocity being around 25 cm/s and the deficit around 5 cm/s.

Apart from the inlet flow and the friction coefficient, which are different because the transversal profile is different, the parameters are the same for the two turbulence models.

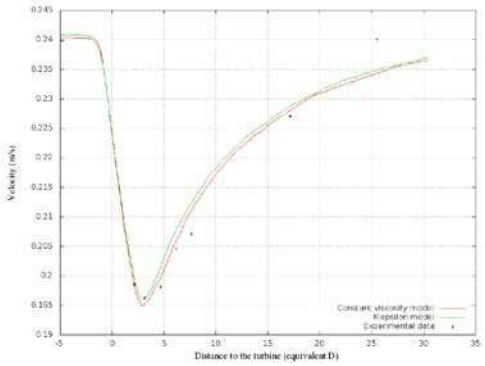

Figure 14. Depth averaged velocity profile along the flume in the axis of the turbine (black points correspond to the experimental data, red curve to the constant viscosity model and green curve to the k-ε model)

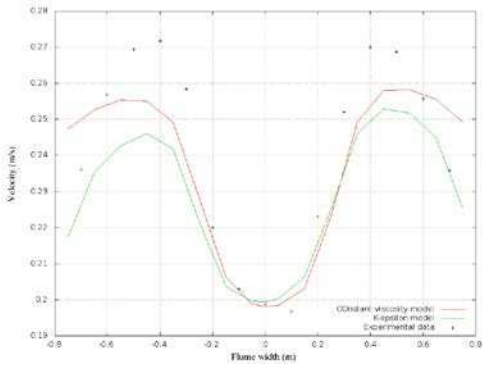

Figure 15. Transversal profile 2.2D downstream the turbine (black points correspond to the experimental data, red curve to the constant viscosity model and green curve to the k-ε model)

D. Generalisation to other TSR

The wake has been mapped for other rotational speeds of the device. For the TSR equal to 3.5 the measured Cd has been increased of 15% (from 0.91 to 1.05) to match the experimental and the simulated wake. Does it exist a law linking the experimental Cd to the one used as a parameter to reproduce properly the velocity deficit into Telemac2D?

Fig. 16 displays the experimental axial wake for the different TSR and associated Cd, as well as the wake obtained with Telemac2D and different values of Cd. As said before in the simulations when Cd increases, the velocity deficit follows the same trend. Whereas it is not the case for the experimental data: for example for a TSR of 3.5 the Cd is 0.91, but the velocity deficit is larger than the one for a TSR of 4.5 and a Cd of 0.97.

This can be understood in an easier way with the sketch of Fig. 17, representing the experimental data: the curve giving the minimum velocity as a function of the TSR is not perfectly the opposite of the drag coefficient curve. A limit of the model used until now is highlighted: according to the drag coefficient curve (cf. Fig. 18), two different TSRs, thus two different rotational speeds (U and R being constant), can lead to the same Cd, thus to the same simulated wake, whereas it is obvious in the experimental results that the two wakes are different. It can also be physically expected that two different rotational speeds, even if the same drag force is applied on the rotor, result in two different wakes.

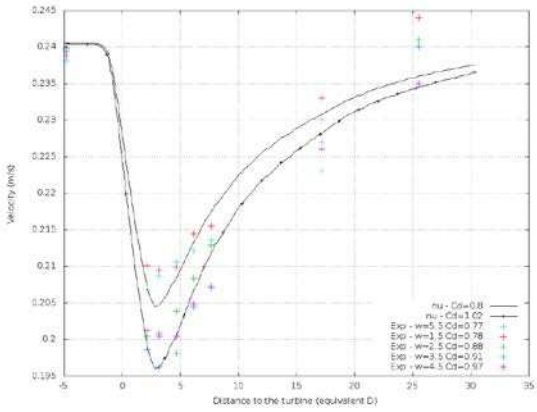

Figure 16. Experimental axial wake for the different TSR and associated Cd (ranking by increasing Cd) as well as the wake obtained with Telemac2D, constant viscosity model and different values of Cd (Cd=0.8 and 1.02)

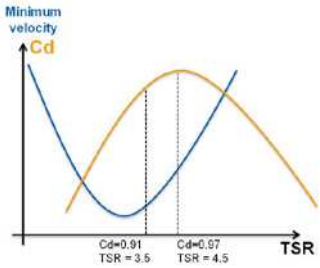

Figure 17. Sketch of the off-set Cd and minimum velocity curves versus TSR, based on the experimental observations

TABLE I. OPTIMAL SET OF PARAMETERS TO REPRODUCE THE EXEPERIMENTAL TEST FOR TSR=3.5

Parameters	***Inlet flow*** ***(m^3/s)***	***Friction coefficient*** ***($m^{1/3}/s$)***	***Cd*** ***(-)***	***D*** ***(m)***	***L*** ***(m)***	***Position,distance from the end of the flume (m)***	***vt (m^2/s) or η (-)***
Constant viscosity model	0.281	80	1.05	0.15	1.0	19.7	0.00005
K-ε model	0.278	100	1.05	0.15	1.0	19.7	0.1

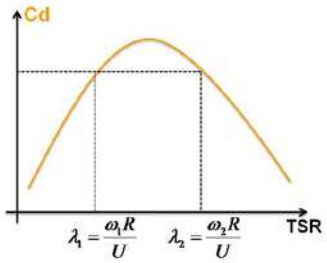

Figure 18. Sketch highlighting a limit of the model : one Cd corresponds to two rotation speed thus two different wakes, which is not the case in the model

V. CONCLUSION

The appropriate numerical options for the study of a free surface flow in a flume around an obstacle and for a Reynolds number around 10^5 have been investigated thanks to the well documented flow around a cylinder. Some relevant conclusions are drawn especially regarding Telemac2D convergence. The DRAGFO routine developed for the tidal converter has also been validated in this simple case, before being applied to the turbine itself.

Simulations are run to perform a parametric study and to reproduce experiments carried out at the LNHE, namely the study of the wake and of the performance of a tidal converter at $1/30^{th}$ scale. For one blade rotational speed it is possible to adjust the model parameters to reproduce the wake with a small error.

However when extending the model to other rotational speeds, a limit of the model is highlighted: one drag coefficient will lead to one simulated wake whereas it may correspond in reality to two different rotational speeds and two different wakes.

Other tests, with different turbulent intensity and different velocity are now investigated to help improve the model. Afterwards, the model will be applied to small arrays to take into account interactions between devices and wakes, and once again compared to experimental data. The final aim is to be confident enough in the simulation method and in the device model to simulate full size arrays at basin scale.

At last, we hope to get very soon results from CADNA in order to perform the numerical verification.

ACKNOWLEDGEMENT

Support from the Energy Technologies Institute (ETI) which commissions and funds the PerAWAT project is gratefully acknowledged. The authors are thankful to Alexei Winter for his help to manufacture and install the turbine for the experimental work.

REFERENCES

[1] J-M. Hervouet, “Hydrodynamique des écoulements à surface libre, modélisation avec la méthode des éléments finis,” Presses de l'école nationale des ponts et chaussées, 2003.

[2] B. Yulistiyanto, “Flow around a cylinder installed in fixed-bed open channel,” PhD dissertation 1631, Ecole Polytechnique Fédérale, Lausanne, 1997.

[3] R. D. Blevins, “Flow-induced vibration,” Krieger publishing company, 1990, pp. 45–47.

[4] C. Norberg, “Fluctuating lift on a circular cylinder: review and new measurements,” Journal of Fluids and Structures, vol. 17, 2003, pp. 57–96.

[5] C. Denis, “Numerical Verification of Indusrial Numerical Codes to Simulate Accurately Efficiently and Accurately Large Scale Events,” SimHydro’2012, Nice, under publication in Springer series.

[6] F. Jezequel, J-M. Chesneaux, J-L. Lamotte,. “A new version of the CADNA library for estimating round-off error propagation in Fortran programs,” Computer Physics Communications, vol. 181(11), 2010, pp. 1927–1928.

[7] M. E. Negretti, G. Vignoli, M. Tubino, M. Brocchini, “On shallow-water wakes: an analytical study,” Journal of Fluid Mechanics, vol. 567, 2006, pp. 457–475.

[8] B. M. Sumer, J. Fresoe, “Hydrodynamics around cylindrical structures,” World scientific, Advanced series on Ocean Engineering, vol. 12, 1999, pp. 1–35.

Wave farm energy yield calculations using a modified spectral wave model

Katherine E. Silverthorne and Matt Folley
School of Planning, Architecture, and Civil Engineering
Queen's University Belfast
Belfast, Northern Ireland, UK
k.silverthorne@qub.ac.uk

***Abstract*—The development and deployment of large arrays (100+ units) of wave energy converters (WECs) require numerical tools that support investigations into the potential effects of the wave farm deployment and make predictions about the wave farm's annual energy production. Tools based on spectral wave models are particularly suited for this task because they can model large numbers of WECs with a lower computational effort than equivalent potential flow models, which are currently the most popular method. In this study, which was undertaken as part of PerAWaT (Performance Assessment of Wave and Tidal Array Systems) and commissioned and funded by the Energy Technologies Institute, a representation of a heaving buoy WEC is developed for the TOMAWAC spectral wave model. The representation solves the WEC dynamics using hydrodynamic coefficients from WAMIT and the incoming wave spectrum from TOMAWAC. The WEC response is then used to calculate the effect on the incident wave field. The results are compared with those from a potential flow model, followed by a discussion of the applications and limitations of the method.**

I. INTRODUCTION

The wave energy industry has reached a stage in development where full scale devices are being built and deployed in ocean sites. Once the prototypes have been tested thoroughly, the next step in the process will be to deploy several devices together in an array in order to generate more power. Ultimately, tens to hundreds of devices will need to be deployed together in a wave farm in order to achieve the targets for marine renewable power production that have been set by UK government, [1]. Careful planning will be required before a wave farm is actually deployed. Once a potential site has been chosen, the development team must have an idea about the optimal arrangement of the array at that site, based on either minimizing negative array interactions or maximizing positive ones and taking into account any bathymetry or resource restrictions. The development team will also have to undertake an environmental impact assessment that predicts the effect of the array on the ocean waves (both close to the farm and further down wave near the coast) and any subsequent consequences of that impact on the sediment transport and ecology of the region where the farm is to be deployed. There are currently no available numerical tools that are capable of capturing both the propagation of waves and the behavior of hundreds of wave energy devices. Therefore, in order to perform pre-deployment assessment of a wave farm, a new numerical modeling tool is needed. The focus of this paper is on the development of just such a tool using the TOMAWAC model that is part of the TELEMAC suite of models developed at EDF, [2]. This work is part of the PerAWaT project (Performance Assessment of Wave and Tidal arrays) which incorporates several research organizations applying numerous numerical and experimental methods for estimation of wave energy farm array power production.

There are several numerical modeling tools that are currently being used to model the interaction of wave energy devices and ocean surface waves, [3]. These include potential flow models (linear and nonlinear), Boussinesq wave models, time-domain models, spectral wave models, and computational fluid dynamics models. Potential flow models, time-domain models, and computational fluid dynamics models directly solve for the interaction of ocean waves with a wave energy device, while spectral wave models and Boussinesq wave models simulate the interaction of ocean waves with a parameterization of a wave energy device (i.e. the wave energy device is not explicitly represented). Because of the computational complexity involved in directly solving for the fluid-structure interaction, it is not feasible to simulate a wave farm with many devices in potential flow models, time-domain models, or CFD models. Spectral wave models are able to cover a larger domain area with a smaller computational load than Boussinesq wave models, and therefore are the best suited for simulation of wave farms.

Spectral wave models were developed in the oceanography community for prediction of surface ocean waves. They solve a surface ocean wave energy conservation equation, and have the ability to represent several ocean wave processes as sinks or sources of energy, including whitecapping dissipation, bottom dissipation, bottom refraction, both quadruplet and triplet nonlinear wave-wave interactions, and wind generation. The ability of spectral wave models to include non-linear sources and sinks of wave energy indicates that it is also possible to incorporate non-linear wave energy device representations, [4]. Another advantage of using spectral wave models is that they can be used with a varying mesh size to cover large computational

domains with reasonable model run time. The main disadvantage to using spectral wave models for the purpose of modeling wave energy devices is the phase-averaging assumption. The phases of the individual ocean waves are not explicitly determined in spectral wave models, but instead are assumed to be randomly distributed. Because of this assumption, phase-dependent processes such as close interactions between the devices and diffraction of waves around the devices are not represented. However, we hypothesize that some of these effects are canceled out when averaging over a large array of devices, so that the average impact will be reasonably represented in the spectral wave modeling tool. Therefore, it is very important that the spectral wave model wave energy farm tool is carefully verified against other numerical tools and validated with experimental data.

There have been previous studies of wave energy farms simulated with a spectral wave model. The primary objective of these studies was to evaluate the effect of the wave farm on the coastal wave environment downstream from the farm. The first approach taken was to represent a wave farm as an obstacle that was a solid rectangular block, [5]. It was assumed that the wave farm absorbed a certain percentage of the incoming wave energy and that the percentage of absorption was constant with frequency, direction, and location. From this, the impact of the presence of the wave farm on the surface wave climate on the coast down wave was deduced. Later, this work was revised to represent wave energy devices as individual obstacles with a frequency dependent absorption percentage, [6]. In another approach from a different research group, the incoming wave spectra were modified in response to the presence of the wave energy devices, with no physical manifestation of the device in the model, [7]. Again, this approach applied a frequency dependent absorption percentage to the incoming wave energy spectrum.

For the work presented here, there are two goals: both to capture the effect of the wave energy farm on the ocean waves (as in the previous studies), and to be able to make predictions of the power capture for the devices. In order to achieve these goals, a method has been developed and tested first on single devices to ensure that they are represented correctly before moving on to simulations involving multiple devices, as in a wave farm. This method uses a sub-grid scale representation in which wave energy devices are located at a single computational node in the mesh. The incoming wave spectrum is modified at the single computational point where the device is located in response to the presence of the device. This approach was first introduced using a simple frequency dependent absorption percentage, [8]. In this paper, a specific representation for a point absorber (heaving buoy wave energy device) is developed where the effect of the wave energy device on the wave energy density is calculated using linear equations of motion for a heaving point absorber and characteristics of the device. This method does not rely on an absorption percentage, but aims to actually calculate the effect of the device on the wave energy spectrum and apply that directly. Additionally, this new method includes the radiation of energy by the heaving point absorber, which has not been included in other representations. In Section II of this paper, the details of the method as well as two validation exercises for the method are described. Two different implementations of the method are tested. In Section III, results from the validation exercises are presented. Section IV contains a discussion of the results, and Section V contains some conclusions.

II. METHODS

Spectral wave models solve the wave action conservation equation. Wave action, which is wave energy divided by the intrinsic frequency, is used because it is conserved even in the presence of variable ocean currents. Spectral wave models include several physical wave mechanisms, such as the convection of wave energy, wind input, whitecapping, nonlinear wave-wave interactions, and bottom friction dissipation. These processes (except for the first one) are represented in spectral wave models as a source term of energy, with a positive source term corresponding to a process that adds energy to the system, and a negative source term corresponding to a process that removes energy from the system. The wave energy device representation was incorporated into the model by introducing another wave energy source term. This source term includes the absorption of energy by the wave energy device. The source term is frequency and directionally dependent and can easily be varied between the various devices in a wave farm.

The wave energy device source term is designed to represent the linear motion of a heaving point absorber buoy. This is a common and simple wave energy device design that is constricted to move only in the vertical direction, which simplifies the equations of motion. The source term first solves for the amplitude of the waves based on the incident wave spectrum in TOMAWAC as follows:

$$a(f,\theta) = \sqrt{2 \cdot \Delta f \cdot \Delta\theta \cdot E(f,\theta)} \qquad (1)$$

Here, a is the amplitude of the wave, Δf is the frequency resolution, $\Delta\theta$ is the directional resolution, and E is the spectral energy density.

Then, the motion of the device is calculated using a linear equation of motion:

$$D = \frac{K(\omega) \cdot a}{h - (\omega)^2 (m + m_a(\omega)) + i\omega(B(\omega) + PTO)} \qquad (2)$$

where ω is the frequency, K is the frequency dependent wave force coefficient, h is the hydrostatic stiffness, m is the mass of the device, m_a is the frequency dependent added mass, B is the frequency dependent added damping, PTO is the power takeoff, or the mechanism that generates energy from the movement of the device, and D is the displacement of the device.

Finally, the power absorbed by the device (P_{abs}) is calculated using:

$$P_{abs} = \frac{1}{2}(\omega D)^2 PTO \quad (3)$$

A. Power absorption verification

The wave energy device representation in TOMAWAC must be able to calculate the power absorption correctly. In order to verify this, another numerical model which resolves the wave-fluid interaction is needed. Because the wave energy device model in TOMAWAC is based on a linear equation of motion for a heaving point absorber, a linear potential flow model (WAMIT) was used to compare with the TOMAWAC results. The WAMIT model explicitly resolves the interaction of the fluid with the structure, including processes such as diffraction and radiation that are not explicitly resolved in the TOMAWAC model. The WAMIT model was run with the same heaving buoy characteristics as those applied in TOMAWAC. The characteristics used in the verification were based on an actual heaving buoy device that was designed for the PerAWaT wave tank testing experiments. The buoy has a cylindrical shape with a hemispherical bottom, is 20 meters in diameter and has a 20 meter draft at full scale, Fig. 1. The frequency dependent hydrodynamic coefficients required to calculate the power absorbed by the device were estimated using the WAMIT model. It was assumed that the buoy operated only in heave motion. The power takeoff system was modeled as a simple linear damping term with a single damping coefficient.

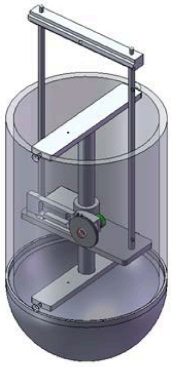

Figure 1. Schematic of the heaving buoy wave energy device modeled here.

The point absorber representation in TOMAWAC was run with one wave energy device in the center of a square domain with several sea states where the frequency, height, main direction, spreading, and spectral shape of the incoming waves were varied (Table I). The sea states were all based on the JONSWAP spectrum, a standard ocean wave spectral shape. The parameters that govern JONSWAP spectra include significant wave height (Hs), the energy period of the ocean waves (Te), and a non-dimensional peak enhancement factor (γ). The directional spreading of the waves was based on a cosine squared representation varying with a parameter, s. The larger the s value, the smaller the directional spread of the ocean wave spectrum.

TABLE I. SEA STATE PARAMETERS

Sea States	Hs (m)	Te (s)	γ	s
SS1	2.0	6.5	2.0	45
SS2	2.0	8.0	1.0	45
SS3	2.0	11.3	1.0	45
SS4	3.0	11.3	1.0	45
SS5	2.0	8.0	1.0	15
SS6	3.0	11.3	1.0	15
SS7	2.0	8.0	1.0	3
SS8	3.0	11.3	1.0	3

The results of the power absorption in both the TOMAWAC and WAMIT models for these sea states were then compared and are presented in Section III.

B. Source term strength verification

In addition to calculating the correct power absorption by a wave energy device, the TOMAWAC model representation must also be able to calculate the correct source term strength, in order to model the effect of the device on the ocean wave climate. The power absorbed variable derived at the beginning of the methods section has the unit of Watts. However, the desired quantity for the source term strength is Watts/meters^2 (power per area), because TOMAWAC solves for wave energy density, or wave energy per unit area. Therefore, in order to convert the power absorbed by the device into a source term strength to be fed into the TOMAWAC model, the area over which the power is absorbed must be designated.

In this paper, two different methods for converting the power absorbed by a wave energy device from the ocean waves into the source term strength for use in TOMAWAC are tested and compared. The first is a transmission coefficient method that has been used previously in [9]. Here, the ratio of transmitted wave energy density to incident wave energy density is equal to the ratio of transmitted wave power to incident wave power:

$$\frac{E_{transmitted}}{E_{incident}} = \frac{P_{transmitted}}{P_{incident}} \quad (4)$$

Therefore, the source term strength (S) used in TOMAWAC to represent the WEC device can be written as:

$$S = \frac{E_{transmitted} - E_{incident}}{\Delta t} = \frac{-P_{abs}}{P_{incident}} \frac{E_{incident}}{\Delta t} = k \frac{E_{incident}}{\Delta t} \quad (5)$$

where P_{abs} is the power absorbed by the wave energy device, Δt is the time step, and k is known as the transmission coefficient because it represents the percentage of the incoming wave energy that is then transmitted on past the wave energy device. This derivation has used the identity that the total incident power is equal to the absorbed power plus the transmitted power. For this method, the incident power is calculated for each device using the incident wave field and the width of the device, and then the transmission coefficient is calculated for each device based on the incident power and power absorbed. This is then applied as a source term strength to represent the wave energy device in the TOMAWAC model.

The second method for converting the calculated power absorbed into a source term strength for the TOMAWAC model involves the direct calculation of the area over which the power is absorbed. In this method, the source term strength is given as follows: $S=P_{abs}/A$, where A is the area that must be designated. For this study, this area is designated as the area comprising that between the computational node where the wave energy device is located and the midpoint between that node and all adjacent nodes, Fig. 2. This area corresponds to 25% of the total area of the triangles surrounding the wave energy device node.

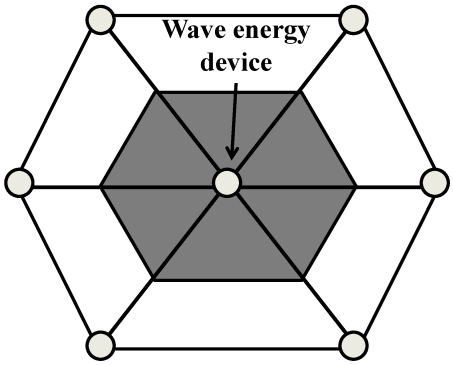

Figure 2. Diagram representing the area conversion method. The center light gray circle represents the computational node where the WEC is located, and the other light gray circles represent adjacent computational nodes. The dark gray area is the area over which the absorbed power is spread.

In order to test both the transmission coefficient method and the direct area method for converting the power absorbed by a wave energy device into a source term strength for wave energy density, a calculation using the output from the TOMAWAC model was carried out. This calculation is based on the divergence theorem, which states:

$$\iint_A \nabla \cdot E\vec{c_g} dA = \oint E\vec{c_g} \cdot \vec{n} dl = P_{abs} \qquad (6)$$

where E is the wave energy spectral density and c_g is the wave group speed. That is, a path integral of the wave energy flux should equal the power absorbed by the device, as long as the integration path is closed and contains the wave energy device. If the conversion from the power absorbed to the source term strength applied in the TOMAWAC model is correct, then the two quantities will be the same. For this experiment, a single wave energy device was placed at the center of a square domain, and ocean waves were propagated through the domain until they reached a steady state. A square integration path was defined using mesh points, Fig. 3. Then, to carry out the divergence theorem calculation, first the group speed was calculated as a function of frequency and direction and then dotted with the normal vector to the integration path. The energy density was next multiplied by the normal group speed. Finally, the resulting quantity was integrated in direction, then frequency, and around the closed path.

According to the divergence theorem, the integrated energy flux from the above described calculation should be equal to the power absorbed by the device as calculated by the model.

For this experiment, the same sea states and wave energy device characteristics that were given in the power absorption verification are used. All of the other source terms besides the wave energy device absorption source term (such as dissipation and wave-wave interaction terms) were deactivated and the depth was constant throughout the domain, so the only physical processes taking place in these model runs should be the removal of energy by the device, and the propagation of energy throughout the domain. To provide verification that the calculation is working correctly, it was tested on model results for a run with no wave energy device. In the absence of sources and sinks of energy in the domain, the path integral of the energy flux should be equal to zero, and indeed the net flux through the integration surface was found to be very small, as expected.

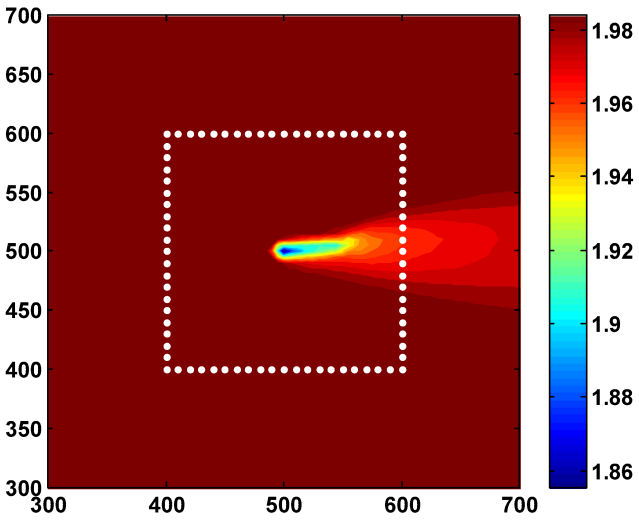

Figure 3. Significant wave height in meters for sea state 2 with the square integration path points overlaid in white.

III. RESULTS

A. Power absorption verification

For each sea state, the power absorption was calculated for the same wave energy device in both the WAMIT and TOMAWAC models. The results for all the sea states show good agreement between the WAMIT and TOMAWAC calculated power absorption, with percent error differences of less than 2%, Table II.

TABLE II. POWER ABSORPTION COMPARISON

Sea States	TOMAWAC power absorbed (kW)	WAMIT power absorbed (kW)	% error
SS1	9.7	9.8	-1.0
SS2	25.1	25.3	-0.8
SS3	65.8	67.1	-1.9
SS4	148.1	150.9	-1.9
SS5	25.4	25.0	1.6
SS6	150.1	149.0	0.7
SS7	25.4	25.0	1.6
SS8	150.1	149.0	0.7

B. Source term strength verification

For each sea state and both the direct area method and the transmission coefficient method, the integrated flux and the power absorbed for the single wave energy device were calculated. The power absorbed by the device depends only on the incoming waves, and therefore does not change between methods. The results for this analysis are given in Table III.

TABLE III. SOURCE TERM STRENGTH METHOD COMPARISON

Sea States	Direct area method (kW)	Trans-mission method (kW)	Power absorbed (kW)	% error: direct area method	% error: trans-mission method
SS1	13.6	34.8	9.7	40	258
SS2	35.5	72.9	25.1	41	190
SS3	93.1	140.7	65.8	41	114
SS4	209.5	316.6	148.1	41	114
SS5	36.3	74.6	25.4	43	194
SS6	214.3	323.9	150.1	43	116
SS7	35.0	71.9	25.4	39	185
SS8	206.7	312.5	150.1	38	109

IV. DISCUSSION

While the calculation of the power absorption by the TOMAWAC model shows good agreement with the WAMIT model, it can be seen from Table III that neither of the source term strength conversion methods seems to give very good agreement between the power absorbed and the integrated energy flux. This indicates that both the methods tested for converting the power absorbed into a source term strength for the model are incorrect. However, the errors for the area method are close to 40% for all of the sea states, while the errors for the transmission coefficient method vary between 100% and 260%. This suggests that it may be possible to use one area for each mesh as in the direct area method, but that the value of the area used for the computation is incorrect. The “correct area” can be found iteratively by repeating the calculation using different areas until the power absorbed matches the integrated flux. This was tested on a series of different meshes, and the calibrated area was found to vary between 31% and 41% of the total area of the triangles surrounding the node where the wave energy device was located. Additionally, varying the main propagation direction of the ocean waves yields a different calibrated area for the same mesh. This suggests there is not a simple relationship between the size of the triangles surrounding the computational node and the correct area needed for the conversion. Instead, it seems there is a more complicated dependence, possibly involving the computational method. When the calibrated area is used, good agreement between the power absorbed and the integrated energy flux is found for all the sea states (Table IV):

TABLE IV. CALIBRATED AREA METHOD RESULTS

Sea States	Calibrated area method (kW)	Power absorbed (kW)	% error
SS1	9.6	9.7	-1.0
SS2	24.9	25.1	-0.8
SS3	65.3	65.8	-0.8
SS4	147.0	148.1	-0.8
SS5	25.5	25.4	0.4
SS6	150.4	150.1	0.2
SS7	24.6	25.4	-2.8
SS8	145.1	150.1	-2.8

Furthermore, the distribution of the power absorbed and the integrated flux with frequency match very well, Fig. 4. This is further indication that it is correct to use a single area to define the conversion between the power absorbed and the wave energy density. It is therefore important to identify the dependence of the calibrated area on the computational parameters (including perhaps mesh size, time step, and others) so that a generic representation of many wave energy

devices in the TOMAWAC model can be more easily implemented.

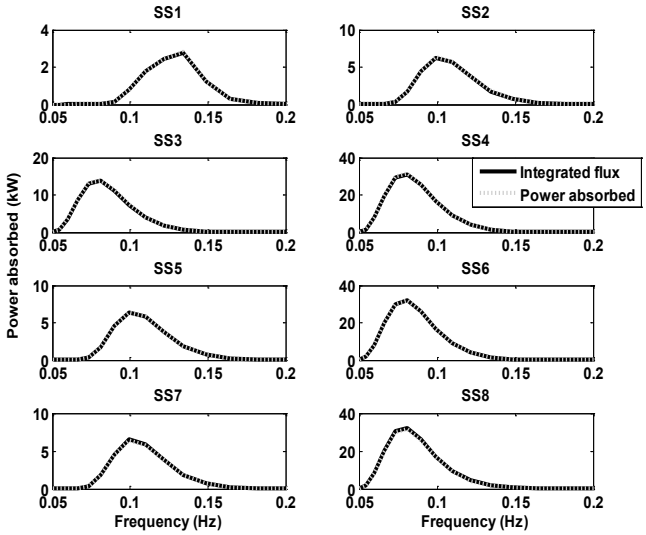

Figure 4. Power absorbed and integrated flux as a function of frequency for 8 sea states using the calibrated area method.

V. CONCLUSIONS

It has been shown in this paper that it is possible to calculate the correct power absorption for a single wave energy device (as compared with the industry standard potential flow model WAMIT) and convert that power correctly to a source term strength in the spectral wave model TOMAWAC. However, the details of the conversion between power absorption and source term strength still need to be worked out. Now that progress has been made with simulating a single wave energy device, simulations of multiple devices can be considered. Multiple buoy simulations, as in a wave farm scenario, are more complicated because the phase-dependent wave processes such as diffraction around the buoys and radiation of waves away from the buoys are not explicitly resolved in spectral wave models. However it is expected that some of these effects may average out over a large array. In order to address these issues, the next phase of the research for development of a numerical tool that can model a wave farm will include comparison of the tool with both other numerical models and wave tank experimental data. This work is already underway as part of the PerAWaT project.

ACKNOWLEDGEMENTS

This work was undertaken as part of the PerAWaT (Performance Assessment of Wave and Tidal Array Systems) project that was commissioned by the Energy Technologies Institute.

REFERENCES

[1] Department of Energy and Climate Change, " UK low carbon transition plan", <http://www.decc.gov.uk/en/content/cms/tackling/carbon_plan/lctl/lctp.aspx>, 2009.

[2] M. Benoit, F. Marcos, and F. Becq, "Development of a third-generation shallow-water wave model with unstructured spatial meshing", Proceedings of 25th International Conference on Coastal Engineering, 1996.

[3] M. Folley et al., "A review of numerical modelling of wave energy converter arrays," Proceedings of the ASME 2012 31st international conference on ocean, offshore, and Arctic engineering, June 10-15, 2012.

[4] M.Folley and T. Whittaker, "Spectral modelling of wave energy converters", Coastal Engineering, vol. 57, pp. 892-897, 2010.

[5] D.L. Millar, H.C.M. Smith, and D.E. Reeve, "Modelling analysis of the sensitivity of shoreline change to a wave farm," Ocean Engineering, vol. 34, pp. 884–901, 2006.

[6] H.C.M Smith, C. Pearce, and D.L. Millar, "Further analysis of change in nearshore wave climate due to an offshore wave farm: An enhanced case study for the WaveHub site", Renewable Energy, vol. 40, pp. 51-64, 2012.

[7] A. Alexandre, T. Stallard, and P.K. Stansby, "Transformation of wave spectra across a line of wave devices", Proceedings of 8th European wave and tidal energy conference, 2009.

[8] K. E. Silverthorne and M. Folley, "A new numerical representation of wave energy converters in a spectral wave model", Proceedings of 9th European wave and tidal energy conference, 2011.

[9] A. Alexandre, T. Stallard, and P.K. Stansby, "Wavefield modification due to a WEC array", Proceedings of third international conference on the application of physical modelling to port and coastal protection, 2010.

Use of tidal harmonic constants databases to force open boundary conditions in TELEMAC

Chi-Tuân PHAM
Laboratoire National d'Hydraulique et Environnement
EDF R&D
Chatou, France
chi-tuan.pham@edf.fr

Florent LYARD
LEGOS
Toulouse, France

***Abstract*—Since version 6.1, TELEMAC-2D users have been able to use a database of harmonic constants to force the open boundary conditions of local models within the near Atlantic Ocean or the English Channel. Version 6.2 enables the use of other databases of harmonic constants over larger domains, for both TELEMAC-2D and TELEMAC-3D. These include the regional NEA (North East Atlantic) atlas, processed by NOVELTIS/LEGOS (Laboratoire d'Études en Géophysique et Océanographie Spatiales/Laboratory of Studies in Spatial Geophysics and Oceanography) in the frame of the COMAPI project funded by CNES, which covers an area from Mauritania to the south of Norway, as well as the TPXO global tidal solution and other regional or local solutions from Oregon State University (OSU). Boundary conditions can vary spatially and temporally.**

The first part of this paper describes the three sets of databases currently available and the developments carried out in TELEMAC for two of them (near Atlantic Ocean and English Channel model + NEA atlas). These databases provide the water depths and horizontal velocity components of harmonic constants with a quite good spatial resolution. In particular, the NEA atlas deals with 47 harmonic constituents for its hydrodynamic solution and 15 harmonic constituents for its solution assimilated with satellite observations.

The second part of this paper compares the results obtained by using these various databases of harmonic constants, and in particular their variants (different regional and local tidal solutions from OSU and prior or optimal solutions for NEA from LEGOS when satellite observations are either assimilated or not). The case used for this comparison is a local model of a candidate area to welcome tidal current turbines in Brittany in France. This is aimed to characterise the area with respect to tidal current potential (tidal currents and the evaluation of tidal energy yield). ADCP measurements are used to calibrate and to compare the results of the model when using the different databases of harmonic constants.

I. INTRODUCTION

Many studies of waterworks use numerical modelling of the tide as their basis. Before version 6.1, TELEMAC users who wanted to model tides used to implement their own calculations of the boundary conditions for modelling tides in the BORD subroutine (from a database of harmonic constants or from time series), sometimes by copying FORTRAN subroutines already used in previous studies. Several modifications may have been necessary for each simulation, as a result of which some errors may have occurred. Moreover, implementation may have had to be changed due to updates of the subroutines (e.g. BORD).

Since version 6.1 of TELEMAC-2D, some developments have been integrated in order to deal with the modelling of tides for two reasons:

- to propose some subroutines to deal with tides in the most automatic way possible in the standard version of TELEMAC-2D. This may facilitate calculations and may also decrease the number of potential errors,
- to supply a database of harmonic constants to the community of TELEMAC users for free.

Thus, since version 6.1, the modelling of tides from one specific calendar day with TELEMAC has been quite straightforward. In version 6.2, subroutines have been implemented that use two other databases of harmonic constants to calculate the boundary conditions of open boundaries for both TELEMAC-2D and TELEMAC-3D.

This paper, firstly, describes the three sets of databases currently available and the developments carried out in TELEMAC for two of them (near Atlantic Ocean and English Channel model + NEA atlas). In its second part, this paper compares the results obtained by using these various databases for harmonic constants, and in particular their variants (different regional and local tidal solutions from OSU and prior or optimal solutions for NEA from LEGOS when satellite observations are either assimilated or not). The case used for this comparison is a local model of a candidate area to welcome tidal current turbines in Brittany in France. This is aimed to characterise the area with respect to tidal current potential (tidal currents and the evaluation of tidal energy yield). ADCP measurements are used to calibrate and to compare the results of the model when using the different databases of harmonic constants.

II. MODELLING TIDES WITH TELEMAC

A. Elements of theory for modelling tides

For each harmonic constituent, the water depth h and horizontal components of velocity U and V are calculated as below, at point M and time t:

$$F(M,t) = \Sigma F_i(M,t) \quad (1)$$

with

$$F_i(M,t) = f_i(t)\, A_{Fi}(M) \cos(2\pi t/T_i - \varphi_{Fi}(M) + u_i^0 + v_i(t)) \quad (2)$$

where F is the water depth h or one of the horizontal components of velocity U or V, i refers to the considered constituent, T_i is the period of the constituent, A_{Fi} is the amplitude of the water depth or one of the horizontal components of velocity of the constituent, φ_{Fi} is the phase, $f_i(t)$ and $v_i(t)$ are the nodal factors and u_i^0 is the phase at the original time of the simulation.

The water depth and velocities of each constituent are then summed to obtain water depths and velocities to prescribe for open boundary conditions:

$$h = \Sigma h_i - z_f + z_{\text{mean}} \quad (3)$$

$$U = \Sigma U_i \quad (4)$$

$$V = \Sigma V_i \quad (5)$$

where z_f is the bottom elevation, and z_{mean} is the level used to calibrate the sea levels.

The coefficients A_{Fi} and φ_{Fi} are constant in time and only depend on the location. This information is highly sought after in the modelling of tides and some databases do exist for different areas. Three of them can now be used with TELEMAC-2D and TELEMAC-3D.

B. Various databases of harmonic constants available to use with TELEMAC

1) JMJ from LNH: Jean-Marc Janin (JMJ) and Xavier Blanchard performed the deterministic simulation of tides throughout a full lunar cycle in order to calculate current fields in the English Channel and the near Atlantic Ocean for the four harmonic constituents M2, S2, N2 and M4 [1]. The results are harmonic constants that constitute a database used to calculate boundary conditions for modelling local areas. The area covered by the model includes the Continental Shelf and the mesh includes 29,229 triangular elements (see Fig. 1). The element size varies from 2 km close to the coast to 40 km offshore. The JMJ model considers four harmonic constituents (M2, S2, N2 and M4). The model gives amplitudes and phases for the tidal elevation and for the two horizontal components of the current.

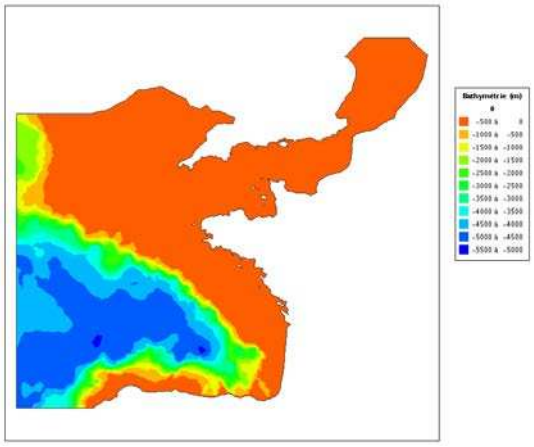

Figure 1. Extent of the JMJ model.

A manual for using this methodology to model tides in the English Channel and near Atlantic Ocean with in version 6.1 of TELEMAC-2D exists in French [2] and is to be translated in English for version 6.2 (including the new developments).

2) NEA from LEGOS: Boundary conditions can also be derived from the regional NEA (North East Atlantic) atlas, processed by NOVELTIS/LEGOS in the frame of the COMAPI project funded by CNES [3],[4]. The atlas covers the North-East Atlantic, from Mauritania to the south of Norway (see Fig. 2). The atlas gives amplitudes and phases for the tidal elevation and for the two horizontal components of the current. The latest version (spring 2010) has 47 harmonic constituents (2MK6, 2MN6, 2MS6, 2N2, 2Q1, 2SM2, 2SM6, ε2, J1, K1, K2, KJ2, L2, λ2, M1, M2, M4, M6, Mf, MK3, MK4, MKS2, Mm, MN4, MO3, MP1, MS4, MSK6, MSN2, MSN6, MSqm, Mtm, μ2, N2, ν2, O1, P1, Q1, R2, ρ1, S2, S4, σ1, SK4, SN4, T2 and Z0). The resolution is roughly 20-25 km for the ocean and 4 km closer to shore.

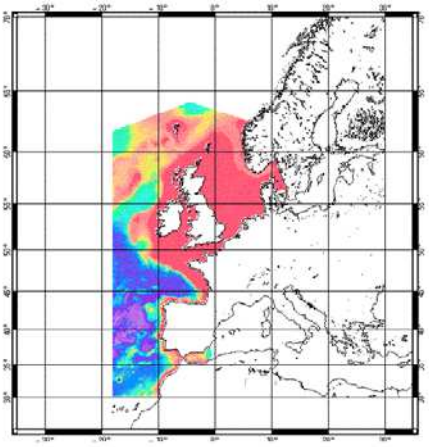

Figure 2. Extent of the regional NEA atlas, processed by NOVELTIS/LEGOS in the frame of the COMAPI project funded by CNES (source [6]).

In addition to the hydrodynamic solutions, the NEA atlas provides 15 harmonic constituents (2N2, K1, K2, L2, M2, M4, MS4, μ2, N2, ν2, O1, P1, Q1, S2 and T2) improved by the assimilation of satellite observations. Hydrodynamic modelling is based on T-UGOm finite element software. Data assimilation, built on the ensemble representer approach, is based on the SpEnOI software (both softwares are available at LEGOS [5]). It must be mentioned that SpEnOI data assimilation can be used with any hydrodynamic software (including of course TELEMAC). Both T-UGOm and SpEnOI outputs are available in unstructured (native) or structured (interpolated) data formats.

NEA atlas (and some others, such as Mediterranean Sea, Persian Gulf, Amazon/Guyana shelf etc.) can be downloaded from Sirocco (an INSU communal service) website under user registration conditions. Please contact sirocco@aero.obs-mip.fr to request them.

3) TPXO global tidal solution and regional/local tidal solutions from OSU: Oregon State University (OSU) provides one global tidal solution (called TPXO) and several regional and local tidal solutions [7]. For example, to model French or UK coasts, the Atlantic Ocean (AO) and the European Shelf (ES) that covers the North-East Atlantic ocean, models exist on a structured grid, with 11 harmonic constituents (M2, S2, N2, K2, K1, O1, P1, Q1, M4, MS4 and MN4) or 13 constituents for the TPXO global solution (same as ES or AO + Mf and Mm). The solutions give amplitudes and phases for the tidal elevation and transport from which the two horizontal components of the current can be deduced (by dividing transport by water depth). The resolutions of the different models are, for example, ¼ degree for the TPXO global solution, 1/12 degree for the regional Atlantic Ocean solution and 1/30 degree for the local European Shelf solution (see Fig. 3). See [7] for further explanation.

These harmonic constants can also be used to reconstruct the initial conditions for the simulation (free surface elevation and/or velocities), even when using other databases of harmonic constants for calculating open boundary conditions.

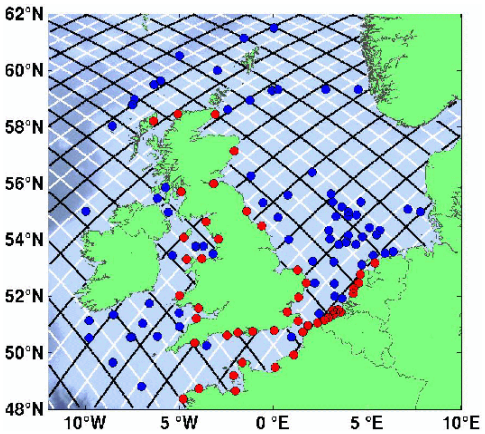

Figure 3. Extent of the local European Shelf (ES) solution (source [7]).

Moreover, an option can be enabled to infer (i.e. deduce) minor constituents (2Q1, σ1, ρ1, M1, χ1, π1, φ1, θ1, J1, OO1, 2N2, μ2, ν2, λ2, L2 and T2) from a small number of them (M2, S2, N2, K2, K1, O1, P1 and Q1). However, one must remember that spectrum extension using admittance functions becomes much less accurate in shallow waters regions. Also, additional non-linear tides might be required to accurately capture the tidal elevation and currents in some regions, typically inside the English Channel.

C. Applications in TELEMAC for JMJ and NEA databases

A steering subroutine for tide may be useful for users (TIDAL_MODEL_T2D or TIDAL_MODEL_T3D) where some parameters that are not defined as keywords may be changed, in particular for the JMJ database.

A tidal harmonic constants file can be generated directly within TELEMAC for the JMJ tidal database [2], whereas it has to be done outside TELEMAC for NEA in version 6.2 (with COMODO tools [8]). The reason for using such a file rather than storing whole databases locally is to save memory. When using tidal databases from OSU (e.g. TPXO, AO or ES), there is no need to generate a harmonic constants file. When using the JMJ model, TELEMAC interpolates the harmonic constants for nodes at the open boundaries of the local numerical model for the JMJ tidal database.

Many mesh coordinates are able to be dealt with in the JMJ or OSU tidal databases:

- WGS84 UTM (North or South) - Universal Transverse Mercator,
- NTF Lambert (1 North, 2 Center, 2 Extended, 3 South, 4 Corsica),
- Mercator for TELEMAC.

Although classical mesh coordinates that are already implemented are strongly recommended for use in building TELEMAC models, users can employ their own geographic system. However, they would have to implement, for themselves, the conversion formulae from the specific system to the geographic WGS84 system (longitude/latitude in decimal degrees). For JMJ, indicating mesh coordinates is necessary only when generating the harmonic constants file; this is not needed for only calculating open boundary conditions with the use of a tidal harmonic constants file that has been generated previously). When needed, the geographic system must be declared as a keyword.

Boundary conditions (water depth and/or horizontal components of velocity when they vary in time) are then calculated at each time step for open boundary nodes.

To calculate the nodal factors ($f_i(t)$, $v_i(t)$) and the phase at the original time of the simulation (u_i^0), Pugh's formulae [9] are used for the JMJ database, whereas Schureman's formulae [10] are used for the NEA database. For these two

databases, different options are available for calculating the multiplier nodal factors $f_i(t)$:

- nodal factors are calculated at the beginning of the computation and are then frozen,
- nodal factors are calculated at each time step.

Three calibration parameters are available for adjusting the results when calculating open boundary conditions. These are keywords for both TELEMAC-2D and TELEMAC-3D:

- one multiplier coefficient to calibrate tidal ranges (called CTIDE in TELEMAC subroutines),
- one multiplier coefficient to calibrate velocities (called CTIDEV in TELEMAC subroutines),
- one multiplier coefficient to calibrate sea level (called MSL in TELEMAC subroutines).

In practice, the previous formulae become:

$$h = \text{CTIDE} \, \Sigma \, h_i - z_f + \text{MSL} \quad (6)$$

$$U = \text{CTIDEV} \, \Sigma \, U_i \quad (7)$$

$$V = \text{CTIDEV} \, \Sigma \, V_i \quad (8)$$

Reference date and hour must be entered in the steering file before simulation (which can be different from the beginning of the simulation).

III. TEST CASE

A. General presentation

A coastal model is used to compare the results of TELEMAC-2D simulations when using the different databases of harmonic constants to force open boundary conditions. This case is a local model of a candidate area to welcome tidal current turbines off Paimpol-Bréhat (in Brittany) in France, connected to the grid in order to generate electricity from the energy of tidal currents. The original aim of using this numerical model is to characterise the area with respect to tidal current potential (tidal currents and the evaluation of tidal energy yield) [11],[12]. ADCP measurements are used to calibrate and to compare the results of the model when using the different databases of harmonic constants. Paimpol-Bréhat tidal current site is located in the English Channel off the coast of Brittany (in the French department of Côtes-d'Armor). The principal port in the zone is Paimpol

B. At sea measurements

Several measurement campaigns were carried out in the Bréhat zone. For this study, only the results of one of these (a campaign lasting three months) are used. This three-month campaign was carried out during spring of 2008 (from the end of March to the end of June). Two ADCPs were deployed to measure flow velocity (magnitude and direction) over the full water column. The two ADCPs were located 0.5 to 1.7 km from the potential site (points 1 and 2 (2008) and around 1.5 km distant from one another, as illustrated in Fig. 4).

During the campaign in 2008, the maximum velocities during flood were somewhat greater than during ebb at the Paimpol-Bréhat site. The tidal rose is asymmetric (in magnitude and direction). The flow is bidirectional with two predominant directions: around 120° clockwise relative to north during flood (i.e. south-east) and around 320° during ebb (i.e. north-west), which means that ebb and flood are not at perfectly opposed angles (but on a bearing of around 200°).

C. Numerical modelling presentation

The area covered by the model is almost square, extending approximately 60 km from north to south and from west to east, respectively. Its extent can be seen in Fig. 4. No tidal current turbines are modelled in this TELEMAC model.

The digital bathymetric data of the zone were purchased from the French Navy Hydrographic and Oceanographic Service (©Copyright 2007 SHOM. Produced with the permission of SHOM. Contract number 67/2007). These consist of probes and a Digital Elevation Model covering the English Channel and Atlantic Ocean metropolitan coasts. Once the location of the potential site was determined, an additional bathymetry measurement campaign was carried out. Fig. 4 represents the bathymetry of the numerical model over the entire study domain.

The mesh used for this numerical model is a finite element mesh generated with the aid of the MATISSE v1.0 grid-generation software. It consists of 14,129 nodes and 27,425 triangular elements. The element size varies from 300 m at the coast to approximately 1.6 km in the zones of the greatest depths (to the west and north of the model). The mesh is progressively refined to 50 m, specifically at potential installation sites for tidal turbines (the zone of interest).

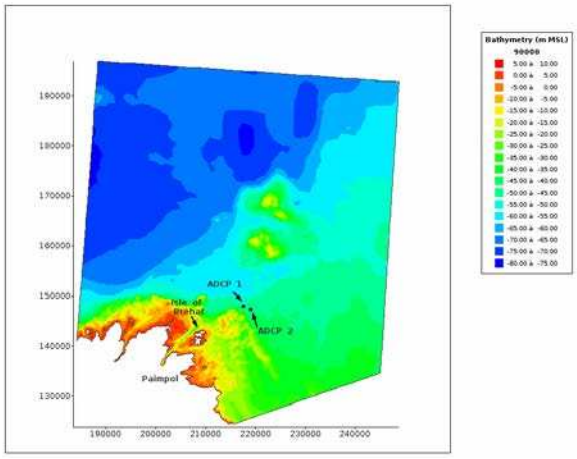

Figure 4. Bathymetry of Paimpol-Bréhat model and location of ADCP deployment.

The physical parameters chosen for the TELEMAC-2D model are the following:

- the dissipation through bed friction is modelled using a uniform Strickler coefficient over the entire study domain,
- the Coriolis effect is taken into account. Neither meteorological effects (wind, atmospheric pressure, surge/wane) nor wave effects are considered. Therefore, all flow velocities shown henceforth only take into account the astronomic tide,
- no specific turbulence model is employed. Therefore, a constant coefficient of viscosity equal to the default value of 10^{-4} is applied over the whole domain.

The chosen numerical parameters of the TELEMAC-2D model are the following:

- the discretisation uses linear triangular elements (P1) with matrix storage by segments, to optimise calculation times,
- equations are solved in the wave equation form,
- the numerical scheme used for the advection of velocities is the method of characteristics,
- for solving the propagation step, the conjugate gradient method has been chosen, with a diagonal preconditioning,
- the boundary conditions for the open liquid boundaries at which the tidal conditions (depth and/or velocity) are imposed are treated using the Thompson method with calculation of characteristics,
- for the suppression of free-surface parasite oscillations, the keyword FREE SURFACE GRADIENT COMPATIBILITY is taken to equal 0.5,
- the chosen time step is 20 s.

To take account of the tidal flats, a correction of the free surface computations by elements is used. Moreover, in order to ensure that water depths remain positive over the entire study domain (particularly given the presence of tidal flats), the following innovation, introduced from TELEMAC version 6.0 onward, is used: no upwind for SUPG, total mass-lumping for depth, correction of velocities at the points with imposed depth where the continuity equation has not been solved and a treatment to suppress negative depths by a limitation of fluxes.

Some specific treatments to model tides are used (the first three of which have been available to use routinely since version 6.2, the treatments for which are described in subsection II.C). Tidal signals for the boundary conditions at the liquid open boundaries are reconstructed from the three databases of harmonic constants, with some variants (see subsection II.B). Two calibration parameters are used in order to correctly reproduce the tidal range and the velocities on the zone (at ADCP locations). The initial conditions on the free surface and velocities are established from the local European Shelf solution, the harmonic constants of which are stored in the binary database for tides. For sea level calibration, it has been found to be necessary to introduce a non-constant mean sea level over the extent of the domain, in order to correctly calibrate the sea levels at the ports on the zone. Thus, a “pseudo” mean level has been generated based on the JMJ numerical model that covers the near Atlantic Ocean, the English Channel and the southern part of the North Sea. These data are read from a binary data file in Serafin format and used in the CORFON subroutine to change the bottom elevation reference.

The TELEMAC-2D computations are carried out on the EDF R&D IBM Debian “Ivanoé” cluster (200 TFlops). The processor specifications are as follows: 24 GB RAM per node (1 node = 2 hexa-core processors, running at 2.93 GHz). The CPU time required for a 4 or 5 day (resp. 3 month) simulation is approximately 1 min (resp. 25 min) for a 12-processor run.

D. Results

Data used to calibrate and compare the results that are obtained using the numerical models of the Paimpol-Bréhat zone come from SHOM data (particularly tidal sea levels) and results from measurement (ADCPs deployed at sea, see subsection III.B).

Models using different databases of harmonic constants have been calibrated with ADCP measurements at two locations during a four-day period from June 3rd to 6th 2008 that corresponds to spring tides. With the use of the two coefficients to calibrate tidal range and tidal velocities and a Strickler coefficient to model the friction through the bed, the various numerical models have been calibrated.

As described in subsection III.C, dissipation through bed friction is modelled with a Strickler coefficient that is uniform over the entire study domain. It is set at 27 $m^{1/3}/s$. The choice of a Strickler coefficient value of 27 (rather than 25 or 30, for example) was made when calibrating the model with the JMJ model to reproduce the maximum velocity during flood in early June 2008. This value has been retained when using the other databases of harmonic constants.

Then, with the chosen parameters, three months corresponding to the duration of the ADCP measurements are simulated and compared. In particular, two periods of spring tides are looked at closely (approximately one and two months before the period of calibration, i.e. April 5th to 9th and May 4th to 8th 2008).

Figs. 5 to 8 illustrate the time series of water depths at the two ADCP locations (ADCP measurements are illustrated by red points, the TELEMAC-2D model by continuous lines); Figs. 5 and 6 show a fragment of the period of time used to calibrate the model (from June 4th to 5th) whereas Figs. 7 and 8 show the two fragments of periods of time to compare the results at location 2. Figs. 9 to 14 illustrate the time series of

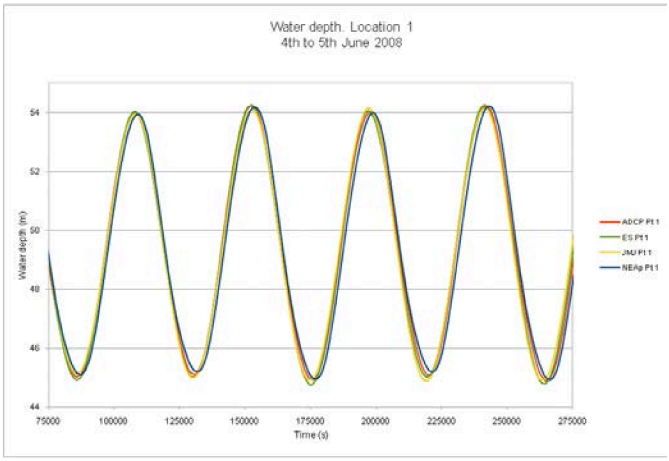

Figure 5. Water depth time series. Comparison between ADCP measurements (in red) and TELEMAC-2D results from June 4th to 5th 2008 at location 1.

Figure 6. Water depth time series. Comparison between ADCP measurements (in red) and TELEMAC-2D results from June 4th to 5th 2008 at location 2.

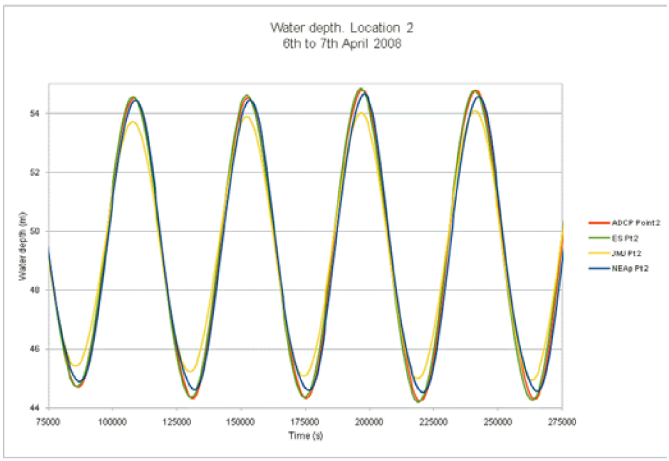

Figure 7. Water depth time series. Comparison between ADCP measurements (in red) and TELEMAC-2D results from April 6th to 7th 2008 at location 2.

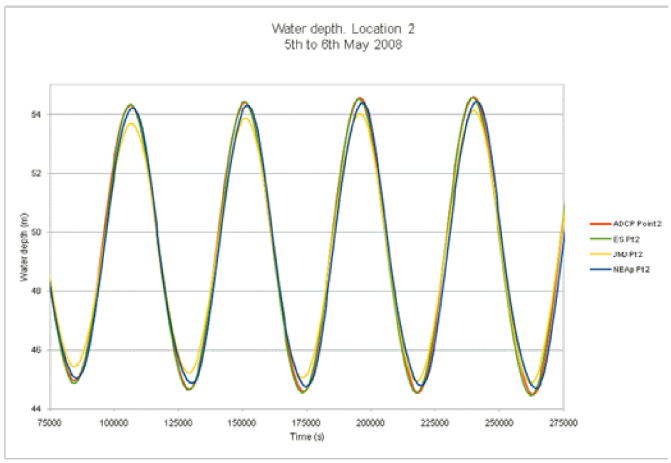

Figure 8. Water depth time series. Comparison between ADCP measurements (in red) and TELEMAC-2D results from May 5th to 6th 2008 at location 2.

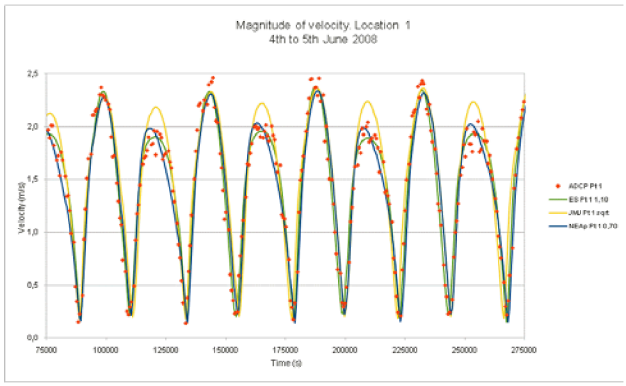

Figure 9. Magnitude of (vertically averaged) current velocity time series. Comparison between ADCP measurements (in red) and TELEMAC-2D results from June 4th to 5th 2008 at location 1.

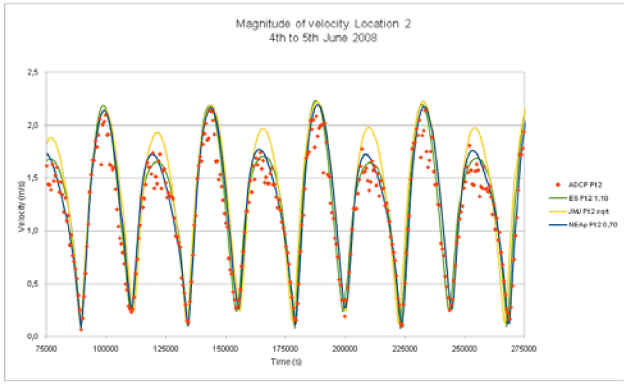

Figure 10. Magnitude of (vertically averaged) current velocity time series. Comparison between ADCP measurements (in red) and TELEMAC-2D results from June 4th to 5th 2008 at location 2.

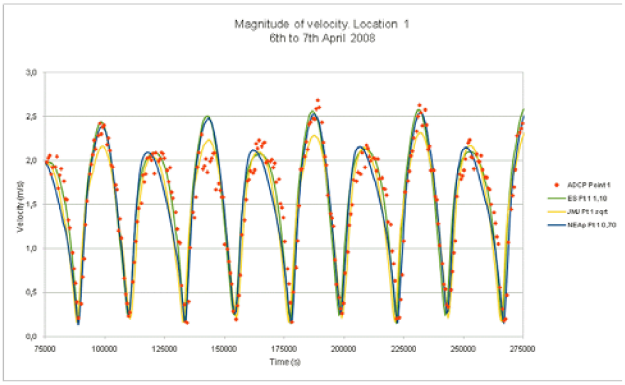

Figure 11. Magnitude of (vertically averaged) current velocity time series. Comparison between ADCP measurements (in red) and TELEMAC-2D results from April 6[th] to 7[th] 2008 at location 1.

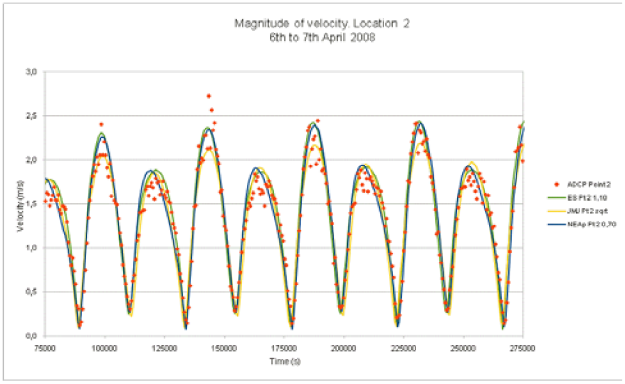

Figure 12. Magnitude of (vertically averaged) current velocity time series. Comparison between ADCP measurements (in red) and TELEMAC-2D results from April 6[th] to 7[th] 2008 at location 2.

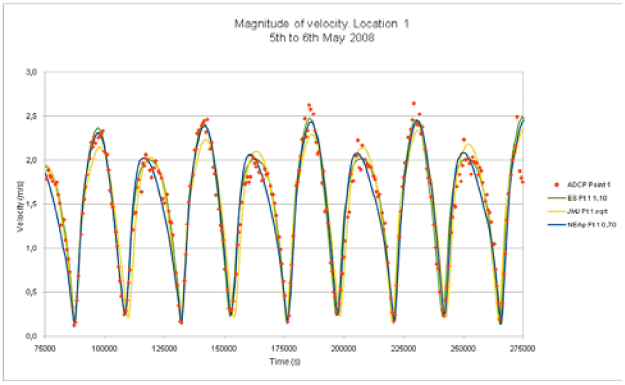

Figure 13. Magnitude of (vertically averaged) current velocity time series. Comparison between ADCP measurements (in red) and TELEMAC-2D results from May 5[th] to 6[th] 2008 at location 1.

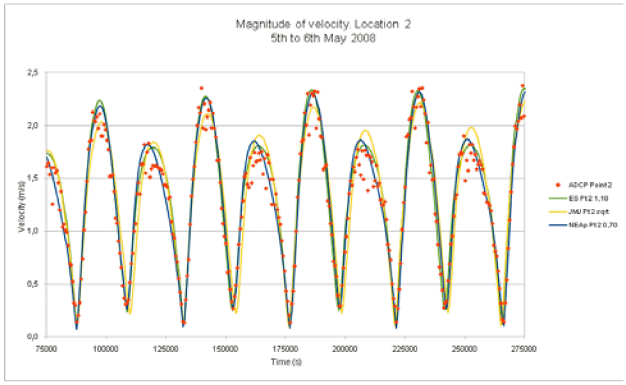

Figure 14. Magnitude of (vertically averaged) current velocity time series. Comparison between ADCP measurements (in red) and TELEMAC-2D results from May 5[th] to 6[th] 2008 at location 2.

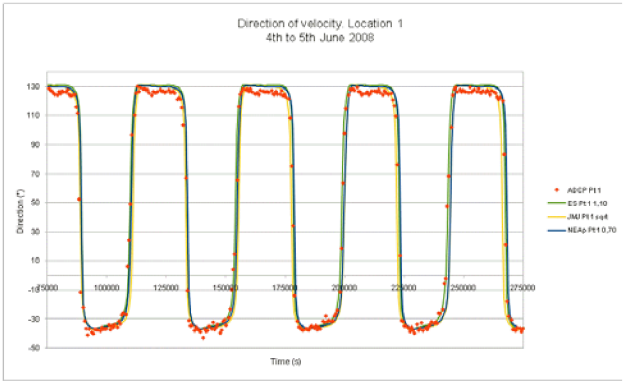

Figure 15. Direction of (vertically averaged) current velocity time series. Comparison between ADCP measurements (in red) and TELEMAC-2D results from June 4[th] to 5[th] 2008 at location 1.

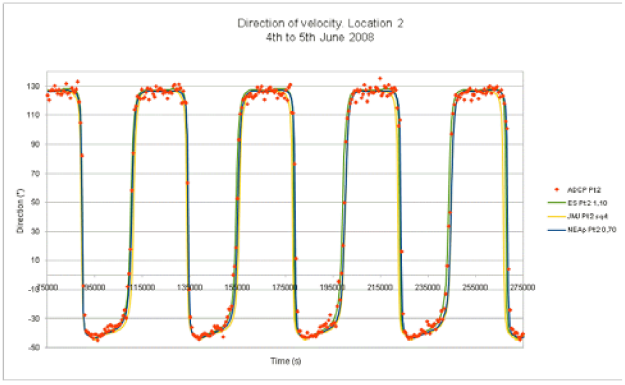

Figure 16. Direction of (vertically averaged) current velocity time series. Comparison between ADCP measurements (in red) and TELEMAC-2D results from June 4[th] to 5[th] 2008 at location 2.

the magnitude of vertically-averaged current velocity, at the two ADCP locations (ADCP measurements are illustrated by red points, theTELEMAC-2D model by continuous lines);

Figs. 9 and 10 show a fragment of the period of time used to calibrate the model (from June 4th to 5th) whereas Figs. 11 to 14 show the two fragments of periods of time to compare the results.

During the four-day period to be calibrated, tidal ranges are well reproduced for all databases, although slightly better for the various OSU solutions (TPXO, AO, ES, etc.) and the NEA atlas. Nevertheless, some differences can be seen when comparing velocities: velocities modelled with the local ES solution or the NEA atlas match rather well with ADCP measurements at the two ADCP locations, whereas the JMJ model is not able to accurately reproduce the maximum flood and ebb velocities with the same choice of calibration parameters.

The qualitative concurrence between the velocities simulated in the model and the measurements is quite satisfactory with regard to measurement points 1 and 2 of the spring 2008 campaign (particularly for direction: see Figs. 15 and 16).

These conclusions are strongly corroborated by simulating the full three months; even tidal ranges are not well reproduced using the JMJ database.

With the regional Atlantic Ocean solution or the TPXO global solution from OSU, huge velocities may appear in the domain in some cases, coming from areas where tidal flats may be present (velocities may be high due to the division of transport by the water depth in the subroutines). Local solutions seem to be required when modelling coastal areas (such as the European Shelf solution). This is confirmed on the website of the OSU Tidal Data Inversion [7]. The larger models covering an ocean or the globe seem to be more useful when tidal flats do not appear.

The optimal assimilated solution for the NEA allows for tidal range results to be reproduced as well as with the prior NEA solution (the hydrodynamic solution that is not assimilated). However, for this test case, velocities are reproduced less well.

IV. CONCLUSION AND PROSPECTS

New developments for modelling tides have been incorporated into version 6.2 of TELEMAC (2D and 3D). Users are now able to calculate open boundary conditions from various databases of harmonic constants, in particular over the European coasts along the Atlantic Ocean, the English Channel or the North Sea, but also all over the world with the solutions from Oregon State University (TPXO global tidal solution and the regional and local tidal solutions). This paper briefly describes the various databases and how they have been implemented in version 6.2 of TELEMAC. A coastal test case is described and used to compare with the results obtained using open boundary conditions calculated with these various databases. European Shelf (ES) and North East Atlantic (NEA) give quite good and solid results for this test case (for elevation and velocities).

A manual is to be published on modelling tides with these various databases in version 6.2 of TELEMAC. Other databases will be available in the future for use with TELEMAC, such as FES2004 global atlas, and the forthcoming (December 2012) FES2012 global atlas from LEGOS. FES2012 atlas will provide tidal currents in addition to tidal elevations (see [13] for project details). One major improvement (compared to previous atlases) is the increased accuracy and resolution of bathymetry that has been used in the production of the prior (i.e. hydrodynamic) tidal solutions. In addition to 2D atlases, a new, experimental tidal 3D currents atlas is in preparation for the NEA domain, expected to be released in early 2013. Finally, CTOH (LEGOS) has released a tidal elevation dataset for shelf/coastal seas derived from along-track altimetry observations [14]. Modelling tides has become less challenging for TELEMAC users.

REFERENCES

[1] J.-M. Janin, X. Blanchard. “Simulation des courants de marée en Manche et Proche Atlantique,” EDF DER–LNH report HE-42/92.58, 1992. [Simulation of tidal flows in the English Channel and the close Atlantic Ocean].

[2] C.-T. Pham. “Méthodologie pour la simulation de la marée en Manche et proche Atlantique avec TELEMAC-2D,” EDF R&D-LNHE report H-P74-2011-02581-FR, 2012. [Methodology to model tides in the English Channel and near Atlantic Ocean with version 6.1 of TELEMAC-2D].

[3] I. L. Pairaud, F. Lyard, F. Auclair, T. Letellier, P. Marsaleix. “Dynamics of the semi-diurnal and quarter-diurnal internal tides in the Bay of Biscay. Part 1: Barotropic tides,” Continental Shelf Research vol. 28 (1011), 2008, pp. 1294–1315.

[4] I. L. Pairaud, F. Auclair, P. Marsaleix, F. Lyard, A. Pichon. “Dynamics of the semi-diurnal and quarter-diurnal internal tides in the Bay of Biscay. Part 2: Baroclinic tides,” Continental Shelf Research vol. 30 (3-4), 2010, pp. 253–269.

[5] http://www.legos.obs-mip.fr/recherches/equipes/ecola/outils-produits

[6] http://sirocco.omp.obs-mip.fr/outils/Tugo/Produits/TugoProduits.htm

[7] http://volkov.oce.orst.edu/tides/

[8] http://www.legos.obs-mip.fr/recherches/equipes/ecola/outils-produits/comodo-tools

[9] D. T. Pugh,. Tides, Surges and Mean Sea-Level, John Wiley & Sons, . 1987, reprinted in 1996

[10] P. Schureman, Manual of harmonic analysis and prediction of tides. U.S. Coast and Geodetic Survey, 1924, reprinted in 1971.

[11] C.-T. Pham, V. A. Martin, “Tidal current turbine demonstration farm in Paimpol-Bréhat (Brittany): tidal characterisation and energy yield evaluation with Telemac,” EWTEC 2009 Proceedings, Uppsala, Sweden, 2009.

[12] C.-T. Pham, K. Pinte, “Paimpol-Bréhat tidal turbine demonstration farm (Brittany): optimisation of the layout, wake effects and energy yield evaluation using Telemac,” ICOE 2010 Proceedings, Bilbao, Spain, 2010.

[13] http://www.legos.obs-mip.fr/recherches/equipes/ecola/projets/fes2012

[14] http://ctoh.legos.obs-mip.fr/products/coastal-products/coastal-products-1/tidal-constants

Simulation of Density-Driven Flow Using a Two-Dimensional Surface Water Model

Mohamed Mahgoub, Reinhard Hinkelmann
Chair of Water Resources Management and Modeling of Hydrosystems
Technische Universität Berlin
Berlin, Germany
mohamed.mahgoub@wahyd.tu-berlin.de

***Abstract*— To understand and quantify the effect of horizontal density variation on the behaviour of two-dimensional (2D) models, three test cases were investigated, two theoretical cases of a rectangular channel and a trapezoidal channel and the third is a real case of the Nile estuary at Rosetta close to the Mediterranean Sea. Having the ability to include the spatial variation of density, TELEMAC-2D modelling system which solves 2D (depth averaged) Saint-Venant equations was used for this purpose.**

For these three cases, three scenarios were simulated in stagnant and flowing water: horizontal density variation only, diffusion only and both density variation and diffusion together. The three scenarios were considered in case of stagnant water for the two theoretical cases; the simulations in flowing water are then closer to the real conditions of the Nile.

The results show that the impact for the density variation is higher than that of diffusion. The results further show that the shape of the cross section (rectangular or trapezoidal) has a considerable influence on the results which was not expected. It can be concluded that the effect of horizontal density variation should be taken into account in 2D simulations of the Nile or other tideless estuaries.

I. INTRODUCTION

The anticipated sea level rise due to climate change could have great impact on estuaries and river mouths. The balance status that is present currently between fresh water and saline water in river mouths could change. Such phenomenon has to be considered in modelling of surface water at estuaries [9]. Meanwhile, estuaries are characterised by the presence of density-driven flow, where the variation of density due to salinity difference forces the saltwater landward. In a tideless sea, as the case of the Mediterranean Sea, the estuary is characterised by strong stratification and saltwater intrusion into the river system. The saltwater layer underlies the freshwater layer of the river [4].

The stratification effect cannot be modelled in a 2D model, because the concentration is averaged over the depth. Nevertheless, the effect of spatial density variation (in the horizontal direction) as a function of salinity concentration can be considered in a 2D model leading to a barotropic and baroclinic pressure gradient (Fig. 1).

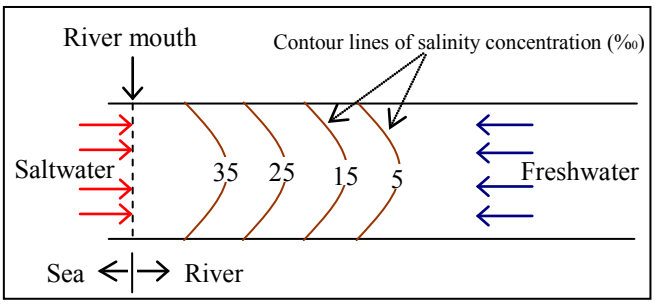

Figure 1. Schematic plan for the spatial variation of salinity at an estuary.

Therefore, the aim of this research is to understand and quantify the effect of horizontal density variation using the method presented in [5] which is detailed hereafter and is embedded in the code of the TELEMAC-2D modelling system used in this research for modelling three test cases including one real case for the Nile River estuary.

II. GOVERNING EQUATIONS

A. Saint-Venant equations

The main governing equations in 2D surface water flow are 2D Saint-Venant equations which have been derived with averaging over the vertical. The equations in their non-conservative form can be written as follows:

Continuity equation

$$\frac{\partial h}{\partial t} + \vec{u} \cdot \overrightarrow{grad}(h) + h \cdot div\vec{u} = Sce \qquad (1)$$

Momentum equations

$$\frac{\partial u}{\partial t} + u\frac{\partial u}{\partial x} + \upsilon\frac{\partial u}{\partial y} = -g\frac{\partial Zs}{\partial x} + F_x + \frac{1}{h} div(h\nu_e \overrightarrow{grad}\, u) \qquad (2)$$

$$\frac{\partial \upsilon}{\partial t} + u\frac{\partial \upsilon}{\partial x} + \upsilon\frac{\partial \upsilon}{\partial y} = -g\frac{\partial Zs}{\partial x} + F_y + \frac{1}{h} div(h\nu_e \overrightarrow{grad}\, \upsilon) \qquad (3)$$

h is the water depth, u and v are the velocity components, Zs is the surface elevation, v_e is the diffusion (molecular turbulent and viscosity), g is the gravitational acceleration, Sce is source or sink of the flow, and F_x and F_y are source or sink terms for momentum; in this case the buoyancy forces due to spatial variation in density (detailed in section B.) and the terms due to bottom friction. The latter can be expressed according to Manning law as follows:

$$F_x^f = -\frac{u}{\cos\alpha \cdot h^{4/3}} gn^2 \sqrt{u^2+v^2} \quad (4)$$

$$F_y^f = -\frac{v}{\cos\alpha \cdot h^{4/3}} gn^2 \sqrt{u^2+v^2} \quad (5)$$

where n is Manning coefficient, α is the angle of bottom slope.

B. Spatial variation of density

The aforementioned equations (1, 2 and 3), as averaged over the vertical, cannot represent the stratification resulting from the vertical variations of density, itself a function of salinity or of the temperature [5].

However, it is possible to consider the horizontal variations in density by the method presented in [5]. If S is the salinity and θ is the temperature, water density (ρ) will be a function ρ (S,θ), where S and θ are variable in space and time. These variations cause two effects which are dilatation of water and differential effects of gravity [5].

The dilatation of water is a secondary effect which can be ignored. The differential effect of gravity due to variations in salinity is very important especially in estuaries, therefore it should be considered. Hervouet [5] used Boussinesq's hypothesis which accounts for the variations in salinity only in terms of gravity.

According to [6], the buoyancy terms in Saint-Venant equations can be integrated from those of Navier-Stokes equation as follows:

$$-\frac{1}{\rho_0}\overrightarrow{grad}\left[\rho g(Zs-z)\right] \quad (6)$$

Z is the elevation of the bottom. Integrating this term between the bottom and the surface while considering the spatial variations of the density will produce two terms which are in the non-conservative form [6]:

- Barotropic pressure gradient: $-\frac{\rho}{\rho_0} g \overrightarrow{\text{grad}}\, Zs$, this term will replace the term $g\overrightarrow{\text{grad}}Zs$ in equations (2) and (3).
- Baroclinic pressure gradient: $-\frac{g}{\rho_0}\frac{h}{2}\overrightarrow{grad}\,\rho$, this term will be added to the bottom friction (4 and 5) to give F_x and F_y in equations (2) and (3).

The density is calculated from the following equation:

$$\rho = \rho_{ref}\left[1-(7(\theta-\theta_{ref})^2-750S)10^{-6}\right] \quad (7)$$

θ_{ref} denotes the reference temperature of 4°C and ρ_{ref} is the reference density at zero salinity (equals to 999.72 kg/m^3).

C. Transport equation

The transport equation in its non-conservative form in 2D can be written as follows:

$$\frac{\partial T}{\partial t} + \vec{u}\overrightarrow{grad}\,T - \frac{1}{h} div(\nu_t \overrightarrow{grad} T) = \frac{(T_{sce}-T)Sce}{h} \quad (8)$$

T is the tracer concentration, T_{sce} is the source value of the tracer and v_t is the diffusion coefficient (molecular and turbulent diffusion).

III. MODELLING SYSTEM

TELEMAC-2D modelling system has been chosen to set up a 2D numerical model for the test cases. TELEMAC-2D simulates open channel flow using Finite Element Method (FEM) for solving the two-dimensional Saint-Venant equations. TELEMAC-2D can consider the transport of a passive tracer. The primary variables are the water depth the velocity and the concentration of tracer averaged over the vertical [7]. The abovementioned equations for spatial variation of density are embedded in TELEMAC-2D, so it is suitable for the purpose of this research.

TELEMAC-2D allows the choice among several laws of friction, turbulence models, stabilisation methods and solvers. In this research the narrow (N) distributive scheme was used for the hydrodynamic and transport modelling. The solver applied in the research is the Generalised Minimum RESidual method (GMRES) for the non-symmetric matrices [11]. TELEMAC-2D generally uses linear triangular finite elements, but it can also work with quadrilateral elements.

TELEMAC-2D has been applied for numerous studies in fluvial and maritime hydraulics [1, 9 and 11]. The modelling process with TELEMAC-2D consists of pre-processing with MATISSE, processing and post-processing with RUBENS.

IV. TEST CASES

Three test cases were analysed in this research, two of them are theoretical cases of a rectangular channel and a trapezoidal channel and the third is a real case of the Nile estuary at Rosetta. For the two theoretical cases, four scenarios were modelled. These are:

1. Stagnant water with horizontal density variation only and ignoring diffusion
2. Stagnant water with diffusion only and ignoring horizontal density variation
3. Stagnant water with both diffusion and horizontal density variation
4. Flowing water with both diffusion and horizontal density variation

The aim of the previous scenarios was to check how the horizontal variation of density can affect the results and to compare its impact with the one of diffusion. In addition, the shape impact was also analysed. The simulations in flowing water are then closer to the real conditions of the Nile, so the scenarios 1, 2 and 3 were also modelled in this case but in flowing water instead of stagnant water.

A. Rectangular channel

The channel dimensions are 5 m, 200 m and 1000 m for the depth, the width and the length respectively, and with zero bottom slope. A triangular grid of 10 m discretisation length was generated by MATISSE; the grid was refined in the middle part of the channel where a 4 m discretisation length was used due to the choice of the initial conditions (see Fig. 3). The total number of nodes is 3303 and the total number of elements is 6344 (Fig. 2).

The channel has two open boundaries which are the upstream (U.S.) boundary, where the flow is given (zero in case of stagnant water and 80 m^3/s in case of flowing water) and zero salinity, and the downstream (D.S.) boundary where a water level of 5 m and a salinity concentration of 35 mg/l are imposed. Manning friction coefficient, similar to that of the Nile case, of 0.022 was employed here. The time step of the simulation was 5 seconds.

The initial condition for salinity was that half of the channel (starting from the D.S. boundary) was saline water and the other half was fresh water as shown in Fig. 3. The viscosity coefficient (molecular and turbulent) was assumed to be 0.001 m^2/s.

The simulation of the rectangular channel showed smaller impact for the diffusion than of density variation as shown in Fig. 4A and 4B for 100 days of simulation time. For longer simulation time the impact of density variation will be much bigger as it still shows slow change while for the case of diffusion no further change was noticed after 10 days of simulation.

As the impact in case of turbulent diffusion only was quite small, combining both diffusion and density variation showed very similar results as the case of density variation only (Fig. 4C).

When introducing a flow from the U.S. boundary (80 m^3/s), the saline water moved towards the D.S. boundary (Fig. 4D) very quickly (Fig. 4D shows the result after about 80 minutes only) due to the momentum produced from the flow velocity which is higher than the one due to the spatial variation of density. No doubt that changing the discharge will impact on the movement speed of the saline water.

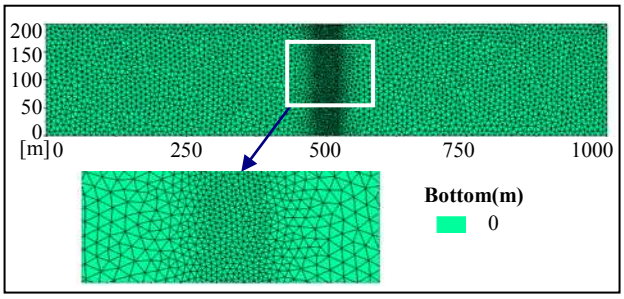

Figure 2. Grid of the rectangular channel.

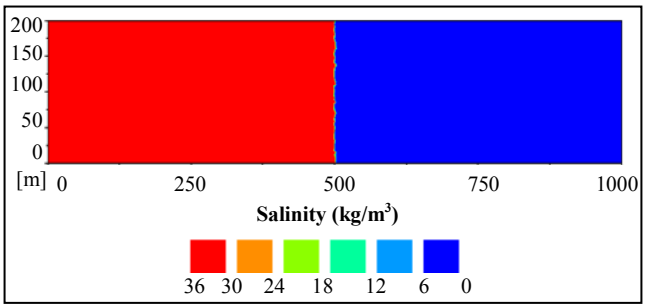

Figure 3. Initial conditions for salinity transport.

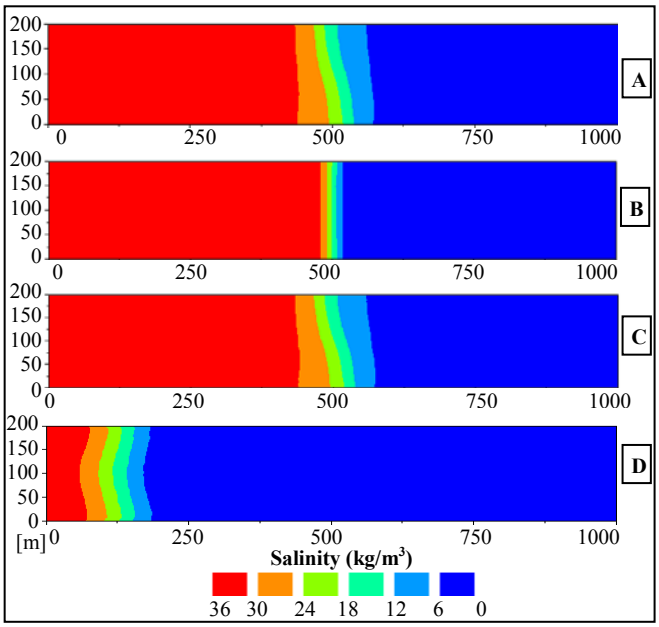

Figure 4. Salinity transport for the rectangular channel for A) stagnant water with horizontal density variation only, B) stagnant water with diffusion only, C) stagnant water with horizontal density variation and diffusion and D) flowing water with horizontal density variation and diffusion.

B. *Trapezoidal channel*

The channel has a total length of 1000 m; the cross section is shown in Fig. 5. The grid configurations, the boundary conditions and the numerical parameters are the same as in the previous case. The total number of nodes is 3325 and the total number of elements is 6388 (Fig. 6). The same initial condition shown in Fig. 3 is used in this case also.

The changes are faster in this case than in the case of the rectangular channel. After 10 days of simulation, an obvious difference can be noticed between the four modelled scenarios. In the case of horizontal density variation only, most of the channel is turned to be saline water, which means that the impact of the salinity difference forced the fresh water to leave the system (Fig. 7A).

Changes in the salinity concentration with respect to the depth variation are also noticed, where higher concentrations are in the deeper parts, this is consistent with the results of [3] where it was concluded that lateral variations of the depth cause a lateral variation of the turbulence and bottom friction which results in a tilt of the gravitational flow responsible for the density driven flow in 2D model. In addition, the horizontal pressure force due to horizontal density gradient is proportional to the depth; therefore the tendency of the heavier salty water to replace the lighter fresh water landward is stronger when increasing the depth [2].

The impact of turbulent diffusion was much smaller than the impact of density variation; it is limited in a small part in the middle of the channel (Fig. 7B). The influence of turbulent diffusion was quite similar in both the trapezoidal channel and the rectangular channel (Figs. 4B and 7B) which is not the case in the density variation impact.

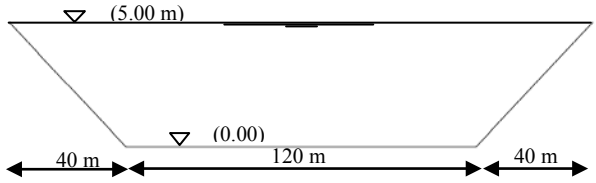

Figure 5. Cross section of the trapezoidal channel.

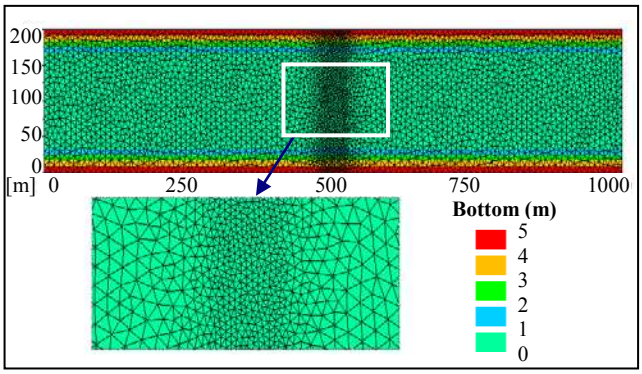

Figure 6. Grid of the trapezoidal channel.

When combining diffusion and density variation together (Fig. 7C), only a slight difference from the case of the density variation only can be seen; instead of the uniform variation with respect to the horizontal axes, the variation of salinity was only in the lower part of the channel.

Like the case of the rectangular channel mentioned earlier, introducing a slow flow to the system (80 m^3/s) caused that the saltwater moves towards the D.S. boundary (Fig. 7D). However the shape of the saltwater wedge is completely different form the case of the rectangular channel. That also emphasises the shape impact on the transport of salinity.

C. *River Nile estuary*

The last controlled reach of Rosetta branch of the Nile River (Fig. 8) is chosen to be compared to the theoretical cases. The reach under study is located between 31.32º and 31.45º north and 30.34º and 30.53º east with a total length of about 35 km. Edfina Barrage controls the flow in the reach under study at U.S. side, and it ends with the Mediterranean Sea at D.S. side.

The water depth ranges from 2.30 m to about 26.5 m. The average width of the domain is about 500 m. The average discharge during the year is 83.6 m^3/s and the average water level at D.S. is 0.37 m above mean sea level (+msl). The average discharge at the U.S. side and average sea level at D.S. side were used for the simulation.

A triangular grid is generated with MATISSE. The discritesation length of the elements is 40 m in parts of the domain, and in specific parts where the bottom level has a sharp slope and in the parts of small width a finer grid with

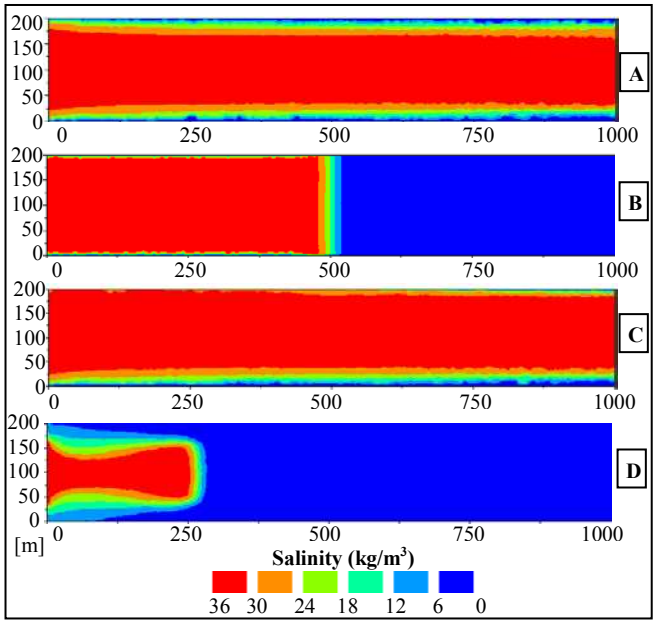

Figure 7. Salinity transport for the trapezoidal channel for A) stagnant water with horizontal density variation only, B) stagnant water with diffusion only, C) stagnant water with horizontal density variation and diffusion and D) flowing water with horizontal density variation and diffusion.

Figure 8. Map of the reach under study.

20 m discretisation length is generated. The total number of nodes is 19448 and the total number of elements is 36669 (Fig. 9).

The model is bounded from its U.S. side by Edfina Barrage where the discharge is known and from the D.S. side with the Mediterranean Sea where the water level is known, so those are considered the only two open boundaries in the domain and all the other boundaries, mainly the banks, are closed.

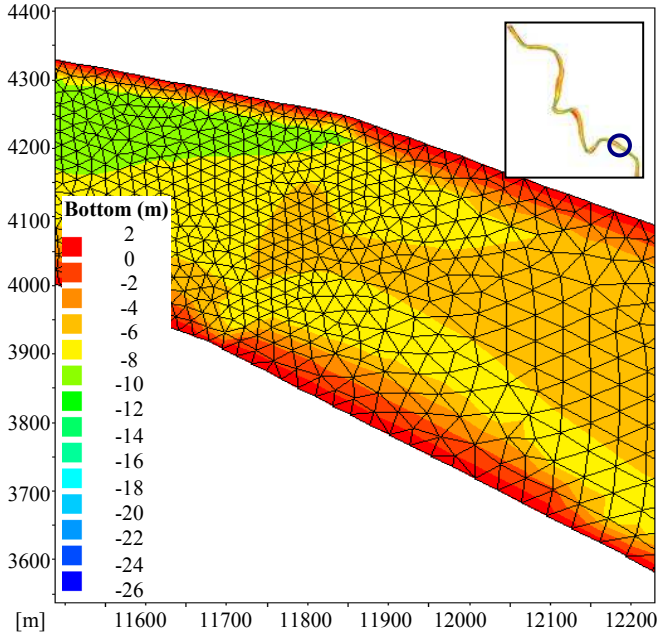

Figure 9. Grid at one position for Nile estuary case.

The simulation was carried out with a time step of 5 seconds. A total simulation time of three days was carried out to reach a steady state condition assuming an initial condition of zero velocity and initial water level of 0.37 m+msl. This steady state case was later employed as initial condition for the transport simulation. Manning friction coefficient of 0.022 [7] and a simple turbulence model with constant viscosity (ν = 0.01 m²/s) being equal to the turbulent diffusion were chosen. The initial condition for salinity concentration was calculated based on the following equation [9]:

$$L_i = \frac{2h_0}{0.5R_e^{-0.25}}\left(\frac{1}{2Fr_{do}^2} - 2 + 3Fr_{do}^{2/3} - \frac{6}{5}Fr_{do}^{4/3}\right) \quad (9)$$

L_i is the intrusion length of the saline water inside the river, R_e is the Reynolds number which is expressed as $4R_h\, u_0 /\nu$, Fr_{do} is the densimetric Froude number which expressed as $u_0 / \sqrt{g\Delta\rho h_0 / \rho}$, h_0 is the water depth at the river mouth, R_h is the hydraulic radius, u_0 is the velocity of river flow at the mouth, ρ is the fresh water density, $\Delta\rho$ is the density difference between saltwater and fresh water and g is the gravitational acceleration. Equation (9) was used to calculate the total length of saltwater intrusion inside the river considering the D.S. boundary with a salinity concentration of 38.5 kg/m^3, the intrusion length was found to be 15329 m. Then a linear change of the concentration was assumed, so the initial condition of salt concentration was set to be as shown in Fig. 10.

Comparing the results after one day of simulation time for the case of horizontal density variation only to the case of turbulent diffusion only (Figs. 11A and 11B) showed that the intrusion length was rapidly decreased in both cases (if

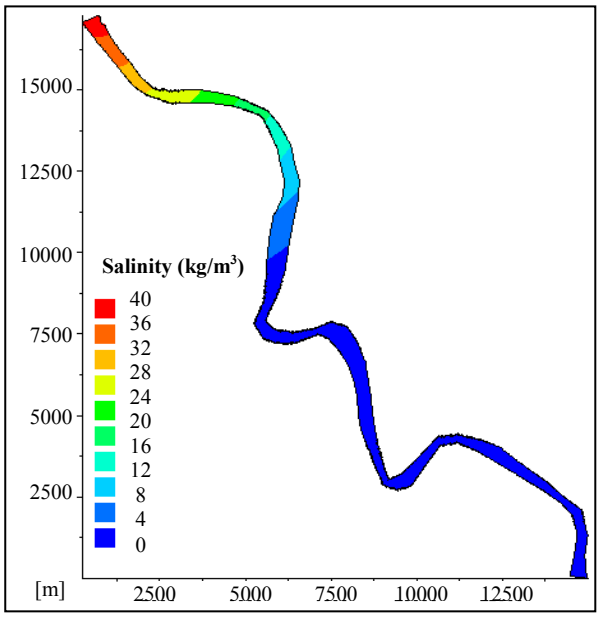

Figure 10. Initial conditions of salt concentration.

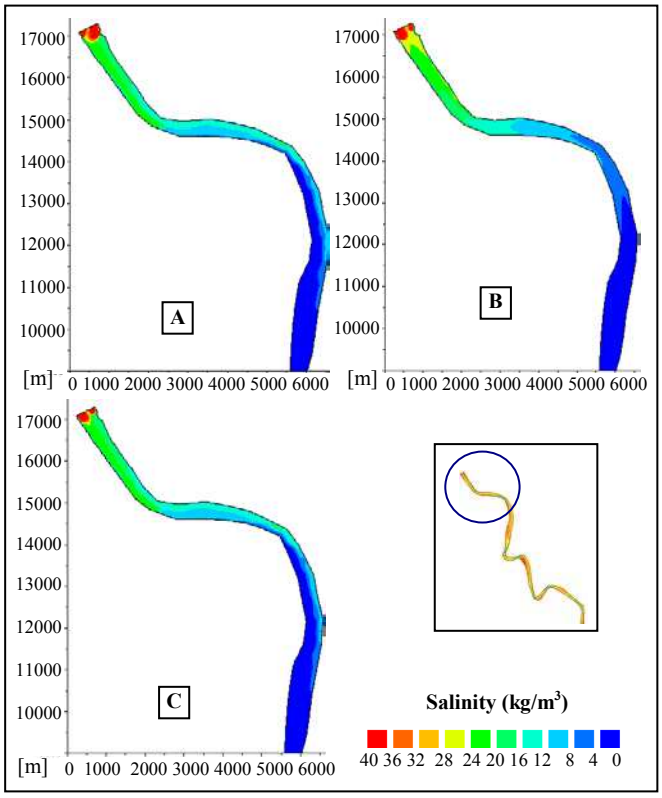

Figure 11. Salt concentration after one day of simulation time for the Nile estuary for: A) horizontal density variation only, B) turbulent diffusion only and C) horizontal density variation and turbulent diffusion.

compared to the initial conditions), however it was less in the case of the turbulent diffusion only. So, the impact of density variation is quite higher than the turbulent diffusion as it causes more momentum, therefore it has higher tendency to resist the momentum of the flow.

For the case of both turbulent diffusion and horizontal variation of density together (Fig. 11C) the results seem to be similar to the one of horizontal variation of density only (Fig. 11A). The results of the Nile case is the same result found in the two theoretical cases described earlier (higher impact for horizontal variation of density than diffusion). However, the results differ much from the initial condition of salinity concentration, which could be because the 1D nature of the equation used for calculating the initial condition.

V. CONCLUSIONS

TELEMAC-2D modelling system was used in this research to understand and quantify the impact of the spatial variation of density in a 2D model with the aid of the method presented in [5]. In addition, the impacts of diffusion and density variation on the flow were compared.

The simulation of the all the case studies revealed that the impact of density variation is higher than the turbulent diffusion. The shape influenced the results, where much faster change is noticed in the trapezoidal channel (approximately the whole domain turned to be saltwater in 10 days simulation time), while the change was quite slow in the rectangular channel. However, the impact of the shape was recorded only for the case of horizontal variation of density and it was not observed for the case of diffusion, thereof the diffusion is independent of the shape. The effect of the water depth was also noticed; higher salt concentration was combined with higher water depth (as described in the case of trapezoidal channel).

For the Nile case study, smaller saltwater intrusion length was also noticed for the case of diffusion only compared to the case of horizontal variation of density for the same simulation conditions, which could be related to the higher momentum caused by the horizontal variation of density. This result confirms the previous ones.

Through this research, it was proved that 2D models can be employed to simulate horizontal density-driven flow and TELEMAC-2D modelling system is suitable for this purpose. In addition, this research emphasises the importance of including the spatial variation of density when simulating tideless estuaries as in the case of the Nile River.

REFERENCES

[1] A. Jourieh, M. Heinl, R. Hinkelmann and M. Barjenbruch, “Simulation of Combined Sewer Overflows Spreading in a Slowly Flowing Urban River“, 33rd IAHR Congress: Water Engineering for a Sustainable Environment, Vancouver, British Columbia, Canada, ISBN: 978-90-78046-08-0, 2009.

[2] C. Li and A. Valle-Levinson, “Separating baroclinc flow from tidally induced flow in estuaries”, Journal of Geophysical Research, vol. 103, No. C5, 405-10,417, 1998.

[3] D. V. Hansen and M. Ratrray, “Gravitational circulation in straits and estuaries”, Journal of Marine Research, vol. 23, pp. 104-22, 1965.

[4] H. Chanson, "Environmental hydraulics of open channel flows", Elsevier Butterworth-Heinemann Linacre House, ISBN: 0750661658, 2004.

[5] J. M. Hervouet, “Hydrodynamics of Free Surface Flows, modelling with the finite element method”, John Wiley and Sons Ltd., England, ISBN 987-0-470-03558-0, 2007.

[6] LNHE, National Hydraulics and Environment Laboratory, “telemac2d concept note”, http://www.opentelemac.org/downloads/MANUALS /TELEMAC2D/prin30_gb.pdf, 2010.

[7] LNHE, National Hydraulics and Environment Laboratory, “telemac2d user manual”, http://www.opentelemac.org/downloads/MANUALS /TELEMAC2D/telemac2d_user_manual_v6p0.pdf, 2010.

[8] M. K. Mahmoud, A. El-Balasy and E. A. El-Ghorab, “Mathematical model of the sedimentation problem at Rosetta promontory”, Tenth International Water Technology Conference, IWTC10, Alexandria, Egypt, 2006.

[9] M. Mahgoub, A. Jourieh and R. Hinkelmann, “Two-dimensional flow and transport simulation of the Nile estuary investigating impacts of sea level rise”, 2nd IAHR Europe Congress, Munich, Germany, June 2012.

[10] M. Markofsky, “Strömungsmechanische Aspekte der Wasser-qualität“, Oldenbourg Verlag, München, Deutschland, 1980.

[11] R. Hinkelmann, “Efficient Numerical Methods and Information-Processing Techniques for Modeling Hydro- und Environmental Systems”, Lecture Notes in Applied and Computational Mechanics, vol. 21, Springer-Verlag, Berlin, Heidelberg, 2005.

HR Wallingford
Working with water

Proceedings of the

XIXth TELEMAC-MASCARET User Conference

18 to 19 October 2012, St Hugh's College, Oxford

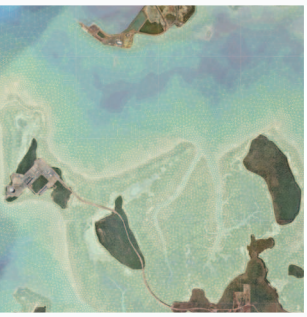

ISBN 978-1-898485-15-5